

# **An Innovative Design for a Separate Sewer System**

*By*

ALAA HENOU ABBAS

A thesis submitted in partial fulfilment of the  
requirements of Liverpool John Moores University  
for the degree of Doctor of Philosophy

Jan 2019

## **Abstract**

The Environmental Protection Agency (EPA) has stated that what was considered state-of-the-art pollution control a century ago is no longer valid today. Designers of new sewer systems must identify the problems inherited from old design concepts and try to use new technology to revisit and upgrade traditional urban drainage management. Separate sewer systems are currently used in all new developments. They are more prevalent than combined sewer systems, the use of which is limited due to numerous environmental regulations. However, the narrow streets commonly found in the UK, Europe and other densely populated areas, are usually occupied by a complex network of infrastructure services, making providing space to place a traditional separate sewer system is therefore challenging.

This research presents an innovative design for manholes, created to overcome the challenges associated with the installation of separate sewer systems in narrow streets. The proposed manhole combines two traditional manholes into one structure with two separate chambers, allowing storm flow and foul flow to pass through the same manhole without mixing. The structural performance and hydraulic properties of the new design have been tested using mathematical modelling, finite element (FE) and computational fluid dynamic modelling (CFD), validated by experimental testing. The results have been compared with the performance of conventional manholes. Testing of the new manhole when buried in soil revealed high stability and resistance under applied traffic loads. With regards to the hydraulic performance of the new manhole, the head loss coefficient and pattern of shockwaves were studied for both manholes (new and conventional),

under the same conditions, using independent, dimensionless parameters for each manhole. The new manhole generates higher head losses, about twice the head loss generated in a conventional manhole. Four shockwaves were identified in the storm chamber of the new manhole, the locations and characteristics of these also determined. The new manhole required a new configuration to setup the two pipes in one trench, the storm pipe over the sanitary pipe. The behaviours of these two flexible pipes were tested using a 3D finite element (FE) model, validated against experimental data from a laboratory investigation. A modified Drucker–Prager soil constitutive model was used to simulate elasto-plastic soil behaviour. The results show that this approach, using a large-diameter flexible pipe set above a small-diameter flexible pipe, mitigates the strain on the smaller pipe and decreases the total deflection of both pipes and the soil. These results led to further development of the Iowa Formula so that it can calculate the deflections of two flexible pipes set in one trench. The Improved Iowa formula was tested and compared with the experimental results.

The use of the new system promises to reduce construction costs, footprint and construction time. The storage capacity and retention time increased by 280% and 200%, respectively.

This new system is an attempt to improve the concept of the design of traditional sewer systems which have been in use for approximately one hundred years. The new system design can be used to install a new separate sewer system or used to separate existing combined sewer systems.

## Acknowledgments

*I would like to express my deep gratitude to:*

- My supervisory team: Mrs Felicite Ruddock, Prof. Rafid Al Khaddar and Dr. Glynn Rothwell.
- The advisory team: Prof. Robert Andoh and the wonderful Dr. Iacopo Carnacina.
- The IP advisor Dr Alison Hardy and United Utilities: Mr. Steve Dempsey and Ms Laura Conroy.
- The wonderful members of staff Liz, Laura, Alexia, Tricia, Natasha and Dr. Bill Atherton
- My inspiration: Prof Adnan Alsimawai
- The wonderful technical staff: Mr. Mal Feegan, Dr. Jeff Cullen, Mr. Gary Lamb, Mr. Ian Munford, Mr. Alan Jones, Mr. Michael Earner, Mr. Chris Byrne, Mr. Neil Kilpatrick and Mr. Anthony Owens.
- The Maritime and Mechanical Engineering Department team: Dr. Mehdi Seddighi, Dr. David Allanson, Dr. Ariyan Ashkanfar, Mr Paul, Mr Steven, Mr. Nail and Mr. Khaled Takrouri.
- The Ministry of Higher Education and Scientific Research in Iraq and the culture attaché staff in London.
- My fellows in the Hub: Anmar, Hassnen, the three Ali's, Hayder, Islem, Salah, Khalid, Ameer, Mohammed, Layth, Keith, Vijay and Kure...
- My brilliant colleagues in Al Ghalowa Company: Razaq, Sadiq, Ahmed, Anwar, Mustafa, Safa, Bahaa, Dr. Sizar, Eng. Salih, Dr. Ghassan, Dr. Muhaned, Eng Khalid and Dr. Tariq....
- My dear parents, sisters and brothers
- My supportive and lovely wife Mrs Massara Abbas and my children.

*Without all of you, this would never have been achieved.*



## **Declaration**

The research reported in this thesis was conducted at Liverpool John Moores University, Civil Engineering Department, between May 2015 and November 2018. I declare that the work is my own and has not been submitted for a degree at any other university.

Alaa H. Abbas

November 2018

## Table of Contents

CHAPTER 1	INTRODUCTION .....	1-23
1.1	Background.....	1-23
1.2	Combined sewer systems .....	1-25
1.3	Separate sewer systems .....	1-26
1.4	Comparing combined and separate systems.....	1-28
1.5	Motivation for this research .....	1-29
1.6	Aim and objectives of the research.....	1-30
1.6.1	Aim.....	1-30
1.6.2	Objectives.....	1-31
1.6.3	Novelty.....	1-32
CHAPTER 2	LITERATURE REVIEW .....	2-33
2.1	Design criteria of sewer systems.....	2-33
2.1.1	Concepts of sewer system design .....	2-33
2.1.2	Computer models and mapping software .....	2-35
2.1.3	Cost.....	2-36
2.1.4	Time .....	2-36
2.1.5	Footprint .....	2-37
2.2	Innovative designs for separate sewer systems.....	2-37
2.2.1	Real-Time Control (RTC).....	2-38
2.2.2	Vacuum or pressurized sewer technology.....	2-39
2.2.3	Sustainable techniques.....	2-39
2.3	Manhole design .....	2-42
2.3.1	Design of the manhole .....	2-43
2.3.2	The structural performance of manholes.....	2-48
2.3.3	The hydraulic properties of manholes.....	2-52
2.3.4	Hydraulic Experiments for manholes .....	2-52
2.3.5	Computational fluid dynamics .....	2-58
2.4	Buried pipes .....	2-64
2.4.1	Empirical methods.....	2-64
2.4.2	FE Method.....	2-79
2.5	Summary.....	2-82
CHAPTER 3	RESEARCH METHODOLOGY AND CHARACTERISATION OF MATERIALS .....	3-84
3.1	Methodology.....	3-84
3.2	Material properties.....	3-86

3.2.1	Soil .....	3-87
3.2.2	Mechanical properties .....	3-88
3.2.3	Elasticity and plasticity properties of the soil .....	3-93
3.2.4	Pipe properties .....	3-107
3.2.5	Concrete and steel properties .....	3-110
3.3	Direct shear stress testing to identify soil-steel friction factors.....	3-111
3.4	Summary.....	3-112
CHAPTER 4 THE EXPERIMENTAL AND FE MODEL SETUP OF THE MANHOLE DESIGN .....		4-113
4.1	The design of the manhole .....	4-113
4.1.1	Conventional manhole.....	4-114
4.1.2	An innovative design for a manhole .....	4-115
4.2	Physical model of manhole.....	4-118
4.2.1	Prototype experimental results.....	4-124
4.3	The FE model .....	4-127
4.3.1	The FE model of the physical model.....	4-128
4.3.2	The full-scale FE manhole model.....	4-134
4.4	Summary.....	4-157
CHAPTER 5 HYDRAULIC MODELS OF THE MANHOLE.....		5-158
5.1	Hydraulic properties of the conventional manhole .....	5-159
5.2	Hydraulic performance of the new manhole design.....	5-162
5.2.1	Physical model .....	5-163
5.2.2	CFD model.....	5-182
5.3	Summary.....	5-204
CHAPTER 6 6-206		
BURIED PIPE MODELLING .....		6-206
6.1	The Physical Model.....	6-206
6.2	FE Model .....	6-214
6.2.1	FE model of physical model.....	6-214
6.2.2	Full-scale FE model.....	6-219
6.3	Development of the Iowa formula to calculate pipe deformation when set vertically in one trench .....	6-233
6.3.1	Distribution of load on buried pipes set vertically .....	6-234
6.3.2	Testing the improved Iowa formula.....	6-240
6.4	Summary.....	6-244
CHAPTER 7 CONCLUSIONS AND ECOMMENDATIONS .....		7-246
7.1	Conclusions.....	7-246
7.2	Recommendations for further work .....	7-252

References	254
Appendices .....	268
Appendix I	268
(CD ) vidoes of the hydrylic exiperimentals applied on the manholes .....	268
Appendix II	Similitude of Applied Loads.....269
II.1	Physical Model.....269
II.1.1	Applied Load on Manhole .....271
II.1.2	Applied Load on the pipe.....271
II.2	Manhole Hydraulic physical Model.....273
Appendix III	ABAQUS Type of Elements.....275
III.1	Type of Elements.....275
III.1.1	Family .....275
III.1.2	Number of nodes.....276
III.1.3	Formulation .....277
III.1.4	Integration.....277
III.2	Continuum elements.....278
III.3	Beam elements .....278
III.4	The methodology followed for selecting elements .....279
Appendix IV	Correlation and Deriving Equations .....285
IV.1	Correlation of the results data .....285
IV.2	Derive equations from the results data.....292
Appendix V	List of Publications.....294
Published journal papers: .....	294
Journal papers under reviewing: .....	294
Published conference papers: .....	294
Patents:.....	295

## List of Figures

Figure 1.1. Elements of a typical urban drainage system (Rossman and Huber, 2016).....	1-24
Figure 1.2 Schematic diagram of a combined sewer system ((Butler and Davis, 2011)) .....	1-26
Figure 1.3 Schematic diagram of a separate sewer system ((Butler and Davis, 2011)).....	1-27
Figure 2.1 Concept of exfiltration system (Li et al, 2015) .....	2-41
Figure 2.2 Typical manhole detail (DEFRA, 2011). .....	2-43
Figure 2.3 Innovative rectangular manhole (a) plan view, (b) cross right section, (c) front cross section (Würmseher, 2014) .....	2-46
Figure 2.4 The combined-separate manhole patent by Willi (1998).....	2-47
Figure 2.5 Setup of manholes (1.2 m and 1.5 m) in the cell test (Sabouni and El Naggar, 2011b). .....	2-49
Figure 2.6 FE model for traditional manhole showing the vertical displacement (Najafi and Sever, 2015a) .....	2-51
Figure 2.7 Series of manholes model to simulate the head loss using re-circulating pipe system (Rubinato, 2015).....	2-53
Figure 2.8 Manhole head loss calculated experimentally (Sangster et al, 1958).....	2-54
Figure 2.9 An Improvement proposed to increase the dispersion in drop manhole using two types of Jet-breaker elements (Granata et al, 2014). .....	2-58
Figure 2.10 The energy loss coefficient with surcharge ratio for 218 mm manhole estimated by (Lau, 2007) .....	2-63
Figure 2.11 Influence of traffic load (H-20) and weight of soil on buried pipe (Corey, 2015)..	2-66
Figure 2.12 Pyramid methods for the distribution of live loads (Abbas et al, 2018).....	2-67
Figure 2.13 Marston's theory of transfer of the load to the buried pipe (Masada, 1996).....	2-69
Figure 2.14 When flexible pipes are used, low rigidity transfers part of the load to the soil because of its lateral deformation. ....	2-70
Figure 2.15 When rigid pipes are used, loads are absorbed by the pipe itself. ....	2-70
Figure 2.16 Spangler hypotheses of distributed stress on the buried pipe (Masada, 1996). ....	2-73
Figure 2.17 Comparison of experimental results with various analytical methods for HDPE pipe (Moser and Folkman, 2008).....	2-78
Figure 2.18 The three dimensions FE model for the buried pipe used by Corey (2015). ....	2-81

Figure 3.1 The set of sieves used to calculate the grain size distribution of the soil.....	3-88
Figure 3.2 Particle size distribution curve of the top soil.....	3-90
Figure 3.3 Particle size distribution curve of the bedding soil.....	3-90
Figure 3.4 Gas Jar Method to determine the specific gravity of the (a) top soil, and (b) bedding layer.....	3-91
Figure 3.5 The mould and compactor used to implement the compaction test.....	3-92
Figure 3.6 The curve of compaction .....	3-93
Figure 3.7 The Mohr-Coulomb failure model (ABAQUS, 2012). .....	3-95
Figure 3.8 The Linear Drucker-Prager Model (ABAQUS, 2012).....	3-97
Figure 3.9 The Mohr-Coulomb and Drucker-Prager models in the deviatoric plane (ABAQUS, 2012). .....	3-98
Figure 3.10 Yield surfaces of the modified Drucker-Prager cap model in the p-t plane. (ABAQUS, 2012). .....	3-99
Figure 3.11 Extracting the soil specimens from the trench.....	3-101
Figure 3.12 The apparatus for the triaxial test .....	3-101
Figure 3.13 Results of the three triaxial tests under different confining pressures.....	3-102
Figure 3.14 Mohr-Coulomb failure criterion.....	3-102
Figure 3.15 Shear stress ( $q$ ) – effective stress ( $p$ ) plotted to identify Drucker-Prager model parameters. ....	3-103
Figure 3.16 Three pieces of apparatus for the one-dimension consolidation test.....	3-104
Figure 3.17 Results of the consolidation test used to identify soil properties.....	3-104
Figure 3.18 Evaluating the modified cap model hardening curve. ....	3-106
Figure 3.19 Parallel-Plate Loading Method for testing pipe stiffness in the laboratory (a) the rig and (b) software (ASTM-D2412, 2008). ....	3-109
Figure 3.20 Direct shear test to identify the friction factor between the steel and filling soil.....	3-111
Figure 3.21 The results of direct shear test between the soil sample and steel plate to identify the friction factor to use in the FE model. ....	3-112
Figure 4.1 Schematic depiction of a cross-sectional view of conventional manholes in a traditional separate sewer system (with permission from Al Ghalowa). ....	4-115

Figure 4.2. 3D design of the innovative manhole.....	4-117
Figure 4.3 Cross section of the new manhole located in a separate sewer system in the street....	4-117
Figure 4.4 The prototype of the new manhole. External chamber = 0.25 x 0.25m, internal chamber = 0.1 x 0.3m.....	4-119
Figure 4.5 The prototype of the conventional manhole with dimensions 0.1 x 0.3m.....	4-119
Figure 4.6 Setup of the trench in the rig and location of measurement instruments on the new manhole surface at three points on the edge.....	4-121
Figure 4.7 Setup of the trench in the rig and location of measurement instruments on the conventional manhole surface at three points on the edge.....	4-123
Figure 4.8 Displacement of the new manhole under different live loads. ....	4-124
Figure 4.9 Displacement of conventional manhole under different live loads. ....	4-125
Figure 4.10 Comparison between the new and conventional manholes under the same conditions and live loads.....	4-126
Figure 4.11 The symmetrical quarter of the new manhole FE mesh model representing the full 3D manhole.....	4-129
Figure 4.12 The symmetrical quarter of the conventional manhole FE mesh model representing the full 3D manhole.....	4-129
Figure 4.13 The displacement of the new manhole at a double heavy load, shown in a 3D quarter symmetric FEA model.....	4-130
Figure 4.14 The displacement at different categories of loads for the centre of manhole along the depth below the new manhole design. ....	4-131
Figure 4.15 Comparison of the displacements from both the experimental work and the FE model for the new manhole in soil, under live loads. ....	4-131
Figure 4.16 The displacement of the traditional manhole at a double heavy load, shown in a 3D quarter symmetric FEA model.....	4-132
Figure 4.17 The displacement at different categories of loads for the centre of manhole along the depth below the conventional manhole.....	4-132
Figure 4.18 Comparison of the displacement results from both experimental works and the FE model for the conventional manhole prototype in soil under live loads. ....	4-133
Figure 4.19 Configuration of the real scale new manhole-soil model. ....	4-135
Figure 4.20 Configuration of the real scale conventional manhole-soil model. ....	4-135

Figure 4.21 The configuration of the manhole cover: (a) the new manhole (b) the conventional manhole .....	4-136
Figure 4.22 Two applied loads on the new manhole (a) two wheels on the storm chamber cover (b) one wheel on the sewage chamber cover. ....	4-137
Figure 4.23 Details of the steel reinforcements for (a) the new manhole and, (b) the conventional manhole. ....	4-138
Figure 4.24 Using hybrid materials to build a new manhole; reinforced concrete for the outer chamber and GRP for the inner chamber. ....	4-139
Figure 4.25 Samples of FE simulation output for the new manhole design exposed to 2HS25 on the storm chamber covers. ....	4-140
Figure 4.26 Displacement of the non-reinforced new manhole under a one wheel applied load on the one cover of the sewage chamber. ....	4-141
Figure 4.27 Displacement of the non-reinforced new manhole under a one wheel applied load on the one cover of the storm chamber. ....	4-141
Figure 4.28 Displacement of the non-reinforced new manhole under a two wheel applied load on both covers of the storm chamber. ....	4-142
Figure 4.29 Displacement of the new reinforced manhole under a one-wheel applied load on the sewage manhole cover. ....	4-143
Figure 4.30 Displacement of the new reinforced manhole under a two-wheel applied load on the storm chamber manholes covers.....	4-143
Figure 4.31 Sample of FE simulation the displacement output for the conventional manhole design exposed to 2HS25 on the manhole cover.....	4-145
Figure 4.32 Displacement of the non-reinforced conventional manhole under a one-wheel applied load.....	4-145
Figure 4.33 Displacement of the reinforced conventional manhole under a one-wheel applied load. ....	4-146
Figure 4.34 A comparison of the displacement for both manholes under different loads (FE model). ....	4-148
Figure 4.35 Displacement of the new manhole using a hybrid material (GRP for the inner walls and reinforced concrete for the outer walls), under a one-wheel applied load.....	4-149
Figure 4.36 Displacement of the new manhole using a hybrid material (GRP for the inner walls and reinforced concrete for the outer walls) under a two-wheel applied load.....	4-150
Figure 4.37 The strains and location of the maximum bending moment in the base of the new manhole body, under a double heavy load (2 x HS25). ....	4-155



Figure 4.38 The strains and location of the maximum bending moment in the base of the conventional manhole body, under a double heavy load (2 x HS25). .....	4-155
Figure 5.1 Velocity distribution and diffusion region in a circular manhole free jet (Alberston et al. 1948).....	5-160
Figure 5.2 Definition plot for flow through a conventional manhole (Gargano & Hager, 2002)....	5-160
Figure 5.3 The physical model used to test the hydraulic properties of the new manhole (a) cross section (b) top view showing the location of shockwaves and (c) the physical model in the laboratory.....	5-165
Figure 5.4 Top view of the new manhole showing the storm flow path and the three points of head loss generated inside the storm chamber. ....	5-167
Figure 5.5 (a) Total loss coefficient as a function of relative bend radius (R/D) and angle of curvature $\delta$ for $Re \geq 10^6$ , (b) Typical open channel bend structure on a treatment station (Hager, 2010). ....	5-169
Figure 5.6 A comparison between the head loss in the new and conventional manholes at different surcharge ratios ( $\beta_{im}$ ). ....	5-172
Figure 5.7 A comparison between the head loss in the new and conventional manholes at different filling ratios ( $\beta_{ip}$ ). ....	5-173
Figure 5.8 Relationship between the head loss coefficient and the non-dimensional dynamic momentum component ( $Fr_o \beta_{ip}$ ) for the new and conventional manholes. ....	5-174
Figure 5.9 The shockwaves generated in the new manhole design at difference filling ratios ( $\beta_{ip}$ ). ....	5-178
Figure 5.10 Shockwaves generated in the conventional manhole design at different filling ratios ( $\beta_{ip}$ ). ....	5-178
Figure 5.11 The amplitude of the average shockwaves ( $Y_i$ ) against the non-dimensional dynamic momentum component ( $Fr_o \beta_{ip}$ ) for both the conventional and the new manhole.....	5-180
Figure 5.12 The wave amplitude ( $Y_i$ ) at different surcharge ratios ( $\beta_{im}$ ) for the flow in the new manhole at different flow rates. ....	5-182
Figure 5.13 The location of points selected to produce the CFD results in (a) the new manhole, and (b) the conventional manhole. ....	5-184
Figure 5.14 A comparison between the velocities measured at the centre of both the CFD and the physical model manholes. ....	5-187
Figure 5.15 A comparison between the differences of head pressure measured at the inlet and outlet of manhole for both the CFD and the physical model. ....	5-187
Figure 5.16 The pattern of flow in the conventional manhole at different flow rates.....	5-193

Figure 5.17 Turbulent amplitude in the conventional manhole at different flow rates using the velocity in x direction as indicator. ....	5-194
Figure 5.18 A comparison between the velocities measured at the centre of the new manhole for both the CFD and physical model. ....	5-196
Figure 5.19 A comparison between the differences in head pressure measured at the inlet and outlet of the new manhole for both the CFD and physical model. ....	5-196
Figure 5.20 The pattern of flow in the new manhole at different flow rates.....	5-201
Figure 5.21 Turbulent amplitude in the new manhole design at different flow rates using the velocity in x direction as the indicator.....	5-202
Figure 5.22 The amplitude of the average shockwaves ( $Y_i$ ) against non-dimensional Reynolds number ( $Re$ ) for both the conventional and new manhole.....	5-203
Figure 6.1 The physical model setup (a) setup of the trench in the hydraulic rig to test the performance of the buried structural pipes, (b) Cross section of the configuration of the physical model in the laboratory, equipped with measurement and recording devices and (c) The physical model in the lab.....	6-209
Figure 6.2 Strain on the small (sanitary) pipe during the soil-filling and compaction processes. 6-211	
Figure 6.3 Comparison of the deflection of the small (sanitary) pipe when set alone in the trench with that when set below a storm pipe under a series of applied live loads (a) H15, (b) H20 and (c) H25. ....	6-213
Figure 6.4 3D FE model used to simulate the physical laboratory model of one pipe set in a trench. ....	6-215
Figure 6.5 3D FE model used to simulate the physical laboratory model of two pipes set in one trench. ....	6-215
Figure 6.6 Visualization results for the FE model with two pipes set in one trench under an H20 live load.....	6-216
Figure 6.7 Comparison of the experimental and FE results for the deflection of the small (sanitary) pipe when set alone in the trench with that when it is set below a storm pipe under an applied (a) H20 live load (b) H25 live load.....	6-218
Figure 6.8 a and b. The model of a 300 mm diameter storm pipe and 200 mm diameter sanitary pipe in one trench.....	6-221
Figure 6.9 a and b. The model of a 1000 mm diameter storm pipe and 500 mm diameter sanitary pipe in one trench.....	6-222
Figure 6.10 Visualization results for the FE samples of the real-scale model when two pipes lie in one trench under an applied H20 live load.....	6-223

Figure 6.11 Comparison between the deflections of a storm pipe (300 mm) when set alone and when set above a sanitary pipe in one trench. ....	6-225
Figure 6.12 Comparison between the deflections of a sanitary pipe (200 mm) when set alone and when set below a storm pipe in one trench. ....	6-225
Figure 6.13 Comparison between the deflections of the soil surface in three cases for two pipes, and when either one sanitary pipe, or one storm pipe, are set in the trench. ....	6-226
Figure 6.14 Comparison between the deflections of the storm pipe (1000 mm) when set alone and when set above a sanitary pipe in one trench. ....	6-229
Figure 6.15 Comparison between the deflections of a storm pipe (1000 mm) when set alone and when set above a sanitary pipe in one trench using an asphalt layer on the surface. ....	6-229
Figure 6.16 Comparison between the deflections of the sanitary pipe (500 mm) when set alone and when set below a storm pipe (1000 mm) in one trench. ....	6-230
Figure 6.17 Comparison between the deflections of the soil surface under three cases for two pipes and when either one sanitary pipe or one storm pipe are in the trench for the second set. ....	6-231
Figure 6.18 Typical intersection between a sanitary pipe and a storm pipe in a traditional separate sewer system. ....	6-233
Figure 6.19 The pattern of load distributions for the flexible pipe (McGrath, 1998). ....	6-234
Figure 6.20 Hypothesized improvements in stress distribution between two flexible pipes: the large pipe at the top and small pipe at the bottom. ....	6-237
Figure 6.21 Nearly all the load from the top pipe will transfer to the bottom pipe when the bottom pipe is laid directly below the top pipe and is of the same size ( $\theta \approx 90^\circ$ ). ....	6-238
Figure 6.22 Comparison of deflection of the sanitary pipe when two pipes are set in one trench using the developed Iowa formula, the original Iowa formula and the experimental results. ....	6-241
Figure 6.23 The setup of the rig with equipment, sand and buried pipes for the new test. ....	6-243
Figure II.1 Sketch of the distribution of the applied load on the soil through the trench at the crown pipe level. ....	272
Figure III.1 Commonly used element family (ABAQUS, 2012). ....	276
Figure III.2 Linear brick, quadratic brick and modified tetrahedral elements (ABAQUS, 2012). ....	277
Figure III.3 Selecting the beam element type for the reinforcement bar in Abaqus FE manhole model. ....	280
Figure III.4 Selecting the continuum elements type for the manhole structure in Abaqus FE manhole model. ....	280

Figure III.5 Selecting the continuum elements type for the soil in Abaqus the FE manhole model.	281
Figure III.6 Selecting the continuum elements type for the system in Abaqus FE buried pipe model.	281
Figure III.7 Selecting the continuum elements type for the pipe in Abaqus FE buried pipe model.	282
Figure III.8 Identify the surface- surface contact regime between the manhole and the surrounding soil in Abaqus FE manhole model.	282
Figure III.9 Identify the surface- surface contact regime between the pipe and the surrounding soil in Abaqus FE buried pipe model.	283
Figure III.10 Identify the nonlinear solution for the step in Abaqus FE buried pipe model.	283
Figure III.11 Identify the number of increments for the step in Abaqus FE buried pipe model.	284
Figure III.12 Identify a full newton solution for the step in Abaqus FE buried pipe model.	284
Figure IV.1 The method used to calculate the $R^2$ for the results presented in Figure 4.15 comparison of the displacements from both the experimental work and the FE model for the new manhole in soil, under live loads.	285
Figure IV.2 The method used to calculate the $R^2$ for the results presented in Figure 4.18 comparison of the displacement results from both experimental works and the FE model for the conventional manhole prototype in soil under live loads.	286
Figure IV.3 The correlation between FE output and experimental results for sanitary pipe deflection, lying in the trench under H20 applied load showed in Figure 6.7 (a).	287
Figure IV.4 The correlation between FE output and experimental results for sanitary pipe deflection, lying in the trench below the storm pipe under H20 applied load showed in Figure 6.7 (a).	287
Figure IV.5 The correlation between FE output and experimental results for sanitary pipe deflection, lying in the trench under H25 applied load showed in Figure 6.7 (b).	288
Figure IV.6 The correlation between FE output and experimental results for sanitary pipe deflection, lying in the trench below the storm pipe under H25 applied load showed in Figure 6.7 (b).	288
Figure IV.7 The correlation between the CFD output and experimental results for the Figure 5.14 a comparison between the velocities measured at the centre of both the CFD and the physical model manholes.	289
Figure IV.8 The correlation between the CFD output and experimental results for the Figure 5.15 a comparison between the differences of head pressure measured at the inlet and outlet of manhole for both the CFD and the physical model.	289

Figure IV.9 The correlation between the CFD output and experimental results for the Figure 5.18 a comparison between the velocities measured at the centre of the new manhole for both the CFD and physical model.....	290
Figure IV.10 The correlation between the CFD output and experimental results for the Figure 5.19 a comparison between the differences in head pressure measured at the inlet and outlet of the new manhole for both the CFD and physical model.....	290
Figure IV.11 The correlation between the experimental results and improved Iowa formula output Figure 6.22 Comparison of deflection of the sanitary pipe when two pipes are set in one trench using the developed Iowa formula, the original Iowa formula and the experiment.....	291
Figure IV.12 Using Excel curve fit method to derive the equations for the data presented in Figure 5.8 relationship between the head loss coefficient and the non-dimensional dynamic momentum component ( $Fro\beta_{ip}$ ) for the new and conventional manholes.....	292
Figure IV.13 Using Excel curve fit method to derive the equations for the data presented in Figure 5.11 the amplitude of the average shockwaves ( $Y_i$ ) against the non-dimensional dynamic momentum component ( $Fro\beta_{ip}$ ) for both the conventional and the new manhole. ....	293
Figure IV.14 Using Excel curve fit method to derive the equations for the data presented in Figure 5.22 the amplitude of the average shockwaves ( $Y_i$ ) against non-dimensional Reynolds number ( $Re$ ) for both the conventional and new manhole.....	293

## List of Tables

Table 1.1: Advantages and disadvantages of combined and separate sewer systems .....	1-28
Table 2.1 The essential data required by most hydraulic model equations (Read, 2004) .....	2-34
Table 2.2 Recommended dimensions for the construction of new manholes (person entry) (DEFRA, 2011). .....	2-44
Table 2.3 Shape factor estimated by Pedersen and Mark (1990). .....	2-55
Table 2.4 Live load data for AASHTO H-20 and H-25 .....	2-67
Table 3-1 Results of Specific gravity (Gas Jar Method) for the filling soil and bedding .....	3-91
Table 3-2 Parameters of the modified Drucker–Prager cap and Mohr–Coulomb constitutive model for the soil and bedding layer .....	3-107
Table 3-3 Parameters of the PVC pipes. ....	3-108
Table 3-4 The parameters of non-reinforced concrete and steel used for FE the model (Najafi and Sever, 2015a) .....	3-110
Table 4-1 Summary of the displacement of the new manhole under different applied loads and type of material. ....	4-144
Table 4-2 Summary of the displacement of the conventional manhole under different applied loads and types of material. ....	4-146
Table 4-3 Percentage difference for the bending moment of each manhole base, the cracking moment and the maximum strain on the body of each manhole, exposed to a one-wheel load at the centre. ....	4-154
Table 4-4 Percentage difference for the bending moment of the manhole base, the cracking moment and the maximum strain on the body of the manhole, exposed to wheel loads on the storm chamber covers .....	4-157
Table 5-1 Experimental ranges of the main dimensionless parameters .....	5-171
Table 5-2 Validated setup parameters for the CFD model .....	5-185
Table 6-1 The mechanical properties of the sand. ....	6-242
Table 6-2 Comparison between the experimental results, the traditional Iowa formula and Improved Iowa formula .....	6-243
Table II-1 The applied load on the Physical model. ....	271
Table II-2 Live load data for AASHTO H-20 and H-25 .....	272

## **List of Abbreviations**

Cc	compression index
CFD	Computational Fluid Dynamics
Cs	swelling index
CSO	Combined Sewer Overflow
CSS	Combined sewer systems
EPA	Environmental Protection Agency
FEM	Finite element methods
FFF	First Foul Flush
Fs	Drucker-Prager failure surface
GRP	Glass fibre reinforced plastics
HDPE	High-density polyethylene
LID	Low Impact Development
PS	Pipe stiffness
PVC	Polyvinyl chloride
RTC	Real-time control
SF	stiffness factors
SSS	Separate sewer systems
SuDS	Sustainable drainage systems
VAF	vertical arching vector
WWTP	Waste Water Treatment Plant

## List of symbols

$A, B, b \text{ and } C$	Shockwaves generated in the new manhole (-)
$B_d$	width of trench (ft) or (m)
$M_{cr}$	cracking moment (kN-m)
$M_s$	constrained modulus of soil (MPa)
$S_H$	pipe hoop stiffness factor
$S_a$	bending stiffness factor, ratio of soil stiffness to pipe wall flexural stiffness
$V_o$	Approach flow velocity (m s <sup>-1</sup> )
$\Delta x \text{ and } \Delta y$	Horizontal and vertical pipe deflection (mm)
$B$	width of tyre footprint (m)
$B(x, y \text{ and } z)$	represents body accelerations acting on the continuum, for example gravity, inertial accelerations or electrostatic accelerations (m s <sup>-2</sup> )
$C_d$	load coefficient
$C_s$	load coefficient which is a function of $B_c / (2H)$ and $L / (2H)$
$d$	cohesion in the p-t plane
$DL$	deflection lag factor
$D_m$	Manhole diameter (m)
$D_p$	Approach pipe diameter (m)
$d\varepsilon, d\varepsilon^e \text{ and } d\varepsilon^p$	total strain, elastic strain and plastic strain
$E$	modulus elasticity of pipe material (MPa)



$e$	modulus of passive resistance of side fill
$E'$	Soil modulus of elasticity (MPa)
$e_0$	void ratio
$Fr_0$	Approach Froude number (-)
$F'$	impact factor (-)
$g$	Gravity acceleration ( $m\ s^{-2}$ )
$H$	height of fill from top of pipe to ground surface (ft) or (m)
$h_0$	Level of water in the manhole (m)
$I$	moment of inertia of pipe wall [ $mm^4/mm$ ]
$K$	ratio of active lateral unit pressure to vertical unit pressure ratio (-)
$K_{ND}$	Head loss coefficient (-) for the new manhole design
$K_0$	Head loss coefficient (-) for the conventional manhole
$L$	Length (m)
$L'$	effective length of conduit (3 ft or less)
$P$	pressure
$Q$	Discharge ( $m^3\ s^{-1}$ )
$r$	mean radius of pipe (m)
$Re$	Reynolds number (-)
S and E	Shockwaves generated in the conventional manhole (-)
$t$	Time (s)
$W$	wheel load (N)

$W_d$	load on rigid pipe ((lb/unit length) or (N/ unit length)
$W_s$	load on pipe (lb/unit length)
$Y_i$	Shockwaves' amplitudes (-), $Y_{i(ND)}$ for the new manhole design and $Y_{i(o)}$ for the conventional manhole.
$p'$	mean effective stress (kPa)
$\xi$	Shape factor
$\beta$	friction angle measured at high confining pressure
$\beta_{im}$	Ratio of surcharge for the manhole (-)
$\beta_{ip} = y_o$	Filling ratio in the approach pipe (-)
$\gamma$	unit weight of backfill (kN/m <sup>3</sup> )
$\Delta H$	Head loss (m)
$\rho$	Density kg m <sup>-3</sup>
$\sigma$	Compressive stress (kPa)
$\tau$	Shear stress (kPa)
$\mu'$	coefficient of friction (-)
$u, v \text{ and } w$	the flow velocity in x, y and z direction sequentially (m s <sup>-1</sup> )
$\nu = \mu/\rho$	kinematic viscosity (m <sup>2</sup> s <sup>-1</sup> )

# CHAPTER 1

## INTRODUCTION

### 1.1 Background

Rapidly increasing urbanization is causing problems regarding increased loads on existing sewer systems as result of replacing areas of vegetation with impermeable surfaces because of increases in city populations. This generates subsequent problems such as pollution, negative impacts on public health, increasing costs of managing sewerage systems and increased flash flooding because of heavy rain (Kleidorfer et al, 2014). These issues are likely to be exacerbated due to the impact of climate change (Abdellatif et al, 2015).

The aim of drainage systems designed at the beginning of the 19<sup>th</sup> century, was to drain away sewage and storm water from places of habitation to protect public health. Later in the mid-19<sup>th</sup> century, when society realized these systems caused pollution of the environment and water resources and were one of the main reasons for the spread of disease, water treatment plants for drinking water and waste water treatment plants for wastewater were established thus improving the general wellbeing of society (Camp, 1966).

The start of the 21<sup>st</sup> century saw the imposition of new infrastructure requirements in the form of sustainability, protection of public health and reduced costs. What was considered state-of-the-art pollution control a century ago is clearly no longer valid today (EPA, 2007). Designers of new sewer systems must identify the problems inherent in old designs and use the new technology

available today to revisit traditional urban drainage management with an innovative outlook. The sewer system is the main component of the sewerage system, this usually including sewer networks, pump stations and treatment plants (Figure 1.1).

The sewer system is the network of pipes used to drain stormwater caused by wet weather as well as the sewage from urban areas. Two systems are mainly used; the old one is a combined sewer, which uses a single pipe to convey both sanitary sewage and stormwater through a single pipe. The new one is a separate sewer system, by which two sets of pipes are used, one to drain the supposedly cleaner stormwater runoff to the nearest watercourse (rivers and lakes etc.) while the second set of pipes collects and conveys sewage water to a Waste Water Treatment Plant (WWTP).

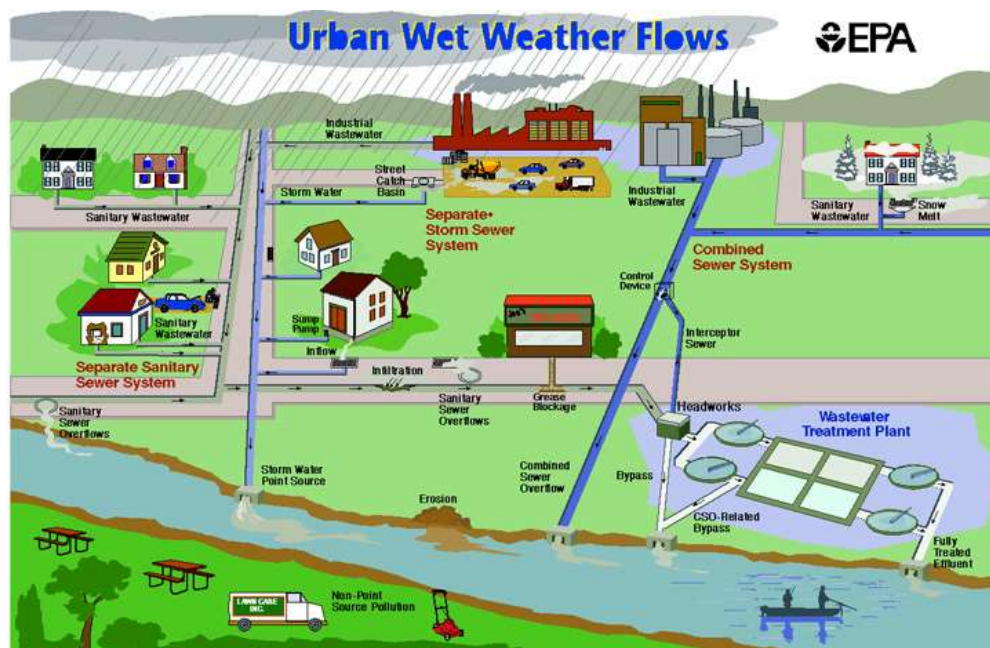


Figure 1.1. Elements of a typical urban drainage system (Rossman and Huber, 2016). [Reprinted with permission from Environmental Protection Agency (EPA)]

## 1.2 Combined sewer systems

The combined sewer system has been used widely, and effectively, in the past because it is a simple system; one pipe is designed to carry sewage water flow in dry weather as well as stormwater following wet weather. For that reason, the WWTP is designed to have a capacity of around three times the dry weather sewage flow. This system makes up about 70% of the sewer systems in the UK and in many EU countries such as Germany, France and Belgium (Read and Vickridge, 1997). However, an increase in the quantity and intensity of runoff during heavy rain events, can mean that the combined sewer system is unable to transfer all the flow to the WWTP within a short period of time to avoid flooding in urban areas. The combined sewage system is designed to release untreated overflow to natural waterbodies through a Combined Sewer Overflow (CSO) in order to keep the hydraulic load at a manageable level (Brombach, 2005). Figure 1.2 shows the location of a CSO within the schematic of a combined sewer system.

The CSO is normally used for flood control (Passerat et al., 2011), this structure diverting all flow which exceeds the design capacity, to the receiving watercourses, thus adding to the pollution load (Isel et al., 2014). CSOs also have a negative aesthetic impact. The Chartered Institution of Water and Environmental Management (CIWEM) considers CSOs to be technically and economically feasible safety valves for systems, even though they have some negative environmental impacts (Water UK, 2009). The number of CSOs in the UK is estimated to be in the region of 25,000, of which approximately one-third are considered to be 'unsatisfactory' (Thompson, 2012).

However, the most recent environmental regulations have banned the use of combined sewer systems, the system no longer designed except as limited extensions, or replacements, for existing combined systems (Bizier, 2007).

Since the middle of the last century, separate sewer systems have been designed to address this situation by increasing the capacity of the drainage system to carry run-off caused by heavy rain, via separate pipelines and thus avoid mixing wastewater and stormwater. Stormwater is discharged straight into a watercourse without being treated (Butler and Davis, 2011).

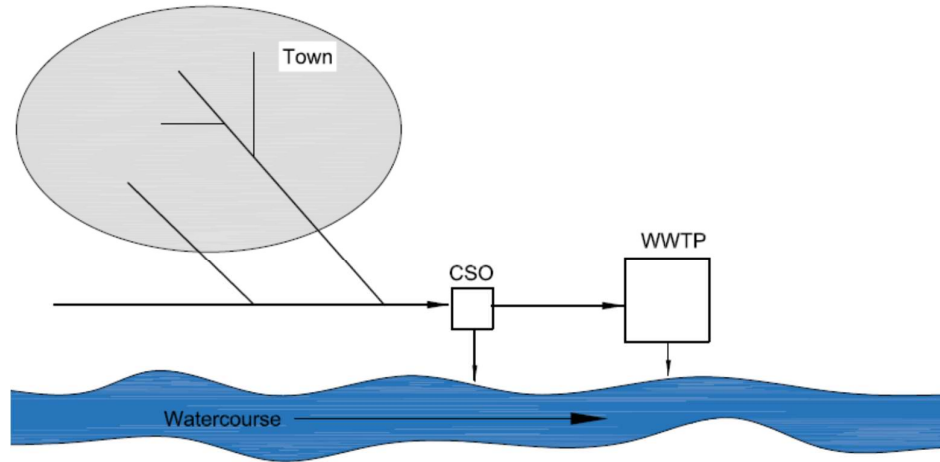


Figure 1.2 Schematic diagram of a combined sewer system (Butler and Davis, 2011). [Reprinted with permission from Taylor & Francis Informa UK Ltd - Books]

### 1.3 Separate sewer systems

Many countries have invested heavily in order to address the impact of CSOs, more so in the USA, where they have studied and evaluated CSO control strategies to effectively reduce, if not eliminate, CSOs and their associated health and ecological risks. One of the strategies often considered in new or exist urban

developments is **sewer separation**, which can be accomplished through installing a new storm or sanitary sewer to be used in conjunction with the existing sewer (Figure 1.3) (EPA), 1999; Costa et al. 2015). However, the cost of separating sewer systems is very expensive as it uses two set of pipelines. For example, the estimated cost to separate the existing sewer system in London is £12-20 billion, according to Ashley et al. (2007, cited in Myerscough and Digman, 2008, p 7). To avoid this cost, an innovative design was proposed to alleviate the impact of COSs in London, this reducing the cost to approximately £4 billion. The tideway tunnel has been designed to collect the overflow from all CSOs along the Thames River, to transport it outside London and gradually deliver it to a WWTP. The tunnel has a diameter of 7 metres and is situated about 65 metres underneath the river. It is approximately 23 km long (Thompson, 2012). This is a good example of how innovation can manage a complex problem.

However, the comparison between separate and combined sewer systems still constitutes ongoing discussion.

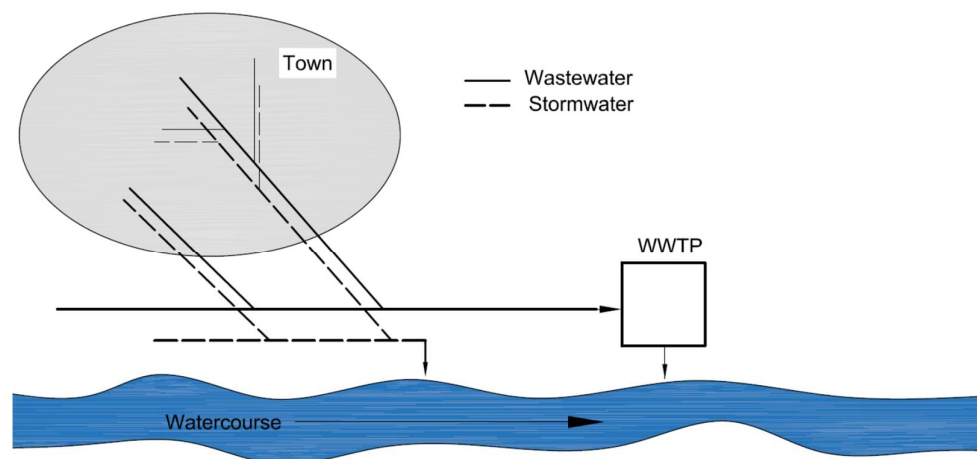


Figure 1.3 Schematic diagram of a separate sewer system (Butler and Davis, 2011). [Reprinted with permission from Taylor & Francis Informa UK Ltd - Books]

#### 1.4 Comparing combined and separate systems

There are two main features of these systems which still cause discussion: the high initial cost of separate systems and the pollution consequences of combined systems. Table 1.1 details the main advantages and disadvantages of both systems.

Table 1.1: Advantages and disadvantages of combined and separate sewer systems

Separate System	Combined System
<b><u>Advantages</u></b> <ul style="list-style-type: none"><li>➤ Less pollution on the watercourse</li><li>➤ Improvements in the hydraulic performance of the sanitary pipe.</li><li>➤ Reduced loading on treatment units.</li><li>➤ When it occurs, flooding comprises only of storm water.</li></ul> <b><u>Disadvantages</u></b> <ul style="list-style-type: none"><li>➤ Expensive as two sets of pipelines.</li><li>➤ Additional space is required to accommodate both pipes.</li><li>➤ There is a high probability of misconnection.</li></ul>	<b><u>Advantages</u></b> <ul style="list-style-type: none"><li>➤ Lower costs for initial pipe construction.</li><li>➤ The space occupied by the single pipe is smaller.</li></ul> <b><u>Disadvantages</u></b> <ul style="list-style-type: none"><li>➤ High levels of pollution caused by heavy rain on watercourses.</li><li>➤ The hydraulic design is complex as dry weather flow through is only sewage, this occupying approximately 20% of the pipe.</li></ul>



### 1.5 Motivation for this research

The economic factors (initial cost) and footprint are the main disadvantages of a traditional sewer system compared to a combined system. However, the economic factor is no longer acceptable as the main focus, as environmental and public health protection has become the main priority worldwide. To treat or address the consequences of pollution as a result of CSS overflow, costs more than the life time costs of the combined system. As such, the general move is towards separate sewer systems (Bizier, 2007).

The most up-to-date environmental regulations and infrastructure policies have banned the use of combined sewer systems in new developments, its use limited to replacing or extending, existing separate sewer systems. For example, in the UK, all new designs using separate sewer systems still link with a combined system somewhere in the network. However, starting the change to separate sewer systems (SSS), is to be ready for the future and the use of full separate sewer systems (DEFRA, 2011).

The cost of separate sewer systems and the space needed to install them are the main barriers to adoption, especially in the narrow streets prevalent in the UK, European cities and many densely populated cities around the world. These streets are already occupied by complex infrastructure services such as potable water, gas, electricity and communication lines, meaning that finding a space to place another sewer pipe is very challenging.

## 1.6 Aim and objectives of the research

### 1.6.1 *Aim*

Considering the above barriers regarding use of separate sewer systems, the author and supervisory team have entered into discussion with water services companies, including United Utilities, about plans for this research. The author has experience regarding the design of sewer systems in the Middle East, facing the same challenges for installation of traditional separate sewer systems in old cities, this the inspiration for the current research.

The aim of this research is to develop an optimum design for a sewer system, using an innovative design for a separate sewer system to decrease the cost, footprint and construction time, and overcome the challenge of installing separate sewer systems in narrow streets. An innovative design for a manhole for separate sewer systems is presented, the novel design allowing the storm flow and foul flow to pass through the same manhole without mixing. The new system gathers the advantages of a combined sewer system and a separate sewer system into one system, complying with 21<sup>st</sup> century requirements (sustainability, protection of public health and reduced cost), as one trench is used to accommodate two separate pipelines, storm pipe (upper) and sanitary pipe (lower).

This research will develop a novel design to separate the existing system, or to install a new system, in areas where space is a scarce of space to place two pipes in two trenches or one large trench. The results of this project will be discussed with reference to the industrial market and in direct comparison to use of conventional manholes.

### 1.6.2 *Objectives*

1- To carry out a comprehensive literature search to explore the innovative methods used to design separate sewer systems and identify the disadvantages of current sewer systems. To outline modifications to such systems to improve the proposed new design. This literature search will help to distinguish the current advances in sewer system design, establishing the novelty of the proposed design.

2- Soil is the media that accommodates sewer system structures both pipes and manholes, therefore, constitutive models to simulate the behaviour of soil are explored, an appropriate model selected to use in the finite element analyses.

3- The Iowa formula is the most popular empirical method to calculate the deflection of buried flexible pipes in a trench. However, this method is limited to testing only one pipe buried in a trench, so the Iowa formula will be improved to apply to two pipelines, overlapping or lying in a single trench, one over the other.

4- This is a novel design for manholes, so it is essential to examine its structural integrity. Both a physical model and FE models are used to assess the structural performance of the new manhole in comparison to the traditional manhole design. The correlation between manhole structure and soil will be investigated.

5- The novel design of the manhole is associated with new positions for two pipes in the separate sewer system i.e. one pipe on top of the other, the storm pipe at the top, the sanitary pipe at the bottom. The structural performance of this arrangement has not been discussed before, therefore, both a physical model and finite element model will be used to study the behaviour of two pipes laid in a single trench.

6- The new manhole design will generate a new pattern and pathway for stormwater flow inside the storm chamber. The hydraulic integrity and flow merits will be studied using a physical model in the lab and a computational fluid dynamic model (CFD). The hydraulic performance will be compared with the hydraulic performance of a traditional manhole.

7- The feasibility of the new system, compared to a traditional separate sewer system, will be discussed in terms of the initial cost, footprint, construction time and hydraulic properties.

### 1.6.3 *Novelty*

This research will develop a novel design to separate existing systems, or install new systems, in areas where there is limited space.

The traditional manhole was designed 150 years ago. The subsequent development of building materials and inspection and maintenance technology, has allowed advances in this old design. The current research will develop a novel manhole, gathering the two conventional manholes together into one structure with two separate chambers, one for stormwater flow, one for sewage flow.

This novel design entails the use of one trench to house both pipes, one over each other.

Both the new design of the manhole and the new configuration of the pipe system will bring many advantages which will be discussed in this thesis.

A patent application No. WO 2018/215746 A1 was submitted to register this design by LJMU.

## CHAPTER 2

### LITERATURE REVIEW

The literature review will consist of four sections. The first will discuss sewer system design concepts and criteria. The second explores innovations in sewer and drainage system designs and their modifications, and how these are used to improve old sewer or drainage systems. The third explains manhole design and characteristics, the fourth examining buried pipe performance.

#### 2.1 Design criteria of sewer systems

##### 2.1.1 *Concepts of sewer system design*

The goal of sewer design is to determine the pipe size required to carry sewage flow, or stormwater flow, and provide a smooth pipe gradient that keeps hydraulic properties within the limitations of sewer design criteria. Manholes used between pipelines, pipeline connections and pump stations are used to raise the hydraulic profile of networks when they have a depth more than that required by design criteria. Sewerage networks end at a WWTP, while storm systems discharge directly into the nearest watercourse (Duque et al, 2016).

A range of data are required in order to calculate the size and gradient of the pipe required for most hydraulic models, Table 2.1 listing the data required for most hydraulic model designs. These are key to determining a suitable diameter and gradient for each pipe in order to keep the flow velocity within the required range, to prevent grit settling (self-cleaning velocity) and also to prevent surcharge under design conditions (Nelson, 2007).

Table 2.1 The essential data required by most hydraulic model equations (Read, 2004)

Essential Data	Units SI	Required sub data
<b>The peak flow rate</b>	Volume per Time	This is extracted from the area served by the pipe by estimating the density of the population in said area and the average production of wastewater from each person. Rainfall intensity and the imperviousness rate for this area are used to estimate stormwater flow rates. Infiltration flow extracted from the catchment area is added to both sewage flow and storm flow in separate sewer systems.
<b>Suitable gradient for each pipe</b>	Length / Length	The topographic gradient, roughness of pipe (material) and pipe route are key to determining a suitable gradient for each pipe, keeping flow velocity within the required range and preventing settled grit (self-clean velocity) thus avoiding surcharges under design conditions.
<b>Optimum Layout of the networks</b>	NA	Awareness of the city master plan, including the existence of other infrastructure services such as water or electricity and ground gradient. This is key for the optimisation of the urban drainage system layout, to allow for an ideal and feasible sewer design (Li and Matthew, 1990)

Typically, combined sewer systems are designed to convey stormwater and sewage in one pipe. The diameter of the pipe needs to be accommodate both flows, so normally the pipes get bigger downstream of the network. The pipe works at full capacity when it rains but only partially in dry weather draining only sewage. The hydraulic design of a combined system is more complex than a separate system as the minimum flow velocity (self –clean velocity) has to be maintained during dry weather, this very challenging because the minimum stormwater flow is approximately 6-10 times the average wastewater flow during normal rain events, reaching 50-100 times the average in heavy rainfall (Butler and Davis, 2011). This wide range of stormflow and foul flow increases the possibility of

settlement of suspended solids on the bed of the pipe. This sediment can be flushed away later by the storm flow due to rain fall, in turn transporting a highly polluted load to watercourses if the system overflows at First Foul Flush (FFF) (Goormans et al, 2009).

#### 2.1.2 *Computer models and mapping software*

Designers need to be aware of the relationship of each element within the whole sewer system; its design, operation and maintenance. As such, it is important to define the roles of all the elements throughout the system (Jurišić et al., 2014). An awareness of the city master plan, including the existence of other infrastructure services such as water or electricity and ground gradient are also key for the optimisation of urban drainage system layout (Li and Matthew, 1990).

Computer models and mapping software have been very helpful to designers and authorities, enabling them to build this vital relationship between elements. Using GIS as a CMP provides efficient and accurate tools for urban drainage systems as it links and exchanges data with other fields such as meteorology, censuses, a city's master plan, hydrology and geology, enabling water authorities to save time and costs usually associated with a conventional approach to infrastructure services. The value of using GIS comes from the fact that more than 80% of water and wastewater infrastructure data has already been geographically referenced. 90% of water authorities in the US use GIS applications in utilities management (Shamsi et al, 1996).

Three factors are important when managing the design of sewer systems; the cost, footprint and construction time.

### 2.1.3 *Cost*

Estimating the cost of a sewer system is a complex process as it comprises many factors such as pipe material, pipe diameter and cover depth, complexity of the construction site, groundwater level and slope of the terrain (Palumbo et al., 2013). Maurer et al., (2010) included an additional factor – the relationship between the size of settlement, high-density population or low-density population, of the area with the combined sewer system. Read and Vickridge, (2004) demonstrated in detail the social and public indirect costs that result from utility works and how this affects communities and business activities, in addition to other factors such as traffic, noise, vibration, air pollution, visual intrusion, plant and materials. Hashemi, (2008) highlighted these effects by making a cost comparison between the traditional open-cut method and trenchless technology. Other researchers have tried to develop an optimal design for sewer systems, taking into consideration the need to achieve sustainable development, this comprising both economic and environment protection factors (Swamee and Sharma, 2013; Cozzolino et al, 2015).

### 2.1.4 *Time*

The time factor is very important when constructing a sewer network as it affects the cost of construction. Sousa et al., (2014) developed a time-cost relationship model using data from 180 sewerage projects. The estimated cost was found to be a good predictor of the estimated length of the project. Nguyen Long et al (2014) studied productivity in sewer construction projects comparing work carried out during the day and at night while Kavvas (2002) illustrated the impact of sewerage projects on community activities.



### 2.1.5 *Footprint*

Marvin and Slater (2007) discussed a new form of intense competition between service utility providers for access to the limited space under roads in UK cities. The study expected an increase in tensions between utilities companies and local authorities because of the competition for urban space under roads. One proposed solution which emerged as to share the space between infrastructures. The space occupied by sewer systems are the larger spaces occupied by utilities, therefore merge the separate sewer system in one system with keep the separate functionality can save significant space use by other utilities.

## 2.2 **Innovative designs for separate sewer systems**

Awareness of the need for a new approach to urban drainage has been growing since the 1970s (Hides et al, 2007). The US Environmental Protection Agency (EPA) has clearly stated that what was considered state-of-the-art pollution control a century ago, is no longer valid today (United States Environmental Protection Agency, 2007). Designers of new sewer systems must identify the problems inherited from old designs and try to use the new technologies available today to revisit traditional urban drainage management with an innovative outlook.

Tait et al (2008) investigated the future of sewer systems in the UK and the impact of changing the methods by which a sewer network could be managed, through to 2080. His study noted that utilizing new technologies such as implementing sustainable drainage systems (SuDS), improving the hydraulic performance of existing pipes, using relining technology and developing real-time control (RTC) will improve sewer network management. To date, many innovative design

solutions for specific case studies have been presented (Khondker and Farag, 2008) the EPA providing an overview of recent work which promises improved sewer drainage system performance for the next century. New technologies that may impact the future configuration of urban drainage management are being considered. Some of the innovative collection system designs discussed by the EPA study (United States Environmental Protection Agency, 2007) are described below.

#### 2.2.1 *Real-Time Control (RTC)*

Developing instruments of measurement, data collection and remote-control technologies, make the monitoring and controlling processes for sewer system management more efficient and accurate. A massive amount of data can be made available by using new computerised and control technology through RTC in sewer systems. This will have a positive effect on the design and operation of sewer systems.

Cembrano (2004) and Polaskova et al (2006) have presented attempts to decrease the discharge from CSOs to receiving watercourses by optimising sewerage systems through a complex system that includes pressure pipes and extra storage tanks fitted with control systems. This increases the storage capacity of the sewer system but is an expensive solution.

### 2.2.2 *Vacuum or pressurized sewer technology*

Vacuum sewer systems use differential pressure to suck sewage from properties instead of draining the sewage, by using gravity created by inclined pipes. These systems have been extensively developed over the last 50 years, having been implemented in several countries around the world (Islam, 2017). Although it is more expensive than the traditional gravity system, it still has many advantages that make it useful in flat areas, such as the use of a shallow and small pipeline. However, the technical operation and maintenance costs are the main limitations of this system (WEF, 2008). The American Society of Civil Engineers (ASCE) implemented a project to separate the combined sewers in three major cities in the US by installing pressure tubing to pump sewage from houses and suspend it in the existing combined sewer system which had been adjusted to transfer stormwater only. Comparing the separation cost to a normal gravity system, the pressure system is more expensive (Jones, 2006).

### 2.2.3 *Sustainable techniques*

Uzomah (2016) conducted a study to assess ecosystem services when using retrofitting sustainable drainage systems (SuDS), i.e. permeable pavements or the area around trees in approximately 100 sites in Manchester. Using these methods created significant environment improvements. However, this system required large areas of land to retrofit the SuDS, something which was challenging in urban areas.

Wang et al (2013) found that retrofitting in the urban environment by intercepting runoff through green areas, is more economical and better protects the environment. They used three green infrastructure models: bioretention

basins (vegetated basins), green roofs and permeable pavements. Their studies showed that employing a green infrastructure will reduce runoff quantity, minimise peak stormwater flows and improve runoff quality. However, this solution also needs large open areas for it to work.

Other studies have suggested adding control equipment by installing inlet flow restrictors in catchment basins and using these to limit the inflow to the hydraulic capacity of the existing combined sewer system. Andoh et al (2005) stated that it is better to find solutions upstream of the system rather than downstream. Their study presented some case studies demonstrating the value of upstream storage, delay controls such as inlet restrictors (Vortex Valve) and partial sewer separation.

The Canadian Mortgage and Housing Corporation (CMHC) and the Canadian Water Network (CWN-NCE), sponsored a project that aimed to highlight successful innovative approaches to stormwater management across Canada. This project presented studies dealing with storm management over three levels or scales: the property level, neighbourhood level and watershed level. The researchers tried to increase storage capacity, pervious surfaces and retention time over these three levels by installing green roofs, using pervious pavements, building a stormwater bond or using parking lots and creating wide riparian buffer zones (Marsalek and Schreier, 2009).

Planning and design criteria, construction and maintenance, performance evaluation and the cost of innovative Low Impact Development (LID) technologies have also been explored. This innovative system includes laying two, perforated Polyvinyl chloride (PVC) pipes of 200 mm diameter below the original storm

sewer system. They are connected to both the downstream and upstream manholes below the storm sewers, as shown in Figure 2.1. Both the storm sewer and the perforated pipes are encased in a granular stone trench, the system designed to store the runoff volume of a 15 mm design storm depth. If the storm depth is over 15 mm, the origin storm sewer pipe which is located above these two pipes, will work to convey the runoff to the watercourse. In a downstream manhole, the two perforated pipes are plugged to be used as storage exfiltration systems making, the exfiltration pipes a storage system instead of a conveyance system. During a storm event, storm runoff from the upstream manhole enters the two perforated pipes and then exfiltrates firstly to the stone trench and subsequently to the surrounding soil. This innovative solution is more economical than constructing a stormwater-quality pond to control the runoff from the site (30.5 hectares, savings of about 80% ) (Li et al, 2015).

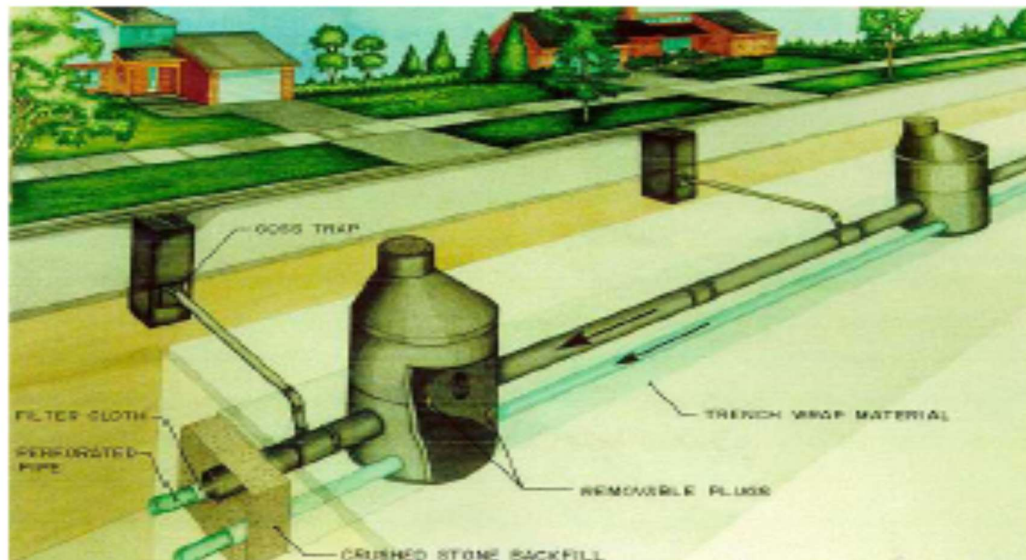


Figure 2.1 Concept of exfiltration system (Li et al, 2015)

[Permission to reproduce this figure has been granted by Computational Hydraulics Int. (CHI)]

### 2.3 Manhole design

The manhole is one of the main elements of a sewer network, used to gain access to the sewer for inspection and maintenance. The construction of manholes has improved, over time, with reference to the materials used. Originally built of brick, significant improvements were made by using concrete and precast materials. However, corrosion to concrete caused by  $H_2S$  means that the inner surface of manholes need to be coated, or newly developed materials such as fiberglass and polyethylene, used instead (Petroff, 1994; Ahn et al, 2009; Hughes, 2009). The maximum space between two manholes and the location of the manhole should be adequate to allow easy use of inspection and maintenance equipment. This means that design criteria require manholes to be sited at every change of alignment, or gradient, and wherever there is a change in the size of sewer pipes. They also need to be spaced at reasonable intervals, somewhere between 50 and 100 metres (BSEN752:2008, 2013).

This section firstly discusses the criteria for the design of manholes and work carried out to improve the design of the shape of the manhole. Following this, the work to test the structure of the manhole and its behaviour when buried in soil under a live load, will be reported. The last section discusses the hydraulic properties of the flow and a head loss through the manhole. Both the structure and hydraulic testing works include experimental and numerical models.

### 2.3.1 *Design of the manhole*

Manholes are either rectangular or circular and need to provide sufficient working space, safe entry and egress for personnel to the sewer system network (BSEN476, 2011). Recently, because of rapid developments in sewer inspection and maintenance equipment technology, many water authorities have started using inspection manholes for equipment rather than personnel access (BSEN752:2008, 2013). Figure 2.2 shows a typical manhole (DEFRA, 2011), Table 2.2 the recommended dimensions (BS\_EN, 2013).

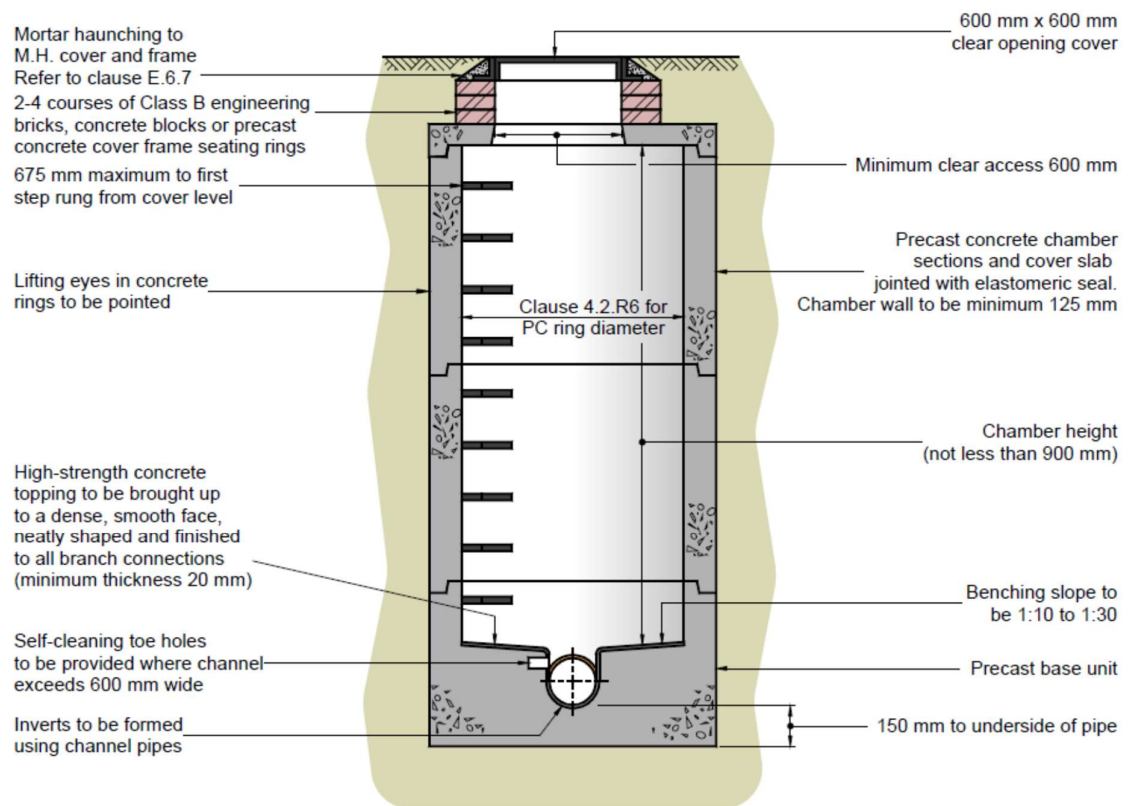


Figure 2.2 Typical manhole detail (DEFRA, 2011).

[Permission to use under the terms of the Open Government Licence (OGL)]

Table 2.2 Recommended dimensions for the construction of new manholes (person entry) (DEFRA, 2011). [Permission to use under the terms of the Open Government Licence (OGL)]

Type of access	Depth to pipe soffit from cover level (m)	DN largest pipe in manhole/means of descent into shaft	Min. internal dimensions <sup>a)</sup>		Min. clear opening size		Remarks
			Rectangular – length and width (mm)	Circular – diameter (mm)	Rectangular – length and width (mm)	Circular diameter (mm)	
Manhole <sup>b)</sup>	<1,5	≤ 150	750 x 675 <sup>c)</sup>	1000 <sup>d)</sup>	750 x 675 <sup>e)</sup> <sup>f)</sup>	na <sup>g)</sup>	Generally in accordance with <i>Safe Work in Confined Spaces</i> – Health and Safety Commission [29]. Larger opening size is required for manholes at shallower depths to permit standing/crouching. Where a ladder is provided the minimum size should be increased see NA.4.3.2 and NA.4.10.2.
		225	1200 x 675	1200	1200 x 675 <sup>h)</sup>		
		300	1200 x 750	1200	1200 x 675		
		375 – 450	1350 x 900	1350	1200 x 675		
		500 – 700	1500 x 1150	1500	1200 x 675		
	≥1,5	750 – 900	1800 x 1350	1800	1200 x 675		
		> 900	1800 x (DN + 775)	The larger of 1800 or (DN + 900)	1200 x 675		
		≤ 225	1200 x 1000	1200	600 x 600	600	
		300	1200 x 1075	1200			
		375 – 450	1350 x 1225	1350			
Manhole shaft <sup>i)</sup>	>3,0	500 – 700	1500 x 1475	1500			Min. clear space between the ladder/steps and the opposite face of the shaft should be approx. 900 mm.
		750 – 900	1800 x 1675	1800			
		>900	1800 x (DN + 775)	The larger of 1800 or (DN + 900)			
		Steps	1050 x 800	1050	600 x 600	600	
		Ladder	1200 x 800	1200			
		Winch	900 x 800	900	600 x 600	600	Winch only – no steps or ladders (permanent or removable)

a) These sizes apply to straight-through pipes, for turning chambers or chambers with several side branches or where specific maintenance requirements are necessary, e.g. disconnecting traps the minimum sizes should be increased.

b) Chamber with a removable cover constructed on a drain or sewer to permit entry by personnel [BS EN 752, 3].

c) The minimum size of any manhole serving a more than one property should be 1200 mm diameter or 1200 mm x 675 mm rectangular.

d) See footnote c.

e) May be reduced to 600 mm x 600 mm or 600 diameter where the configuration of the manhole chamber permits a safe system of work.

f) May be reduced to 600 mm x 600 mm diameter where required by highway loading considerations, subject to safe system of work being specified.

g) Not applicable due to working space needed.

h) See footnote f.

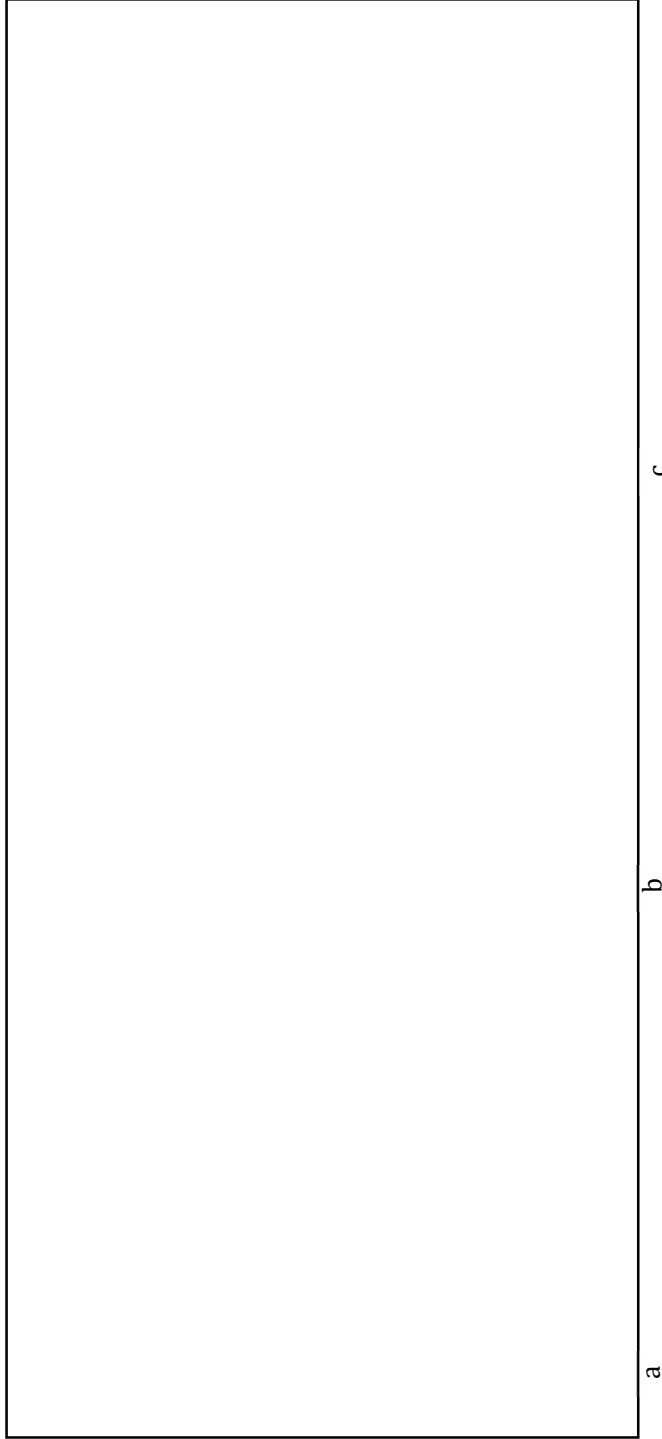
i) Minimum height of chamber in shafted manhole 2m from benching to underside of reducing slab.



From a review of the literature, it is clear that there is a paucity of research on manhole shape or structural performance (Bettez et al, 2001; Saricimen et al, 2003), specifically regarding combined manholes.

A combined manhole (one manhole with two chambers, one for wastewater, the other for rainwater) has been patented by a German company (Würmseher, 2014); Figure 2.3 show details of this manhole, which is rectangular in design. The pipes are laid next to each other and some pipes will cross inside the sewage chamber.

This rectangular manhole is different from the circular manhole which is proposed in this research, in both shape and siting position of the pipes; the circular one also does not have any pipes crossing inside it, a feature which makes maintenance more complicated in rectangular manholes.



Storm Chamber (RWK), Sewage chamber (SWK), storm pipe inlet (RWHL), sewage pipe inlet (SWHL), storm pipe outlet (RWA), sewage pipe outlet (SWA), lateral storm pipe (RWZ), lateral sewage pipe (SWZ).

Figure 2.3 Innovative rectangular manhole (a) plan view, (b) cross right section, (c) front cross section (Würmseher, 2014)  
The diagram originally presented here cannot be made freely available via LjMU Digital Collections because of 'copyright'. The diagram was sourced from European Patent Office (EPO).

Another proposal for a separate manhole was patented by Willi (1998). The design has the same size as a conventional manhole but can be either rectangular or circular with two stage chambers arranged vertically, storm chamber over sanitary. The design does not meet the standard requirements for easy access and enough space to do the maintenance required by regulation. Figure 2.4 illustrates the details of the separate manhole.

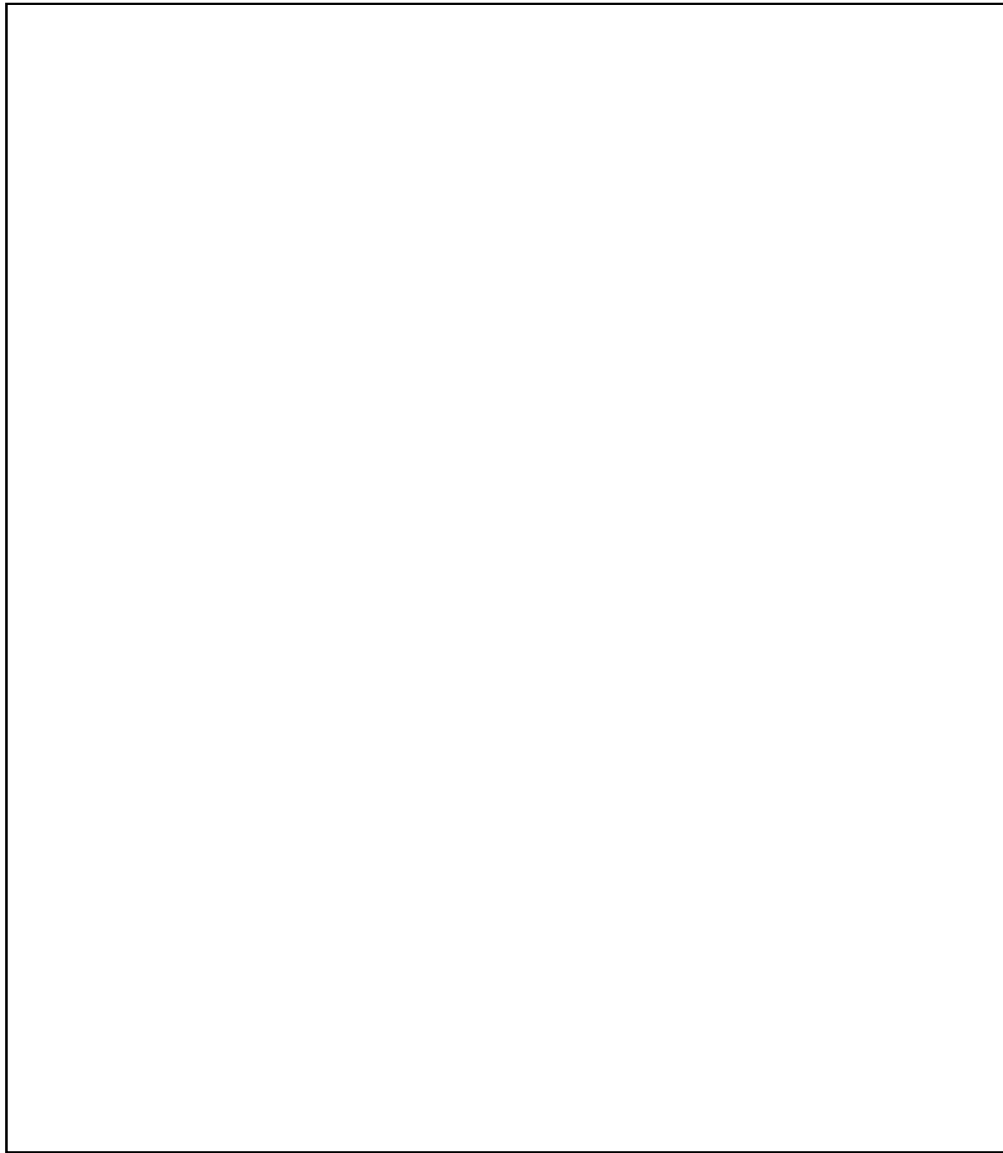


Figure 2.4 The combined-separate manhole patent by Willi (1998).

The diagram originally presented here cannot be made freely available via LJMU Digital Collections because of 'copyright'. The diagram was sourced from European Patent Office (EPO).

### 2.3.2 *The structural performance of manholes.*

Circular concrete, or precast concrete manholes, are widely used in sanitary sewer and storm water systems. However, there is a paucity of literature regarding the structural performance of concrete manholes, as most studies concentrate on durability issues (Saricimen et al, 2003)) or hydraulic performance (Guymer et al, 2005). The American Concrete Pipe Association (ACPA, 2008) do however provide a technical description of the design loads and maximum allowed depth of precast concrete manholes.

The most important work examining the structural performance of traditional manholes was carried out by Sabouni and El Naggar (2011a). They used three manholes, two of diameter 1200 mm (one reinforced, the other not), the third of diameter 1500 mm, both built from precast concrete. They used a large-scale (4.5 m x 4.5 m x 7.62 m) geotechnical cell for testing and followed the Canadian Highway Bridge Code as a guide for the application of live loads (Figure 2.5). They found that the range of displacement of the manholes ranged between 1.3 mm and 5.6 mm for all loading tests. They concluded that frictional resistance along the manhole structure mitigated the effect of truck loading. All their manholes withstood truck loads, even the non-reinforced one. Sabouni and El Naggar (2011b) used these results to validate a 3-dimensional, Finite Element model (FE) for circular, precast and concrete manholes. This model was used to test a different combination of concrete manholes in native soil conditions, including soil compaction, groundwater level, trench dimensions and method of installation. They found that soil water content (groundwater level), creates more stress on manhole bases than any other factor.

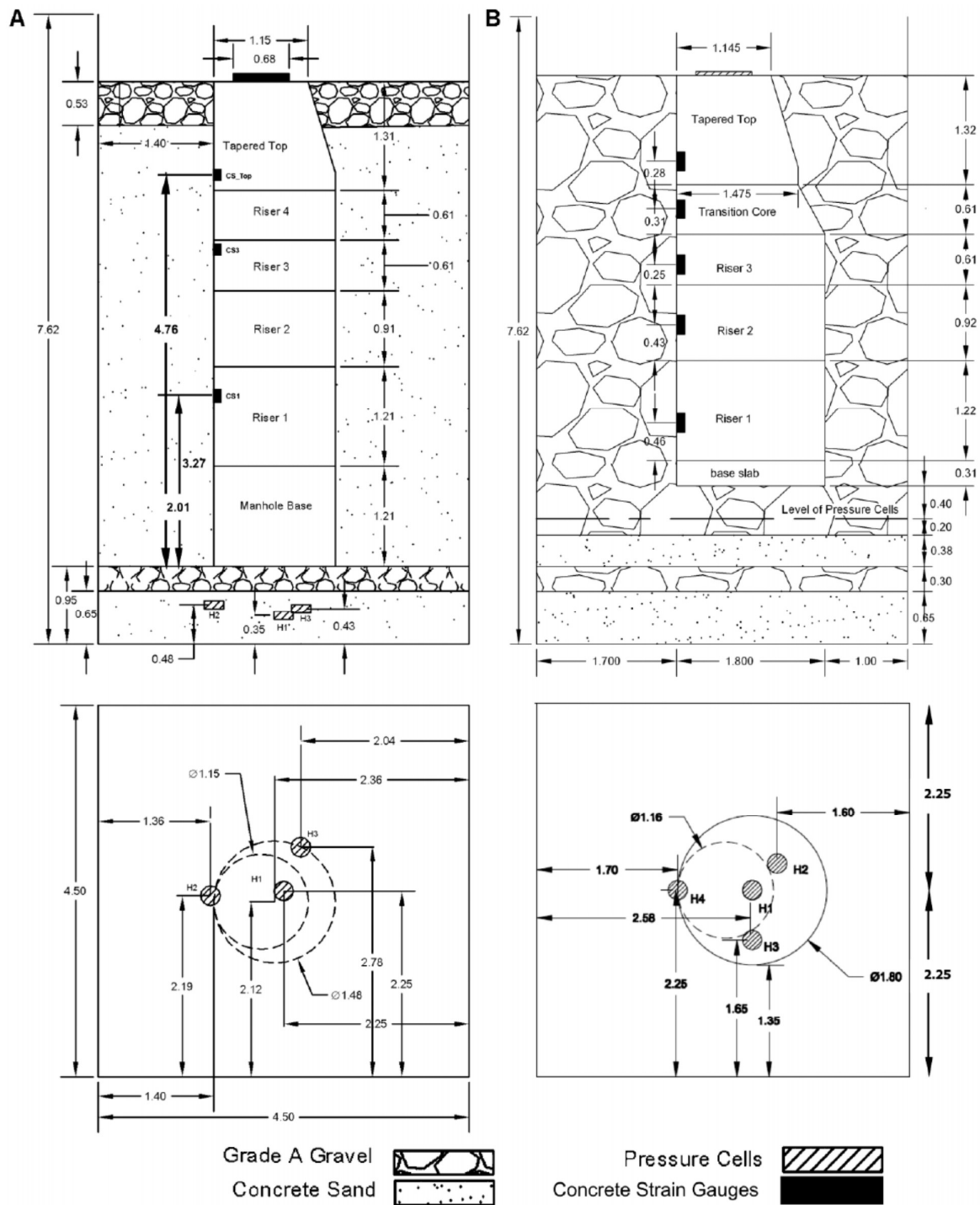


Figure 2.5 Setup of manholes (1.2 m and 1.5 m) in the cell test (Sabouni and El Nagggar, 2011b). [Permission to reproduce this figure has been granted by Canadian journal of civil engineering]

Al-Saleem and Langdon (2016) presented the results of structural tests of a manhole under a single live load, this part of work to develop and upgrade standardised design guidelines for precast concrete manholes in New Zealand (CPAA, 2016). They concluded that the service life of a manhole is typically 100 years and that the designer needs to be aware that the standard design is for normal application but that the manhole can be modified to meet any special site requirements or project applications. IKT (2012) who estimated the total number of manholes in Germany at ten million, conducted a full-scale, comparative laboratory experiment study, using cementitious and polymeric coatings to line manholes to improve their structure, and to treat those which were deteriorating. A substantial study was carried out by Najafi and Sever (2015b), who estimated the number of manholes in the USA to be approximately 20 million. Their study tested the structural capabilities of the manhole when lined with specific materials using structure strength tests, mathematical modelling and evaluated case histories. The procedure involved using a small-scale model to validate an FE model, the results of which were used to upgrade the FE model to full scale as shown in Figure 2.6. The results from both Germany and the USA, revealed that manhole structural performance was not affected by the type of lining or deterioration in its lining. Bandler (2007) conducted a study to test two types of manhole materials; unreinforced concrete and masonry. Manholes were exposed to axisymmetric pressure to simulate horizontal effective loads, the effect of the coating material assessed in order to improve the structural performance of the manhole.

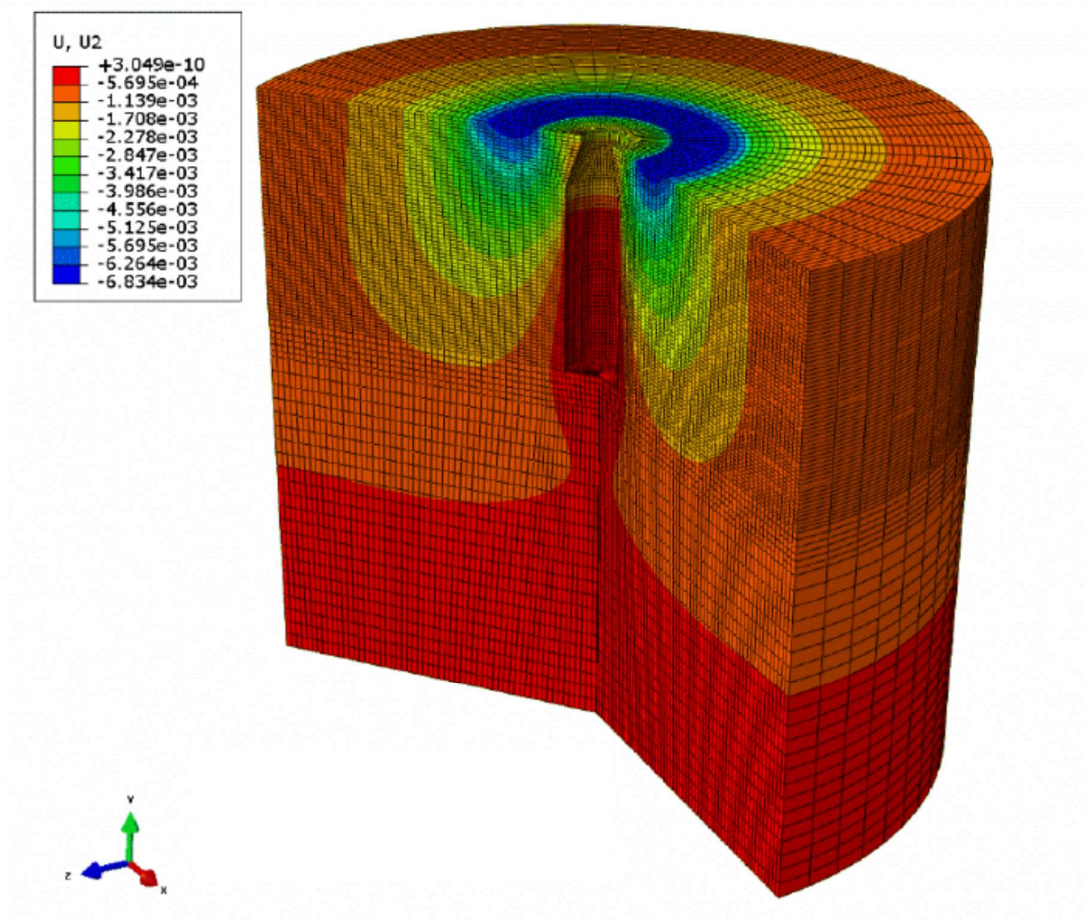


Figure 2.6 FE model for traditional manhole showing the vertical displacement (Najafi and Sever, 2015a) [Reprinted with permission. © Water Environment Research Foundation]

Brown and Brown (2000) studied the structural performance of manholes and the combination of vicinity asphalt surfacing under wheel loadings, finding that surface displacement is a result of subgrade deformation rather than manhole deformation.

### ***2.3.3 The hydraulic properties of manholes***

The flow in sewer systems can be described as subcritical on a mild slope when the flow in the pipe is less than 50% capacity and  $Fr < 0.7$ . The flow changes to supercritical when the discharge from the system increases because of medium or heavy rain, especially in hilly regions. The potential damage associated with uncontrolled energy dissipation inside the manhole is substantial. For example, fast flow occurs when the sewer is laid at a steep gradient and the flow becomes supercritical. This often is seen in hilly regions; when the gradient eventually flattens, the flow becomes subcritical and a hydraulic jump occurs.

There are commercial software packages available which evaluate the hydraulic performance of sewer systems. These are founded on physically based approaches using De Saint-Venant equations based on the concept of one-dimensional, gradually varied, unsteady, open channel flow. Sewer systems are simulated with links (pipes) and nodes (manholes or other sewer appurtenances) by these packages. However, this method is unable to account for the flow patterns in complex manhole designs such as drop, bending or junction manholes because the manhole flow is neither one dimensional nor gradually varied. As a consequence, simulating essential hydraulic behaviour is a complex task (Hager and Gissoni, 2005)).

### ***2.3.4 Hydraulic Experiments for manholes***

In addition to needing access to sewer systems for maintenance, manholes are used as a control structure to aerate the flow to force-free surface flow, therefore identification of the hydraulic properties of flow inside the manhole is



important. The study of the hydraulic properties of manholes started in the middle of the last century examining head loss and a wide range of geometrical configurations of manholes such as those with different ratios of inlet and outlet pipe diameters, drop manholes and manholes with lateral junctions or bending. The majority of the research was carried out on laboratory scale models simulating the flow in the sewer system through wet weather (stormwater flow). A laboratory physical model has been effectively used to simulate flow characteristics for different manhole designs. Rubinato (2015) investigated energy losses under steady and unsteady flow conditions, using a physical scale model for sewer systems, under different hydraulic scenarios (Figure 2.7). The results of this study were used to evaluate the computer model, showing that the performance of the model could be improved when it included accurate method to estimate head losses in their calculation.



Figure 2.7 Series of manholes model to simulate the head loss using re-circulating pipe system (Rubinato, 2015). [Reprinted with permission from the author - University of Sheffield]

Sangster et al (1958) proposed an analytical method to determine the energy loss ( $\Delta H$ ) of flow inside the manhole, extrapolated from the difference of pressure between the inlet and outlet of the manhole (Figure 2.8) this giving the coefficient of energy loss (Equation 2-1)

$$\Delta H = K \frac{v^2}{2g} \quad \text{Equation 2-1}$$

Where:

$v$ =mean pipe velocity

$g$ =acceleration due to gravity

$K$ =head loss coefficient.

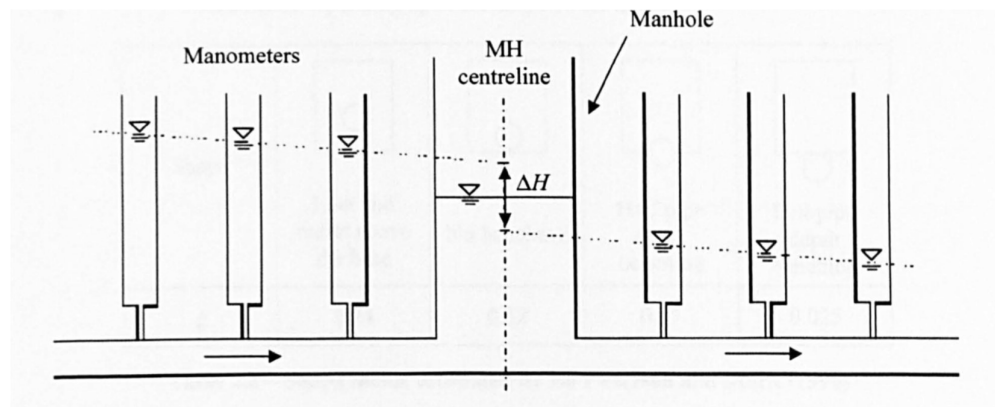


Figure 2.8 Manhole head loss calculated experimentally (Sangster et al, 1958).  
[Reprinted with permission from American Society of Civil Engineers (ASCE)]

The effect of manhole shape and the position of conduit of flow inside a manhole on the coefficient of energy loss, was considered by Pedersen and Mark (1990). They developed a method to calculate the head loss in the manhole using submerged jet theory to correlate the energy loss coefficient to the ratio of

manhole diameter to pipe diameter, and manhole shape (Equation 2-2). Shape was represented by shape factor (Table 2.3), this method used in some commercial sewer design packages to calculate the head loss through manholes.

$$K = \xi \left[ \frac{D_m}{D_p} \right] \quad \text{Equation 2-2}$$

Where:

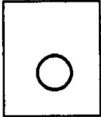
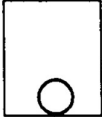
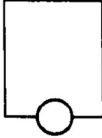
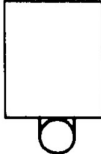
$\xi$  = is a factor depending upon the shape of the manhole

$D_m$  = manhole diameter

$D_p$  = pipe diameter

$K$  = head loss coefficient.

Table 2.3 Shape factor estimated by Pedersen and Mark (1990).  
[Reprinted with permission from American Society of Civil Engineers (ASCE)]

Shape				
	Inlet and outlet above the base	No benching	Half pipe depth benching	Full pipe depth benching
$\xi$	0.24	0.12	0.07	0.025

The head loss is increased when the flow in the inlet pipe changes from partial flow to full, this phenomena associated with a drop in water level at the manhole (Zhao et al, 2006).

The drop manhole is the old effective technique used to reduce the flow velocity in hilly regions. Using a drop manhole allows the design of an adequate slope to the sewer pipe to maintain minimum and maximum velocity for the flow and avoid using topographic declines of the area as a slope for pipes. The hydraulic behaviour of drop manholes has been tested in combined sewer systems experimentally, the study showing that the drop manhole did not improve the hydraulic properties of the manhole under supercritical flow conditions but can generate a serious challenge due to dissipation (De Martino et al, 2002). Gargano and Hager (2002) conducted an experimental study to investigate a supercritical flow across manholes in combined sewer systems using straight flow, and a U shape for the conduit in the manhole. The study determined three waves in the manhole: (1) wave due to the transition of circular flow to open flow at the manhole inlet, (2) swell due to reversal of flow, and (3) wave due to shock front at the manhole outlet. The research cited that “ *It was found that in order for free surface flow to be maintained the common design standard for sewers with a supercritical approach flow have to be revised. These implications have to be accounted for in future designs*”. Changing or merging the flow direction inside the manhole generated a significant alteration in hydraulic properties. These cases were investigated by Hager and Gissonni (2005), who tested three different manhole cases: a through-flow manhole, a bending manhole and a junction manhole. Their results indicated that it is necessary to maintain a supercritical flow from upstream to downstream because a breakdown in the free surface flow led to complex and dangerous flow phenomena. They found that the current bending manhole design used to change the direction of the sewer direction by 45 or 90 degrees, is not efficient enough to maintain a supercritical flow. A 2D length

extension was added to the existing design to improve the capacity of the manhole and avoid outer wave impingement effects on the bend.

Saldarriaga et al (2017) studied the hydraulic behaviour of symmetrical junction manholes, under supercritical conditions, using two physical models to explore entry flow combinations from three manhole inlets. This study showed that the probability of surcharged and pressurized flow increases when uniting the flow in the manhole junction as a result of the three types of wave generated from this flow.

From the above, it can be stated that there has been no significant work carried out to develop the existing manhole design but there have been some attempts to improve the hydraulic properties of manholes through the installation of extra accessories. Granata et al (2014) stated that the non-dissipated, flow energy, upstream sewer network leads to high downstream flow velocity which increases the risk of flooding and creates poor operating conditions. Their study investigated the hydraulic performance of drop manholes under supercritical flow conditions. They tried to improve the hydraulic performance of the traditional drop manhole by the installation of dissipative tools: two different types of jet-breaker, a plane jet-breaker and a wedge jet-breaker. They tested the effects of these tools on the hydraulic behaviour by conducting experimental tests, Figure 2.9 illustrating the test setup. They built a correlation between the diameter of manhole, approach flow and distance of drop between inlet and outlet pipes of manhole (Equation 2-3).

$$l = \left( \frac{2 \cdot S}{g} \right)^{0.5} \cdot \frac{V_o}{D_M} \quad \text{Equation 2-3}$$

where:

$S$  = drop height

$g$  = gravity acceleration

$V_o$  = approach flow velocity

$D_M$  = Manhole diameter.

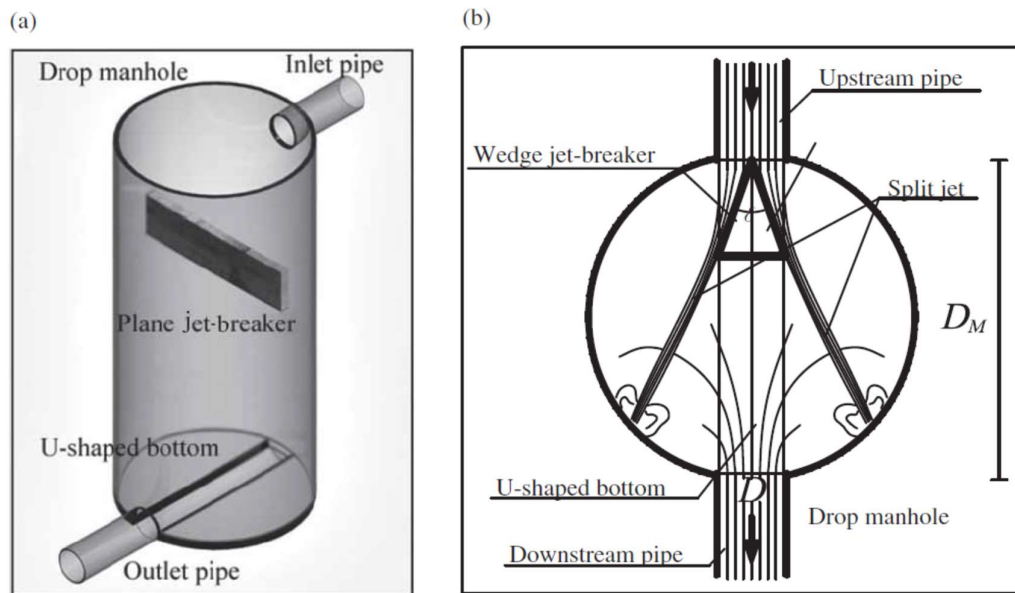


Figure 2.9 An Improvement proposed to increase the dispersion in drop manhole using two types of Jet-breaker elements (Granata et al, 2014). [Reprinted with permission from the publisher Taylor & Francis]

### 2.3.5 Computational fluid dynamics

Computational Fluid Dynamics (CFD) is a mathematical method for simulating fluid dynamics, heat and mass transfer, flow combustion and associated transport phenomena, by means of computer-based simulations. Use of CFD principles began at the start of the twentieth century through application of numerical solutions of differential equations to simulate physics and engineering problems mathematically. This technique has been rapidly developed

due to the emergence of the digital computer and its increasingly powerful capacity to carry out complex calculations. It is widely used today in design and research fields, providing a quick evaluation of engineering design and detailed information of flow or thermal transection (Chung, 2010).

#### 2.3.5.1 Mathematical Principles

The mathematical models used to simulate fluid dynamics are based on the fundamental principles of mass (continuity) and momentum equations of fluid govern fluid motion equations:

- Continuity

Rate of increase of mass in fluid element = Net rate of flow of mass into fluid element (Chung, 2010)

$$\frac{\partial \rho}{\partial t} + \frac{\partial \rho u}{\partial x} + \frac{\partial \rho v}{\partial y} + \frac{\partial \rho w}{\partial z} = 0 \quad \text{Equation 2-4}$$

The density of an incompressible liquid (mass per unit volume) is constant, therefore the equation can be simplified to:

$$\Delta \equiv \frac{\partial u}{\partial x} + \frac{\partial v}{\partial y} + \frac{\partial w}{\partial z} = 0 \quad \text{or} \quad \Delta \equiv \frac{\partial u_i}{\partial x_i} = 0 \quad \text{Equation 2-5}$$

- Conservation of Momentum

Rate of increase of momentum of fluid particle = Sum of forces on fluid particle - Newton's second law. The equations governing the motion of an incompressible Newtonian fluid are known as Navier-Stokes equations (Chung, 2010).

$$\begin{aligned}
\rho \left( \frac{\partial u}{\partial t} + u \frac{\partial u}{\partial x} + v \frac{\partial u}{\partial y} + w \frac{\partial u}{\partial z} \right) &= \rho B_x - \frac{\partial p}{\partial x} + \mu \left( \frac{\partial^2 u}{\partial x^2} + \frac{\partial^2 u}{\partial y^2} + \frac{\partial^2 u}{\partial z^2} \right) \\
\rho \left( \frac{\partial v}{\partial t} + u \frac{\partial v}{\partial x} + v \frac{\partial v}{\partial y} + w \frac{\partial v}{\partial z} \right) &= \rho B_y - \frac{\partial p}{\partial y} + \mu \left( \frac{\partial^2 v}{\partial x^2} + \frac{\partial^2 v}{\partial y^2} + \frac{\partial^2 v}{\partial z^2} \right) \\
\rho \left( \frac{\partial w}{\partial t} + u \frac{\partial w}{\partial x} + v \frac{\partial w}{\partial y} + w \frac{\partial w}{\partial z} \right) &= \rho B_z - \frac{\partial p}{\partial z} + \mu \left( \frac{\partial^2 w}{\partial x^2} + \frac{\partial^2 w}{\partial y^2} + \frac{\partial^2 w}{\partial z^2} \right)
\end{aligned}$$

Equation 2-6

where:

$P$  = pressure

$u, v$  and  $w$  = the flow velocity in  $x, y$  and  $z$  directions sequentially.

$t$  = time

$B_{(x, y \text{ and } z)}$  = represents body accelerations acting on the continuum, for example gravity, inertial accelerations, electrostatic accelerations.

$\rho$  = density

$\nu = \mu/\rho$  = kinematic viscosity

CFD provides the solution to governing equations of flow subject to specific initial and boundary conditions. These equations are nonlinear and very difficult to solve analytically. CFD simplifies these equations by applying specific boundary conditions so that some of the terms can be deleted or be considered negligible. Various numerical techniques have been developed for each specific application of the general flow equation e.g. *Finite difference method* (FDM), *Finite volume method* (FVM) or the *Finite element method* (FEM). In general, these methods can lead to systems of algebraic equations which give solutions that do not correspond to the original continuous system. e.g. with *Finite difference method* (FDM), CFD generates a mesh for the flow domain to discretize the diffusion equation using a forward difference formula for the time derivative and a central difference formula for the spatial derivative (Equation 2-7).



$$\frac{u_i^{n+1} - u_i^n}{\Delta t} = \frac{u_{i-1}^n - 2u_i^n + u_{i+1}^n}{\Delta x^2} \quad \text{Equation 2-7}$$

where:

$u_i$  velocity expressed in terms of the Taylor series for two points ( $i+1$ ) and ( $i-1$ ), with a small distance  $\Delta x$  from the central point, ( $i$ ).

The accuracy of the CFD solution is only as good as the initial/boundary conditions provided for the numerical model, or as the physical models on which they are based, comparison with experimental results or with analytical solutions used as validation (Ashgriz and Mostaghimi, 2002; Sawko, 2012).

CFD is increasingly used in the water industry. It has significant benefits over laboratory-based studies in that once a numerical model has been validated, it may be used to examine the impact of change to the geometry, or flowrate, with comparative ease.

#### 2.3.5.2 Solute transport in manholes

Extensive research has been conducted at Sheffield University to investigate solute transport in manholes, beginning with Guymer and O'Brien's work in 1995. This subject is currently not included in scope of this research and will be recommended as future work. A brief summary will be presented about the current state of research though.

Research has been carried out using laboratory tracer experiments with physical scale models to measure the longitudinal dispersion through a surcharged manhole. Dye, Rhodamine WT, is injected into the flow upstream of the manhole to simulate the solute in flow. A concentration distribution of dye through the manhole, monitored using fluorometers. Temporal concentration profiles are then analysed using the Advection Dispersion Equation (ADE) and aggregated

dead zone (ADZ) models. The (ADE), derived by Taylor (1954), was originally used to estimate the transport of a solute in pipe flow. The ADZ model, developed by Beer and Young (1983), used the retention time and mass of solute for a single ADZ element, or a number of ADZ elements, to calculate the residence time. This allows separate descriptions of the effects of advection and dispersion processes in water quality models (Dennis, 2000; Guymer and O'Brien, 2000; Bennett, 2012). Recently, researchers have used the Residence Time Distribution (RTD) instead ADE and ADZ, a nonparametric model which can describe the mixing processes taking place in a urban drainage structure (Sonnenwald, 2014).

Lau (2007) studied the impact of scaling methodologies, using a physical lab scale manhole, on the mixing process and hydraulic properties of a manhole. This study investigated head losses through the manhole using experimental work to validate the CFD model for the same scale of physical model. However, this study did not clearly illustrate flow behaviour in the transition case using CFD. It is only highlighted that *"The existence or not of a hydraulic transition in the numerical models is thought to be critical in determining CFD could be used for studying the effects of physical scale of surcharged manholes"*. Experimentally, a sharp transition in the energy loss coefficient between low and high surcharges, was noted for surcharge ratios (the ratio of water depth in the manhole to pipe diameter) of between 2.0 and 2.5. The coefficient values are reduced by half compared to the values in the pre-threshold region, yielding a coefficient value of around 0.45 after the transition region (Figure 2.10). The solute dispersion was investigated in this study using ADZ and ADE models, concluding that there is a small effect of the scaling procedure on the results of hydraulic properties simulation for the manhole.

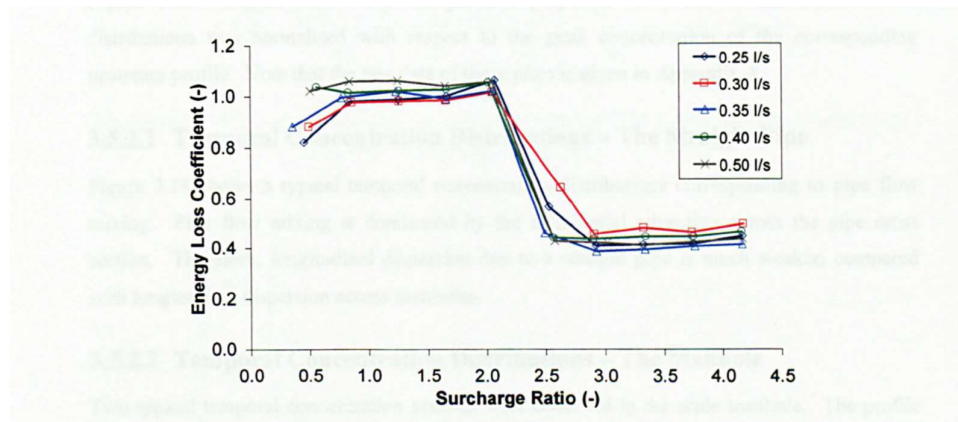


Figure 2.10 The energy loss coefficient with surcharge ratio for 218 mm manhole estimated by (Lau, 2007). [Reprinted with permission from the author - University of Sheffield]

The accuracy of CFD outputs has been explored by two researcher, Stovin et al (2008) discussed the approaches used to validate CFD against the hydraulic experimental results produced using the Particle Image Velocimetry (PIV) method. Their study identified a validation process using longitudinal velocity because CFD produces a temporal mean velocity while the PIV produce a mean velocity at a specific time. This identified an approximate 50% overestimation in a large zone within the manhole. Difficulties come from the influence of a multitude of factors such as the boundary conditions (wall roughness, inlet and outlet conditions) and the flow pattern.

Can-Hua et al (2008) tried to simulate the experimental results presented by Zhao et al (2006) using a CFD model to identify hydraulic properties and to establish a numerical model for the rectangular junction manhole. Their study found a good match between the CFD output and experimental results. This can help improve the design of manholes, improve the understanding of sediment transport in sewers and the implications of this for water quality.

## 2.4 Buried pipes

The pipeline is the main element of infrastructure services, used to convey potable water, gas to the city and to carry away sewage and stormwater. The structural performance of buried pipes in soil has been subject to substantial research regarding a variety of pipe materials. This started in the early 1900s with the Marston load theory, created to calculate the applied load on buried pipes to avoid the environmental and economic consequences of collapsing pipelines. Prior to this, a physical lab model was used to test the performance of buried pipes, field cell tests later developed to test full-scale models. The development of computational capacity has provided sophisticated tools for the designer, allowing the use of numerical methods and soil constitutes to simulate pipe-soil correlations. This section discusses the empirical theories used to test the structural performance of buried pipe, the majority designed to test the behaviour of one pipe buried in a trench. The second part of this section illustrates the use of the FE method to simulate buried pipe performance.

### 2.4.1 *Empirical methods*

#### 2.4.1.1 *Categories of pipe*

Typically, there are two categories of pipe dependant on the strength of the pipe material; rigid pipes e.g., concrete/cast iron, or flexible pipes such as High-Density Polyethylene (HDPE), Polyvinyl Chloride (PVC), steel or Glass-fibre Reinforced Plastics (GRP). A flexible pipe is defined as one able to deflect at least

2% - 5% without structural distress; pipes that do not meet this criterion are considered rigid. The use of flexible pipes has recently become more common in sewer systems because of their flexibility, lightness and ease of joining as well as to avoid the corrosion that affects rigid pipes (Bizier, 2007; Moser and Folkman, 2008; Kang et al, 2013a). The stiffness of the pipe is a function of the modulus of elasticity of the pipe material, thickness of the pipe wall and the pipe diameter. The lifetime of the pipe ranges between 50-100 years depending on the durability of the pipe and the ability of the pipe material to resist environmental effects over time (Beieler et al, 2013).

#### *2.4.1.2 Loads on the pipe*

Three types of load can be impose on buried pipes: a static load, generated from the weight of the soil above the pipe; surface loads from traffic and hydrostatic loads from water pressure - the pressurised flow inside the pipe, or water table outside the pipe. Hydrostatic pressure capacity is normally determined by the manufacturer of the pipe and limited for use by the designer.

Both the effects of surface and static loads are considered critical for shallow buried pipes. These include potable water networks or sewer networks, where pipes are normally buried between 1 and 6 metres deep. The effect of traffic loading is negligible on a pipe buried deeper than 3 metres. Figure 2.11 illustrates the combination of an H20 traffic load and the static load on the pipe at different depths (Corey, 2015).

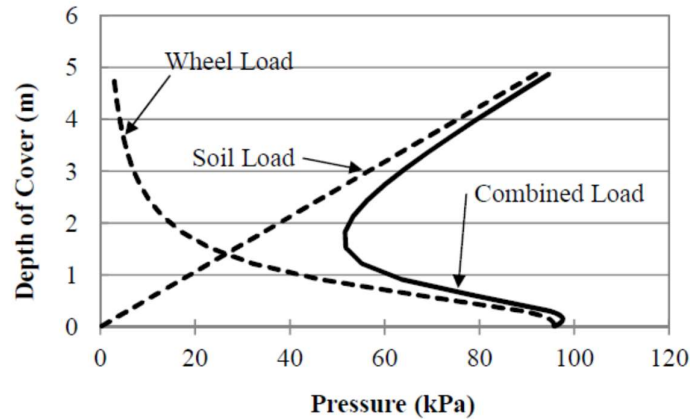


Figure 2.11 Influence of traffic load (H-20) and weight of soil on buried pipe (Corey, 2015). [Reprinted with permission from the author - Kansas University]

Traffic loads are based on the AASHTO H-25 or AASHTO H-20 configurations representing 25 or 20 tons (Table 2.4). The Boussinesq solution is used to calculate the distribution of stress from the load point at the surface, decreasing with the depth of elastic isotropic medium. This method was integrated by Hall and Newmark (1977) to create a load coefficient, later developed to calculate distributed loads such as the live wheel load on a buried pipe (Equation 2-8).

$$W_s = C_s p F' B_c \quad \text{Equation 2-8}$$

where:

$W_s$  = load on pipe (lb/unit length)

$p$  = concentrated loads (lb)

$F'$  = impact factor

$L$  = effective length of conduit (3 ft or less)

$C_s$  = load coefficient which is a function of  $B_c / (2H)$  and  $L / (2H)$

$H$  : height of fill from top of pipe to ground surface (ft).

Table 2.4 Live load data for AASHTO H-20 and H-25

Cover depth (m)	AASHTO H-20	AASHTO H-25
	Live load transferred to pipe (N/mm <sup>2</sup> )	Live load transferred to pipe (N/mm <sup>2</sup> )
0.3	0.0862	0.108
0.6	0.0383	0.048
0.9	0.0288	0.036

Pyramid methods (Equation 2-9) are used conservatively to calculate the minimum cover depth for a buried pipe by using the tyre footprint simulated by a rectangular plate of size (56 cm x 18cm). The transferred load is distributed on the area which increases vertically with depth, a pyramid slope normally of 30° - 35°, depending on the soil friction angle. The pressure on the pipe (p) is the pressure at the base of the pyramid (Figure 2.12).

$$P = W / (B+H)(L+H) \quad \text{Equation 2-9}$$

where:

W = wheel load

B = width of tyre footprint

L = length of tyre footprint

H = depth

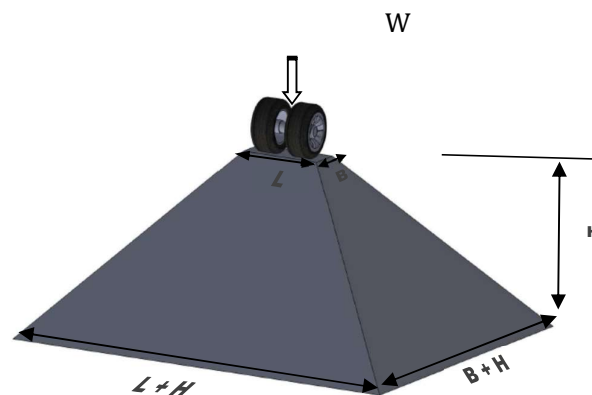


Figure 2.12 Pyramid methods for the distribution of live loads (Abbas et al, 2018). [Permission to reproduce this figure has been granted by Canadian journal of civil engineering]

The theory proposed by Marston cited by Moser, (2008) is used to calculate the static load on a buried pipe. Static loads are generated by the weight of the fill soil above the pipe, this dependent on the type of soil (density of soil). The applied load resists friction forces between the filling soil and native soil at the two sidewalls of the trench, the effects of this friction dependent on the type of native soil and the dimensions (height and width) of the trench. The above parameters are used to calculate the load coefficient ( $C_d$ ). Equation 2-10 and Figure 2.13 illustrate the concepts of this theory.

$$C_d = \frac{1 - e^{-2K\mu'(\frac{H}{B_d})}}{2K\mu'} \quad \text{Equation 2-10}$$

where

$K$ =ratio of active lateral unit pressure to vertical unit pressure ratio

$\mu'$  = coefficient of friction

$B_d$ = width of trench

$H$  = the depth of buria



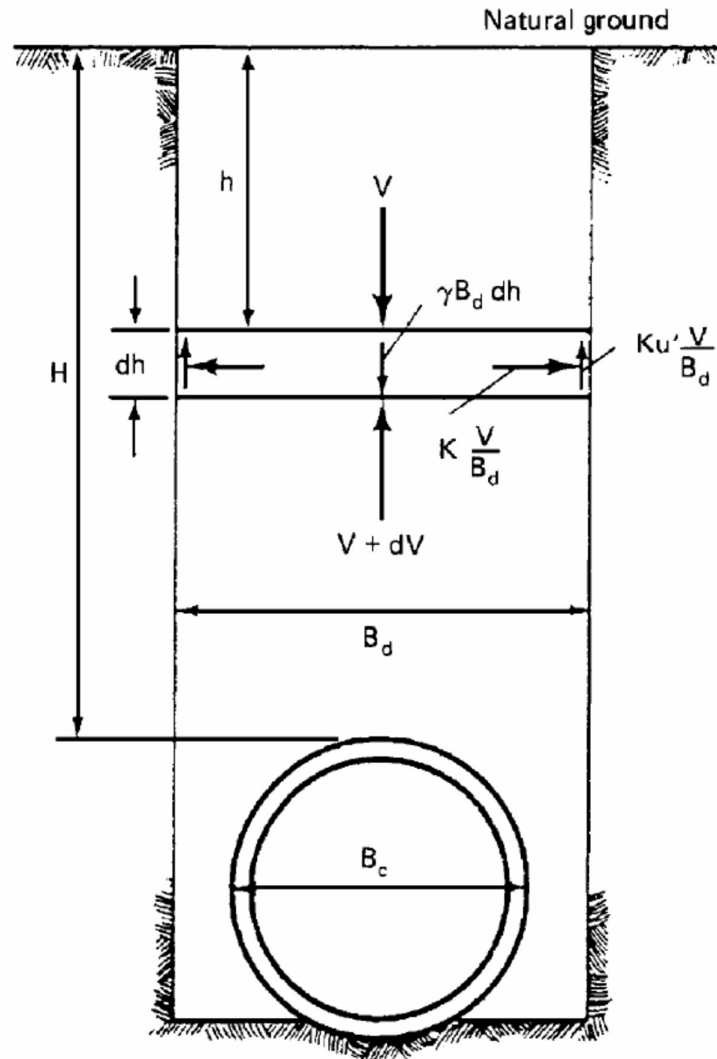


Figure 2.13 Marston's theory of transfer of the load to the buried pipe (Masada, 1996). [Reprinted with permission from the author - Ohio University]

Marston calculated  $K$  and  $u'$  experimentally for different types of soil and backfill, the load on rigid pipes calculated using Equation 2-11:

$$W_d = C_d \gamma B_d^2$$

Equation 2-11

where:

$W_d$  = load on rigid pipe

$C_d$  = B load coefficient

$\gamma$  = unit weight of backfill

$B_d$  = width of trench.

Flexible pipes buried in soil are generally studied as one system because of the support the soil provides at the sides of the flexible pipe against horizontal deformation of the pipe ( $\Delta X$ ). Early observations by Marston and Spangler (1941) identified pipe flexibility and soil-pipe interaction as the main reasons why the load on a rigid pipe is more than that on a flexible pipe under the same loading conditions (Figure 2.14 and Figure 2.15).



Figure 2.14 When flexible pipes are used, low rigidity transfers part of the load to the soil because of its lateral deformation.

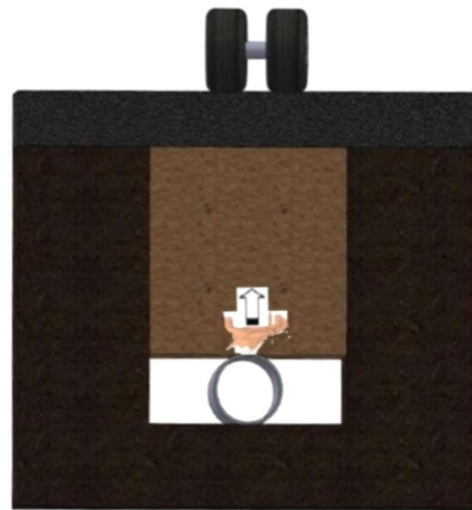


Figure 2.15 When rigid pipes are used, loads are absorbed by the pipe itself.

Marston simplified this such that when the relative stiffness of the pipe to the backfill soil are equal, the load can be proportioned on the basis of area using Equation 2-12.

$$W_c = C_d \gamma B_c B_d \quad \text{Equation 2-12}$$

Alternatively, the design load of a flexible buried pipe, the prism load (the total weight of a vertical prism of soil over the pipe), can be used. Research data indicates that the effective load on a flexible pipe for long-term use, tends to reach the prism load as maximum load imposed on the flexible buried pipe. The prism or embankment load is calculated using Equation 2-13.

$$P = B\gamma H \quad \text{Equation 2-13}$$

where:

$P$  = pressure due to weight of soil at depth

$\gamma$  = unit weight of soil

$H$  = depth at which soil pressure is required

#### 2.4.1.3 Deflection of flexible pipe

The phenomenon ‘soil arching’ explains why the load on the rigid pipe is higher than the load on a flexible pipe. The soil columns on both sides of a rigid pipe are more compressive than the prism soil above the rigid pipe, and they have larger settlement than the prism soil. The differential settlement between both the side soil and prism soil generate a downward shear force making the load over the rigid pipe higher than the weight of the prism soil. This phenomena is reversed when the pipe is flexible, as the prism soil will settle more than the side soil because the flexibility of the pipe and the shear force between the side soil and prism will be upwards, making the load on the flexible pipe less than the weight of the prism soil (Sargand and Masada, 2003).

Spangler (1941) examined this phenomenon by including both soil and pipe rigidity to develop a method to calculate deflections of buried flexible pipes, known today as the Iowa formula. Spangler used the method developed by Marston to estimate the loading on the buried pipe, including pipe flexibility (pipe stiffness) and passive pressures, to represent the side soil resistance of the pipe to the outward movement of pipe deflection in the x-axis (

Figure 2.16). This then enabled the derivation of the original Iowa formula (Equation 2-14) (Moser and Folkman, 2008).

$$\Delta x = \frac{D_L K W_c r^3}{EI + 0.061 e r^4} \quad \text{Equation 2-14}$$

where:

$\Delta x$  = horizontal pipe deflection

$D_L$  = deflection lag factor

$K$  = bedding constant

$W_c$  = Marston's load per unit length of pipe

$r$  = mean radius of pipe

$E$  = modulus elasticity of pipe material

$I$  = moment of inertia of pipe wall

$e$  = modulus of passive resistance of side fill

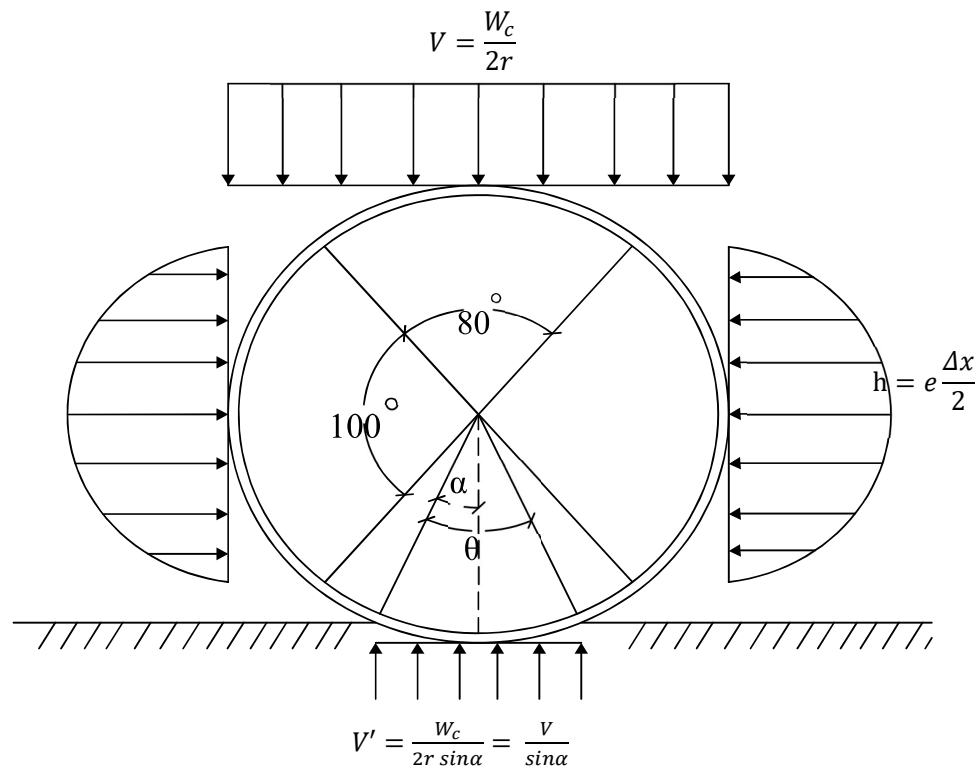


Figure 2.16 Spangler hypotheses of distributed stress on the buried pipe (Masada, 1996). [Reprinted with permission from the author - Ohio University]

Given that much of the pipe strength is developed by the surrounding soil which supports the pipe laterally as the pipe deforms, Watkins (1957) improved this formula by including the modulus of soil reaction ( $M_s = er$ ), instead of the soil modulus of passive resistance of side fill, which makes it dimensionally consistent. This modulus has been included in the final version of the modified Iowa formula used in ASTM-D2412 (2008), as shown in Equation 2-15.

$$\Delta x = \frac{D_L K W_c r^3}{EI + 0.061 M_s r^3} \quad \text{Equation 2-15}$$

Masada (2000) derived the relationship between horizontal and vertical deflections ( $\Delta y$ ) using a numerical derivation of the modified Iowa equation and the same assumptions used by Spangler (Equation 2-16).

$$\frac{\Delta y}{\Delta x} = 1 + \frac{0.0094 M_s}{PS} \quad \text{Equation 2-16}$$

where:

$$PS \text{ is the pipe stiffness} = \frac{EI}{0.149 r^3} \quad \text{Equation 2-17}$$

Many researchers have commented on the limitations of the Iowa formula, often criticized for the extensive assumptions behind its theoretical formulation and the empirical nature of some of its coefficients. A comparison study examining the calculated deformation of flexible pipes buried in soil, was conducted using the

modified Iowa Equation, an empirical approach, finite element analysis and the German Standards method (ATV-DVWK, 2000) with measured deformation values. It was concluded that the output from the Iowa approach tended to overestimate deflection values (Arockiasamy et al, 2006; Akinay and Kilic, 2010; Chaallal et al, 2015). Wang et al (2016) conducted a full-scale field test to determine soil pressure and the deflection of 300 mm and 600 mm high-density polyethylene (HDPE) pipes during installation in fine-grained soils. It was discovered that the vertical soil pressure above the top of the pipe was lower than the pressure calculated using the Marston theory. However, the simplicity of the Iowa formula makes it attractive to many designers.

McGrath (1998) used Burns and Richard (1968) theory for rings embedded in an elastic medium to calculate the bending stiffness factor, this categorizing the rigidity or flexibility of the pipe based on the relative stiffness between the pipe and soil, as seen in Equation 2-18.

$$S_a = \frac{M_s r R^3}{EI} \quad \text{Equation 2-18}$$

where:

$S_a$  = bending stiffness factor, ratio of soil stiffness to pipe wall flexural stiffness

$M_s$  = constrained modulus of soil

$E$  = Pipe material modulus of elasticity

$I$  = Pipe wall moment of inertia,  $R$  = radius of pipe

McGrath (1998) explained that thermoplastic pipe such as polyethylene, has a lower hoop stiffness compared with corrugated metal pipe. This factor should be taken into consideration for designs using pipes. Equation 2-19 is used to calculate pipe hoop stiffness.

$$P_{sh} = \frac{EA}{R} \quad \text{Equation 2-19}$$

where:

$P_{sh}$  = pipe hoop stiffness

$A$  = pipe wall area

The interact parameter derived from combining the soil stiffness with pipe hoop stiffness, is shown in Equation 2-20

$$S_H = \frac{M_s}{P_{sh}} = \frac{M_s R}{EA} \quad \text{Equation 2-20}$$

$S_H$  = hoop stiffness factor

These two parameters are used to calculate the vertical arching vector (VAF) as shown in Equation 2-21 and Equation 2-22.

Under full-bond interface:

$$VAF = 1.06 - 0.96(S_H - 0.7/S_H + 1.75) \quad \text{Equation 2-21}$$

Under free-slip interface:

$$VAF = 0.76 - 0.71(S_H - 0.7/S_H + 1.75) \quad \text{Equation 2-22}$$



Combining the Iowa expression (which used steel pipe as flexible pipe in Spangler (1941) experiment) with deflection due to circumferential shortening, results in Equation 2-23, by incorporating both the hoop stiffness and the bending stiffness of the pipe-soil system. This new formulation improved the accuracy of the predicted total deflection of buried flexible pipes (McGrath et al, 2009):

$$\Delta y = \left[ \frac{W_c}{\frac{EA}{r} + 0.57M_s} \right] \left[ \frac{D_L K W_c}{\frac{EI}{r^3} + 0.061M_s} \right] \quad \text{Equation 2-23}$$

This equation has also been tested using HDPE and polyvinyl chloride (PVC) pipes using a full scale laboratory test, and was found appropriate for calculating the deflection for both pipes (Dhar et al, 2002). The debate about the comparison between the Iowa formula and Burns and Richard (1968) method used by McGrath (1998) is still underway (Figure 2.17) (Sargand and Masada, 2003; Moser and Folkman, 2008). Both theories have, at times, produced the same results. For example McGrath (1998) showed that for a pipe with a high hoop stiffness, both Spangler's expression and the Burns and Richard elasticity solution are essentially identical. Moser and Folkman (2008) also provided several examples where the Spangler equation and Burns Richard solutions yielded similar results.

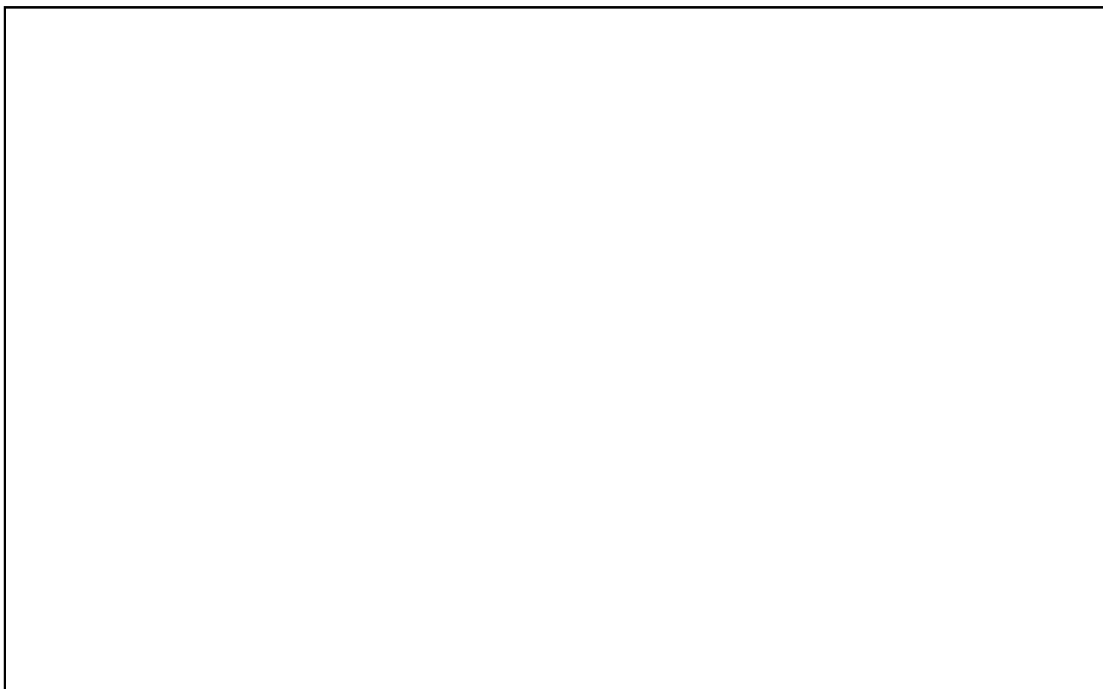


Figure 2.17 Comparison of experimental results with various analytical methods for HDPE pipe (Moser and Folkman, 2008).

The diagram originally presented here cannot be made freely available via LJMU Digital Collections because of 'copyright'. The diagram was sourced from Moser and Folkman (2008)

#### 2.4.2 *FE Method*

The Iowa equation and the McGrath equation were designed to calculate the deflection of one flexible pipe buried in soil assuming soil behaviour to be elastic, which not the case. This shortcoming in both methods led to an error compared to test data and finite element data.

The FE method has been found to provide more reliable results for testing buried pipe performance than the traditional empirical approach (Kouretzis et al, 2013; Jung et al, 2014; Zhou et al, 2017). The FE method is a convenient one to use to study the behaviour of buried flexible pipes and avoid the cost of field tests; this method allows the inspection of many scenarios and testing of a variety of factors that influence the behaviour of buried pipes (Akinay and Kilic, 2010; Tian et al, 2015; Tsai et al, 2015). However, the accuracy of the FE results depends on the selection of an appropriate constitutive model to simulate soil-pipe interaction, the calibrated material properties of the model (ABAQUS, 2012), *'the finite element method often has to be calibrated by comparing FEA results with results from physical tests'* (Moser and Folkman, 2008). As such, experiments become essential to validate models and the properties of materials and to establish the correct input data to ensure an accurate simulation (Suleiman, 2002).

Kang et al (2013b) studied the maximum and minimum cover depth for laying plastic pipes under roadways, using a 2D FE model (ABAQUS) to investigate the geometric nonlinearity behaviour of the pipe- soil system. They incorporated nonlinear Duncan and Selig soil models to simulate soil behaviour and to identify the associated parameters. The pipes were PVC and HDPE with diameters of 0.3, 0.6, 1.2 and 1.5 m. The dimensions of the FE model were approximately three

times the pipe diameter. Laboratory test data presented by McGrath et al (2009), were used to calibrate and validate the FE model, which illustrated satisfactory agreement between the FE results and the measured deflections for both the HDPE and PVC tests. This study recommended a maximum cover depth for corrugated HDPE and PVC of 13 and 14 m, respectively, for pipes of diameters less than 1.2 m and 6 and 8 m, respectively, and for pipe diameters greater than 1.2 m. They recommended minimum cover depth was 0.9 m to protect the buried pipe from the effect of surface load; this is the cover depth used in this research.

Sargand et al (2005) monitored the performance of flexible pipe (specifically, HDPE) subjected to a backfill soil depth of 6.1 and 12 m, for two years. The field results indicated that the flexible pipe performed satisfactorily. The FE model used to simulate this incorporated a series of triaxial compression tests conducted in the laboratory, to identify soil properties. The conclusion was that the FE results tended to overestimate the soil pressure acting against the pipe and to underestimate pipe deflection.

McGrath et al (2009) used a 2D FE model to develop the design procedures for buried plastic pipes (HDPE and PVC). A laboratory test was also conducted using the biaxial cell designed by Brachman et al (2001). The experimental results were compared with the FE model to evaluate the model's effectiveness at estimating pipe behaviour under deep burial conditions. It was found that the FE model can be used effectively and that its readings are essential in order to select the appropriate constitutive model to characterize soil behaviour.

The FE method can also be used effectively to study complicated factors which can impact the buried pipe. Jung (2011) simulated soil-pipeline interaction when

vertical and lateral movement occurs due to earthquake or liquefaction. The Mohr-Coulomb (MC) constitutive was used to simulate non-linear behaviour, the results found to agree with full-scale experimental results. The impact of environmental conditions (external weather conditions) on the soil of buried pipes was investigated by Saadeldin (2016) using an FE model. This study established a relationships between soil-pipe correlations and climate change in one case study. Corey (2015) utilized a non-linear, three-dimensional FE model (Figure 2.18) to explore the effects of surface load on buried flexible pipe, under low cover depth, using geogrid (Geosynthetic material) to protect the pipe. The FE model was calibrated using full-scale laboratory experimental results. This study revealed that using flexible materials above the pipe reduces the strain and deflection on the pipes.

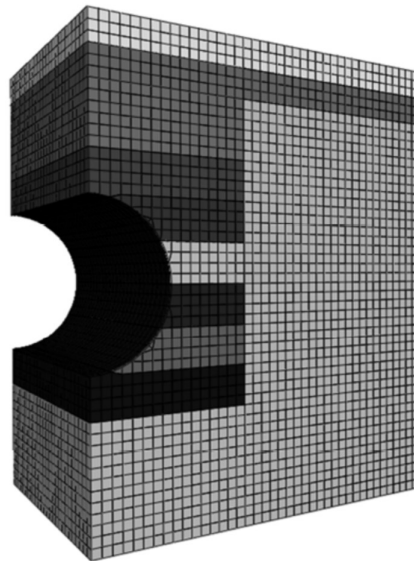


Figure 2.18 The three-dimensional FE model for a buried pipe used by Corey (2015). [Reprinted with permission from the author - Kansas University]

## 2.5 Summary

Based on the literature review, many conclusions can be reached on the state of research with respect to sewer design. Existing designs belongs to the previous century but the development of inspection and maintenance equipment, make it possible to revisit the design. Separate sewer systems are more common in comparison to combined sewer systems. The novel design presented in this research proposes to overcome the substantial challenge that designers, contractors and water companies face: the installation of a traditional separate sewer system in an area where is a lack of space.

Manhole structural performance does not appear to have received much in the way of research attention. New designs for manholes require testing regarding structural performance, as it they are heavier than traditional manholes.

The hydraulic performance of the conventional manhole has been tested and the parameters regarding loss of energy inside the manhole identified. There is a need to improve the shape of the manhole, specifically the stormwater chamber, to efficiently hydraulic integrity and establish the head loss through this chamber.

Flexible pipes buried in trenches have received a lot of research attention but the same cannot be said when there are two flexible pipes set in one trench. This is of concern as this configuration is found in traditional separate sewer systems where storm pipes intersect with sanitary pipes at street crossings. Most of the empirical methods discussed address the behaviour of one pipe buried in the trench.

FE is a powerful tool used to predict the behaviour of buried structures, such as pipes or manholes, in soil. Using an FE model allows the designer to avoid short comings in empirical methods such as using non-linear constitutive for the material and stress dependent. However, the accuracy of the FE model is dependent on selecting the appropriate constitutive model to simulate the materials and the correct identification of boundary conditions and material properties. As such, a validation process is required to conduct the correct simulation for any structure using an FE.

## CHAPTER 3

# RESEARCH METHODOLOGY AND CHARACTERISATION OF MATERIALS

This chapter describes the methodology used to carry out the research, including the laboratory models built in LJMU, and the laboratory tests conducted to identify the properties of the materials used in the models.

### 3.1 Methodology

One of the main objectives of this research was to test the hydraulic and structural integrity of the novel manhole design. This involves identifying the hydraulic properties of the new pattern of storm water flow inside the storm chamber and the structural performance of the two flexible pipes installed in one trench. The new configuration of the separate pipe system has necessitated the development of a novel empirical method to calculate flexible pipe displacements in their new position.

Early discussions between the researchers and United Utilities Company (UU) led to the methodology for this research. UU's recommendation was to investigate design performance in the laboratory before upgrading to full scale field testing.



The laboratory testing was carried out in two stages:

- Stage 1: building the physical laboratory models:
  - A physical model of a trench was built to test the structural performance of both the new manhole design and the new configuration of two separate pipes set in the trench.
  - A physical model of the manhole was built for hydraulic testing of the stormwater flow in the new storm manhole chamber.
- Stage 2: Establishing numerical models to simulate structural performance and hydraulic properties:
  - An FE model was used to simulate the structural behaviour of both the new manhole buried in soil and the new installation method of separate pipes.
  - A CFD model was used to simulate the hydraulic behaviour of the flow of stormwater in the new design.

The results of both physical laboratory models were used to validate the numerical models (FE and CFD), using the same materials and circumstances to then develop the numerical model from lab scale to full scale reliably.

To make a clear distinction between experiments applied on the manhole design and the tests conducted on the buried pipe performance, separate chapters present these discussions: one chapter to discuss the manhole design and structural performance, the second to discuss the hydraulic properties of the stormwater flow in the new design. A further chapter will discuss the structural performance of the pipes when set in their new positions.

The results of the structural performance, the hydraulic properties of the experimental works and numerical methods for the new manhole design, will be compared with results for a conventional manhole to identify improvements made by the new design. Similarly, the structural performance of the pipes in their new position will be compared with the traditional method of pipe installation (each pipe in a separate trench) to explore differences and improvements. Both the new manhole design and the new pipe configuration have been checked with design standard requirements for sewer systems to validate the safety of the new design.

The economic advantages of using the new design compared to a traditional one have been discussed, in term of construction cost, construction time and footprint.

The conclusions, recommendations and future research chapter are presented at the end of the dissertation justifying further application in the field, making a significant improvement in existing sewer system designs and a development for separate sewer system for future system designs.

### **3.2 Material properties**

Accurate identification of the properties of materials to be used, is one of the main requirements when running a precise simulation using FE methods. This section will discuss the properties of the materials and methods used to define them. The materials used in this research are two types of soil; one for filling, the other to create a bedding layer and also PVC pipes, GRP, steel and concrete (reinforced and non-reinforced).

### 3.2.1 *Soil*

Soil is a media in which many objects are embedded such as concrete and steel structures, pipelines and a variety of underground structural materials. The ability to predict the interactive behaviour of these materials with the soil is considered one of the more complicated challenges, due to the complex texture of soil. This can include different types of solid matter, peppered with voids which can be filled by air, water or other liquids, creating a variety of soil stiffness, subject, in turn, to a variety of loading and unloading conditions. Because of this, it is important to identify the properties of the soil to predict soil behaviour when designing sewer works. The comparison of the cost of compaction, through selection of a filling material of a suitable type and thickness to bed the pipe, is considered one of the more important criteria regarding the safety and economic design of any drainage system (Rani et al, 2014).

A normal composite soil (corresponding to the soil used within the UK to bed sewer systems), was used to bury the manhole and the pipe system, a specific bedding layer used as per HM-Government (2010) guidelines. A series of laboratory tests were conducted to identify the mechanical and elastoplastic soil properties.

### 3.2.2 *Mechanical properties*

#### 3.2.2.1 *Sieve Analysis*

Sieve analysis (grain size distribution), was applied to identify the physical properties of both the soil and the bedding layer, using a set of standardized sieves. Sieves with opening sizes ranging from 0.075 mm (sieve No. 200) to 4.75 mm (sieve No. 4), were used to analyse the top soil, while sieves ranging from 0.3mm (sieve No. 50) to 11.2 mm, were used to analyse the bedding layer. Figure 3.1 shows the sieves fixed on the vibrator used to calculate the grain size distribution of the soil.



Figure 3.1 The set of sieves used to calculate the grain size distribution of the soil.

The results from this test were used to classify the type of the soil based on the Unified Soil Classification System (USCS). Three samples were selected randomly from the raw soil to conduct the test, the results presented in Figure 3.2 showing the top soil classified as SP-SM (silty sand, sand-silt mixtures, more than 50% passes no. 4 sieve, more than 50% retained on no. 200 sieve) according to (USCS). This soil is of medium grade, based on values of uniform coefficient  $C_u=6.6$  and curvature coefficient  $C_c=0.5$ , making it suitable for use as a filling soil (Moser and Folkman, 2008). Figure 3.3 gives the size distribution of the manufactured bedding material, classified as uniformly graded, medium, gravel based on uniform coefficient  $C_u=1.01$  and curvature coefficient  $C_c=1.28$ .

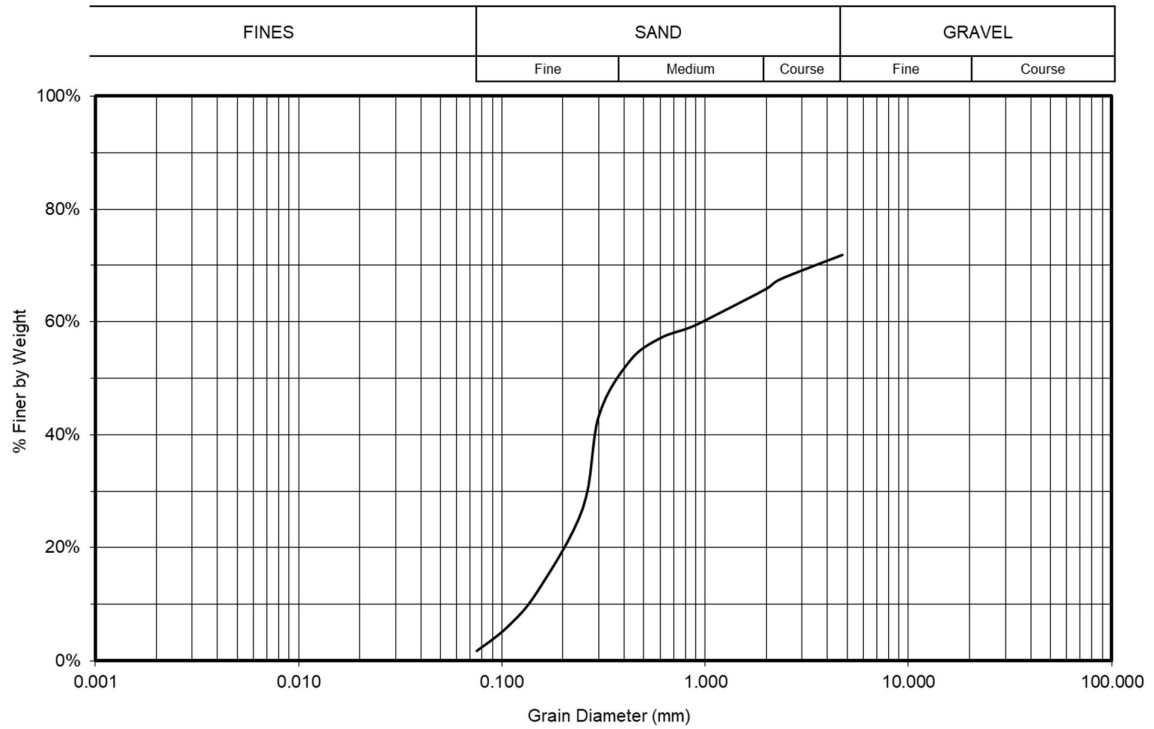


Figure 3.2 Particle size distribution curve of the top soil

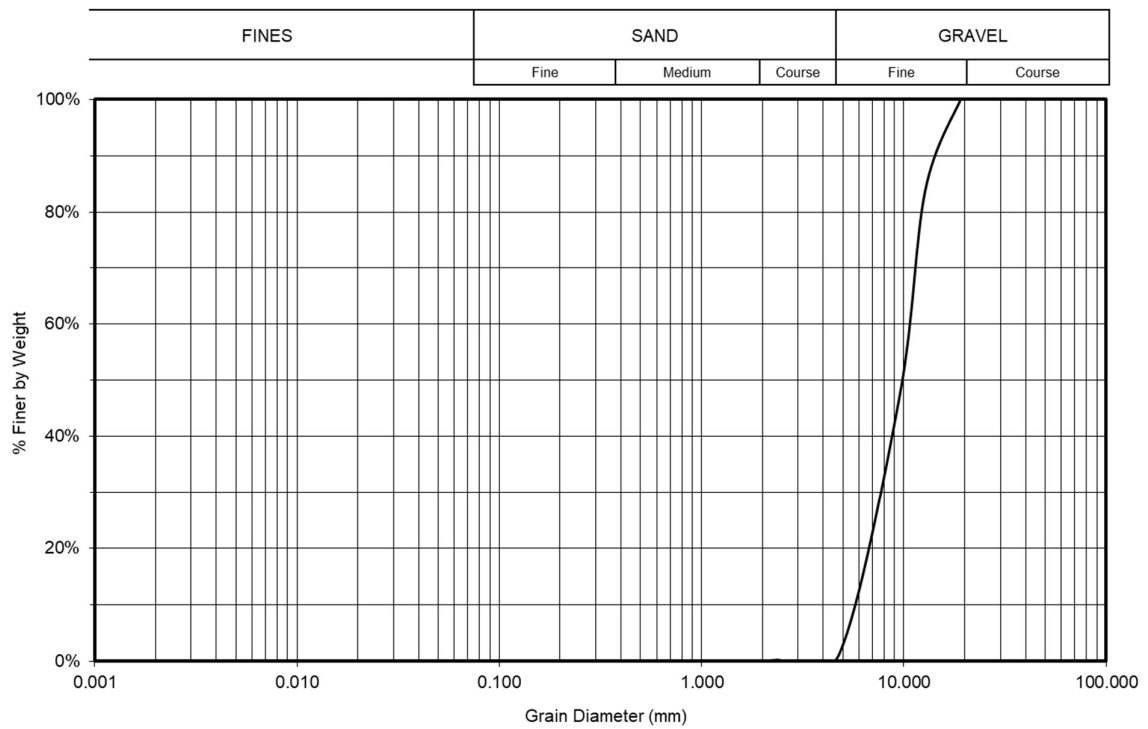


Figure 3.3 Particle size distribution curve of the bedding soil

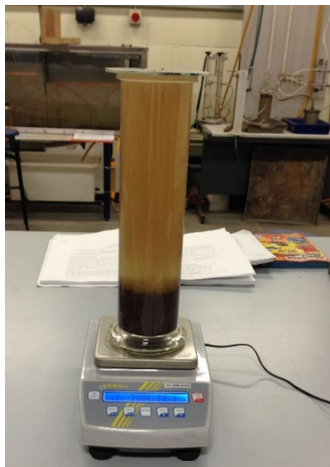
### 3.2.2.2 Specific gravity ( $G_s$ )

Specific gravity is the unit weight of soil solids to the unit weight of water.

A jar test was conducted to identify the specific gravity for both the filling soil and bedding layer. Figure 3.4 shows the jar test and Table 3-1 presents the results.

Table 3-1 Results of Specific gravity (Gas Jar Method) for the filling soil and bedding

Item	Filling Soil	Bedding
Mass of gas jar and plate (g) (m1)	862.2	862.18
Mass of gas jar, plate and dry soil (g) (m2)	1112.25	1339.35
Mass of gas jar, plate, soil and water (g) (m3)	2254.25	2396.88
Mass of gas jar and water (g) (m4)	2102.6	2102.43
Calculation of $G_s$ : $(m_2 - m_1) / ((m_4 - m_1) - (m_3 - m_2))$	<b>2.54</b>	<b>2.61</b>



(a)



(b)

Figure 3.4 Gas Jar Method to determine the specific gravity of the (a) top soil, and (b) bedding layer.

### 3.2.2.3 *Standard proctor test*

To determine and achieve the required compaction for the filling soil, a 90%-95% compaction degree, the standard protector test (Figure 3.5), was applied to the specimen of filling soil to determine the maximum dry unit weight ( $\gamma_d$ -max) and the corresponding optimum moisture content ( $\omega_{opt}$ ). These were 1.828 g/cm<sup>3</sup> and 12.6 %, respectively. Figure 3.6 illustrates the results of the compaction test.



Figure 3.5 The mould and compactor used to implement the compaction test



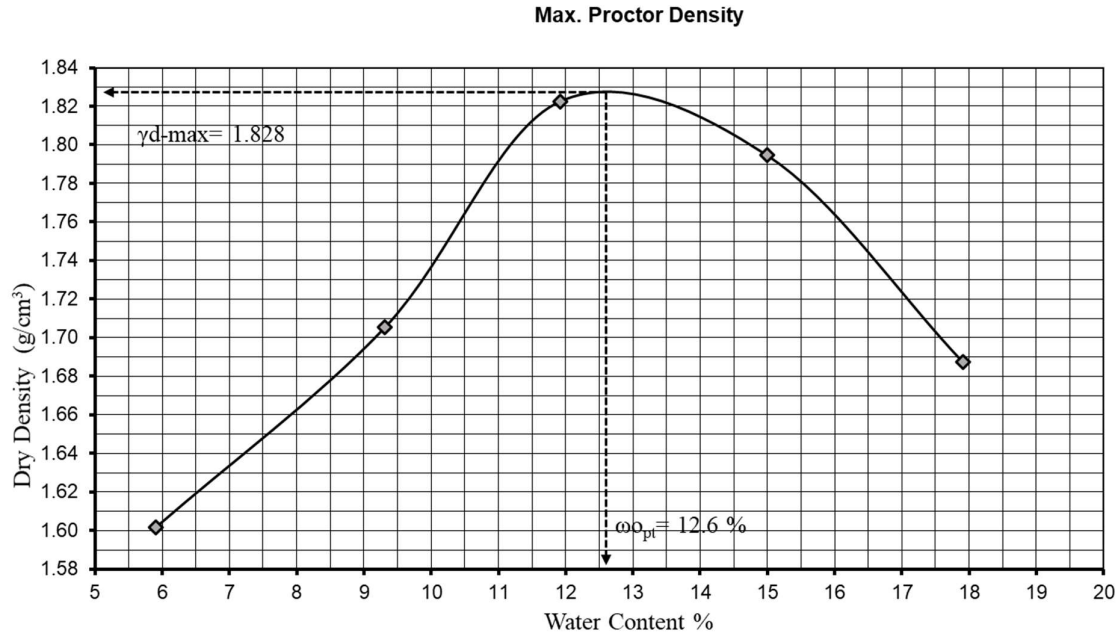


Figure 3.6 The curve of compaction

### 3.2.3 Elasticity and plasticity properties of the soil

Soil is considered an elastic-plastic material within which strain increments are additively composed of part elastic and part plastic (Equation 3-1). This is according to conventional plasticity theory, such as the Mohr–Coulomb hypothesis and Drucker-Prager’s criterion, which are used as a yield or fracture condition, predominantly for granular and geological materials (Gross and Seelig, 2011).

$$d_{\epsilon} = d_{\epsilon}^e + d_{\epsilon}^p \quad \text{Equation 3-1}$$

where:

$d_{\epsilon}$  = total strain

$d_{\epsilon}^e$  = elastic strain

$d_{\epsilon}^p$  = plastic strain

There are many soil constitutive models which propose to simulate elastoplastic soil behaviour. However, designers often face difficulties selecting the most appropriate constitutive soil model for numerical modelling. The analysis method, type of material and range of pressure/stress, in addition to an in-depth understanding of the concepts of constitutive methods, are the main factors which direct the choice of model. Limitations and advantages of each model in solving engineering case studies, the type of input data which is required and availability of data obtained from a range of laboratory tests, are other factors of consequence when choosing a constitutive model (Ti et al, 2009).

Two models have been used in this research: the Mohr-Coulomb constitutive model and the modified Drucker-Prager cap constitutive model. Both these models identify specific soil parameters such as soil modulus  $E'$  and Poisson's ratio, to identify the elastic components of the stress-strain relationship and unload-reload test, thereby identifying the plasticity of the soil.

#### *3.2.3.1 Mohr-Coulomb Plasticity M-C*

The Mohr-Coulomb plasticity model is one of the most commonly used strength theories. It is described by a friction angle and cohesion (strength is dependent on confining stress), geotechnical engineering application that simulates the response of materials under monotonic loading (ABAQUS, 2012). This model uses the classical Mohr-Coulomb yield criterion as shown in Figure 3.7, which assumes that yield occurs when the shear stress on any point in a material, reaches a value that depends linearly on the normal stress in the same plane, and on an irregular hexagonal section in the deviatoric plane. However, the ABAQUS

Mohr-Coulomb model has a completely smooth flow potential instead of the classical hexagonal pyramid (Simpson, 2009).

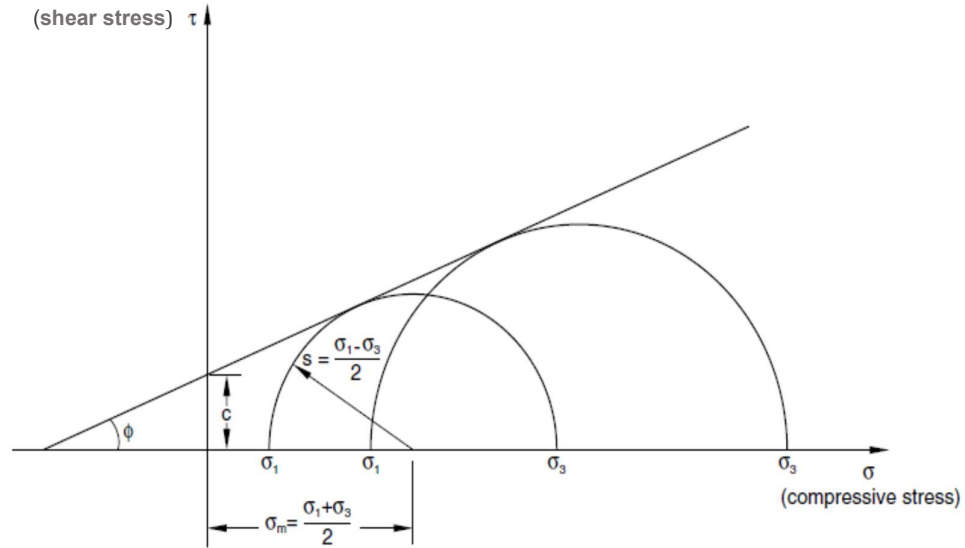


Figure 3.7 The Mohr-Coulomb failure model (ABAQUS, 2012). [Reprinted with permission from Dassault Systemes Simulia Corp]

$$\tau = c - \sigma \tan \phi \quad \text{Equation 3-2}$$

where:  $\sigma$  is negative in compression. From Mohr's circle

$$\tau = s \cos \phi \quad \text{Equation 3-3}$$

where:

$$s = \frac{1}{2} (\sigma_1 - \sigma_3)$$

$$\sigma = \sigma_m + s \sin \phi \quad \text{Equation 3-4}$$

The Mohr-Coulomb model assumes that the major principal stress,  $\sigma_1$ , is independent of the intermediate principal stress,  $\sigma_2$ , for the M-C criterion, and that the yield surface on the deviatoric plane is an irregular hexagon, something which is considered a shortfall when compared with the Drucker-Prager model. This is because it impairs the convergence in flow theory because of the presence of six sharp corners. This can limit the accuracy of calculations, especially in cases where flow localization is important. When the M-C model is applied to soil material, both the cohesion and friction angle can control the stiffness of the material (hardening or softening), while plastic behaviour is related only to cohesion when the internal friction remains constant during plastic deformation (Rani et al, 2014).

#### 3.2.3.2 *Drucker-Prager Model D-P*

Drucker-Prager is used to model frictional materials which are typically granular, such as soils and rock, exhibit pressure-dependent yields, and where the compressive yield strength is greater than the tensile yield strength (the material becomes stronger as the pressure increases). The Drucker-Prager plasticity model (Figure 3.8), has been widely used in finite element analysis programs for a variety of geotechnical engineering applications because of its ability to consider the effect of intermediate principal stress, stress path and dilatancy. The onset of plastic behaviour is determined by the Drucker-Prager failure surface.

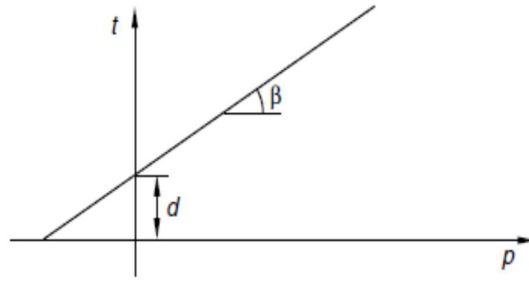


Figure 3.8 The Linear Drucker-Prager Model (ABAQUS, 2012). [Reprinted with permission from Dassault Systemes Simulia Corp]

$$Fs = t - p \tan \beta - d$$

Equation 3-5

where:

$Fs$  = the Drucker-Prager failure surface

$\beta$  = the friction angle measured at high confining pressure

$d$  = cohesion in the  $p$ - $t$  plane

$p$  = the mean stress

$t$  = a measure of shear stress as defined below

$$t = \frac{q}{2} \left[ 1 + \frac{1}{K} - \left[ 1 - \frac{1}{k} \right] \left[ \frac{r}{q} \right]^3 \right]$$

Equation 3-6

$K$  is the ratio of the yield stress in triaxial tension to the yield stress in triaxial compression, thus controlling the dependence of the yield surface on the value of the intermediate principal stress. To ensure that the yield surface remains convex requires  $0.778 \leq K \leq 1$ .

When  $K=1$  and  $t=q$ , this implies that the yield surface is a von Mises circle in the deviatoric principal stress plane, in which case the yield stresses in the triaxial tension and compression are the same. The Drucker–Prager failure surface is represented by a simple cone while that of the Mohr-Coulomb model is hexagonal. The DP model shares the same advantages and limitations as the Mohr-Coulomb model except that the yield is circular (Figure 3.9), from the centre to the yield surface (ABAQUS, 2012).

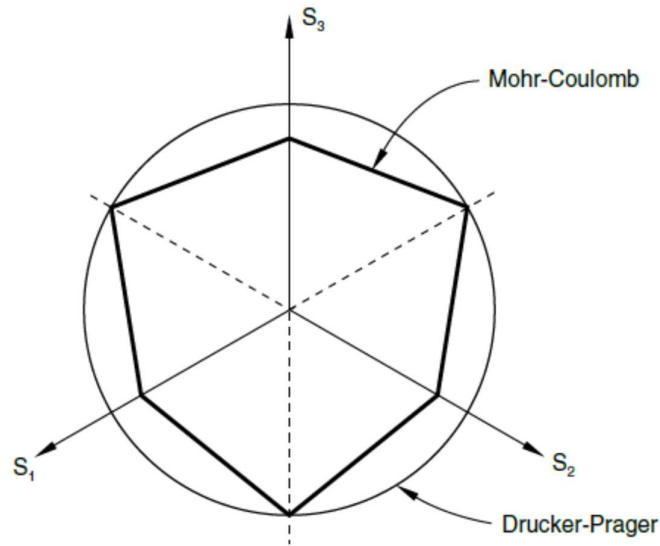


Figure 3.9 The Mohr-Coulomb and Drucker-Prager models in the deviatoric plane (ABAQUS, 2012). [Reprinted with permission from Dassault Systemes Simulia Corp]

### 3.2.3.3 Modified Drucker-Prager/Cap plasticity

This model gathers the Drucker-Prager shear failure and compression cap yield surface which causes the material to compact. It is appropriate for soil behaviour because it is capable of considering the effect of stress history, stress path, dilatancy and the effect of intermediate principal stress (Figure 3.10).

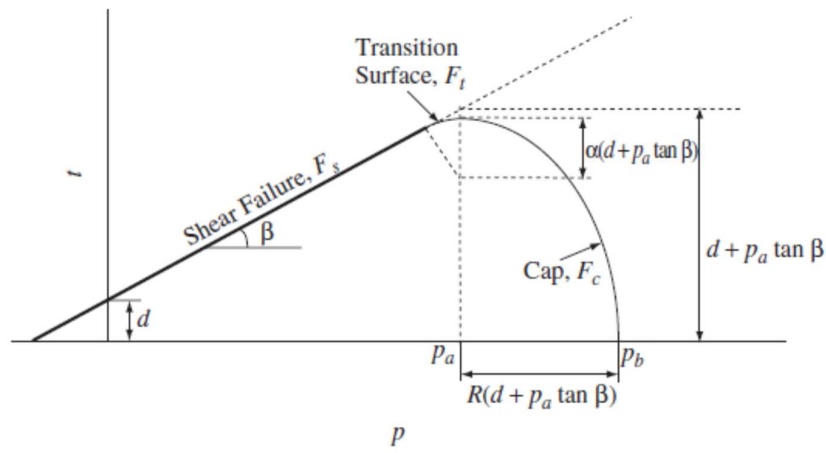


Figure 3.10 Yield surfaces of the modified Drucker-Prager cap model in the  $p$ - $t$  plane. (ABAQUS, 2012). [Reprinted with permission from Dassault Systemes Simulia Corp]

The cap yield surface is defined in Equation 3-7, as a function of volumetric plastic according to the consolidation mechanism.

$$F_c = \sqrt{(p - p_a)^2 + \left( \frac{Rt}{1 + \alpha - \alpha / \cos \beta} \right)^2} - R(d + p_a \tan \beta) = 0 \quad \text{Equation 3-7}$$

where:

$R$  is a material parameter that controls the shape of the cap

$\alpha$  is a small number (typically 0.01 to 0.05), used to define a smooth transition surface between the Drucker–Prager shear failure surface and the cap:

$$F_t = \sqrt{(p - p_a)^2 + \left[ t - \left( 1 - \frac{\alpha}{\cos \beta} \right) (d + p_a \tan \beta) \right]^2} - \alpha(d + p_a \tan \beta) = 0 \quad \text{Equation 3-8}$$

Hardening–softening behaviour is described by an evolution parameter ( $p_a$ ) which is a function of the volumetric plastic strain ( $P_b = P_b(\varepsilon_{plvol})$ ) and the mean effective (yield) stress.

A one-dimension consolidation test is used to obtain this function using unloading–reloading cycles. Equation 3-9 is used to calculate the evolution parameter ( $p_a$ ).

$$P_a = \frac{P_b - R_d}{1 + R \tan \beta} \quad \text{Equation 3-9}$$

Both, the Mohr–Coulomb and Drucker–Prager produced nearly the same results when applied in this research (Abbas et al, 2017). The modified Drucker–Prager cap constitutive model was selected to use in the simulation because of its accuracy and ability to simulate the plastic behaviour of soil relative to effective stress over the long term, such as when it is exposed to moving loads. Triaxial and consolidation tests were carried out to identify the model parameters for the soil.

#### 3.2.3.4 Triaxial test

The triaxial compression test is an effective method to determine the stress–strain behaviour of soil under different confining pressures, this used by



the FE package to identify the elastoplastic properties of the soil. A triaxial Consolidated-Undrained (CU) test was conducted on undisturbed soil specimens obtained from the physical models, after the soil was compacted in the trench. Figure 3.11 shows the location of the soil specimens extracted from the first layer of soil underneath the buried pipes. The test was conducted for each filling soil layer: below and above the buried pipes and below the buried manholes. Figure 3.12 shows the sample setup and the apparatus used to implement the test. In total, 12 tests were conducted.



Figure 3.11 Extracting the soil specimens from the trench



Figure 3.12 The apparatus for the triaxial test

Figure 3.13 shows the results of the three triaxial tests.

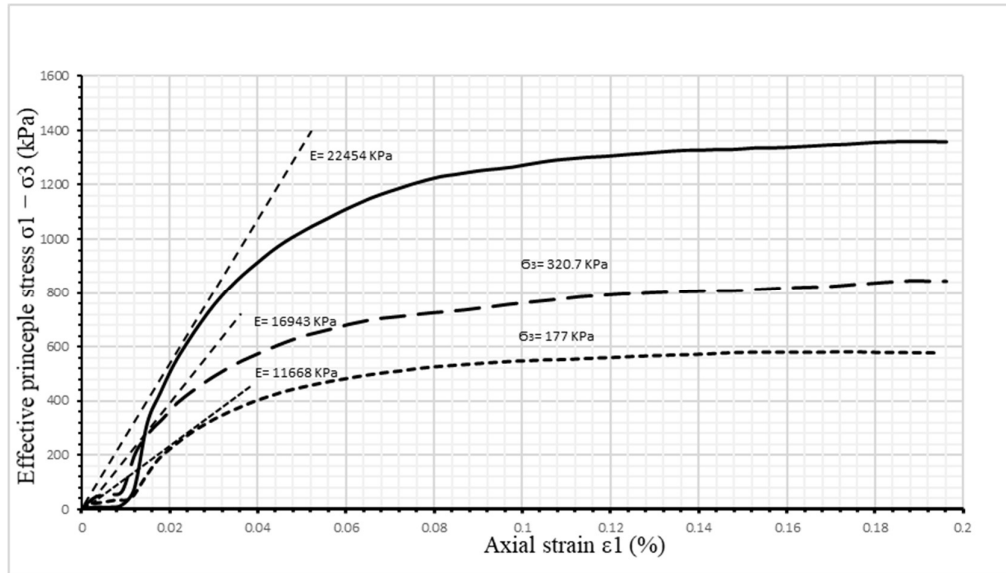


Figure 3.13 Results of the three triaxial tests under different confining pressures.

Mohr-Coulomb constitutive model parameters (the internal friction angle of the soil ( $\phi$ ) and cohesion ( $C$ )) were derived from the triaxial test. Figure 3.14 shows the three Mohr's circles corresponding to failure stresses obtained from the triaxial test results.

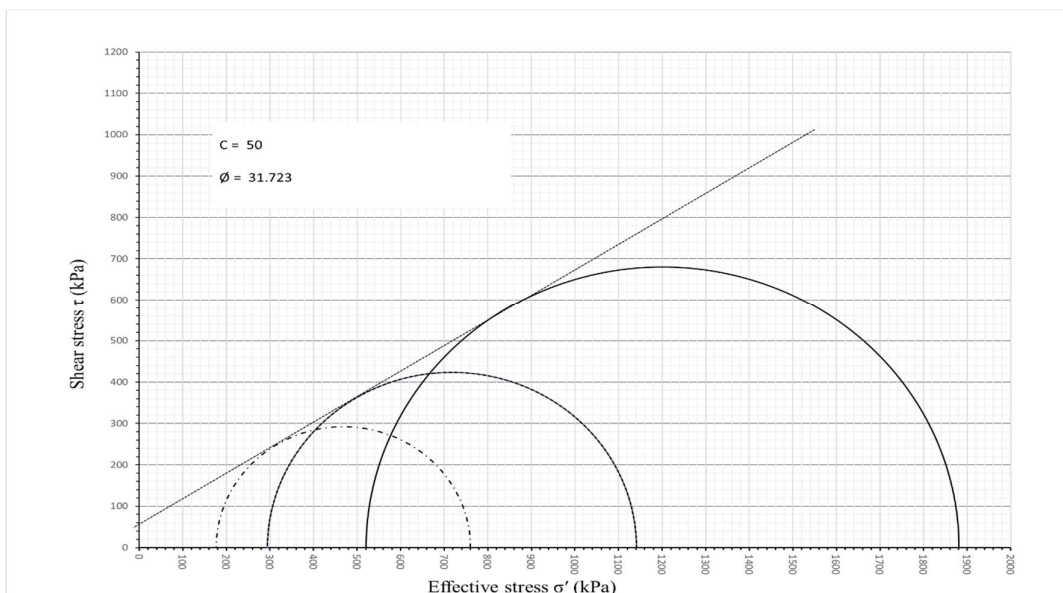


Figure 3.14 Mohr-Coulomb failure criterion.

The triaxial test results were also used to identify the soil friction angle and cohesion for the Drucker–Prager model. Figure 3.15 illustrates the soil friction angle ( $\beta$ ) and cohesion ( $d$ ) for the Drucker–Prager model from the effective stress ( $p$ ) plotted against shear stress ( $q$ ).

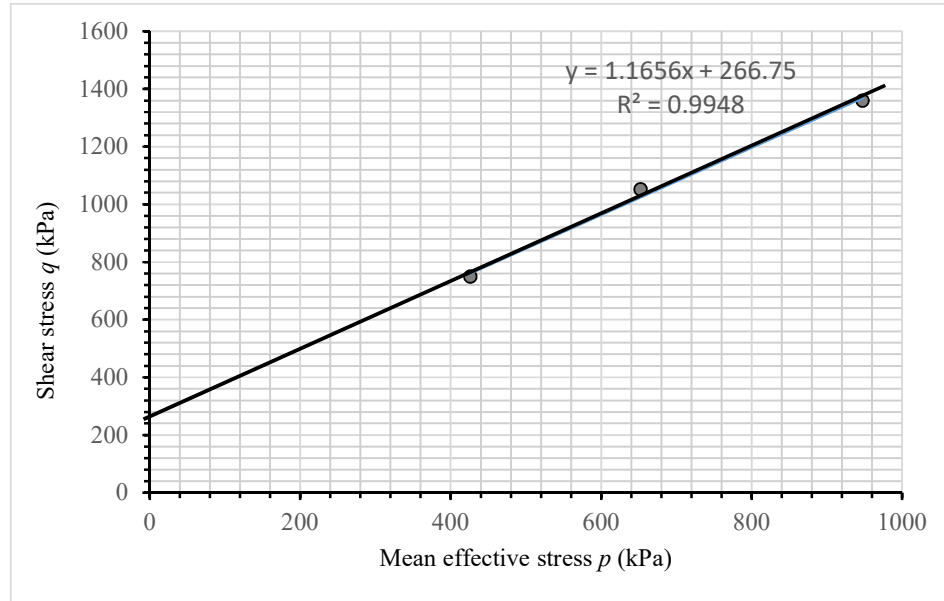


Figure 3.15 Shear stress ( $q$ ) – effective stress ( $p$ ) plotted to identify Drucker–Prager model parameters.

#### 3.2.3.5 Consolidation test

An isotropic consolidation test was used to identify the plastic strain of the soil through applied loading–unloading cycles, and to calculate the volumetric elastic strain that can be subtracted from the volumetric total strain (Helwany, 2007). Three isotropic consolidation tests were conducted on the soil specimens extracted from the trench, from three different points. In total, 9 tests were conducted. Figure 3.16 shows the sample setup and the instruments used to carry out the test. The results for the sample extracted from a point located in the middle of the trench, where the applied load effect is at greatest, were selected to

establish the soil parameters and curve of cap hardening. Figure 3.17 shows the results of the consolidation test.



Figure 3.16 Three pieces of apparatus for the one-dimension consolidation test

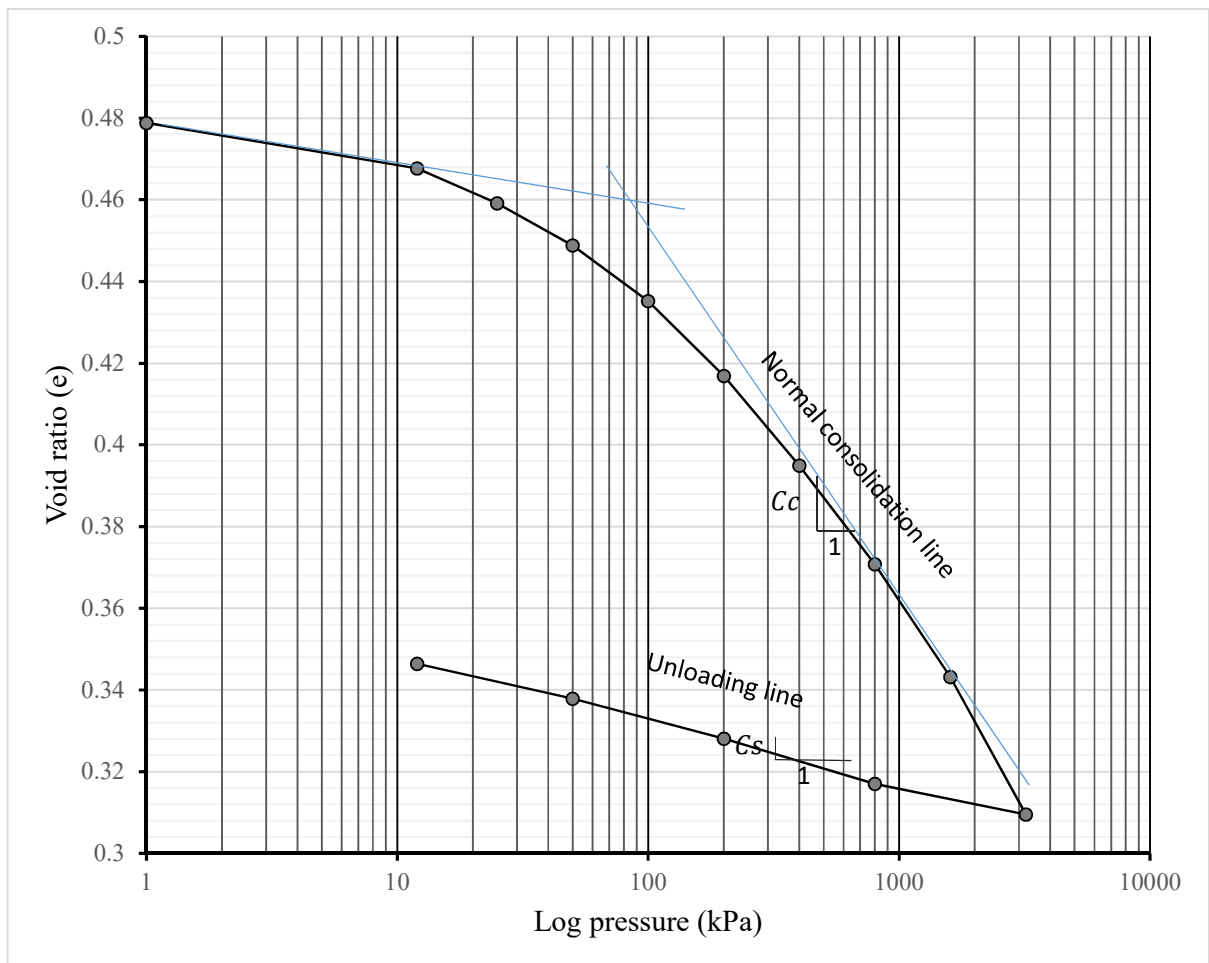


Figure 3.17 Results of the consolidation test used to identify soil properties.

The compression index ( $C_c$ ) and swelling index ( $C_s$ ) obtained from the isotropic consolidation test, were used to calculate the  $\lambda$  and  $\kappa$  slopes of the normal consolidation and loading-unloading lines in the  $e$ - $\ln p$  plane, using Equation 3-10 and Equation 3-11, respectively (Helwany, 2007).

$$\lambda = \frac{C_c}{\ln 10} \quad \text{Equation 3-10}$$

$$\kappa = \frac{C_s}{\ln 10} \quad \text{Equation 3-11}$$

These two parameters were used to establish the cap hardening curve that describes the evolution of the soil's plastic volumetric strain ( Figure 3.18). The plastic volumetric strain ( $\varepsilon_v^p$ ) was calculated using Equation 3-12 (Helwany, 2007).

$$\varepsilon_v^p = \frac{\lambda - \kappa}{1 + e_0} \ln \frac{p'}{p} \quad \text{Equation 3-12}$$

where:

$p$  = effective stress

$p'$  = mean effective stress

$e_0$  = void ratio

$\lambda$  and  $\kappa$  are the slopes of the normal consolidation and loading-unloading lines, respectively.

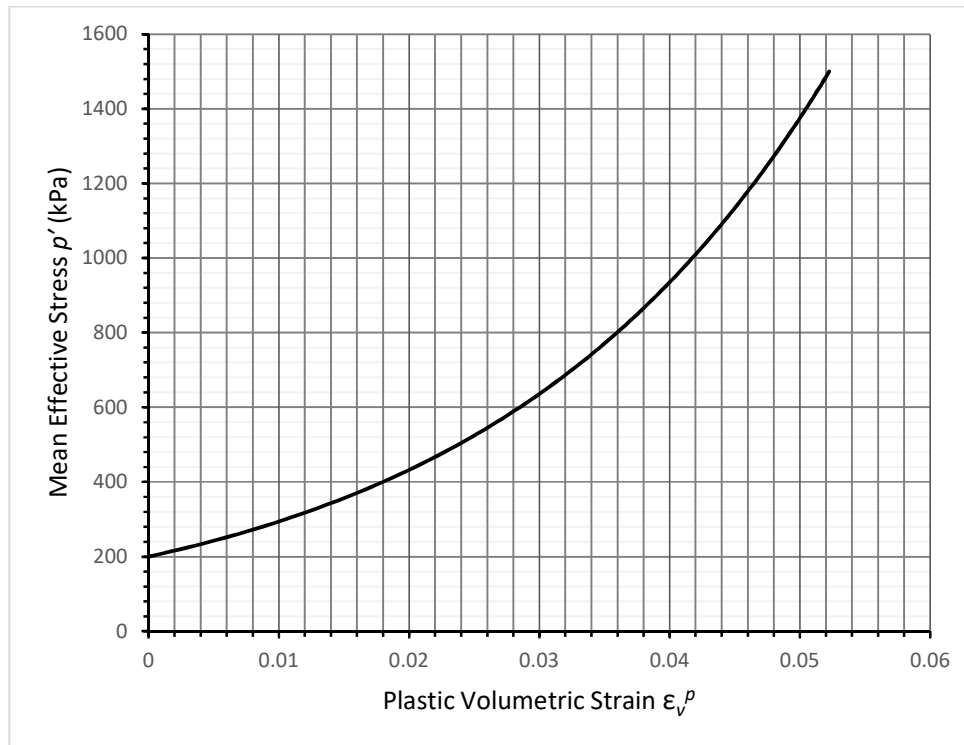


Figure 3.18 Evaluating the modified cap model hardening curve.

The soil parameter properties produced through the laboratory tests above, are summarised in Table 3-2.

Table 3-2 Parameters of the modified Drucker–Prager cap and Mohr–Coulomb constitutive model for the soil and bedding layer.

Items	Parameters	Value
Soil	Density	1685 kg/m <sup>3</sup>
	E	16.943 MPa
	ν	0.295
	<b>Drucker–Prager</b>	
	β	55
	K	0.8
	ψ	15
	λ	0.044
	κ	0.0056
	e <sub>0</sub>	0.48
	<b>Mohr–Coulomb</b>	
	φ	31.7
Bedding	C	50
	Density	1855 kg/m <sup>3</sup>
	E	100 MPa
	φ	35
	C	0
	ν	0.4

#### 3.2.4 Pipe properties

Two PVC pipes of diameter 160 mm (storm pipe) and 80 mm (sanitary pipe), were selected for the physical model. The soil–pipe system works as an integrated single environment, therefore to establish the behaviour of this system under loading, it is necessary to know the mechanical properties of both elements. These properties are required as input for any empirical or mathematical model, including the Iowa Formula. The ASTM-D2412 (2008) method was used to test the pipes to identify the stiffness (Figure 3.19). Pipe stiffness (*PS*) and stiffness factors (*SF*) can be calculated using Equation 3-13 and Equation 3-14, as shown below:

$$PS = \frac{F}{\Delta y} \quad \text{Equation 3-13}$$

$$SF = EI = 0.149 \frac{Fr^3}{\Delta y} = 0.149 r^3 (PS) \quad \text{Equation 3-14}$$

where:

$PS$  = pipe stiffness

$F$  = load per linear length

$r$  = pipe radius

$\Delta y$  = vertical deflection

$E$  = pipe modulus of elasticity

$I$  = the moment of inertia

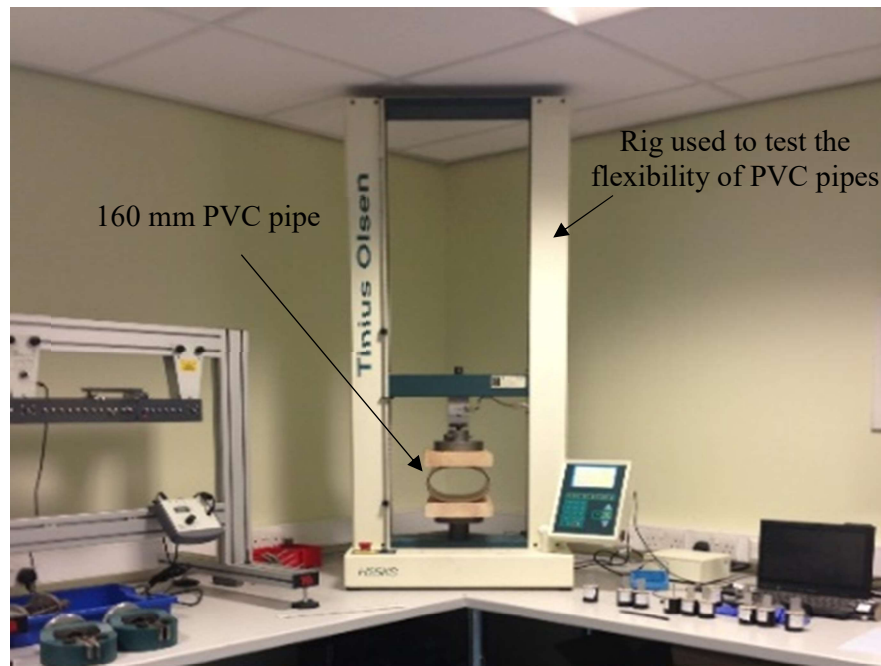
$SF$  = pipe stiffness factor

Table 3-3 shows the properties of both pipes tested for a deflection of 5%.

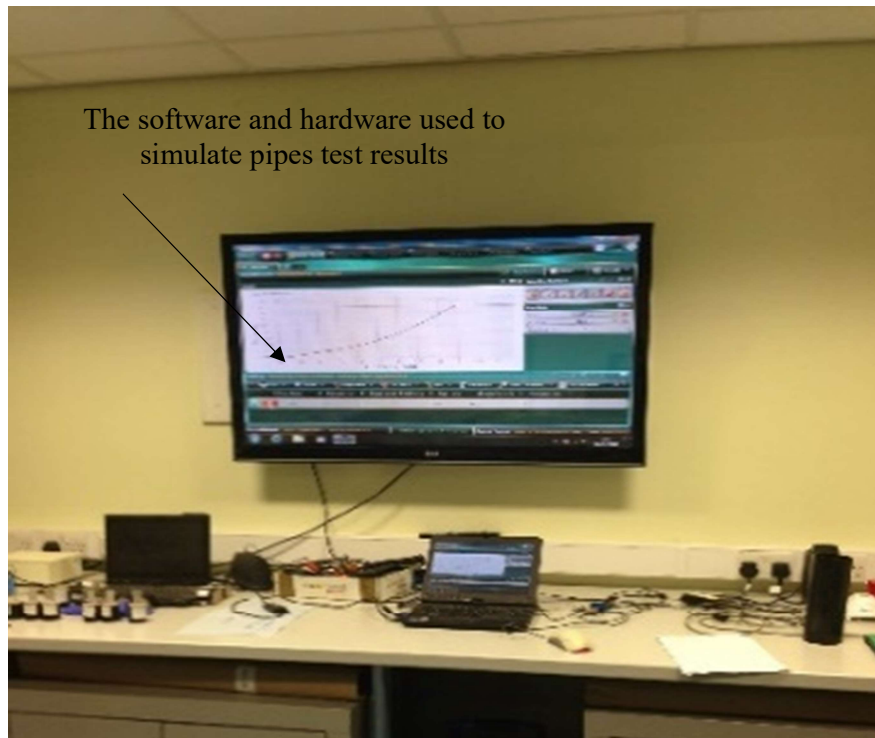
Table 3-3 Parameters of the PVC pipes.

Pipe Dimeter	F	$\Delta y$	$PS$	$EI$	$I$
[mm]	[N/mm]	[mm]	[N/mm/mm]	[N.mm]	[mm <sup>4</sup> /mm]
160	1000/200	8	0.472	36000	28.5
80	1200/200	4	0.825	7867	10.5





(a)



(b)

Figure 3.19 Parallel-Plate Loading Method for testing pipe stiffness in the laboratory (a) the rig and (b) software (ASTM-D2412, 2008).

### 3.2.5 Concrete and steel properties

Reinforced and non-reinforced concrete materials were used in the full-scale FE models of the manholes. Najafi and Sever (2015a) carried out a series of lab tests on non-reinforced concrete manholes used in a FE model, to identify the properties of these materials. The same procedure and materials used by Najafi and Sever (2015a), were applied in this research. They used non-reinforced concrete with a cylinder compressive strength of 40 MPa. Table 3-4 shows the properties of the concrete used for the manhole. The properties of the steel used were determined from the literature (Najafi and Sever, 2015a) and are also included in Table 3-4.

Table 3-4 The parameters of non-reinforced concrete and steel used for FE the model (Najafi and Sever, 2015a).

Items	Parameters	Value		
Steel	Density	7850 kg/m <sup>3</sup>		
	E	210,000 MPa		
	$\nu$	0.3		
Concrete	Density	2200 kg/m <sup>3</sup>		
	E	29,992 MPa		
	$\nu$	0.2		
	<b>Plasticity</b>			
	Dilation Angle	38		
	Eccentricity	0.1		
	$f_{b0}/f_{c0}$	1.16		
	K	0.667		
	Viscosity Parameter	10 <sup>-7</sup>		
	<b>Compressive Behaviour</b>			
	Compressive strength	27MPa	40 MPa	
	Inelastic Strain	0	0.01	
	<b>Tensile Behaviour</b>			
	Cracking strength	5 MPa	2.200 MPa	0.05 MPa
	Cracking strain	0	0.006	0.015

### 3.3 Direct shear stress testing to identify soil-steel friction factors

This test was carried out to measure the frictional resistance between the steel and filling soil. This friction factor, calculated at 0.49, is required to identify the contact between the area for the steel prototype manhole, and the filling soil in the FE model. Figure 3.20 shows the instruments and samples used to conduct this test, Figure 3.21 the results.

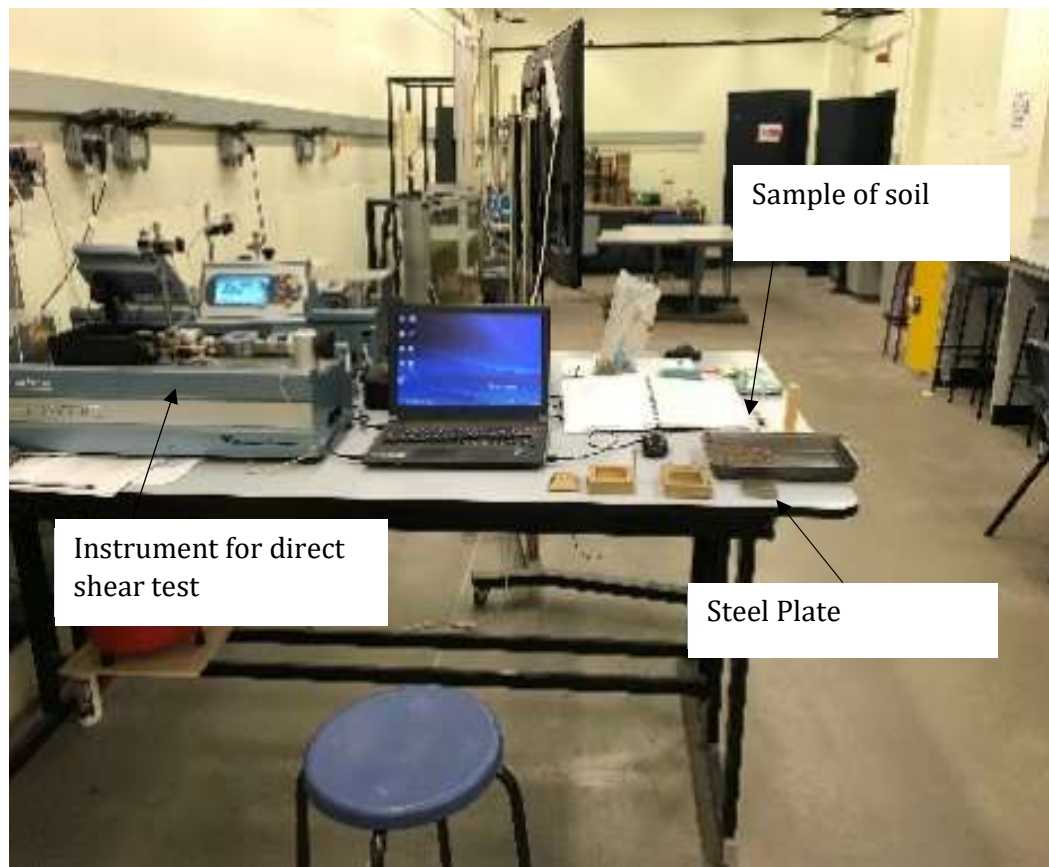


Figure 3.20 Direct shear test to identify the friction factor between the steel and filling soil.

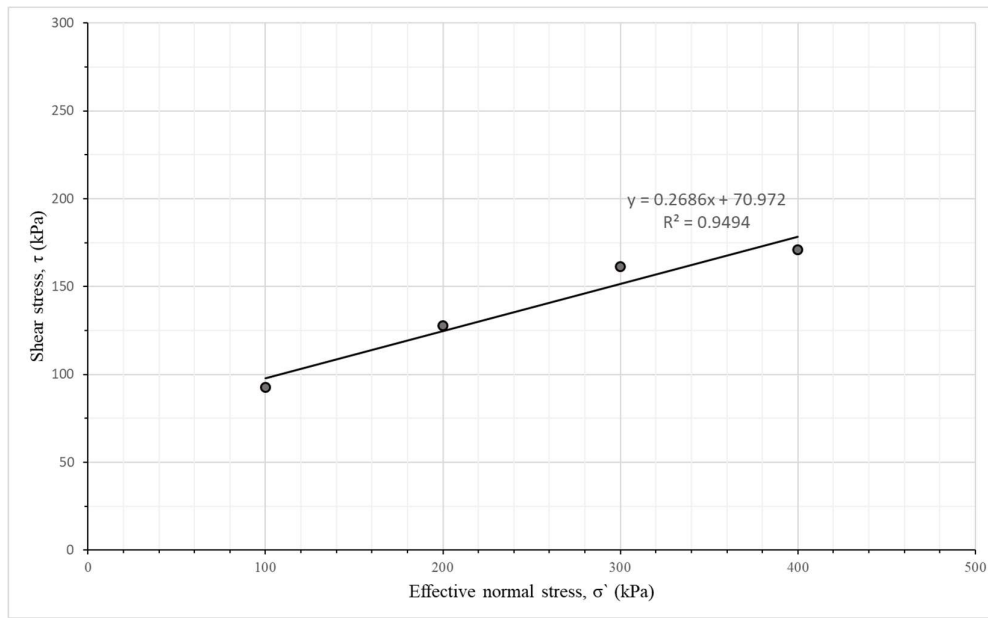


Figure 3.21 The results of direct shear test between the soil sample and steel plate to identify the friction factor to use in the FE model.

The friction factor between the PVC pipe and soil was determined from the literature to be between 0.3 and 0.43, depending on the depth of cover (Alam et al, 2013; Hassan et al, 2014).

### 3.4 Summary

This chapter has described the methodology followed to investigate the structural performance for both the new manhole design and the new method of installing the pipes system, as well as the hydraulic integrity of the new manhole. Three approaches were used to achieve this target, building physical models in the lab used to validate the FE and CFD model. These models required the identification of the properties of the material used in the test, this carried out in this chapter. The selected soil constitutive model used to simulate elastoplastic soil behaviour and identify its parameters, were also discussed in this chapter. The output of these tests will be used in subsequent chapters.

## CHAPTER 4

### THE EXPERIMENTAL AND FE MODEL

#### SETUP OF THE MANHOLE DESIGN

The main aim of this research is to develop a novel design for manholes, combining the conventional separate sewer system manhole into one structure. The new shape for the manhole is discussed in this chapter, the structural behaviour tested and compared with the structural performance of the conventional manhole. A physical model was built in the laboratory to test the structural performance, the results used to validate the FE model which was then upgraded to a full-scale FE model.

#### 4.1 The design of the manhole

Manholes typically are of a standard design, the dimensions limited by the criteria which usually is proposed by the water authority for each area. For specific cases, and pipes which required a larger diameter such as a trunk line, special designs are required. Normally, the dimensions of a conventional manhole are between 1 and 1.8 metres diameter at the intermediate sewer network (between the lateral pipes and trunk pipelines, of the diameter of the pipe ranging from 200 mm to 1000 mm), the exact size dependant on the diameter of the inlet-outlet pipe serving that manhole as illustrated in Table 2.2. The depth of the manhole is dependent on the level of the outlet pipe and has to be as minimum of 1 meter at the beginning of the network, increasing to a maximum depth of 7 metres before a lift station is used to raise the hydraulic gradient back to 1 meter.

The range of manholes which are the focus of this research, are those used for intermediate networks with a range of inlet-outlet pipe diameters from 200 mm to 1500 mm. It is possible to extend this range from 1000 mm to 1500 mm because the storm chamber is larger in the new manhole compared to a conventional stormwater manhole.

#### 4.1.1 *Conventional manhole*

The design for conventional manholes was described in section 2.3, where it was highlighted that the dimensions of the manhole are directly related to the dimensions of both the inlet and outlet pipes. The traditional separate sewer system has two manholes: one for sewage, the other for stormwater. Typically, the sewage manhole is deeper than the storm manhole because a deeper sewage system installation facilitates the movement of sewage flow from long internal pipe networks inside properties. Stormwater is collected from short internal pipes at properties, and from the surface of street. Stormwater manholes become bigger downstream compared to sewage manholes, as stormwater pipes increase in size downstream to be able to receive large quantities of stormwater. The volume of stormwater can increase rapidly in a short period (time concentration, the time that storm water needs to reach the inlet of the network from a surface road). In contrast, sewage flow is typically more stable and may be calculated depending on the number of properties and/or a population density in the area served by the network. In general, the diameter of sewage flow pipes is smaller than pipes required for stormwater flow, and any increase in size downstream in the network is more gradual. Figure 4.1 illustrates a typical section of a separate sewer system in the street, showing a sanitary (sewage) manhole and a storm manhole.

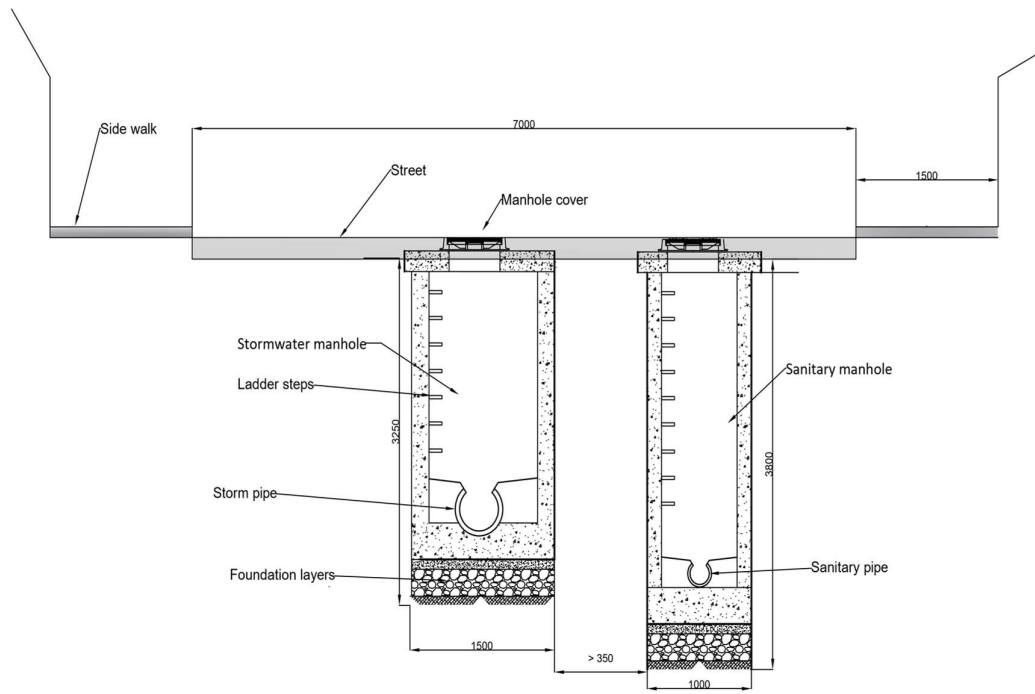


Figure 4.1 Schematic depiction of a cross-sectional view of conventional manholes in a traditional separate sewer system. [Reprinted with permission from Al Ghalowa Co.]

#### 4.1.2 *An innovative design for a manhole*

This research presents a novel manhole design, integrating the storm and sanitary system into one combined structure, while keeping both systems separate. The system is designed to ensure that there is no mixing of storm and sewage water. The manhole is cylindrical and has two chambers which are arranged coaxially. The external one is used as the storm manhole, the internal one used as the sanitary manhole. The base of the storm chamber is at the level of the bottom of the inlet storm pipe, while the sanitary chamber extends to the same level as the bottom of the inlet sanitary pipe. Figure 4.2 provides details of the manhole design and the separation technique. Regarding the internal chamber

used for sewage flow, the net diameter can range from 0.7 to 1 metre. The external chamber used for the storm flow, can have a net diameter ranging from 2.1 to 2.5 metres, depending on design needs. With reference to BSEN476 (2011), these dimensions are appropriate for an inspection manhole which allows equipment to be placed into the system and limited human access. The sanitary pipe extends below the external manhole and ends at the internal manhole, connected in the same way as the traditional system. The storm pipe ends at the edge of the external manhole, the flow moving around the sides of the inner wall of the sewage chamber before arriving at the outer storm pipe. Figure 4.3 illustrates the section of the new manhole as placed in situ in the street.

The manhole itself can be concrete or plastic, e.g. HDPE, PVC or GRP; the same materials are available for conventional manhole manufacture. The use of lighter materials for the external chamber requires more research. Because of this, there should be no difference in the lifetime service of the new manhole in comparison to a conventional manhole. A reinforced and non-reinforced concrete manhole was used to simulate the full-scale model in this research, replacing the inner chamber wall by GRP in one case.



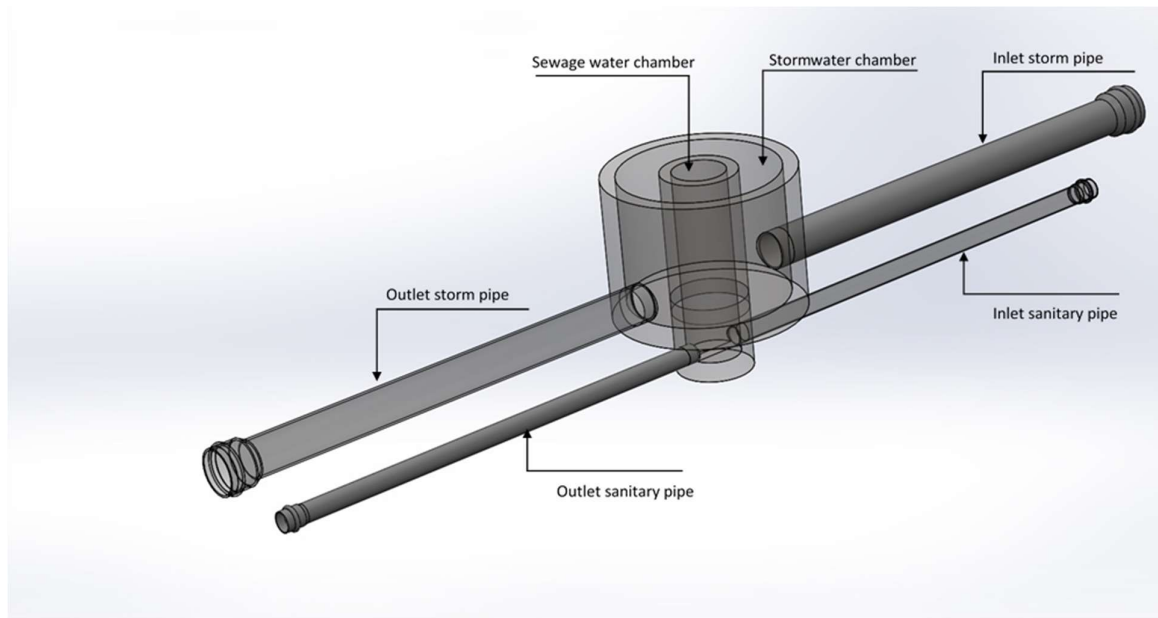


Figure 4.2. 3D design of the innovative manhole.

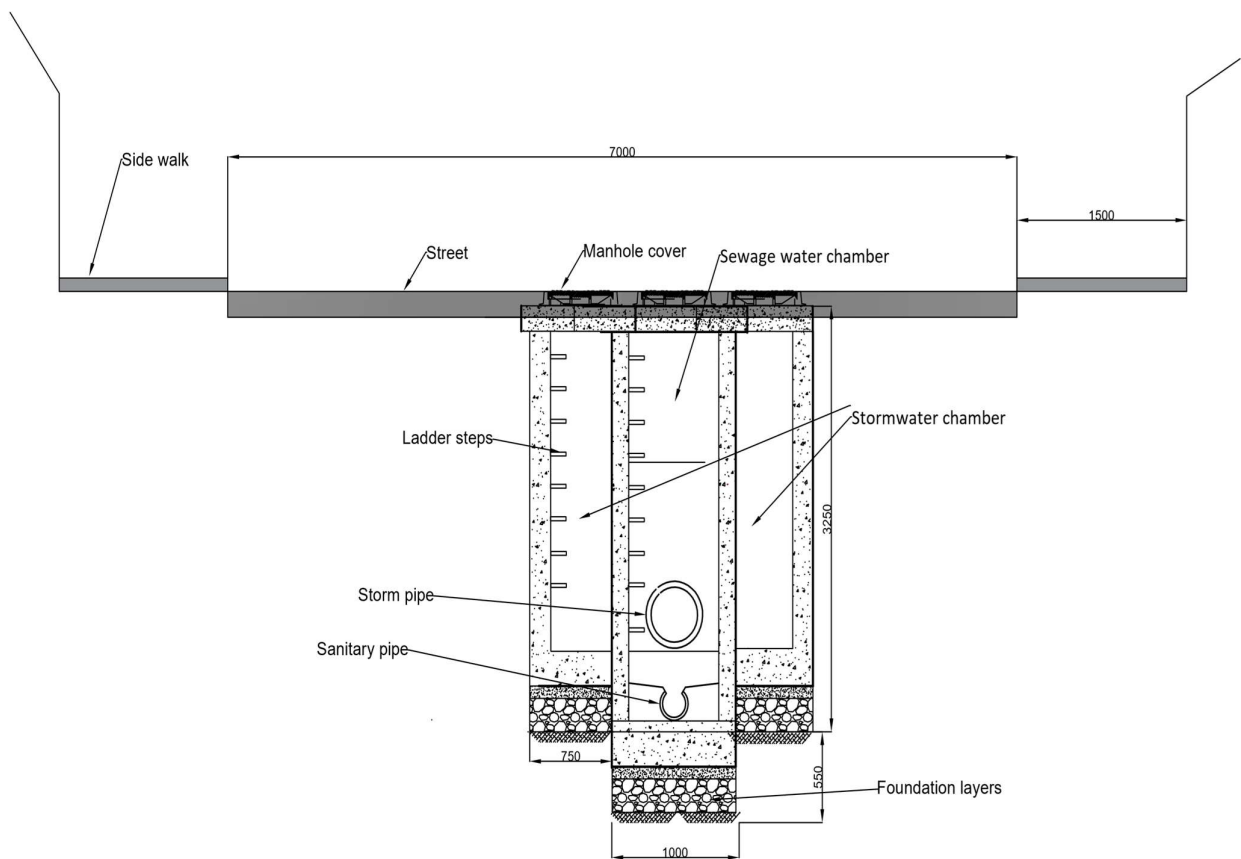


Figure 4.3 Cross section of the new manhole located in a separate sewer system in the street.

## 4.2 Physical model of manhole

A comparative experimental study between the new manhole and a conventional manhole, was carried out to explore the structural performance of the new manhole. Two prototypes scaled 1/10 were built: one for the conventional manhole with a diameter of 10 cm and depth of 30 cm, the other for the new manhole which had the same inner chamber dimensions but a diameter of 25 cm and depth of 25 cm for the external chamber. Figure 4.4 and Figure 4.5 show the two manhole prototypes. The aim of conducting the test on the new manhole and conventional manhole is to eliminate scale effects of the prototype and investigate the impact of changing the manhole geometry on the soil-manhole correlation. Steel was used to build the prototype manholes because this research focuses on exploring the performance of the geometry of the manhole buried in a soil (displacement) and not the stress of the manhole structure (material), as well as the difficulties of building a concrete prototype at such a small scale. The results from the physical model were used to validate the small-scale FE model, this validation allowing an upgrade to a full-scale FE model.

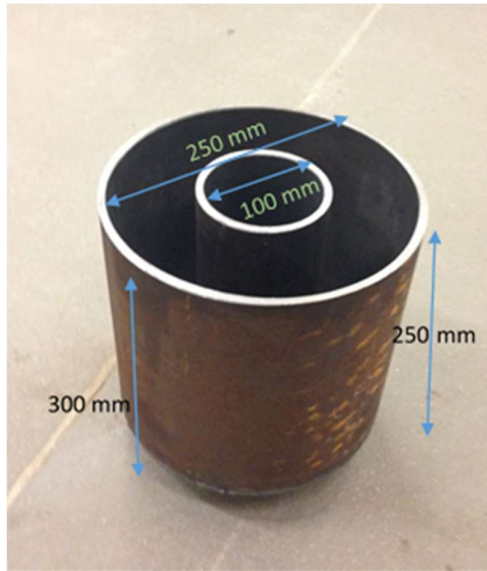


Figure 4.4 The prototype of the new manhole. External chamber = 0.25 x 0.25m, internal chamber = 0.1 x 0.3m.

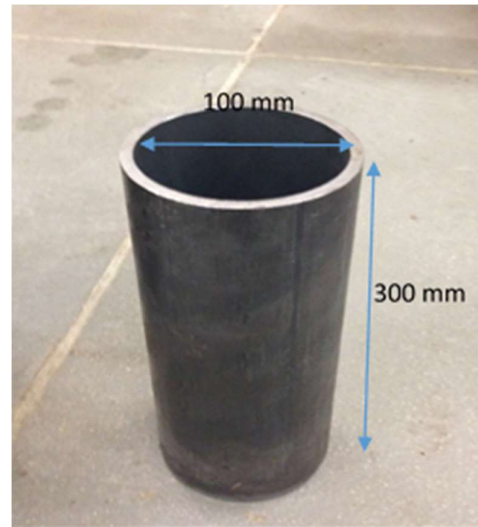
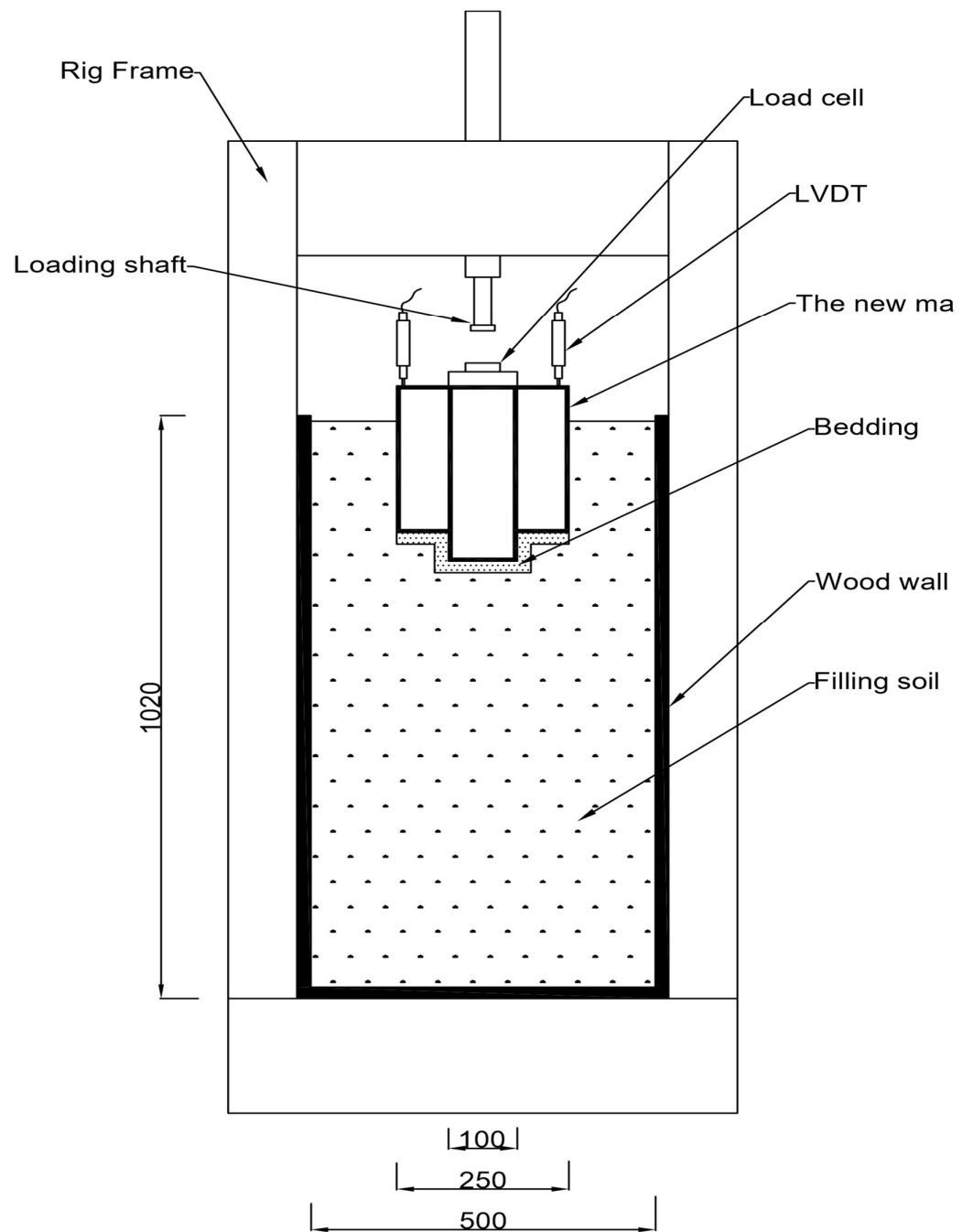
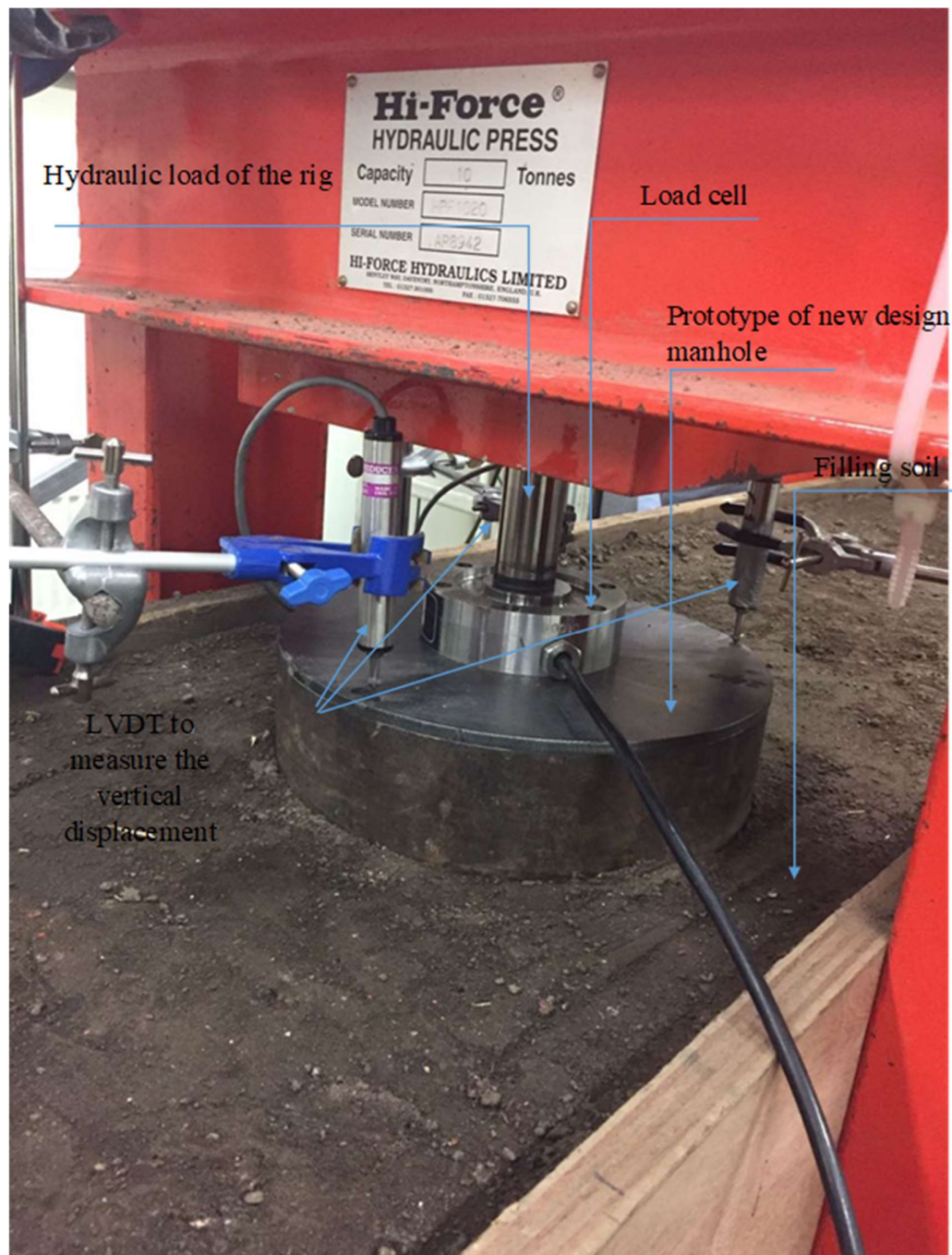


Figure 4.5 The prototype of the conventional manhole with dimensions 0.1 x 0.3m.

A physical model was created in LJMU to test the manholes buried in soil. A wooden trench of dimensions 2.5 x 0.5 x 1 metres was built in the laboratory. The trench was in a hydraulic rig which was used to apply the live loads to a maximum of 10 tons, and to provide side supports to the trench walls to avoid displacement. The cell load and Linear Variable Differential Transducers (LVDTs), were used to monitor applied loads and displacement of the manhole structures, the data recorded by an MC3 recorder. Figure 4.6 a and b illustrate the setup of the trench in the rig; the buried manholes, the location of the load cell and the three (LVDTs) for the new manhole. **Error! Reference source not found.** a and b show the same set up for the conventional manhole. Appendix II presents the methods used to calculate the applied load on the physical models in the laboratory.

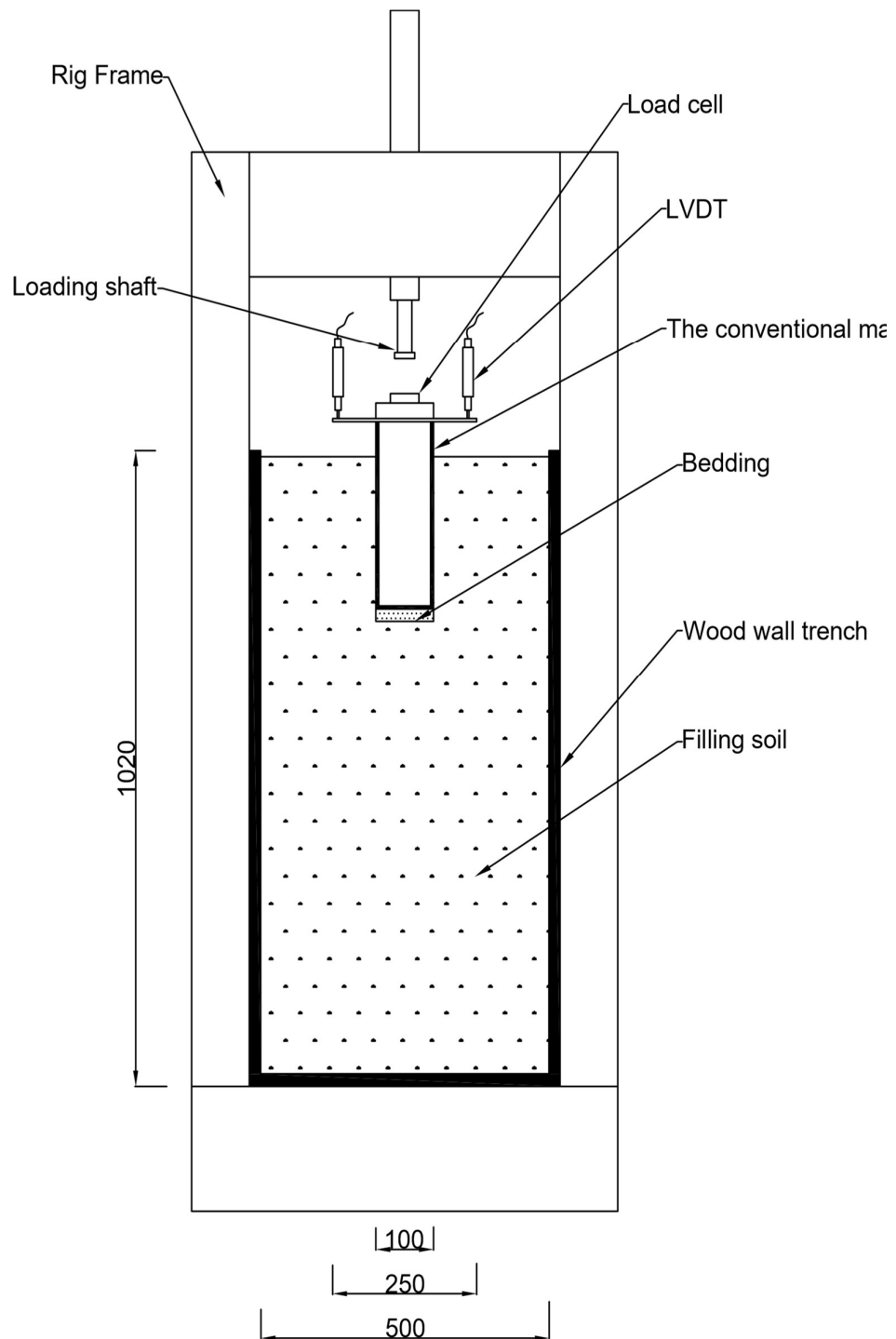


(a)



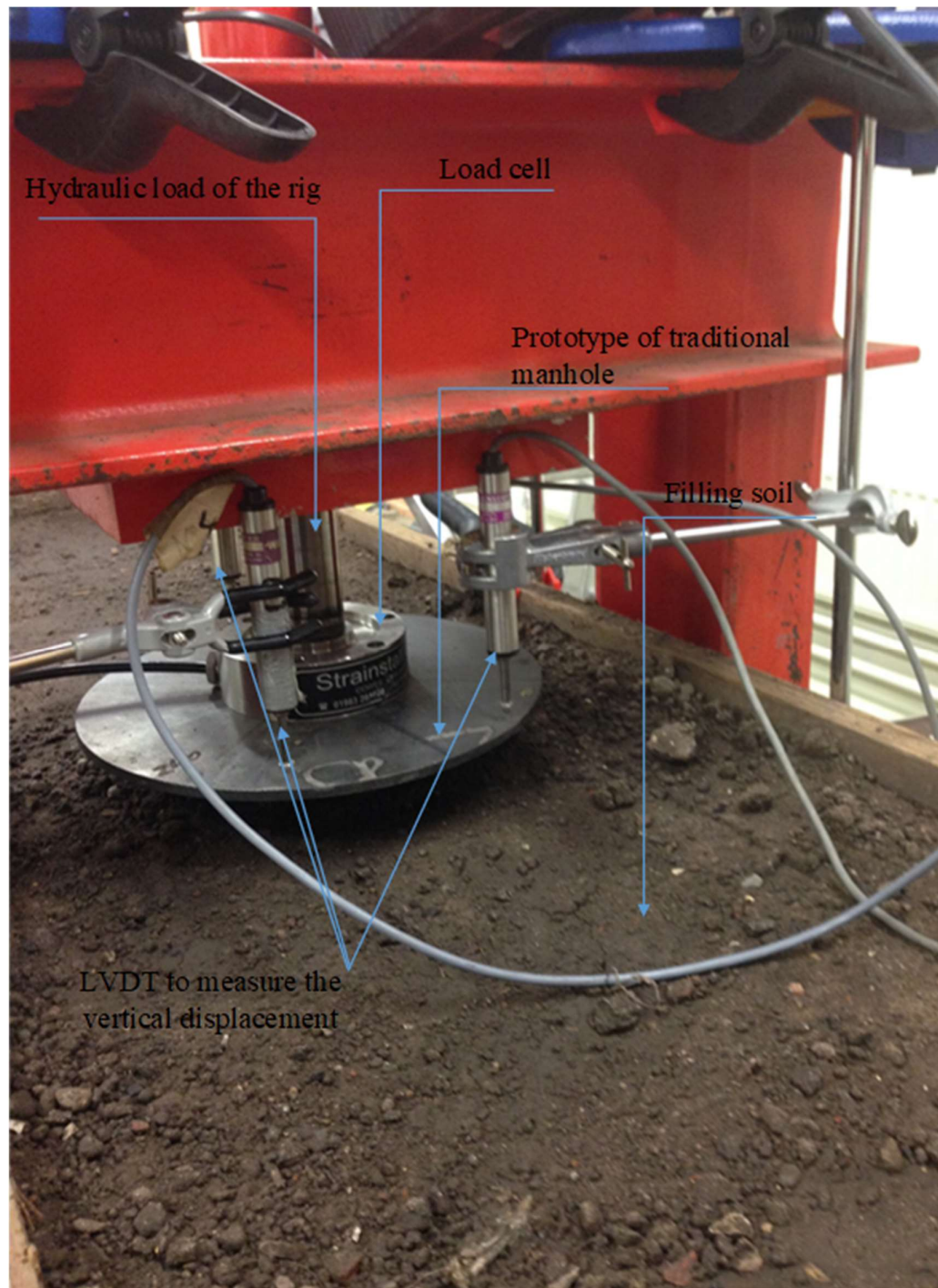
(b)

Figure 4.6 Setup of the trench in the rig and location of measurement instruments on the new manhole surface at three points on the edge.



(a)





(b)

Figure 4.7 Setup of the trench in the rig and location of measurement instruments on the conventional manhole surface at three points on the edge.

#### 4.2.1 *Prototype experimental results*

Loads were applied to verify the capacity of the new manhole, compared to a conventional manhole, and to explore the manhole shape – soil correlation. Four categories of loads were applied: medium traffic (HS15), heavy traffic (HS20 and HS25) and overload (double heavy traffic). Figure 4.8 details the response of the new manhole under static applied loads HS15, HS20, HS25 and a double HS25 as well as a moving double HS25, applied at the end of the test to establish the maximum resistance.

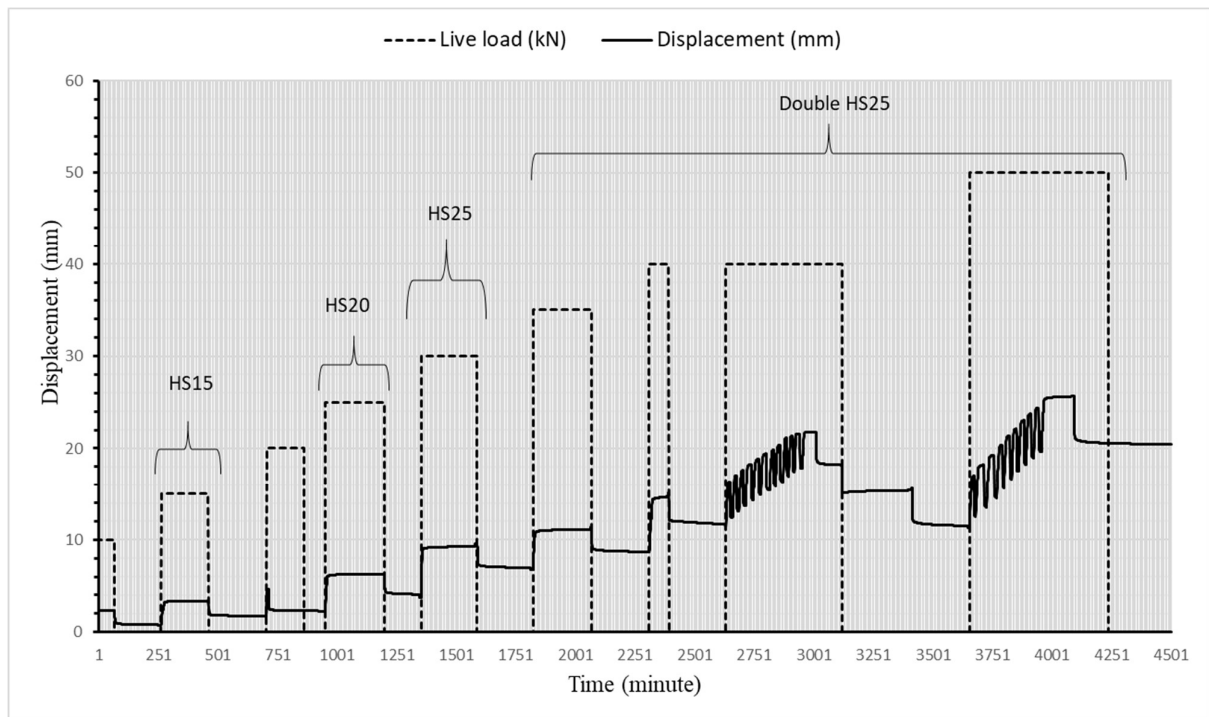


Figure 4.8 Displacement of the new manhole under different live loads.

Displacement was 3.3 mm at HS15, 6.2 mm at HS20 and 9.2 mm at HS25. When the applied load was increased to over load (twice the heavy load HS25), the new manhole continued to be stable, but the displacement increased to 22 mm. Soil density and the degree of compaction of the filling soil, play a significant role in



the stability of buried manholes under live loads as well as the geometry of the manhole (Abolmaali and Kararam, 2010). The same set of load categories were applied to the conventional manhole, the results presented in Figure 4.9. Displacements were 2.9 mm for a load of HS15, 7 mm for HS20, 14.3 mm for HS25, the manhole sinking into the soil when HS25 was doubled. The friction factor between the steel and soil is less than the friction factor between concrete and soil, meaning that the degree of displacement will be lower when concrete is used because the friction factor will be greater.

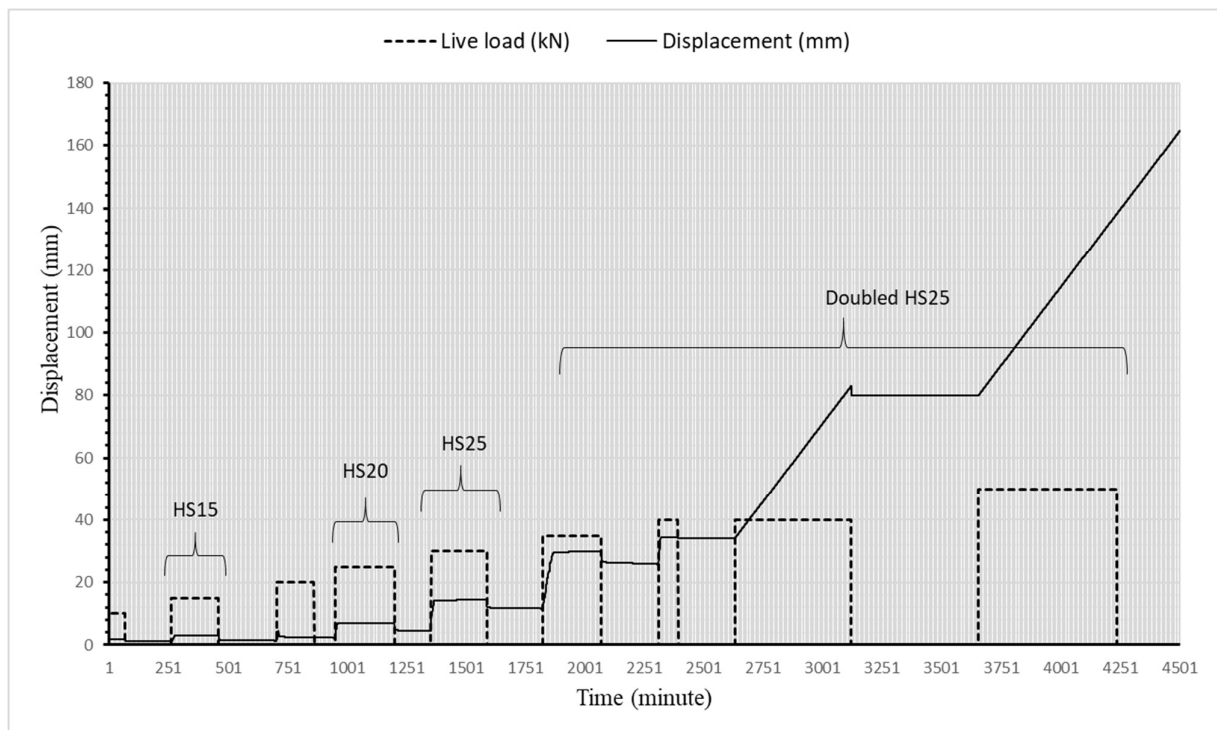


Figure 4.9 Displacement of conventional manhole under different live loads.

Comparisons between the displacement of the new manhole with the conventional manhole in Figure 4.10, show that under a medium load (HS15), the conventional manhole has less displacement compared to the new manhole. This is because the new manhole is heavier than the conventional one, thus adding a

significant dead load. However, the effect of manhole weight is reduced when the traffic load is increased. Against the application of heavy loads, the geometry of the manhole plays an important role, improving the resistance of the manhole. The new manhole design shows high stability and resistance under a high applied load, compared to the conventional manhole.

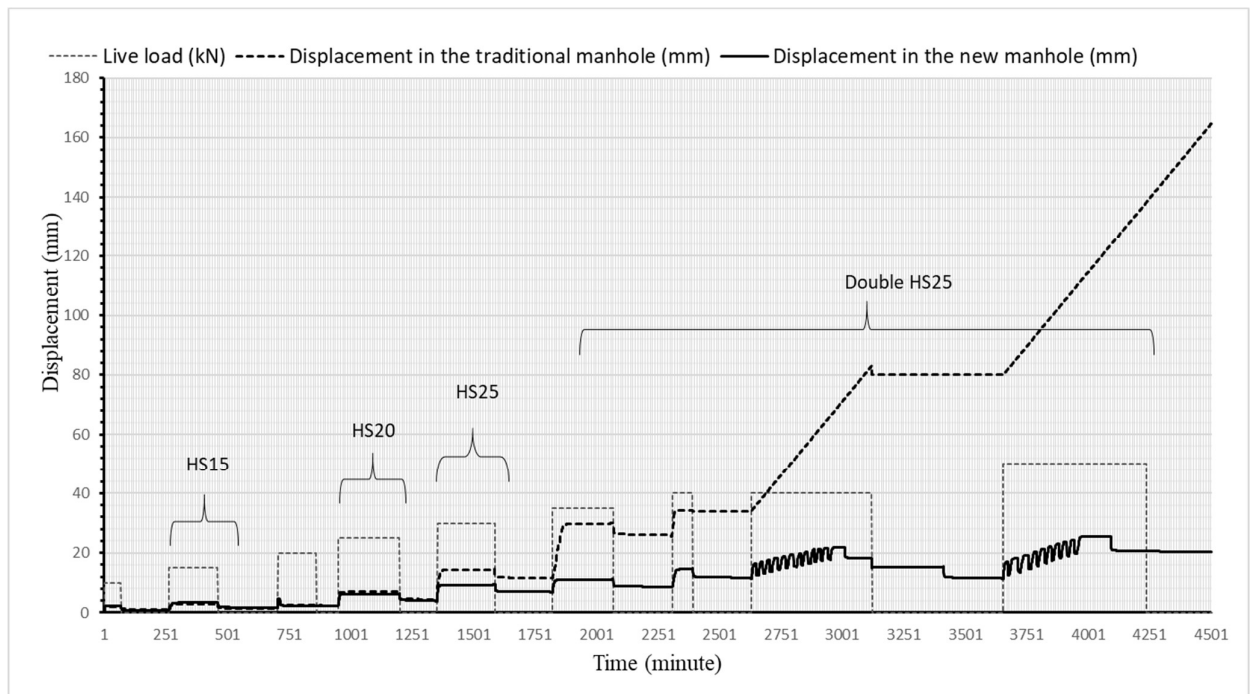


Figure 4.10 Comparison between the new and conventional manholes under the same conditions and live loads.

### 4.3 The FE model

A wide range of tools are available to carry out finite element analyses (FEA), including commercial packages such as ABAQUS, designed for use where there are complicated geotechnical issues (Pichler et al, 2012). The development of mathematical tools and improvements to the library of material applicable to FEA, allows geotechnical engineers to select which tools to use to successfully solve geotechnical structural problems, and to simulate structural behaviours, when manholes are embedded in soil. That said, engineers still need to have both a geotechnical background and a good understanding of the principles of FEA to avoid misjudgements.

A two-stage, finite element approach was used in this research. In the first stage, the finite element model for the case study was built, all the input criteria determined using lab tests to identify the properties of the materials. Prototypes and experimental work were used to identify the boundary conditions necessary to validate the results from the mathematical model (Brinkgreve, 2013). The second stage used the mathematical model to ascertain the real scale dimensions of both the conventional and novel manholes. The FEA used ABAQUS 2017 to test the manhole-soil correlation and identify degree of displacement under four loading categories; weight of manhole, heavy traffic loads (HS20 and HS25) and one overload (double heavy traffic load HS25), thus testing the maximum capacity for both manholes.

#### 4.3.1 *The FE model of the physical model*

Two FE models were created for the prototype simulation in the current research: one to simulate the new manhole, the other a conventional manhole. The same experimental conditions, dimensions, boundary conditions and materials were used. Restrictions at the base prevented any movement while allowing displacement in the y-axis for the external model's faces. The symmetry around the x-axis and z-axis for internal faces was used to simulate full model behaviour. The symmetry of the model around the x-axis and z-axis, allows the use of a quarter model via the specific tools in ABAQUS. The creation of a symmetrical model and use of one quarter of the model, decreases the run time while giving the same results as a full 3D model. Surface to surface contact interaction was fixed with a friction factor of 0.49 between the soil and steel, this determined from the experimental test (section 3.5). A convergence study was conducted to decide mesh quality, Figure 4.11 showing the mesh for the symmetrical quarter of the new manhole model comprising 45370 nodes, 35350 elements, 35269 linear hexahedral elements of type C3D8R, and 81 linear wedge elements of type C3D6. Figure 4.12 shows the mesh for the symmetrical quarter of the model of the conventional manhole comprising 40532 nodes, 34928 elements, 34856 linear hexahedral elements of type C3D8R, and 72 linear wedge elements of type C3D6. Appendix III presents a description of the selection of type of elements used by Abaqus 2017 in the FE model.

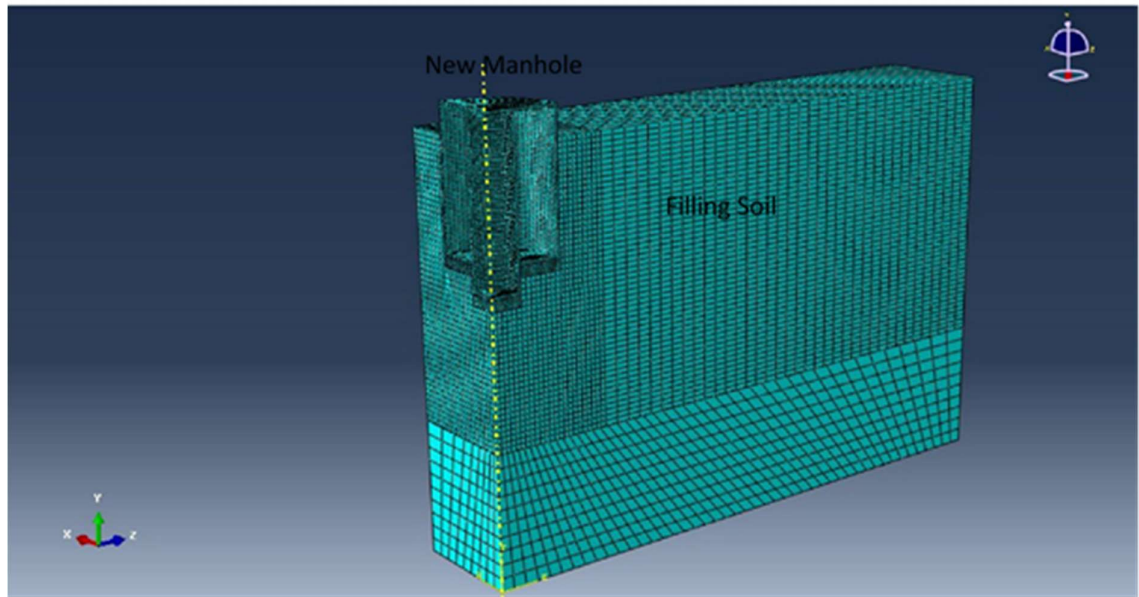


Figure 4.11 The symmetrical quarter of the new manhole FE mesh model representing the full 3D manhole.

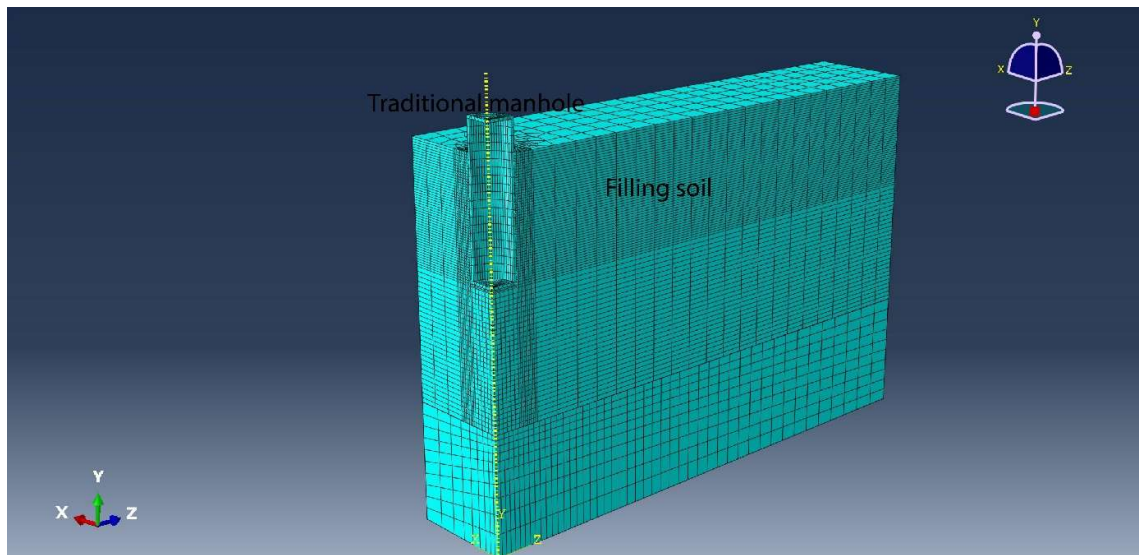


Figure 4.12 The symmetrical quarter of the conventional manhole FE mesh model representing the full 3D manhole.

#### 4.3.1.1 The results from FE model of the physical model.

The same series of loads (HS15, HS20, HS25 and double HS25) and the exact boundary conditions as for the physical model, were applied on manholes using an FE model. Selecting the proper constitutive model, in this case the Modified Drucker-Prager/Cap plasticity, to simulate soil behaviour, is an important aspect to consider when using FE for soil models (Lees, 2012). A point at the centre of the manhole was selected to record displacement results because the maximum displacement occurs at the centre. Figure 4.13 shows a sample of the results when a double heavy load was applied. The results for each applied load show displacement at the same point, presented in Figure 4.14, these compared with the results of the measurements taken at the cover of the manhole for the experimental tests, under the same series of loads.

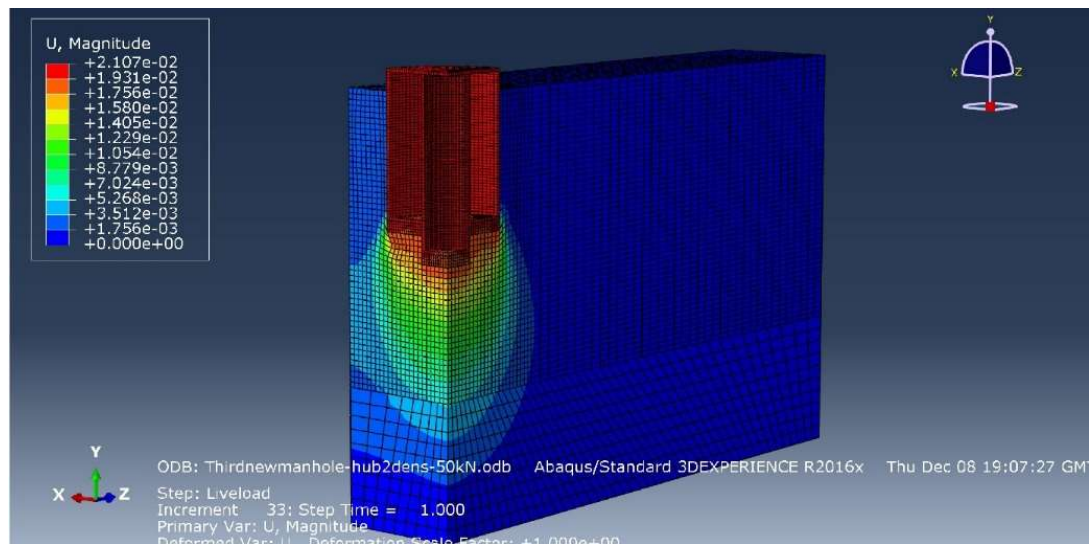


Figure 4.13 The displacement of the new manhole at a double heavy load, shown in a 3D quarter symmetric FEA model.

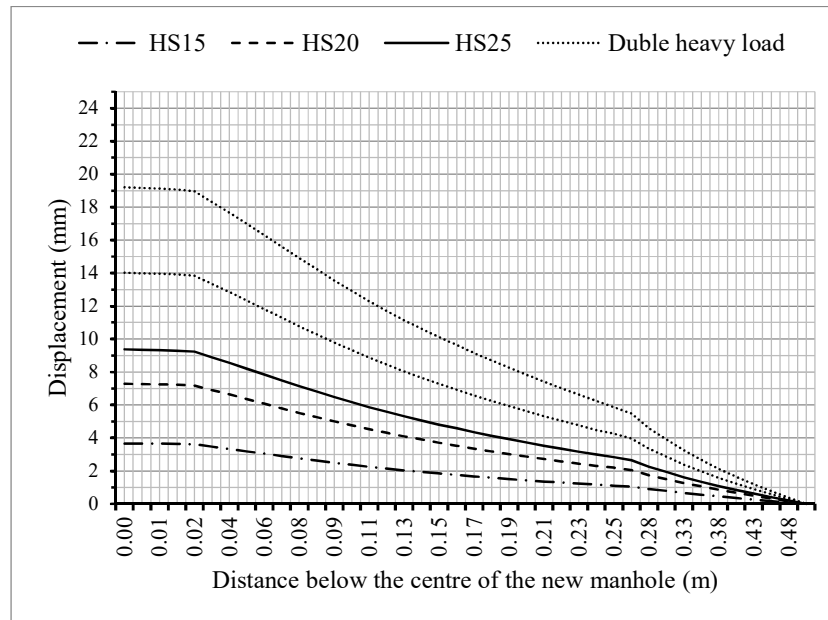


Figure 4.14 The displacement at different categories of loads at the centre of the manhole by depth below the new manhole design.

The FE model output and the experiment model have a very close match ( $R^2=0.98$ , Appendix IV) regarding the displacement of the new manhole under live loads, as shown in Figure 4.15.

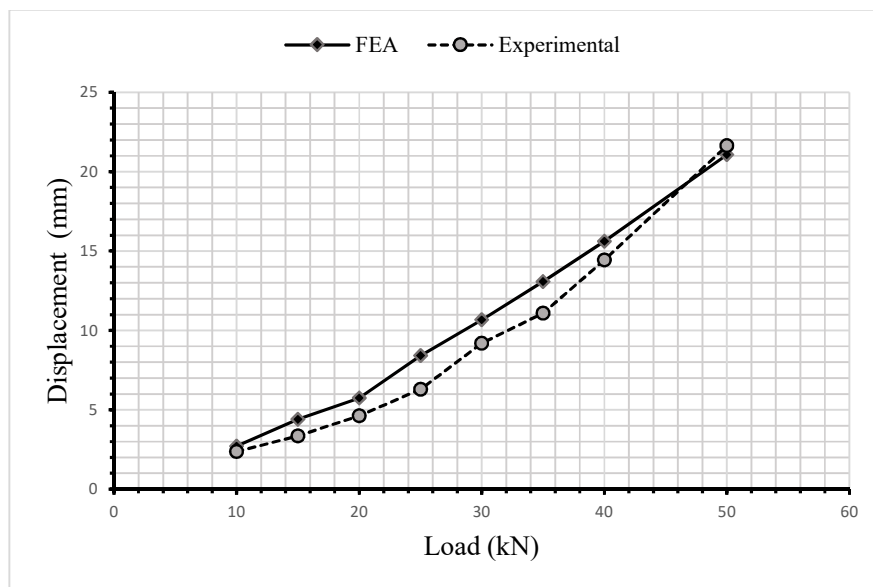


Figure 4.15 Comparison of the displacements from both the experimental work and the FE model for the new manhole in soil, under live loads.

The same point was selected to show the displacement results for the conventional manhole, a sample of the results at a double heavy load presented in Figure 4.16. Figure 4.17 illustrates the displacement along the depth below the centre of the conventional manhole, under different loading categories.

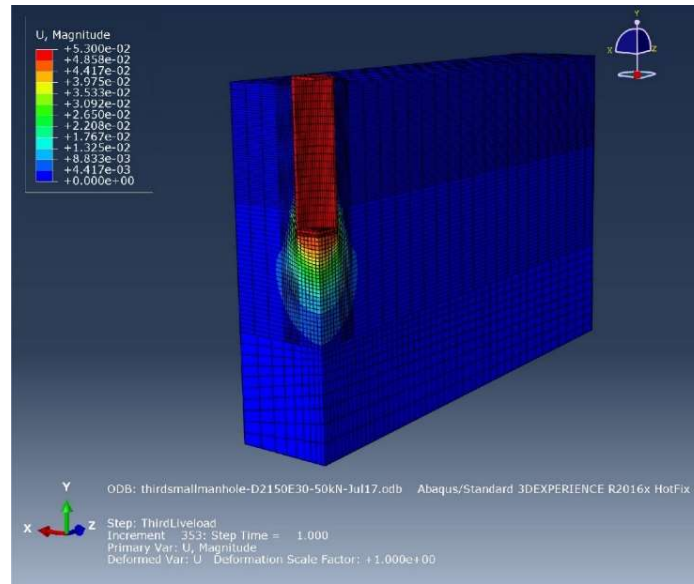


Figure 4.16 The displacement of the traditional manhole at a double heavy load, shown in a 3D quarter symmetric FEA model.

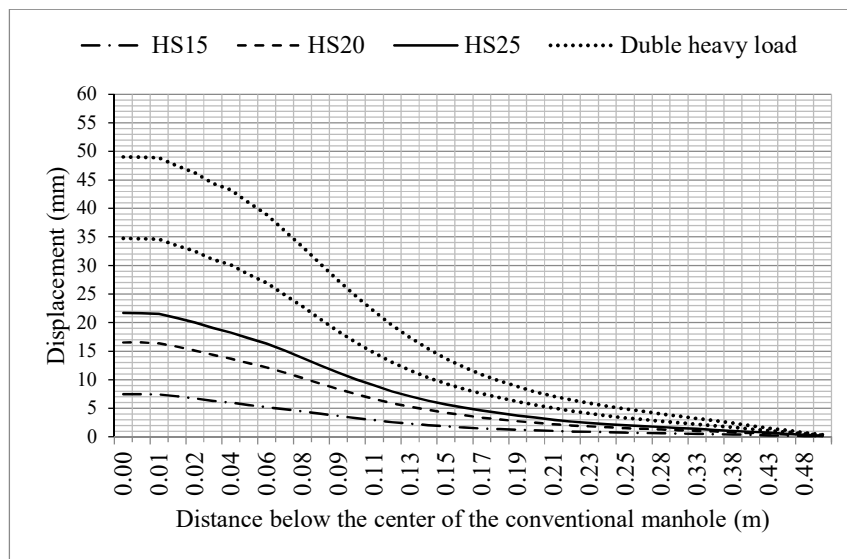


Figure 4.17 The displacement at different categories of loads at the centre of the manhole by depth below the conventional manhole.



The comparison of the results from the FE model and the experiment model reveal a close match ( $R^2=0.93$ , Appendix IV) regarding displacement at low loads and between displacements for the conventional manhole under high live loads. The experimental measurements and FEA results gave a reliable assessment of the behaviour of the geometry of the manhole and estimations of the margins of error of approximately 10% expected from the FEA (Moser and Folkman, 2008). The comparison between the experimental test and the FE model results for the conventional manhole are presented in Figure 4.18.

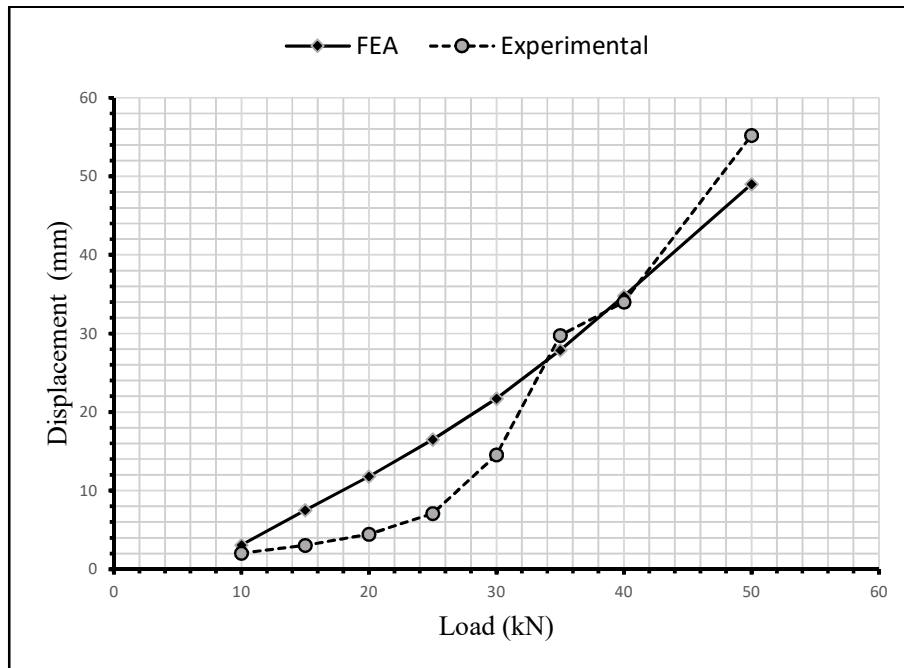


Figure 4.18 Comparison of the displacement results from both experimental works and the FE model for the conventional manhole prototype in soil under live loads.

#### 4.3.2 *The full-scale FE manhole model*

One of the important validation processes is the comparison of the FE model with lab experimental results, to eliminate uncertainty and manage discrepancies in the model, thus increasing confidence in the real application (Moser and Folkman 2008). Validation makes the designer more aware of the inevitable inaccuracies between a real case study and an FE model (Mar 2002). The two stages explained above, illustrate that all necessary steps to check and validate the accuracy of the FE model were taken. All the boundary conditions, contact interactions, material properties and steps were identified correctly, meaning it was possible to upgrade the FE model to test a full-scale model with a confidence procedure. Normally, the dimensions of traditional manholes used in most sewer networks are 1 to 1.8 metres diameter, the depth ranging from 1 to approximately 7 metres. Real scale dimensions were selected for intermediate networks in the sewer system, where new systems were expected to be located. The conventional manhole was 1.3 metres in diameter, including its walls and the depth was 3.4 metres; the storm chamber of the new manhole was 2.8 metres in diameter including its walls, the depth 2.65 metres. The sanitary chamber had the same dimensions as the conventional manhole. The soil was of 8.5 metres radius and 15 metres deep to identify the maximum area affected by forces applied on the buried manhole (Brinkgreve 2013). The same soil properties as for the prototype model, were used for the real scale model. Non-reinforced concrete (Najafi and Sever 2015b) and reinforced concrete, were used as the manhole materials. The new manhole had 385085 elements, the element types C3D6, C3D8R, B31 and T3D2. Figure 4.19 illustrates the configuration of the new manhole in soil. Regarding the conventional manhole, the number of elements was

273240; the element types the same as for the new manhole. Figure 4.20 illustrates the configuration of the conventional manhole model in soil.

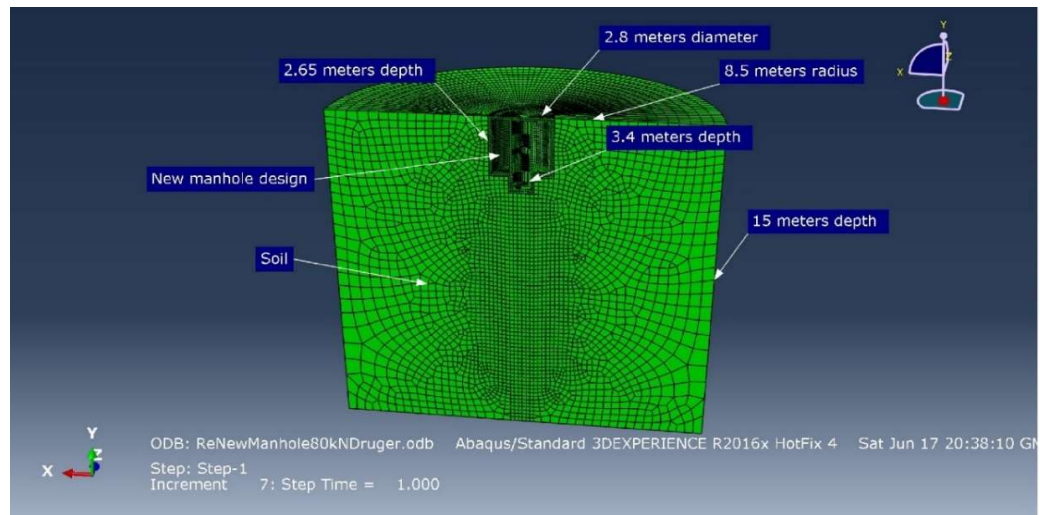


Figure 4.19 Configuration of the real scale new manhole-soil model.

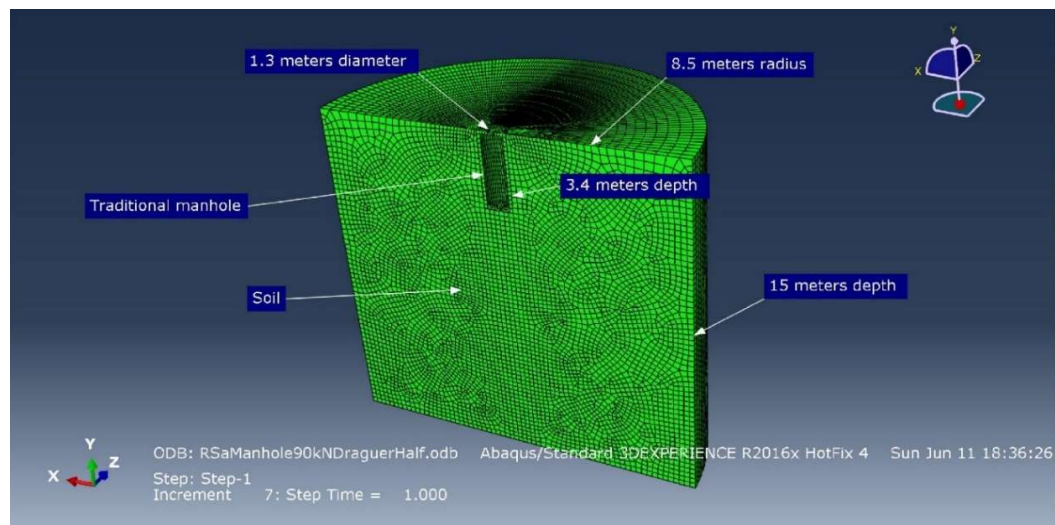


Figure 4.20 Configuration of the real scale conventional manhole-soil model.

The conventional manhole design typically has a steel cover 60 cm in diameter, the manhole cover level with the street. Normally, applied traffic loads effect the manhole through the manhole cover, therefore the area of the manhole cover has had a live load applied to it in the FE model.

The new manhole has three access holes (three steel covers): one at the centre for the sewage chamber and two for the storm chamber at both sides of the inlet and outlet pipes. Figure 4.21 a and b illustrate the locations of the manhole covers for both manholes. The new manhole was tested using three different live loads. The first case used one wheel load applied to the centre of the manhole cover (the sewage chamber cover). The second used two wheels load applied on the storm chamber covers (one wheel for each cover) because the dimensions of the new manhole allows two wheels to travel over the manhole at the same time. Figure 4.22 shows the first two cases of applied loading. The third is when only one wheel load is applied to one storm chamber manhole cover.

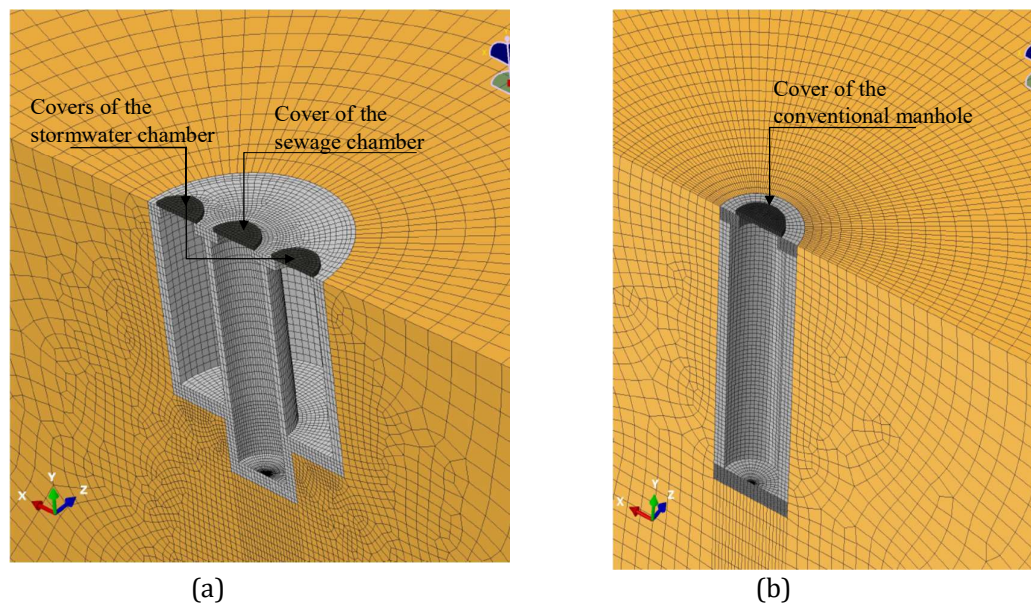


Figure 4.21 The configuration of the manhole cover: (a) the new manhole (b) the conventional manhole

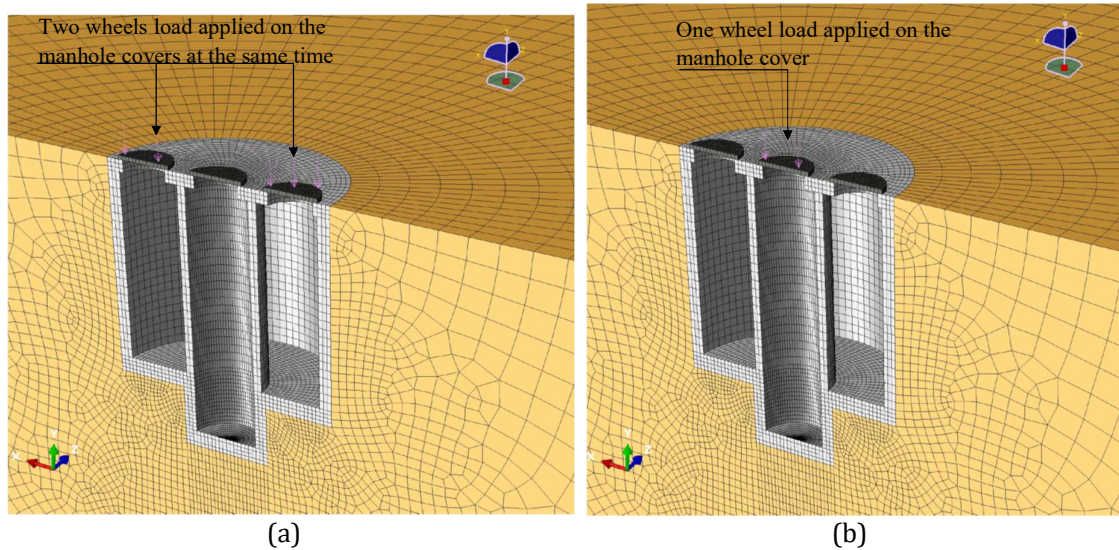
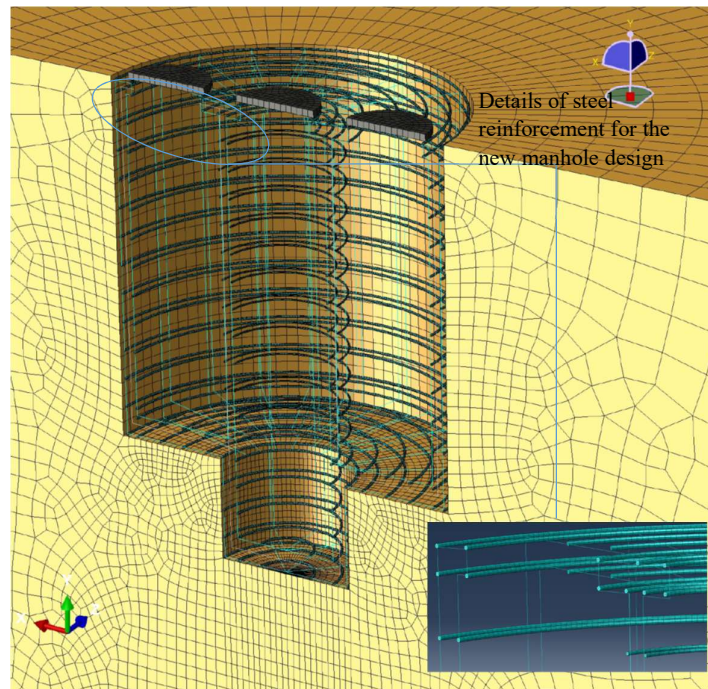


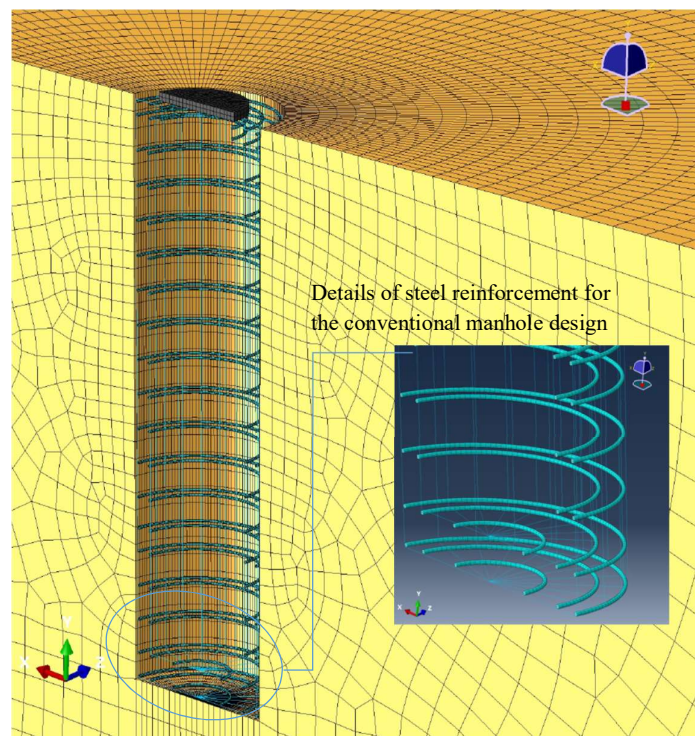
Figure 4.22 Two applied loads on the new manhole (a) two wheels on the storm chamber cover (b) one wheel on the sewage chamber cover.

Two materials were tested. The first was non-reinforced concrete, the second reinforced concrete, as precast reinforced concrete is more common in sewer systems. The reinforced concrete comprised both 12 mm@15 cm horizontal reinforcement bars and 10 mm @15 cm longitudinal reinforcement bars. Figure 4.23 illustrates the steel reinforcement in (a) the new manhole and (b) the conventional manhole, these designed according to the requirements set out by the Ministry of Construction and Municipalities code in Iraq. Two techniques were used to generate the steel reinforcement elements in the FE model: wire elements were used for the longitudinal bars and beam elements for the horizontal bars, this making it easier to draw the reinforcement bars for the more complicated shape of the new manhole using ABAQUS.





(a)



(b)

Figure 4.23 Details of the steel reinforcements for (a) the new manhole and, (b) the conventional manhole.

In one case, the concrete wall of the inner chamber was replaced by a GRP material, the structural performance of this hybrid material investigated as seen in Figure 4.24. The GRP wall was 5 cm thick, its properties gleaned from a literature review (Faria, 2005). The use of lightweight materials such as GRP, PVC or HDPE, are promising alternatives regarding the manufacture of manholes (BS, 2013) as they have the potential to enhance structural performance by decreasing the weight of the manhole.

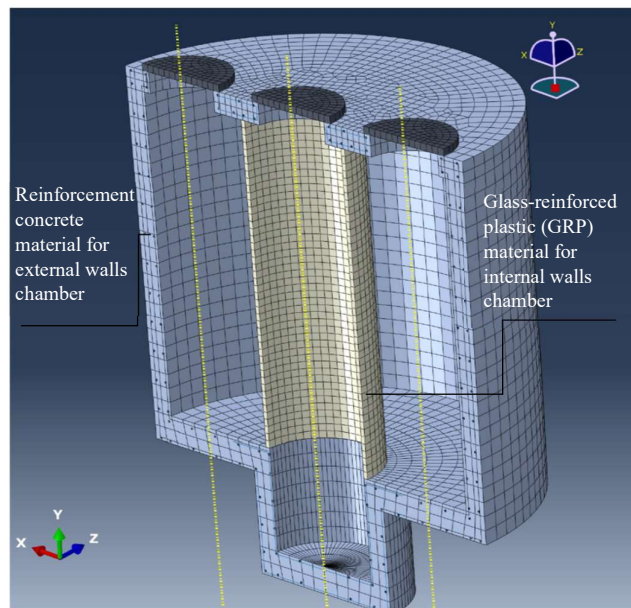


Figure 4.24 Using hybrid materials to build a new manhole; reinforced concrete for the outer chamber and GRP for the inner chamber.

#### 4.3.2.1 The results of the FE real-scale model.

The data regarding the FE model were taken at the centre point of the manhole base at soil depth to explore the impact of both the geometry and applied loads on the soil underneath both the new and conventional manholes. The maximum displacement at the base of both manholes was noted for both the non-

reinforced and reinforced manholes. Figure 4.25 shows a sample of the simulation output of the new manhole under 2xHS25, with a two wheels load.

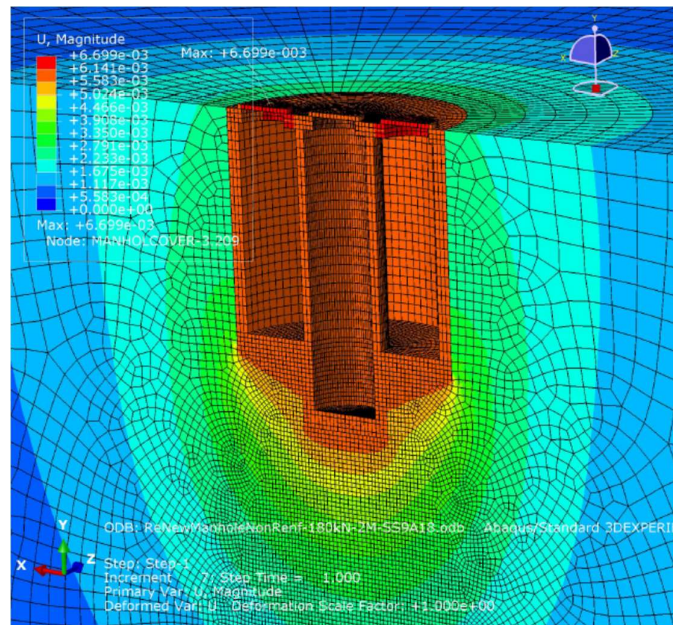


Figure 4.25 Samples of FE simulation output for the new manhole design exposed to 2HS25 on the storm chamber covers.

The displacement of the new manhole made from non-reinforced concrete, is shown in Figure 4.26 under four categories of applied loads: weight of manhole, HS20, HS25 and Double HS25 applied by a one wheel traffic load on the cover of the sewage chamber. The double heavy load was applied to test the maximum capacity of the new manhole compared to a conventional manhole. In reality, it is rare to see two wheels of loading HS25 pass over a manhole cover at the same time. In the second test, the one wheel load was applied to the storm chamber cover, the results presented in Figure 4.27. The large area of the new manhole allows two wheels to pass over the manhole at the same time. This scenario, the load applied in two positions on the manhole (on the two, stormwater chamber covers) was simulated in a third test, the results presented in Figure 4.28.



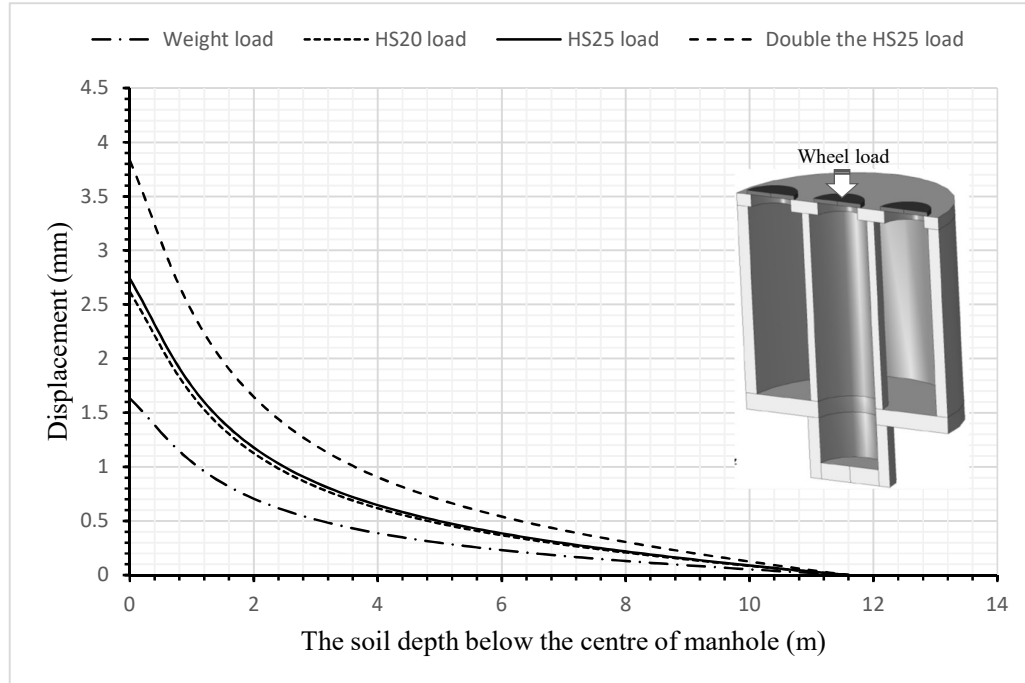


Figure 4.26 Displacement of the non-reinforced new manhole under a one wheel applied load on the one cover of the sewage chamber.

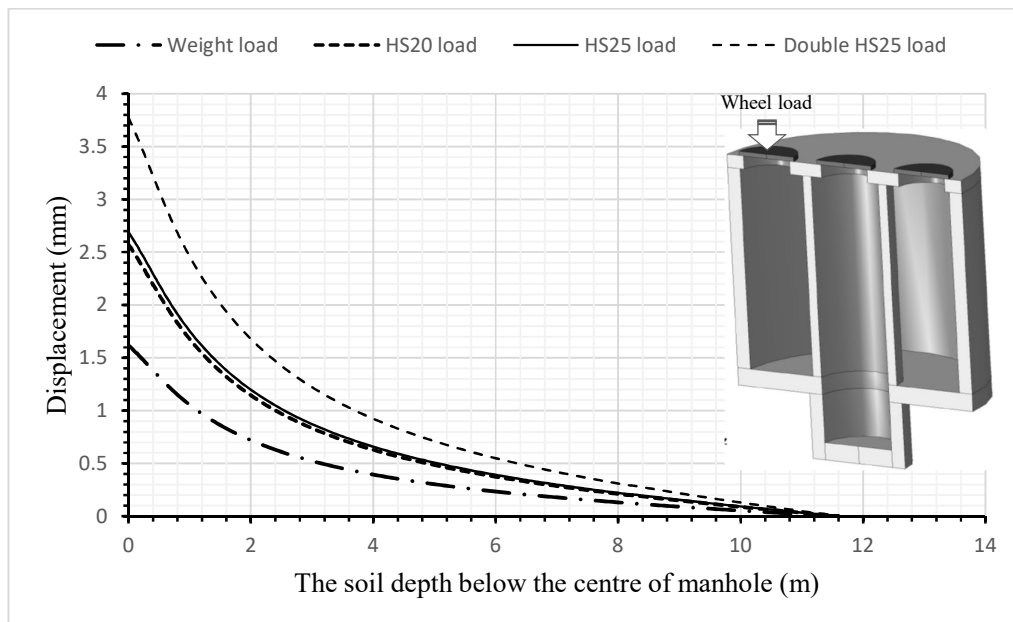


Figure 4.27 Displacement of the non-reinforced new manhole under a one wheel applied load on the one cover of the storm chamber.

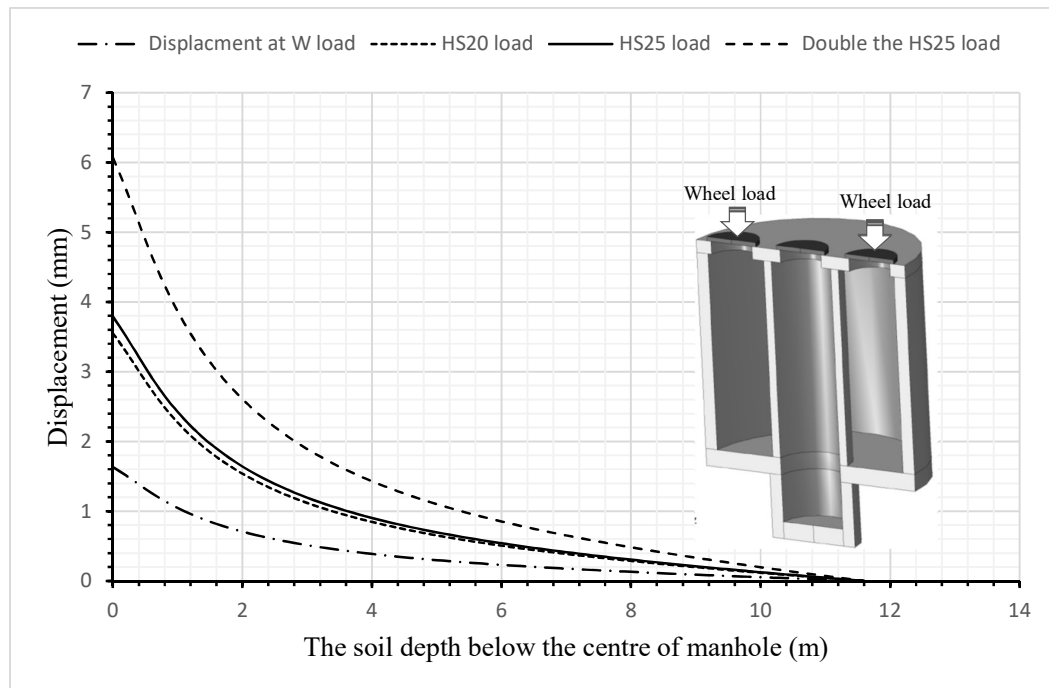


Figure 4.28 Displacement of the non-reinforced new manhole under a two wheel applied load on both covers of the storm chamber.

The same tests were used for when one wheel passed over the sewage manhole cover and when two wheels passed over the two storm chamber covers. This time, reinforced concrete was used to build the new manhole. Figure 4.29 presents the displacements of the new manhole under a one-wheel traffic load, Figure 4.30 illustrating the displacement when under two-wheel traffic loads.

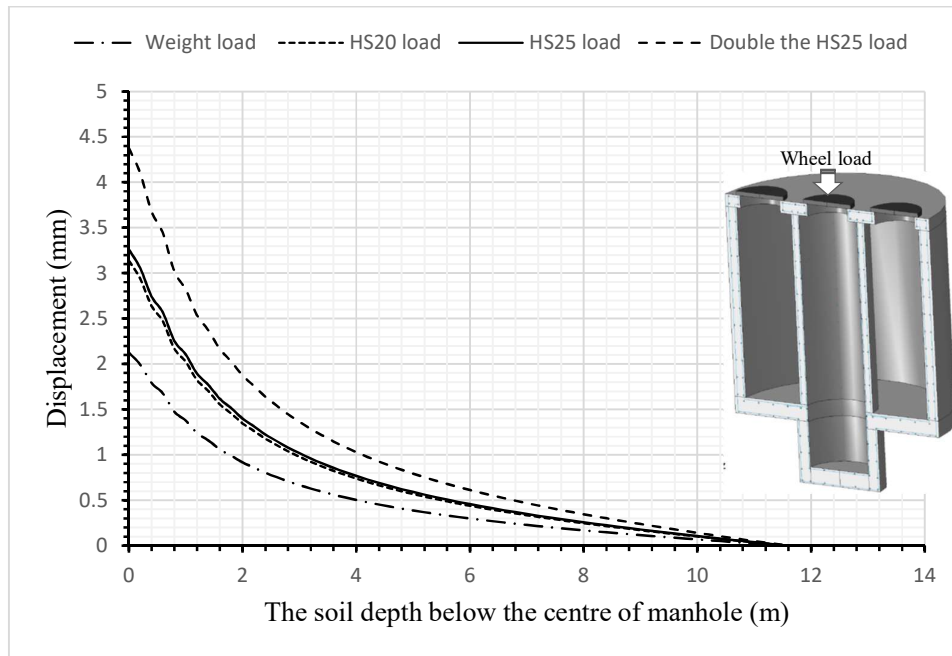


Figure 4.29 Displacement of the new reinforced manhole under a one-wheel applied load on the sewage manhole cover.

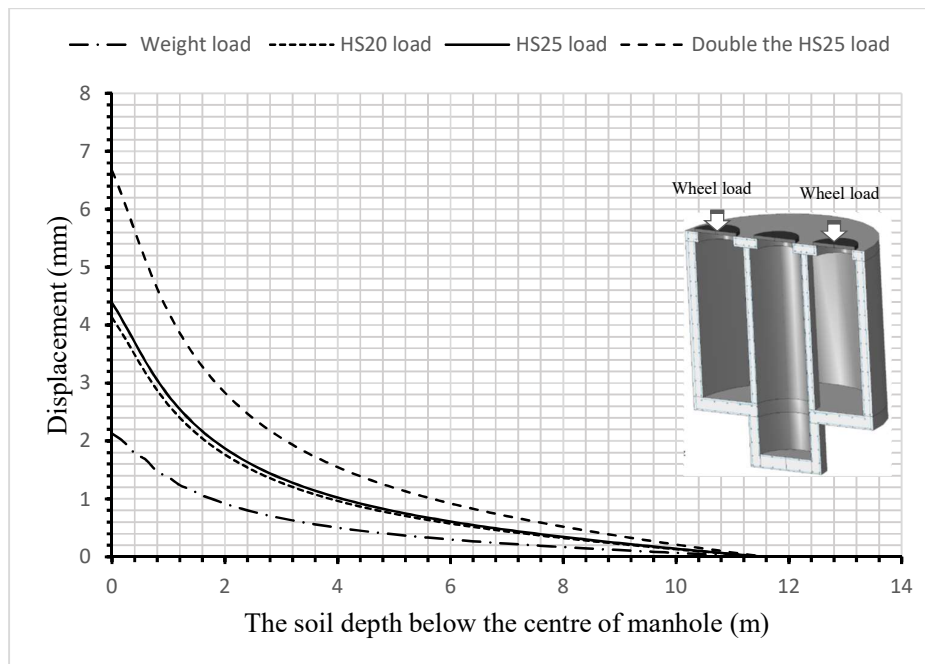


Figure 4.30 Displacement of the new reinforced manhole under a two-wheel applied load on the storm chamber manholes covers.

Table 4-1 summarizes the maximum displacement of the new manhole under one wheel load and two wheel loads, using non-reinforced concrete and reinforced concrete.

**Table 4-1 Summary of the displacement of the new manhole under different applied loads and type of material.**

The new manhole case	Location of applied load	The maximum displacement of soil below the centreline of manhole			
		Weight load	HS20 load	HS25 load	Double HS25 load
Non-reinforced concrete	One wheel on the sewage chamber cover	1.63	2.61	2.73	3.83
	Two wheels on the storm chamber covers	1.63	3.55	3.79	6.07
Reinforced concrete	One wheel on the sewage chamber cover	2.12	3.14	3.26	4.38
	Two wheels on the storm chamber covers	2.12	4.12	4.38	6.67

The results show the high stability of the new manhole when loads are applied. When tested under a double heavy load (twice HS25), applied on two positions on the new manhole, the maximum displacement was 6.67, which is below allowable limits for manhole displacement (13 mm) (Sabouni and El Naggar, 2011a). The weight of reinforcement added small margin of displacement, in the region of 0.5 mm.

The same series of traffic loads were applied on the cover of the conventional manhole, Figure 4.31 illustrating samples of the simulation outputs under a double heavy load. The simulation shows that the conventional manhole has less effect on the surrounding soil compared to the new manhole.

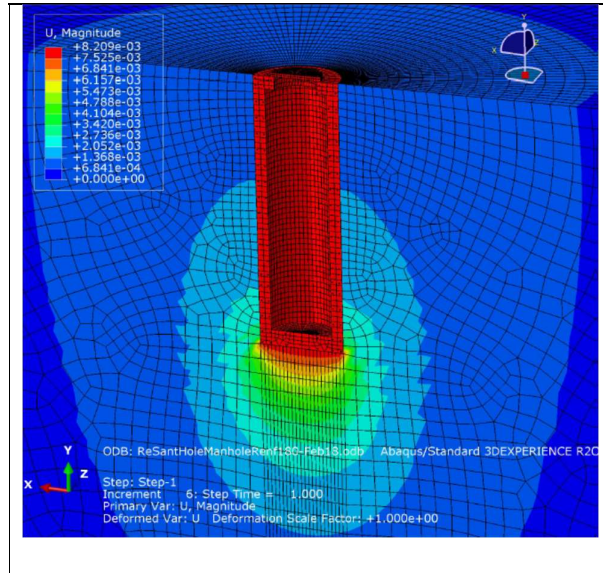


Figure 4.31 Sample of FE simulation of the displacement output for the conventional manhole design exposed to 2HS25 on the manhole cover.

Figure 4.32 presents the results for the non-reinforced concrete manhole, Figure 4.33 presenting the results of the reinforced concrete manhole under different categories of applied loads.

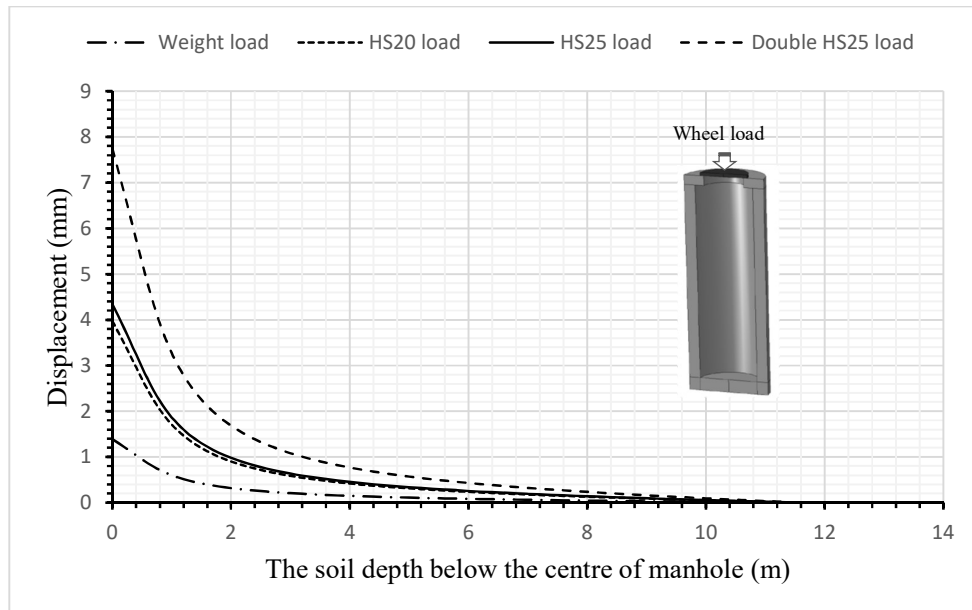


Figure 4.32 Displacement of the non-reinforced conventional manhole under a one-wheel applied load.

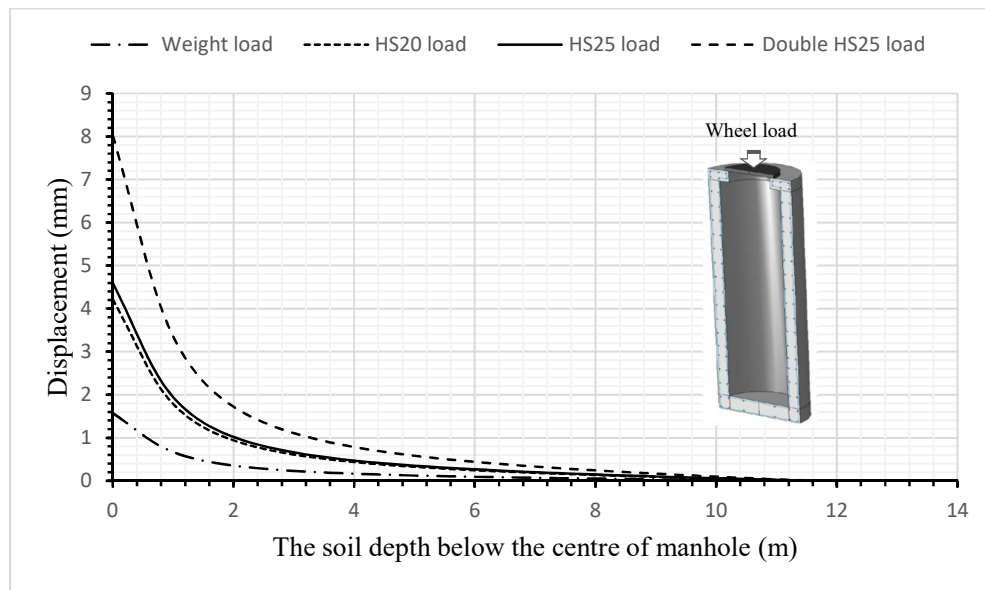


Figure 4.33 Displacement of the reinforced conventional manhole under a one-wheel applied load.

Table 4-2 summarizes the maximum displacement of the non-reinforced and reinforced concrete conventional manhole.

Table 4-2 Summary of the displacement of the conventional manhole under different applied loads and types of material.

The conventional manhole case	Location of applied load	The maximum displacement of soil below the centreline of manhole			
		Weight load	HS20 load	HS25 load	Double HS25 load
Non-reinforced concrete	One wheel on the manhole cover	1.39	3.97	4.35	7.74
Reinforced concrete	One wheel on the manhole cover	1.57	4.22	4.60	8.02

The increased weight of the new manhole has a clear effect on the initial settlement of the manhole when buried in soil. The displacement results were larger than the displacement of the conventional manhole. This settlement is expected to occur at the construction stage and will not create any risk to the safety of the manhole through its operational lifetime. The results show that the new manhole is stable, even under high loading (a double heavy load), the displacement of the soil below the manhole centreline being 3.38 mm under a one-wheel double heavy load and 6.07 mm under a two-wheel double heavy load, using a non-reinforced manhole. For the reinforced manhole, the displacement was 4.38 mm under a one-wheel double heavy load and 6.67 mm under a two-wheel double heavy load. These results reflect high stability under very high loads, more than double the loads that normally occur. The impact of a heavy load on the conventional manhole is more obvious. The conventional manhole had less stability in terms of displacement under high loads (double heavy load) because the area of the base is smaller than that of the new manhole. The displacement of soil below the manhole centreline was 7.74 mm at double heavy load when using a non-reinforced concrete and 8.02 mm when using reinforced concrete.

The conventional manhole has less displacement under light and medium loads and about the same displacement under heavy loads, compared with the displacement of the new manhole under the same loads. It also experiences higher displacement under over-loads in comparison to the new manhole. The displacement of the new manhole is significantly less than the displacement of the conventional manhole when a one-wheel load is applied. Figure 4.34 shows a comparison of the displacement of the soil below the new and conventional manholes when using reinforced concrete.

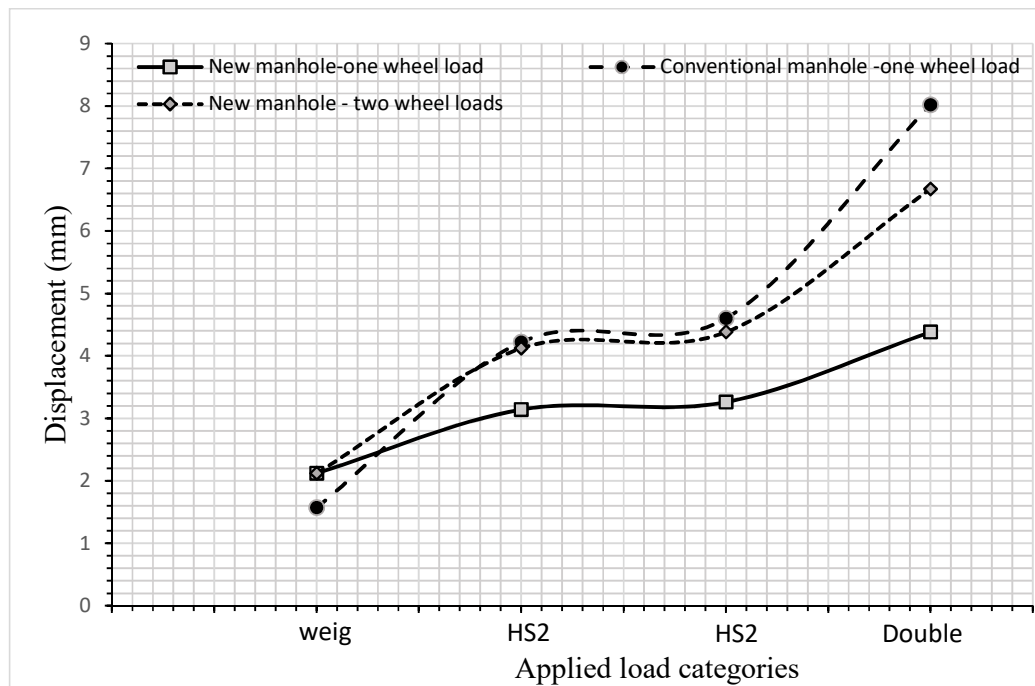


Figure 4.34 A comparison of the displacement for both manholes under different loads (FE model).

The increased weight of the new manhole is one of the main disadvantages of the new design. However, the effect of this additional weight can be countered by using lightweight materials such as GRP for either the inner or outer chambers. In one test in the current study, the inner chamber walls were replaced by GRP material, the manhole tested under same series of applied loads. Reinforced concrete was used for the outer chamber and the sewage section located below the storm chamber. Figure 4.35 shows the results of the subsequent soil displacement below the centreline manhole at one-wheel loading applied on the sewage chamber cover. Figure 4.36 shows the results for the new manhole when a two-wheel load is applied to both storm chamber covers. Both results show a significant reduction in displacement compared with the same manhole when reinforced concrete alone is used, the displacement reduced from 4.38 to 2.3



under a one-wheel double HS25 load and from 6.67 mm to 3.78 mm under a two-wheel double HS25 load. The displacement results due to the weight of the manhole, decrease to approximately 1 mm when the inner manhole material is changed from reinforced concrete to GRP.

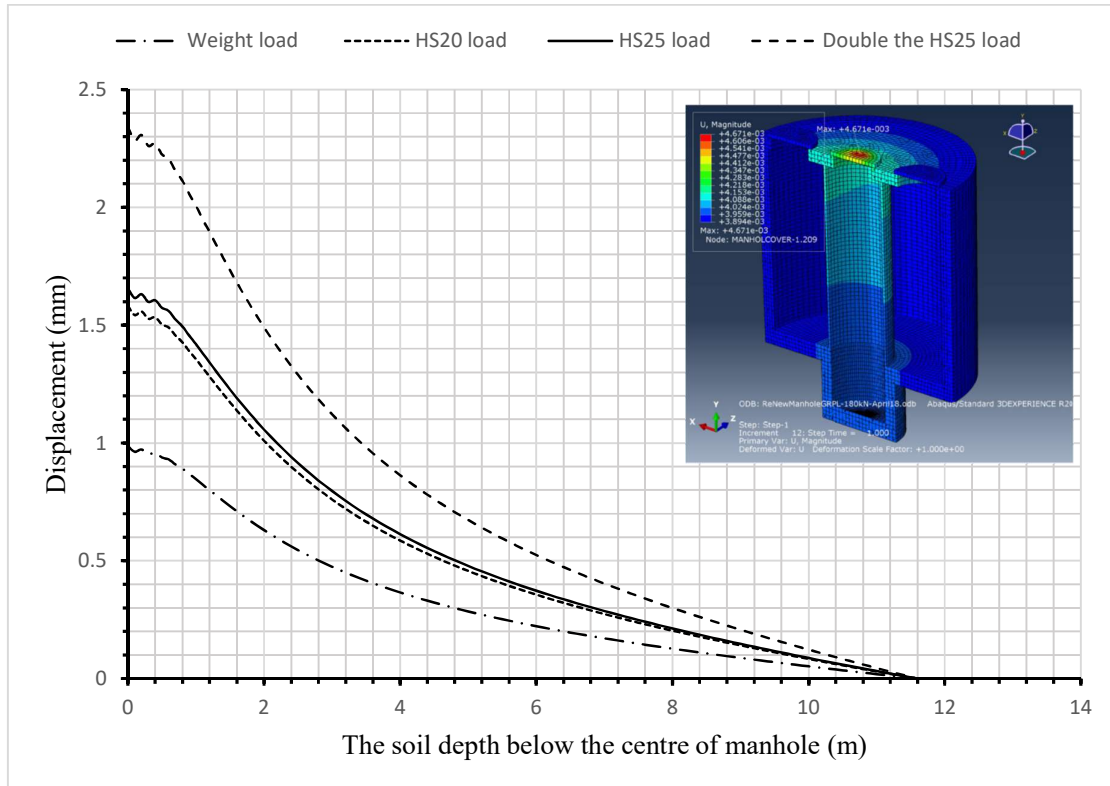


Figure 4.35 Displacement of the new manhole using a hybrid material (GRP for the inner walls and reinforced concrete for the outer walls), under a one-wheel applied load.

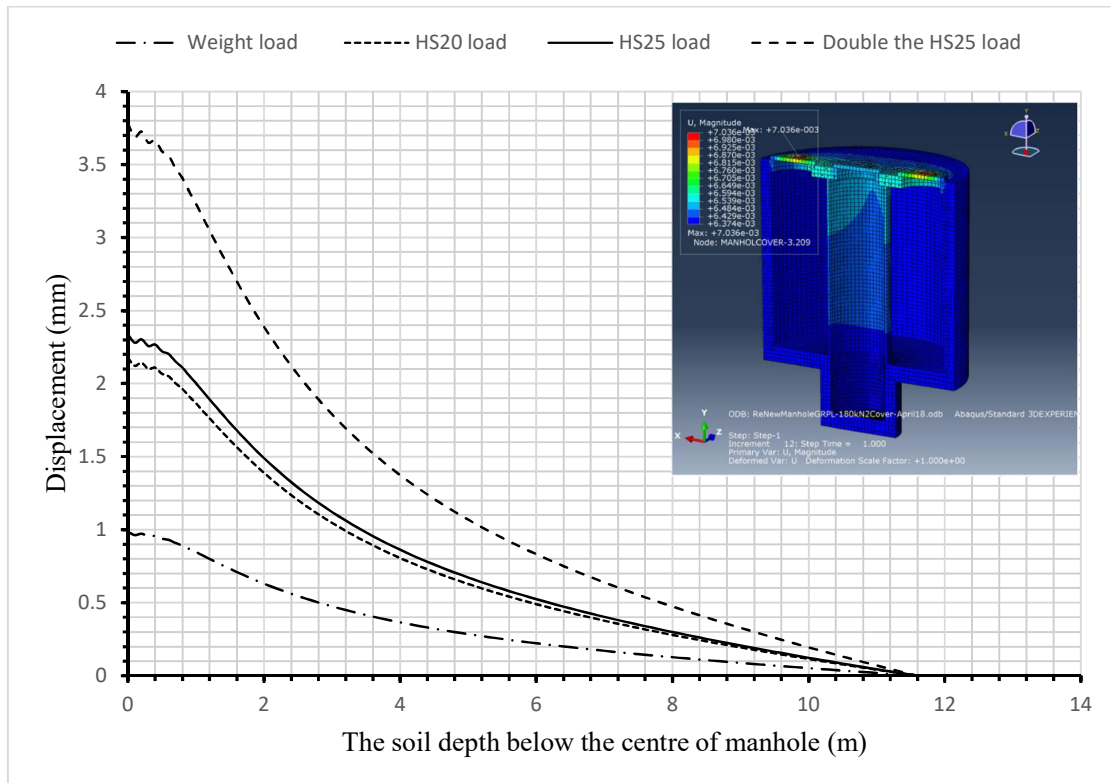


Figure 4.36 Displacement of the new manhole using a hybrid material (GRP for the inner walls and reinforced concrete for the outer walls) under a two-wheel applied load.

Manholes can have an impact on the surrounding surface soil and the layers which make up the road (Chang et al, 2014). Therefore, the results for displacement to both manhole covers, and the soil surface were explored using the FE model. The new manhole was identified as having more impact on the surrounding soil as it was displaced by between 1-2 mm under heavy loads, over a 3-meter circle around the manhole. This displacement increased to between 2-3.5 mm under a double-heavy load. The displacement measured at the manhole cover represents a summation of the soil displacement below the manhole and deformation of the manhole material. The displacement increases from 6.67 mm to 7.1 mm under a double heavy load, from 4.38 mm to 4.6 mm when the load is HS25 and from 4.1

mm to 4.33 mm when the load is HS20, when two wheel passed over the reinforced manhole. These surface displacements need to be taken into consideration when designing road surfaces as the soil displacement below the manhole base effects connecting manhole pipes. This is critical as seen in many cases of sewer collapse where the point of collapse is often at the connection joint between the pipes and the manhole because of relative displacement, which ought to be no more than 13mm (Sabouni and El Nagggar, 2011a).

There was less displacement with the new manhole, both the total surface and of the soil below the manhole. This increases the safety of sewer systems subject to very high loads. The displacement occurring in the conventional manhole surface increased from 8.02 mm to 8.21 mm under double heavy loads. This includes the displacement of the soil underneath the manhole and manhole structure deformation. It increased from 4.6 mm to 4.7 mm when the load was HS25, from 4.2 mm to 4.3 mm when the load was HS20, both when one wheel passed over the reinforced manhole. A conventional manhole has less impact on the surrounding surface soil, displacements of approximately 1 mm across all loads.

The stress in the surrounding soil generated by the conventional manhole was approximately 3 times higher than that experienced by the new manhole. This is because the new manhole has a larger surface area working to mitigate load stresses. This reduction in stress is promising as it may allow the use of lightweight materials such as GRP, HDPE or PVC to build the whole, or part of, the manhole e.g. the inner chamber, while using concrete for the external chamber (the storm chamber). There is also the potential to decrease the thickness of the walls, or to minimise the amount of reinforced steel required.

The structural performance of the manhole itself needs to be analysed and designed to avoid cracking or failure in the manhole body itself. This research assessed the structural performance of the new manhole when using non-reinforced concrete but not when using GRP, something recommended for future research.

#### *4.3.2.2 Investigation of the manhole body structure*

The change in the manhole geometry, created a change in its structural behaviour. The non-reinforced traditional manhole has previously been tested by Sabouni and El Naggar (2011a) who used two manholes of 1200 mm and 1500 mm diameter. They used 52 MPa as the cylinder compressive strength for the concrete base of the manhole, this a relatively high strength. Their results indicated that both manholes were able to withstand applied loads, the maximum overall calculated strain approximately 75% in the 1200 mm manhole and 83% in 1500 mm manhole, these less than the base cracking strain. Sabouni and El Naggar (2011b) also generated a numerical model (FE) for both manholes. They found that the cracking moments ( $M_{cr}$ ) for the bases were 16.3 kN·m/m for the 1200 mm manhole and 62.4 kN·m/m for 1500 mm manhole, the average bending moment calculated at 4.8 kN·m for the 1200 mm manhole and 10.25 kN·m for the 1500 mm manhole. Further to this, Najafi and Sever (2015a) carried out testing and created an FE study for a manhole of 1200 mm, reporting the maximum strain as 0.00019, the maximum cracking moment as 1 kN·m/m compared with a calculated cracking moment of 15.43 kN·m/m. They used non-reinforced

concrete, which has a 40 MPa cylinder compressive strength. It should also be noted that they applied a low load (HS15), approximately 53 kN, to the manhole.

The same procedure and materials as used by Najafi and Sever (2015a), were used in this research. The applied load however, was different as conservative traffic loads were applied to the manhole. ACI318 limits the strain in the concrete to 0.003. The cracking moment of the concrete was calculated using an ACI318 equation (3), 22.7 kN-m for the base of the traditional manhole and 34.1 kN-m for the new manhole. These limits were used to compare the output of both structural manhole models. Table 4-3 illustrates the maximum strain on the manhole body and the percentage of difference for the bending moment of the base of the manholes, compared with the cracking moment when a one-wheel load is applied to the sewage chamber cover.

According to ACI318, the cracking moment of the concrete is calculated as follows:

$$M_{cr} = \frac{f_{cr} I_g}{y_t} \quad \text{Equation 4-1}$$

For the rectangular section concrete slabs, it is

$$M_{cr} = \frac{f_{cr} b h^2}{6} \quad \text{Equation 4-2}$$

where  $I_g$  is the gross moment of inertia ( $m^4$ );  $b$  and  $h$  are the width and thickness of the manhole base slab, and  $f_{cr}$  is the flexural cracking strength.

Table 4-3 Percentage difference for the bending moment of each manhole base, the cracking moment and the maximum strain on the body of each manhole, exposed to a one-wheel load at the centre.

Load categories	New Manhole			Traditional manhole		
	Bending moment	% Diff from the $M_{cr}$	Max Strain	Bending moment	% Diff from the $M_{cr}$	Max Strain
HS15	11.90	65%	$4.29 \times 10^{-5}$	4.27	81%	$3.60 \times 10^{-5}$
HS20	13.73	60%	$4.89 \times 10^{-5}$	4.87	78%	$4.10 \times 10^{-5}$
HS25	15.38	55%	$5.50 \times 10^{-5}$	5.46	75%	$4.50 \times 10^{-5}$
Double heavy load	30.23	11%	$10.00 \times 10^{-5}$	10.68	53%	$8.90 \times 10^{-5}$

Figure 4.37 and Figure 4.38 show the strain and location of the maximum bending moment at the base of each manhole, under a double heavy load (2HS25). The new manhole nearly failed under double heavy loads, this the extreme case, while the traditional manhole was able to withstand this extent of loading. Double heavy loads are used in this study to test the maximum structural capacity of the manhole. The structure of the new manhole can be effected by the degree of compaction of the soil underneath the two chambers of the manhole. Any difference in soil stiffness below these chambers can led to differential settlement which generates more stress in the body of the manhole, depending on the location of the applied load.

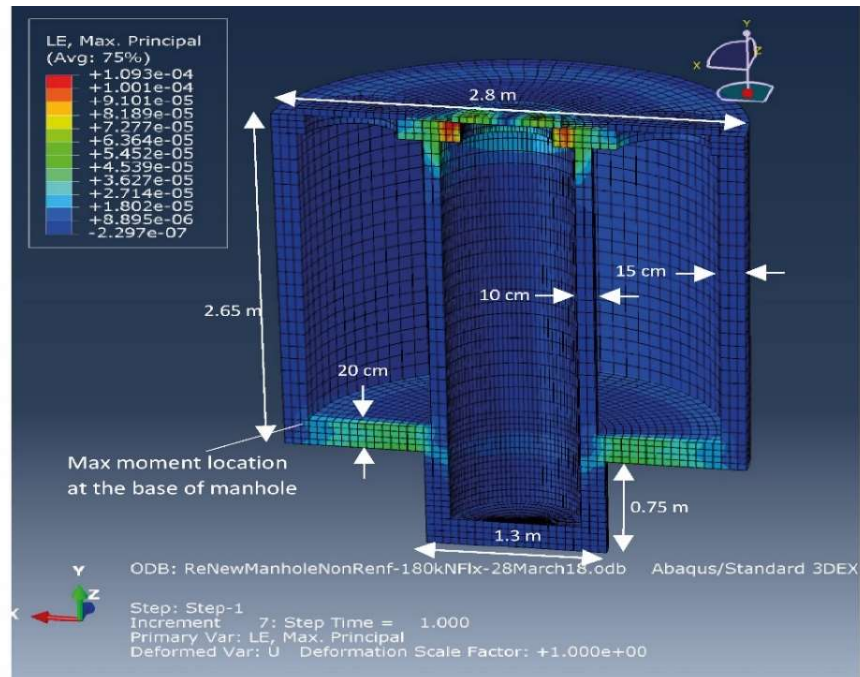


Figure 4.37 The strains and location of the maximum bending moment in the base of the new manhole body, under a double heavy load (2 x HS25).

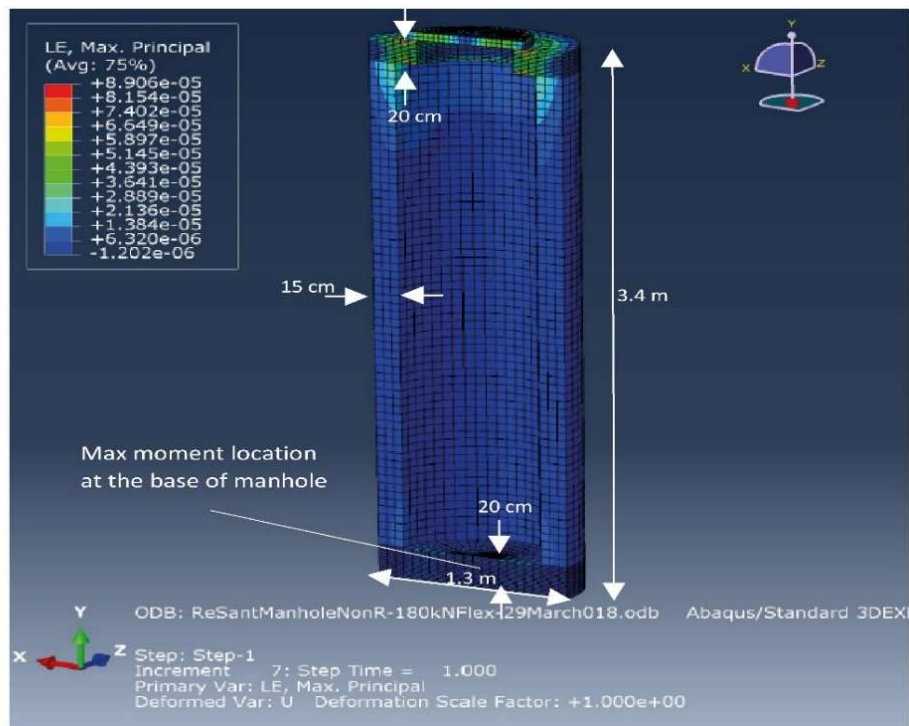


Figure 4.38 The strains and location of the maximum bending moment in the base of the conventional manhole body, under a double heavy load (2 x HS25).

There is no guarantee that the required compaction for both the soil under the inside manhole and the outside manhole, can be achieved as this is dependent on the site conditions, soil types and material used for the construction of the manhole. However, this is a practical installation problem. This has been discussed with reference to non-reinforced concrete, exposed to a two-wheel load on the storm chamber covers and a one-wheel load on one storm chamber cover, using different degrees of soil stiffness underneath the sewage chamber (approximately 95% compaction degree) and the soil below the storm chamber base (approximately 90% compaction degree).

Table 4-4 shows that the new manhole can withstand the impact of this when there is a difference in soil stiffness. The worse-case scenario was when a one-wheel load was applied on the sewage chamber cover, approximately 11% the difference between cracking moment and bending moment. The reason for this is that the weight of the manhole and the applied load accumulated at the centre of the manhole producing differential settlement between the storm chamber and sewage chamber. This suggests that reinforced concrete is required for the new manhole, specifically the external chambers (storm chamber and the part of sewage chamber below the storm base level), when it is not being laid in a narrow street and can be exposed to double heavy loads.



Table 4-4 Percentage difference for the bending moment of the manhole base, the cracking moment and the maximum strain on the body of the manhole, exposed to wheel loads on the storm chamber covers.

Load categories	New Manhole: two-wheel loads			New Manhole: one-wheel loads		
	Bending moment	% Diff from the $M_{cr}$	Max Strain	Bending moment	% Diff from the $M_{cr}$	Max Strain
HS20	9.16	73%	$7.46 \times 10^{-5}$	10	71%	$7.11 \times 10^{-5}$
HS25	9.85	71%	$8.30 \times 10^{-5}$	11	68%	$8.00 \times 10^{-5}$
Double heavy load	16.70	51%	$16.50 \times 10^{-5}$	20.1	41%	$8.90 \times 10^{-5}$

#### 4.4 Summary

This chapter investigated the structural performance of the new manhole using 3D finite element analysis validated by experimental tests. The structural performance was compared to the performance of a conventional manhole. The results revealed that the extra weight of the new manhole in addition to the loads applied on the new manhole, increases the displacement, making it higher than that for a conventional manhole under a small live load (H15). Under heavy loads, both the new and conventional manhole exhibit the same settlement and both operate within standard limitations. The new manhole has very good stability under extremely high loads while the conventional manhole experienced more settlement under the same load. However, the bending moment was close to the cracking moment at the base of the storm chamber under a double heavy load; therefore, reinforcement was recommended for the slab cover and the base of the manhole. The structural improvements tested by the mathematical model and calibrated by the experimental work, allow the safe use of this new manhole, and allow further work to test the hydraulic behaviour of the new manhole in comparison to a conventional manhole.

## CHAPTER 5

### **HYDRAULIC MODELS OF THE MANHOLE**

This chapter presents a hydraulic study of the geometry of the new manhole which is comprised of two chambers in one structure to manage separate flows. The sewage flow chamber is the same as that of a conventional manhole therefore there is no change in its hydraulic properties. The new manhole however, generates a new flow pattern for stormwater flow so the present study focuses on exploring the hydraulic performance of the stormwater chamber, usually characterized by significant head loss and shockwaves associated with different flow regimes. A physical model was used to carry out a systematic experiment to explore the flow characteristics of the manhole, under subcritical and transitional flow conditions. Measurements collected from the physical model (velocity, pressure and shockwaves) were used to conduct validation tests between the CFD model and the physical model. The validated CFD model can then be used in subsequent research to test improvements in design and to further develop the hydraulic design of the new manhole.

### 5.1 Hydraulic properties of the conventional manhole

A manhole is one of the main elements of the sewer system, making it an important hydraulic structure, affecting the hydraulic performance of the entire sewer network. Manholes are used to aerate the sewer system as well as to gain access to carry out cleaning, maintenance and inspection procedures. They are located at a maximum spacing range between 50 m and 100 m or at any change in inlet or outlet pipe diameter, direction or level (Hager, 2010). Typically, the municipal sewage flow produced by human activity (residential, commercial and industrial), is stable and predictable when compared with stormwater runoff meaning it is easier to design a sanitary sewer system with appropriate safety factors against flood risk and surcharge and to characterize its hydraulic performance.

The pattern of flow through a conventional manhole was described by Albertson (1948) using a jet into an infinite volume (Figure 5.1). This theory has been used to calculate head losses generated at conventional manholes for different surcharge ratios (Pedersen and Mark, 1990). At a constant flow rate, a small surcharge in the level of the incoming jet will interact violently with the free surface, increasing energy loss and causing flow exchange. The impact of the transitional flow on the manhole wall generates shockwaves associated with swell, the heights and locations of these waves for conventional manholes determined by Gargano and Hager (2002); Hager and Gissonni (2005) as shown in Figure 5.2. The effect of the jet flow and shockwaves dissipates as the surcharge height increases (Guymer et al, 2005).

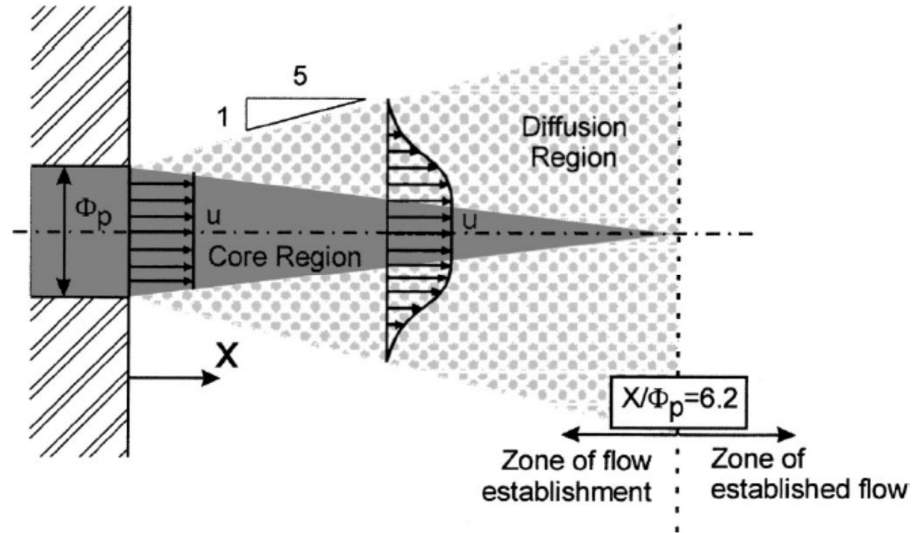


Figure 5.1 Velocity distribution and diffusion region in a circular manhole free jet (Alberston et al. 1948) [Reprinted with permission from American Society of Civil Engineers (ASCE)]

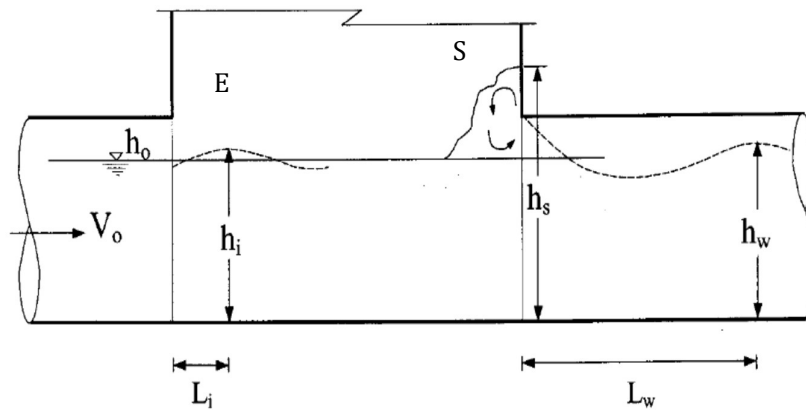


Figure 5.2 Definition plot for flow through a conventional manhole (Gargano & Hager, 2002) [Reprinted with permission from American Society of Civil Engineers (ASCE)]

Sewers are normally designed to maintain free surface conditions for predicted storm intensities and a fill ratio of 85% for the flow in the pipe. Hager

(2000) recommends this be 75%, this offering the same discharge capacity of a circular full pipe under gravity flow. The flow in a sewer/manhole system is typically subcritical for  $Fr < 0.7$ , transitional for  $0.7 < Fr < 1.5$  and supercritical for  $Fr > 1.5$  (Hager and Gisonni, 2005), depending on the pipe gradient and flow rate. Additionally, when the filling ratio of a pipe is  $\beta_{ip} = h_o/D_p < 0.5$ , there is no shockwave at the outlet of the manhole. The transition, changing  $\beta_{ip} > 0.5$ , is associated with an interrupted flow which impinges at the outlet manhole (also known as flow choking), and changes the flow from free surface to pressurized air–water flow (Gargano and Hager, 2002). However, designing the storm sewer system with a prescribed filling ratio can be problematic, as there may be difficulties in accurately predicting rainfall intensity and the average quantity of inlet storm water to the sewer network caused by heavy rain. Next to inherent design uncertainties, climate change can further exacerbate the correct design of a stormwater sewer. Transitional and supercritical flows are more common in the rainy season, seen in both storm networks and combined networks.

To date, there have been no significant works to develop the design of existing manholes but there have been many attempts to improve the hydraulic properties of the conventional manhole through the installation of extra accessories to enhance the dissipation of energy inside the manhole. A non-dissipated, flow energy upstream sewer network leads to high downstream flow velocity, which increases the risk of flooding and erosion and creates poor operating conditions. Granata et al (2014) investigated the hydraulic performance of drop manholes under supercritical flow conditions. They attempted to improve the hydraulic performance of the conventional drop manhole by installing a dissipative component, as described in section 2.3.3.1. Increasing the flow path of

storm water reduced the height of shockwaves specifically in the junction manhole and bend manhole, this associated with an increase in the manhole storage capacity. Both these characteristics were identified through experimental tests conducted by Pfister and Gisonni (2014) for the junction manhole, and by Hager and Gisonni (2005) for the bend manhole. Froude number ( $Fr$ ) of approach flow and filling ratios were used as the parameters to describe the shockwaves inside the manhole. Saldarriaga et al (2017) analysed the flow patterns in a symmetric junction in a manhole under supercritical flow conditions, recommending that improvements in the geometry could subsequently improve the hydraulic performance at a conventional junction manhole.

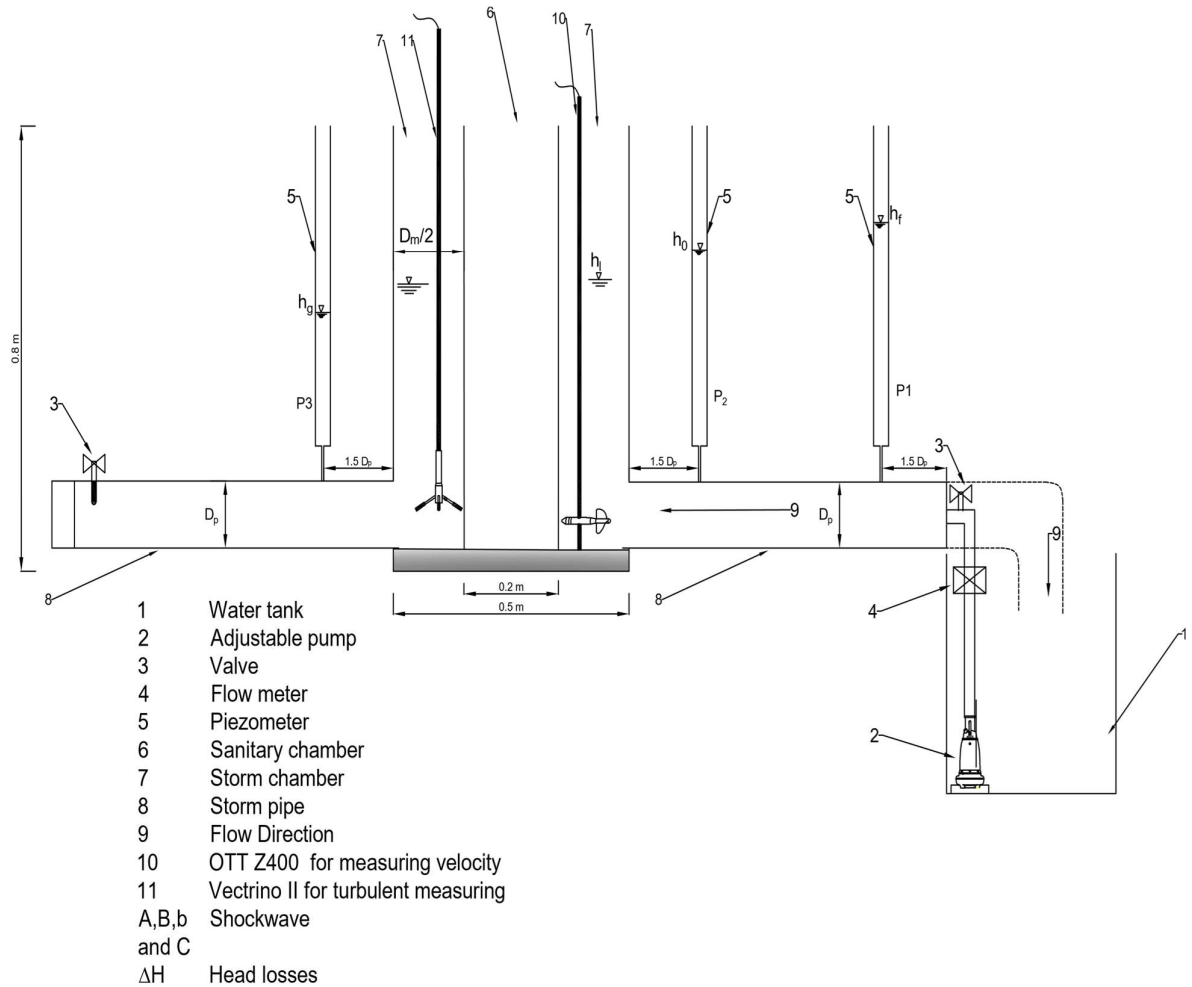
## **5.2 Hydraulic performance of the new manhole design**

The new manhole design presented in this research will improve the performance of the sewer network because of its streamlined design, when compared to conventional manholes, where various additional accessories could involve the use of more design parameters. The novel design uses a new shape of manhole to reduce installation costs and the required area, this allowing the installation of a separate sewer system in narrow streets where space is at a premium. It also increases the storage capacity of the storm water chamber, extends the path of flow inside the chamber and creates an obstacle to the flow path using internal walls. All these features can improve the dispersion flow energy inside the storm manhole chamber. The hydraulic properties of the new manhole were explored and compared with the performance of conventional manholes using a physical model, built in the hydraulic laboratory of LJMU.

### 5.2.1 *Physical model*

The aims of this experiment was to explore the energy dispersion of storm flow under different flow rates, compared to that of a conventional manhole; to measure shockwaves produced as a reaction to any alteration of the flow inside the storm chamber, and to determine velocity distribution at selected points. A prototype model was built to a 1/5 scale, simulating the new combined manhole shape. The inner chamber was simulated by a Plexiglas pipe, 20 cm in diameter, the outer chamber 50 cm in diameter. Both chambers were fixed on one plane base and were 80 cm in length. The inlet pump with an adjustable flow rate (max capacity 500, l /minute), was set in a water storage tank used to cycle flow water through the system, a flow meter fixed next to the pump to measure the flow rate. Two Plexiglas pipes were connected to the outer chamber of the manhole, an inlet pipe and outlet pipe; both were 10 cm in diameter and equipped with two valves to control flow rates and depth of flow. Three piezometers were fixed in the system to monitor drops in pressure through the model and measure energy loss, one positioned at the inlet pipe by the manhole, the second at the outlet pipe, the third in the pipe at the flow starting point, after the pump. A gate valve was placed upstream after the pump to control the water level at the outlet pipe, a second gate valve placed downstream after the manhole to control the flow (Approach Fraud number  $Fr_o$ ) and the filling ratio ( $y_o$ ) at the inlet pipe. A camera was used to record the flow pattern and shockwaves under different flow rates. Two rulers were fixed in the new manhole, one on the external wall, the second on the internal wall to measure the amplitude of the shockwaves. A portable OTT Z400 with an accuracy of  $\pm 0.01s$ , was used to measure the velocity at the inlet and outlet pipes, and at selected points inside the manhole, distributed around the centre and the

edge of the manhole. A Doppler Vectrino II was used to measure the turbulent velocity of three axes, X, Y and Z, at one point inside the manhole. Conventional manhole head loss, shockwaves and velocities were measured by removing the inner sanitary chamber and using the external chamber as the conventional storm manhole model with a scale of 1/3. All other facilities used for the new manhole are the same as those used to monitor the flow and head loss through the conventional manhole. Figure 5.3 a, b and c illustrate the setup of the physical model for the new manhole.



(a)





The new manhole was designed to increase the head loss of stormwater flow through the storm chamber when compared with a conventional storm manhole, and to increase both the storage capacity and retention time of the flow inside the storm chamber. Accordingly, this work will first analyse the head loss coefficient for a different approach Froude number and downstream boundary conditions, attempt to quantify and study shockwave amplitude and finally, compare these results with the hydraulic performance of the conventional manhole.

#### 5.2.1.1 Head loss

An analytical method was used to determine the head loss ( $\Delta H$ ) of flow inside the manhole from the difference of head pressure between the inlet and outlet of the manhole, thus giving the coefficient of energy loss (Equation 5-1) (Sangster et al, 1958).

$$\Delta H = K \frac{v^2}{2g} \quad \text{Equation 5-1}$$

where

$v$ =mean pipe velocity;

$g$ =acceleration due to gravity

$K$ =head loss coefficient.

The impact of changing conventional manhole geometry on the head loss coefficient has been tested through a number of studies on specific manhole design (Arao et al, 1999). The new manhole design here generated a new path for

the storm water flow, as shown in Figure 5.4, where three points can disturb the flow and cause head losses in the storm chamber. The first point is the inner chamber wall which blocks the storm flow path and splits it into two paths ( $\Delta H_w$ ); the second is at the two conduit bends inside the manhole ( $\Delta H_b$ ) and the third is the expansion and contraction at the entrance and outlet pipes, ( $\Delta H_e$ ) and ( $\Delta H_o$ ).

$\Delta H_e$  and  $\Delta H_o$  are, at first approximation, similar to the head loss that occurs in the entrance and outlet of the conventional storm manhole; the impact head loss at the entrance was limited by the distance equal to the diameter of the inlet pipe inside the manhole. This study also considers two new head losses,  $\Delta H_w$  and  $\Delta H_b$ , generated by the new design of the manhole storm chamber. To simplify the calculation, it is assumed that the entrance and outlet head losses,  $\Delta H_e$  and  $\Delta H_o$ , are equal in both manholes, and so, were calculated from the measurement of the head loss in a conventional manhole.

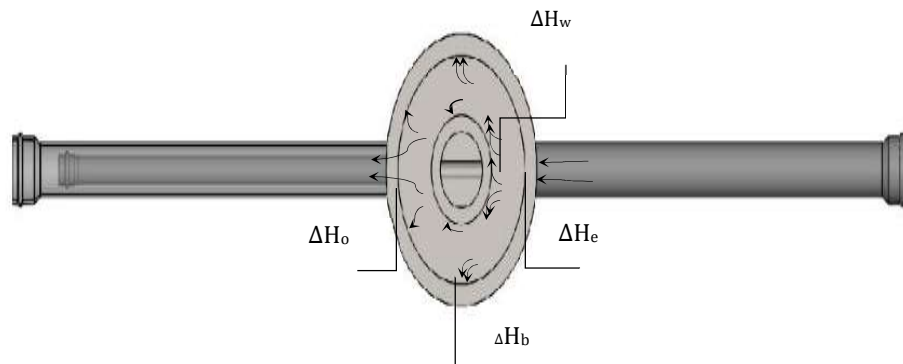


Figure 5.4 Top view of the new manhole showing the storm flow path and the three points of head loss generated inside the storm chamber.

The head loss of flow through a conduit bend was investigated by Ito (1960). The head loss coefficient was calculated using the ratio of the bend mid-radius ( $R$ ) and the channel diameter ( $D$ ) from one side and the angle of curvature of the bend and the Reynolds number from the other side. Ito demonstrated that the minimum head loss coefficient occurred at the  $R/D = 2$  (Figure 5.5), where  $\xi_k = \Delta H_b$  is the head loss as calculated by Equation 2-1. This method, as used by Ito (1960), and the curves extracted from experimental works, were applied to the new manhole design to calculate the head loss coefficient at the conduit bend. The new manhole is designed to have relatively fixed dimensions between the inner chamber (sewage) and the outer chamber (stormwater) where the  $R/D$  ratio is approximately 1.167 with an angle curvature of  $45^\circ$ . The head loss coefficient was found to be approximately 0.1 for the corresponding velocity, equal to  $1 \text{ ms}^{-1}$ , using Ito's (1960) chart. This is expected to be approximately twice that of the head loss coefficient which occurs at the curvature wall of the conventional manhole, as the new manhole has two bends.

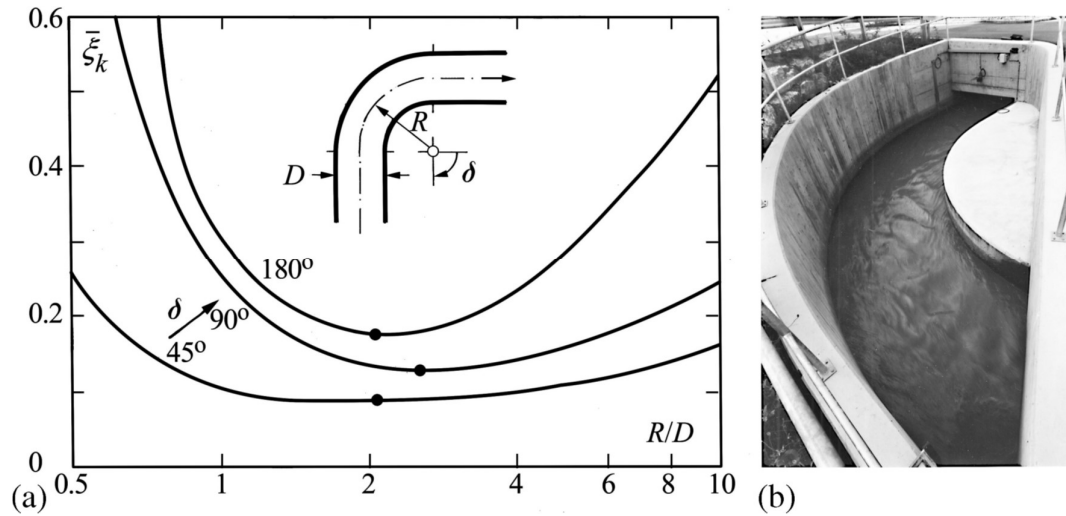


Figure 5.5 (a) Total loss coefficient as a function of relative bend radius ( $R/D$ ) and angle of curvature  $\delta$  for  $Re \geq 10^6$ , (b) Typical open channel bend structure on a treatment station (Hager, 2010). [Reprinted with permission from Springer Nature]

Experimental tests were conducted on both the new and conventional manholes, under the same boundary conditions, to identify the difference between the head loss generated in a conventional manhole and the head loss generated in the new manhole. Said head loss is mainly a result of obstacles to the storm flow path created by the inner chamber wall ( $\Delta H_w$ ) in the new manhole design.  $\Delta H_e$  and  $\Delta H_o$  are the same in both manholes and can be identified from the calculation of the head loss in the conventional manhole. The  $\Delta H_b$  of the new manhole is approximately twice the  $\Delta H_b$  at the bend in the conventional manhole. The main independent, dimensionless parameter for each manhole (conventional and new), were selected to reduce scale effects and used to characterize the hydraulic properties: (1) ratio of surcharge ( $\beta_{im}=h_o/D_m$ ), (2) approach flow Froude numbers which were simplified by Hager (1999) for a circular channel, see below, and (3) filling ratios  $\beta_{ip}=y_o=h_o/D_p$

$$Fr_o = \frac{Q}{\sqrt{gD_p h_o^4}} = \frac{Q}{\sqrt{gD_p^5 \beta i_p^4}} \quad \text{Equation 5-2}$$

where:

$D_m$  = the manhole diameter

$D_p$  = the inlet pipe diameter

$h_o$  = the level of water at the inlet of the manhole

$Q$  = the water discharge.

Tests were programmed to use a variety of filling ratios ( $\beta i_p$ ), the first starting from  $y_o = 0.25$  up to  $y_o = 0.85$  for the free surface, the second set from the free surface flow to full flow ( $y_o > 1$ ), a full flow more common in a combined or storm network during heavy rain. The same range of flow rate was used for both manholes, varying between  $0.3$  and  $6.5 \times 10^{-3} \text{ m}^3 \text{ s}^{-1}$ , with  $Fr_o$  between  $0.2$  and  $0.9$ . Table 5-1 presents the ranges of the dimensionless parameters used to characterize the flow for both manholes. The direct flows used for both manholes were without lateral connection, 154 tests conducted in total. The results indicated that the flow was subcritical when  $Fr < 0.7$ , and free surface conditions were maintained when the depth of flow was less than  $0.5$  in the inlet pipe ( $y_o = h_o / D_p < 0.5$ ), changing to a flow choking associated with shockwaves, when the flow transitioned from a free surface to a pressurized flow ( $y_o > 0.5$ ).

Table 5-1 Experimental ranges of the main dimensionless parameters.

Manhole	$\beta i_m$	$\beta i_p$	Re	Fr <sub>o</sub>
New design	0.1 – 0.5	0.3 – 1.5	9500 -71500	0.25 – 0.9
Conventional	0.05 – 0.3	0.2 – 1.3	15000 -72000	0.4 – 0.9

Figure 5.6 shows the comparison between the head loss coefficient generated in the new manhole with the head loss coefficient of the conventional manhole, under the same boundary conditions, at various ranges of surcharge ratios ( $\beta i_m$ ). The data shows a significant increase of flow energy dissipation (increases in head coefficients), at a low  $\beta i_m$  for the new manhole when compared with the conventional manhole. This difference gradually decreases with an increase of the surcharge ratio  $\beta i_m$  in both manholes until the flow transitions from a free surface flow to a pressurized flow (approximately  $\beta i_m = 0.33$  for the new manhole and  $\beta i_m = 0.2$  for the conventional manhole). The head loss coefficient tends to be constant under pressurized flow (full flow) conditions. The conventional manhole head loss coefficient fluctuates when the flow moves from free surface flow to full flow, while the head loss coefficient showed some stability in the new manhole.

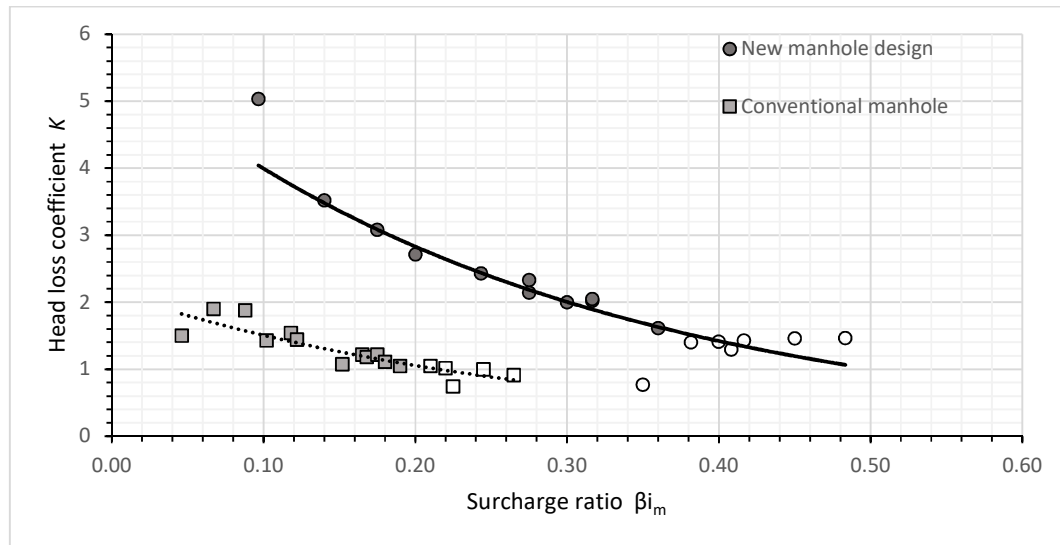


Figure 5.6 A comparison between the head loss in the new and conventional manholes at different surcharge ratios ( $\beta_{im}$ ).

The head loss coefficient increased with an increase in the filling ratio of the inlet pipe for both manholes, when the filling ratio was below half of the pipe diameter ( $\beta_{ip} < 0.5$ ), as shown in Figure 5.7. A comparison of data relating to the head loss coefficient for both manholes at different filling ratios, illustrates a tendency for the head loss coefficient to decrease when the filling ratio is  $0.5 < \beta_{ip} < 0.85$ . It drops sharply at the transition between free surface flow and filling flow. The coefficient tends to be constant after transitioning from a free surface to pressurized flow ( $\beta_{ip} > 1$ ). These results are the same as those of Arao and Kusuda (1999) for a straight, conventional manhole without drops or changes in direction.



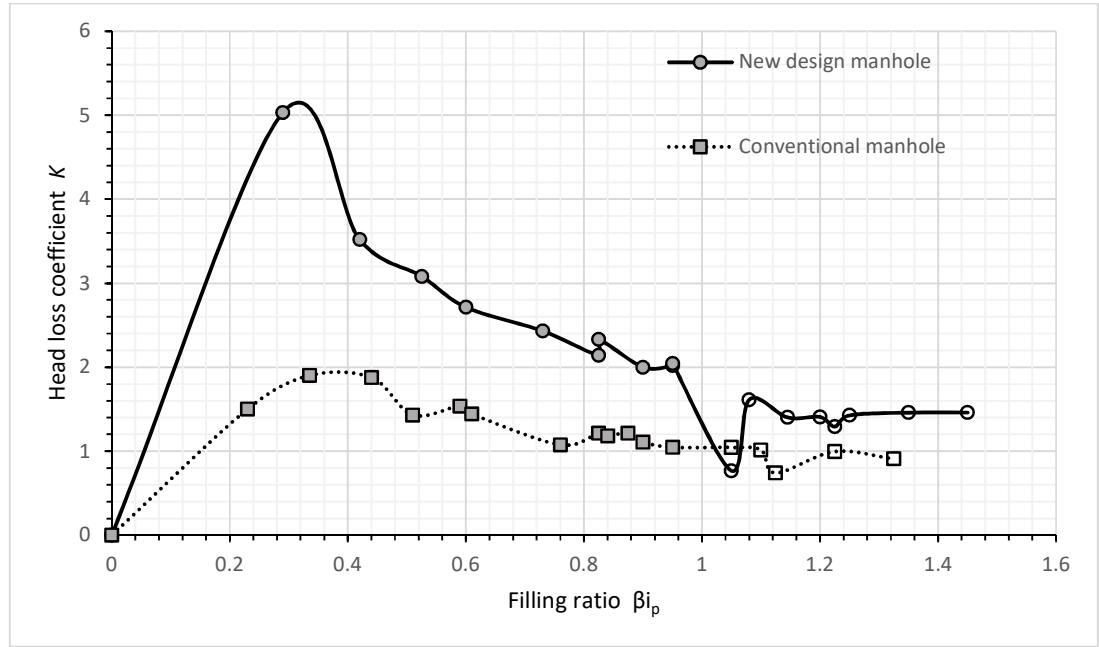


Figure 5.7 A comparison between the head loss in the new and conventional manholes at different filling ratios ( $\beta_{i_p}$ ).

The head loss coefficient can be correlated to the non-dimensional dynamic momentum component ( $Fr_o \beta_{i_p}$ ) to extract preliminary design equations for both manholes (Gargano and Hager, 2002). The data presented in Figure 5.8 to simulate the head loss coefficient with non-dimensional dynamic momentum components, were used to fit Equation 5-3 for the new manhole, and Equation 5-4 for the conventional manhole (Appendix IV).

$$K_{ND} = 0.96(Fr_o \beta_{i_p})^{-0.65} \quad \text{Equation 5-3}$$

$$K_0 = 0.75(Fr_o \beta_{i_p})^{-0.4} \quad \text{Equation 5-4}$$

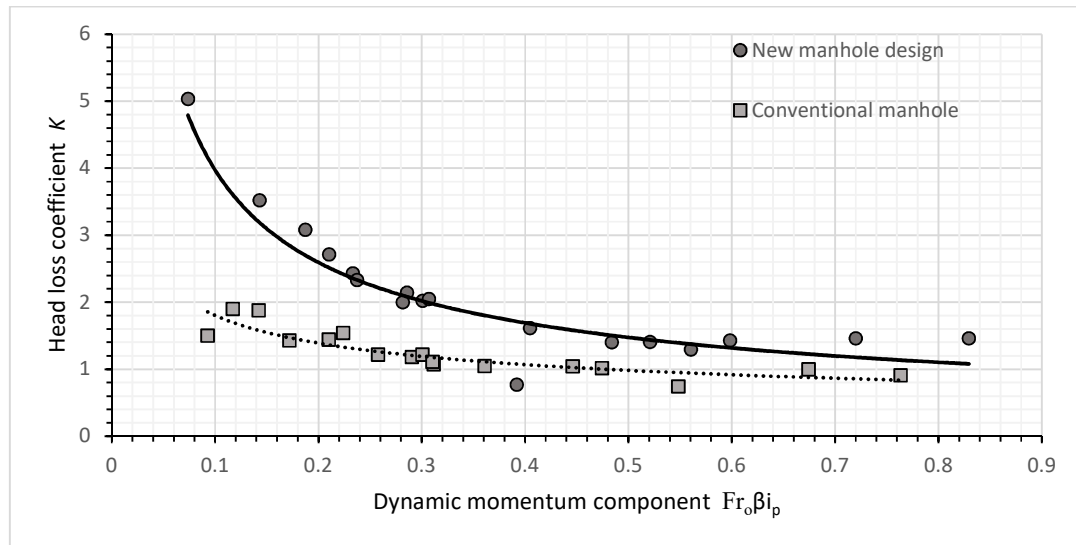


Figure 5.8 Relationship between the head loss coefficient and the non-dimensional dynamic momentum component ( $Fr_0\beta i_p$ ) for the new and conventional manholes.

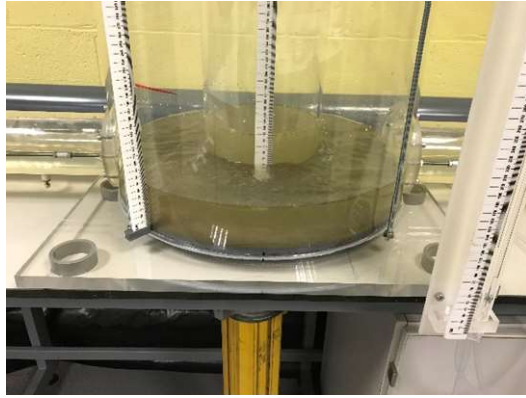
The increase in the head loss coefficient (energy dissipation) upstream of the storm network, improves the hydraulic performance of the network as it delays the peak flow downstream. This alleviates the risk of flooding in the downstream section of the network. Increasing the retention time of the storm water flow upstream in the network, allows the downstream network to initially drain its flow. When the storm runoff increases upstream, the head loss will decrease and enable the sewer system to drain at an optimal performance level. This is particularly beneficial in densely populated areas where there is limited space exists for natural stormwater storage schemes such as SuDS (Dhakar and Chevalier, 2017). The head loss coefficient is at a low level at high dynamic momentum for both manholes. The hydraulic capacity of the sewer system will work at a maximum when storm runoff is high.

#### 5.2.1.2 Shockwaves and choking

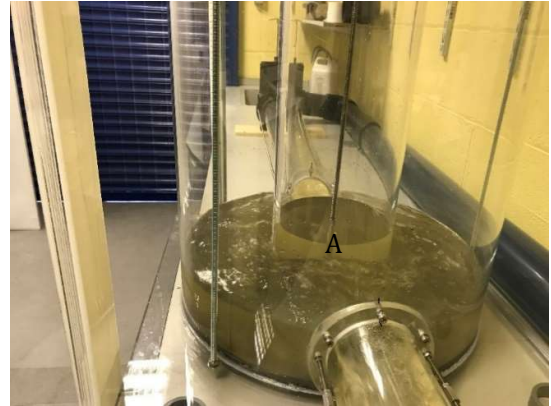
The pattern of flow for conventional manholes was investigated by Gargano and Hager (2002) who identified different types of waves inside the manhole. Figure 5.2 shows a small shockwave resulting from expansion at the manhole entrance (E) and where the flow impinges on the arc-shaped sides and the top wall on the outer manhole, this resulting in a so-called swell wave and choking (S). This research allowed exploration of the main hydraulic features of the new manhole, including shockwave profiles and variations in velocity. Hereafter, the focus lies on the pattern of shockwaves generated by the inner manhole and changes in the flow path in the storm water chamber of the new manhole, in comparison with that in the conventional manhole, for both subcritical and transitional flow conditions.

Four shockwave patterns were identified inside the storm chamber at A, B, b and C (where C is equivalent to shockwave S in the conventional manhole), as shown in Figure 5.3 b. There are no shockwaves present during the subcritical flow when  $Fr < 0.7$  and the filling ratio is below half the capacity of the inlet pipe ( $\beta_{ip} < 0.5$ ), as shown in Figure 5.9 a. The first shockwave (A) appeared when the filling ratio was over  $\beta_{ip} > 0.5$ , as shown in Figure 5.9 b; it continued to be the main shockwave of the flow at  $0.5 < \beta_{ip} < 0.85$ . This main wave, (A), results from impingement of the direct flow in the inlet pipe on the inner manhole wall; it is a continuous wave in the new design associated with transitional flow. The second two symmetrical shockwaves propagated in the storm chamber (B and b), were generated by a change in flow direction caused by two bends in the storm chamber. When  $0.5 < \beta_{ip} > 0.85$ , these shockwaves were had low amplitude. The amplitude of these two

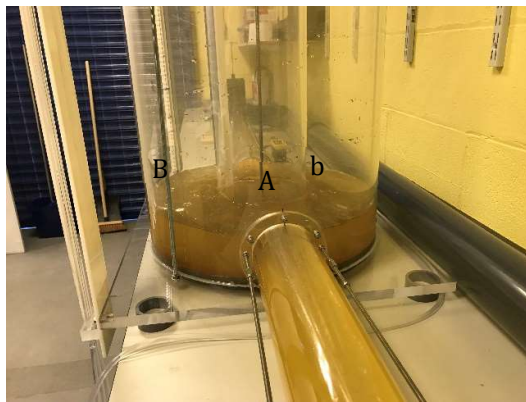
shockwaves increased with an increase in  $\beta_{ip}$ , but were still less than shockwave A when  $\beta_{ip} < 0.85$ , as demonstrated in Figure 5.9 c and d. The generation of these two shockwaves is associated with a swing, or slushing phenomena, experienced by the flow inside the storm chamber. When  $\beta_{ip} > 0.85$ , the amplitude of these shockwaves (B and b) increased above that of shockwave A, as illustrated in Figure 5.9 e and f. The characteristics of the symmetrical shockwaves B and b, generated in both bends of the new manhole, are similar to the shockwaves generated in the bend of the conventional manhole as described in detail by Hager (2010). The last wave, C, was generated by the flow choking at the outlet manhole at  $\beta_{ip} > 0.85$ , as shown in Figure 5.9 g. The domain of swirls that result from the choking wave, was less than that observed in the conventional manhole because the B and b shockwaves were predominated on the C wave. Altogether, these three shockwaves and choking generate a significant swing wave observed in the storm chamber during transitional flow. Figure 5.10 a and b present the pattern of flow recorded for the conventional manhole; it can be observed that there is no significant shockwave when the filling ratio is less than 0.5 (Figure 5.10 a). The choking wave (S) occurs in the conventional manhole when  $0.6 < \beta_{ip} < 0.75$  (Figure 5.10 b) as described by Gargano (2002).



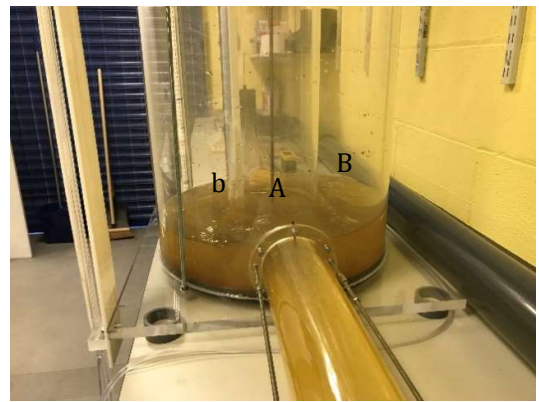
(a) No significant shockwave noted when the filling ratio is  $\beta_{ip} < 0.5$ .



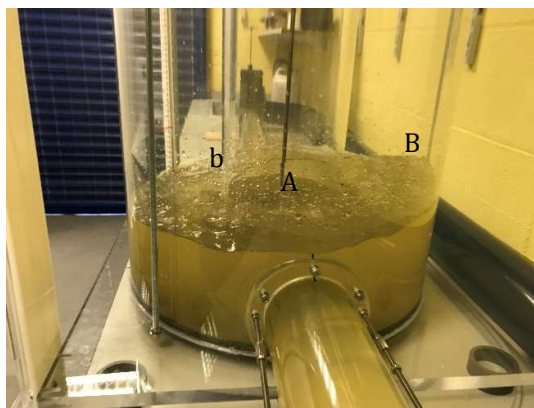
(b) The first and main shockwave (A) appeared when  $\beta_{ip} > 0.5$ .



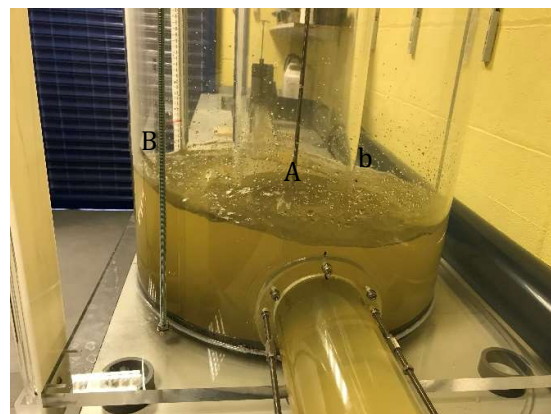
(c) The second shockwave B associated with A, appeared when  $0.5 < \beta_{ip} < 0.85$ . A is still the main shockwave.



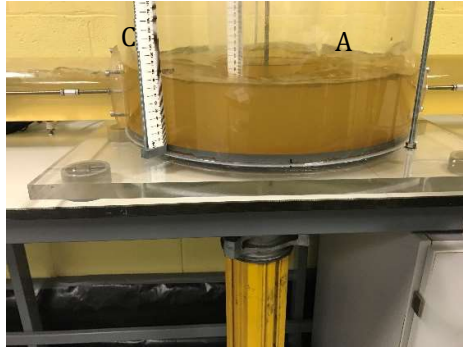
(d) A swing phenomena which appeared when  $0.5 < \beta_{ip} < 0.85$ .



(e) Shockwaves B and b are larger than shockwave A when  $\beta_{ip} > 0.85$ .

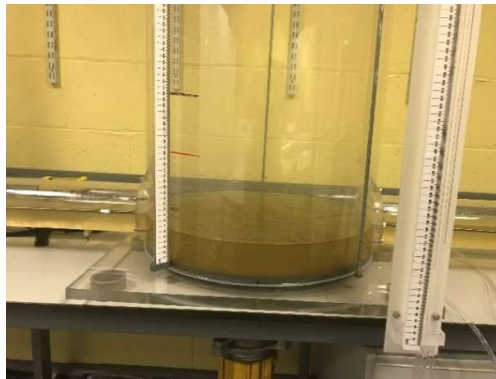


(f) Shockwaves B and b are larger than shockwave A when  $\beta_{ip} > 0.85$  and is associated with an increase in the swing phenomena.

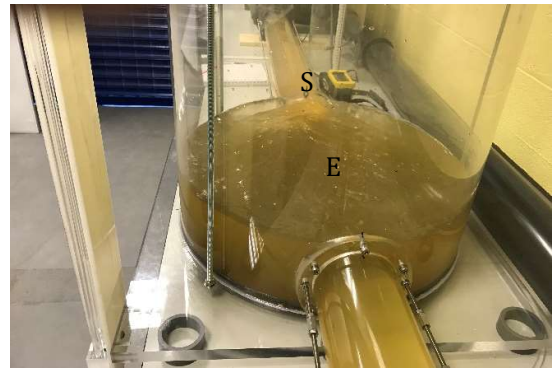


(g) Shockwave C appeared with A when  $\beta_{ip} > 0.85$ .

Figure 5.9 The shockwaves generated in the new manhole design at difference filling ratios ( $\beta_{ip}$ ).



(a) The flow pattern for the conventional manhole when the filling ratio is  $\beta_{ip} < 0.5$ . There is no shockwave.



(b) The flow pattern for the conventional manhole when the filling ratio is  $\beta_{ip} > 0.5$ . Shockwave S is generated at the outlet, E at the inlet expansion.

Figure 5.10 Shockwaves generated in the conventional manhole design at different filling ratios ( $\beta_{ip}$ ).

The general swing wave generated from the four shockwaves, was used to estimate the characteristics of the average wave amplitude inside the storm chamber of the new manhole. The relatively high amplitude shockwaves  $Y_i = (h_i - h_l)/h_l$ , which vary with the non-dimensional dynamic momentum  $Fr_0\beta_{ip}$ , are used to quantify the pattern of shockwaves, where  $h_i$  is the wave amplitude observed in the manhole. Figure 5.11 illustrates the  $Y_i$  over  $Fr_0\beta_{ip}$  relationship for both the conventional and new manhole. The experimental results illustrate how high amplitude shockwaves increase rapidly when the flow changes from free surface flow to pressurized flow in the new manhole. The conventional manhole has smaller amplitude shockwaves. The main shockwave, a choking wave, normally occurs at the transition between free surface flow and pressurized flow for the conventional manhole, this increasing with increased dynamic momentum. The swing of the waves recorded in the conventional manhole, was less than that in the new manhole, attaining a maximum of  $Fr_0\beta_{ip} > 0.5$ . This then became constant for larger values of  $Fr_0\beta_{ip}$  as the wave transitioned from 0.1 to 0.05 (De Martino, 2002). The fluctuation range and the location of the choking wave recorded in these experiments for a similar filling ratio ( $\beta_{ip}$ ), was comparable to the shockwave (S) identified by Gargano and Hager (2002) in the conventional manhole. These relationships were quantified for both manholes, using Equation 5-5 for the new manhole and Equation 5-6 for the conventional manhole (Appendix IV).

$$Y_{i(ND)} = 0.12 \ln (Fr_0 \cdot \beta_{ip}) + 0.32 \quad \text{Equation 5-5}$$

$$Y_{i(o)} = 0.03 \ln (Fr_0 \cdot \beta_{ip}) + 0.09 \quad \text{Equation 5-6}$$

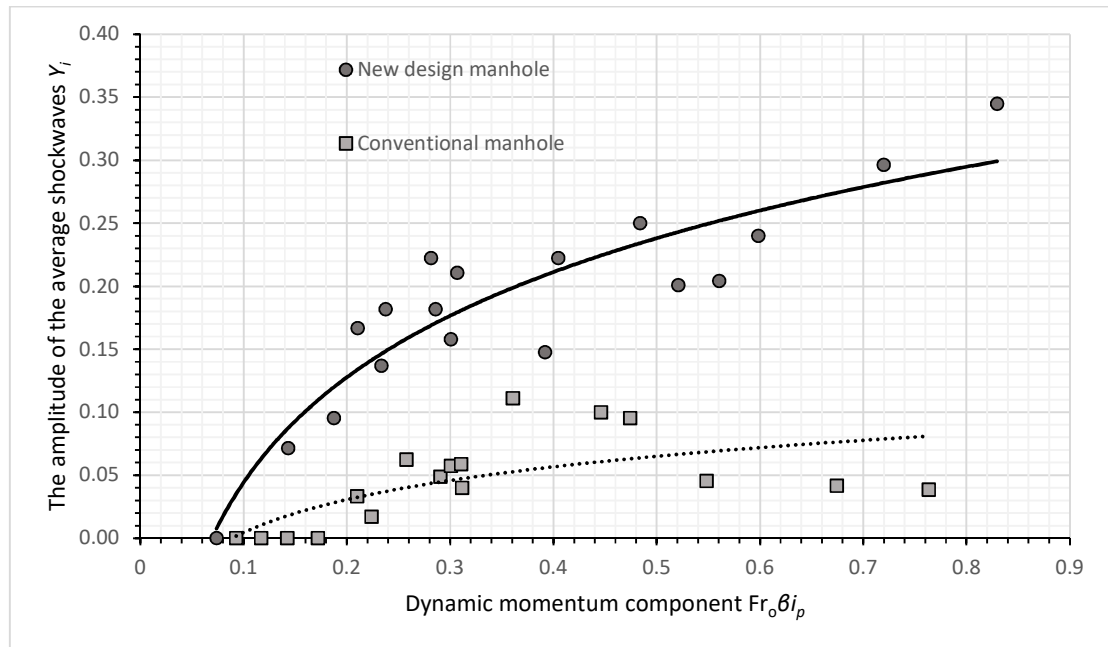


Figure 5.11 The amplitude of the average shockwaves ( $Y_i$ ) against the non-dimensional dynamic momentum component ( $Fr_o \beta i_p$ ) for both the conventional and the new manhole.

A high swing amplitude associated with the transitional flow in the new manhole, can cause damage to the manhole structure and decrease its hydraulic capacity, making it is an important design parameter. Shockwaves increased the flow depth beyond the shock front, the hydraulic jump resulting from the broken transitional or supercritical flow, this associated with a backwater effect and water hammer in the downstream portion of the sewer network. This phenomenon causes a decrease in discharge capacity which may result in geysering of storm water out of the manhole onto the street (Hager and Gissonni, 2005). In light of this, the experimental results were extended, using the physical model to test the amplitude of shockwaves when a breakdown occurs in the flow downstream of the model. The gate valve located downstream of the physical model, the valve



after the manhole, was used to disturb the flow and generate a backwater effect. The data generated provided a better understanding of manhole flow behaviour as well as testing the hydraulic integrity of the new manhole.

The surcharge ratio ( $\beta_{im}$ ) of the new manhole and the conventional manhole, can also be related to the amplitude of shockwaves at a fixed flow rate and for a variety of flow rates at transitional flow. Figure 5.12 illustrates the impact of the surcharge ratio ( $\beta_{im}$ ) on shockwave amplitude ( $Y_i$ ) for the new manhole. Maximum  $Y_i$  were observed at a low surcharge ratio for the transitional flow. The wave amplitudes decreased until close to zero (when the surface water level in the manhole was stable) with an increase in surcharge ratio ( $\beta_{im}$ ). The amplitude and swing of shockwaves are around zero when the surcharge ratio is approximately equal to the diameter of the manhole ( $D_m$ ) (surcharge ratio  $\beta_{im} = 1$ ). The reduction in shockwaves provides an acceptable safety feature, mitigating high hydrostatic pressure loads inside the manhole generated from the swing of the wave at a high surcharge ratio. However, this may create pressure flow conditions within the network. High value shockwave amplitudes inside the storm chamber of the new design at low surcharge levels, are associated with an increase in the retention time of the storm flow inside the storm chamber; this increases the capacity of the storm system and mitigates the load downstream of the sewer network, particularly in hilly regions. A higher retention time improves the hydraulic performance of the storm network and decreases the flooding risk downstream of the network. It can also decrease the depth of the drop manhole that is typically utilised in these areas.

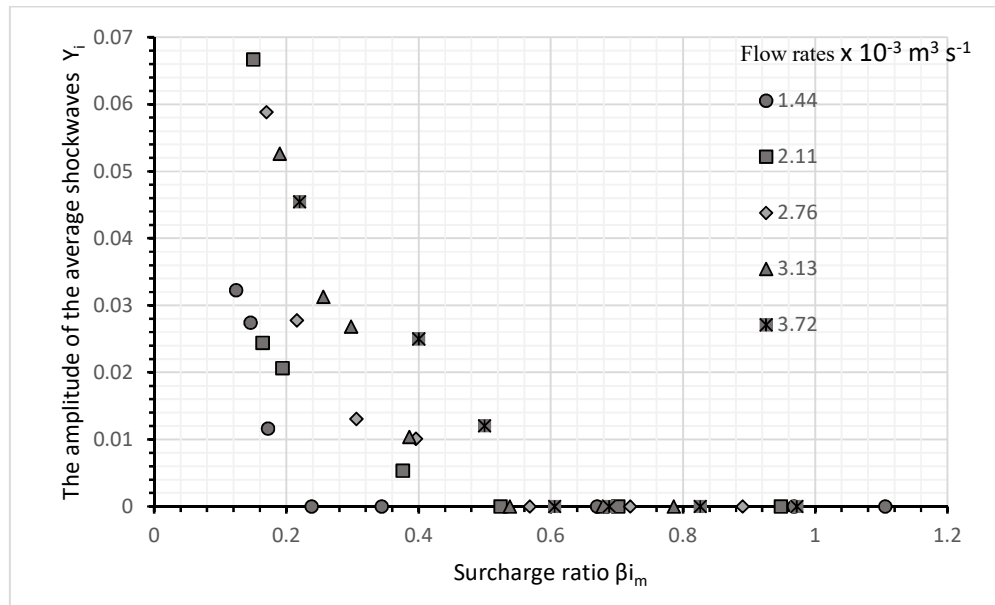


Figure 5.12 The wave amplitude ( $Y_i$ ) at different surcharge ratios ( $\beta_{im}$ ) for the flow in the new manhole at different flow rates.

### 5.2.2 CFD model

The accuracy of the output from CFD testing of the hydraulic performance of the manhole, has been explored by two researchers (Stovin et al, 2008), who discussed the approaches used to validate CFD against the hydraulic experimental results produced using a Particle Image Velocimetry (PIV) method. Their study employed a validation process using the longitudinal velocity. The results identified an approximate 50% of CFD output compared with the experimental results because CFD produces a temporal mean velocity whilst PIV produces a mean velocity at a specific time. Difficulties come from a multitude of factors such as boundary conditions (wall roughness, inlet and outlet conditions) and the flow pattern. Lau (2007) studied the impact of scaling methodologies on the mixing process and hydraulic properties of a conventional manhole using a physical scale

manhole. This study investigated head losses through the manhole, using experimental results to validate the CFD model, which was the same scale as the physical model. However, this study did not clearly illustrate the flow behaviour in the transition case using the CFD. Experimentally, a sharp change in the energy loss coefficient, between low and high surcharges, was noted for surcharge ratios of between 2.0 and 2.5. Coefficient values are reduced by half compared with the values in the pre-threshold region, yielding a coefficient value of around 0.45, after the transition region.

Therefore, using CFD tools for testing and developing a new manhole is a challenging task which requires validation using physical models. As such, CFD models were established for the new and conventional manholes using *SOLIDWORKS 2018*. The same dimensions and circumstances as in the laboratory model were used: the diameter of the inner manhole was 200 mm, the diameter of the outer manhole 500 mm for the new design and 500 mm for the conventional manhole. The diameters of the inlet and outlet pipes were 100 mm, the same length and layout as the physical model for both manholes. Inside the manholes, specific points on the inlet and outlet pipes at different levels, were selected to measure the velocity in the physical model and to illustrate the results of the CFD models of both manholes, as shown in Figure 5.13 a, b. Points 3 and 6 were used to measure the pressure in both manholes and in both models. Points 16 and 21 were used to measure the velocity at the centre of both manholes in both models. Point T was used to explore the turbulent velocities for the three axes and for both physical manholes.

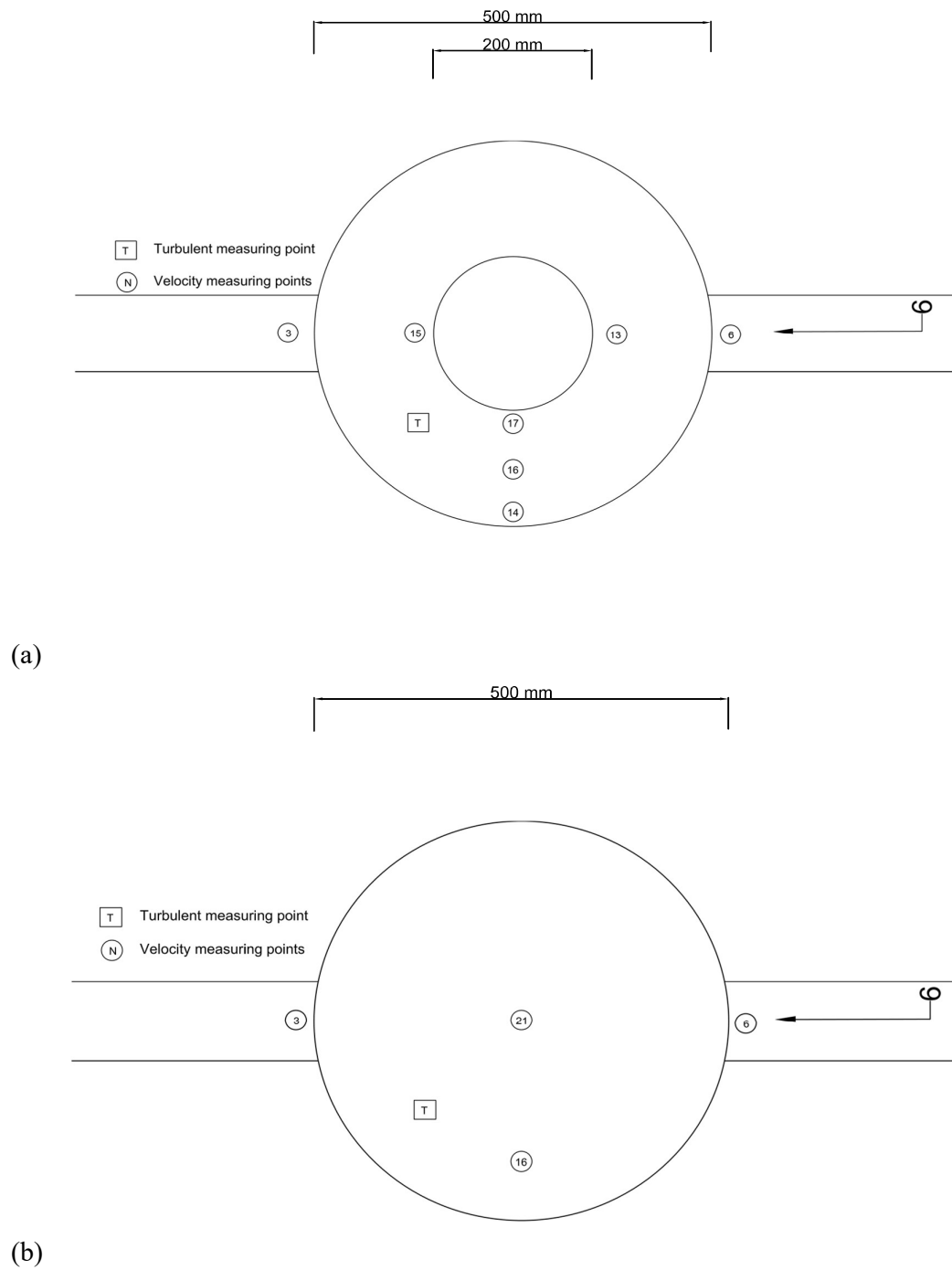


Figure 5.13 The location of points selected to produce the CFD results in (a) the new manhole, and (b) the conventional manhole.

The parameters used to setup the CFD model are listed in Table 5-2; water was used as a fluid and air as a gas, the same range of flowrates identified in the physical and CFD model  $0.5 - 6.5 \times 10^{-3} \text{ m}^3 \text{ s}^{-1}$ . Atmospheric pressure was used at the manhole covers and outlet pipes. The roughness of the Plexiglas walls for the pipes and manhole was  $4 \times 10^{-5} \text{ m}$ . The free surface tools and time independents, which have recently become available in *SOLIDWORKS 2018*, were used to simulate the interaction between the air and water. The model is supposed to fill with air so that the flow of water can be identified at the inlet pipe. Seventy-two points in the new manhole and eighty-two points in the conventional manhole, were selected as goals to produce the CFD results; these included points that were selected as measurement points for the physical models. Velocity, pressure, mass water friction and fluid turbulence were the parameters to be measured from the CFD models for both manholes. *SOLIDWORKS 2018* provides a significant improvement in flow simulation compared with older versions, allowing physical model parameters to be simulated using water and air, something that was difficult to achieve using older versions.

Table 5-2 Validated setup parameters for the CFD model.

Parameter	Setting/value
Fluid	Water and Air
Analysis type	Internal, Time-dependent
Flow type	Laminar and Turbulent
Wall condition	Roughness
Pressure	Environmental pressure
Boundary	Inlet the flow rate
Free surface	Yes
Turbulence model	k-ε
Gravity	Yes

Three parameters were selected for comparison between the CFD model and the physical model: velocity, pressure (as these two parameters were measured in both models) and the flow pattern (shockwaves), recorded for both manholes, under more or less the same circumstances. This process of validation of the CFD performance for the new manhole and conventional manhole, enables models to be developed to full scale to test the hydraulic performance of the manhole design under different circumstances and to highlight said differences in subsequent research.

#### 5.2.2.1 *Conventional manhole*

This research explored the dispersion of energy through both the conventional and new manhole. Velocities and pressures at the inlet, outlet and centre of the manholes (measuring points 3, 21 and 6) were selected as parameters to valid between the CFD and physical models. Figure 5.14 shows the velocities measured in both models at corresponding flow rates. The correlation between the CFD output and experimental results was 95%, this illustrating the change from free surface flow to pressurised flow at  $4.2 \text{ l s}^{-1}$ . Figure 5.15 details the differences in head pressures between the inlet and outlet manholes, the correlation between CFD and experimental model being 55%. There was a flocculation in pressure between the manhole inlet and the outlet at transitional flow  $3.5 \text{ l s}^{-1} - 4.5 \text{ l s}^{-1}$ . The results show a close match between the pressure value produced by the CFD and the physical model at corresponding flow rates, but the same was not found for velocity.

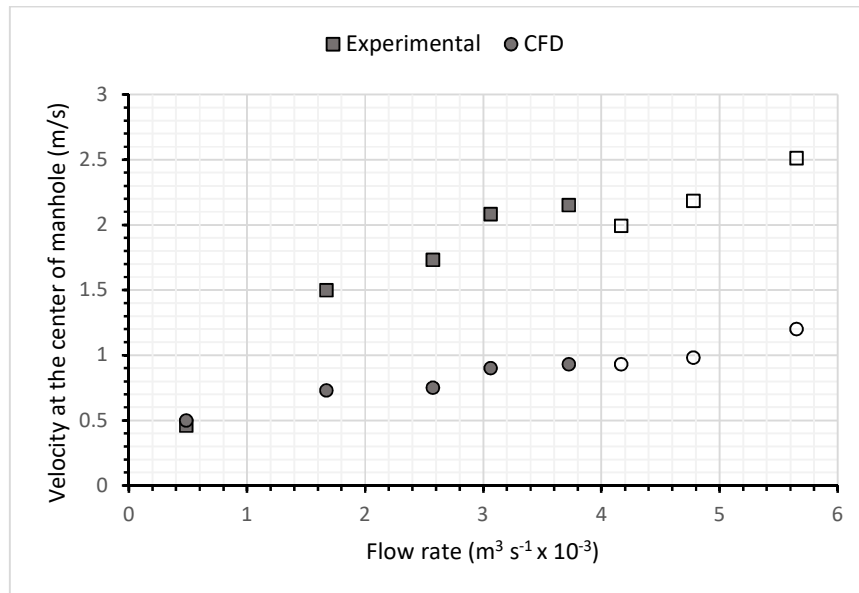


Figure 5.14 A comparison between the velocities measured at the centre of both the CFD and the physical model manholes.

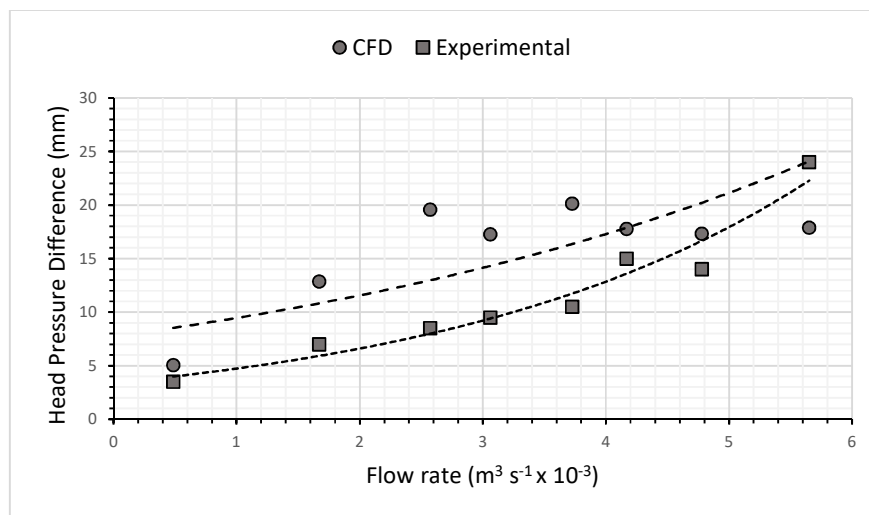
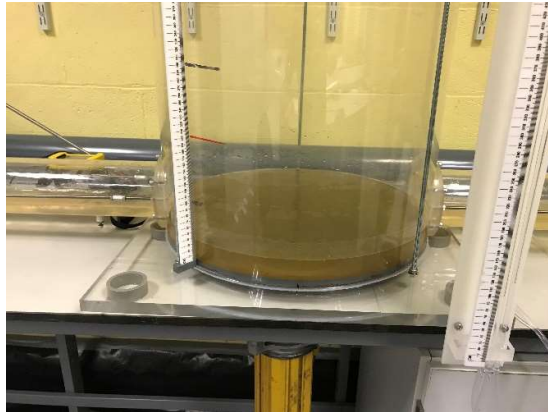


Figure 5.15 A comparison between the differences of head pressure measured at the inlet and outlet of manhole for both the CFD and the physical model.

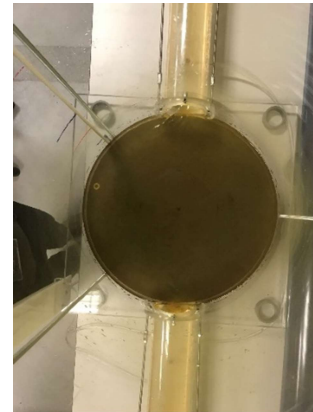
The pattern of flow for a conventional manhole described by Gargano and Hager (2002), as types of waves, was substantiated through testing the conventional manhole in this research using the physical model results and CFD simulation.

Figure 5.16 a, b, c, d and e illustrate the patterns of flow for 0.5, 1.5, 3, 4 and 5.5 l s<sup>-1</sup> flow rates. Photographs may not be a suitable medium to describe the pattern of flow, so the research includes supplementary videos for each flow rate showing the patterns of flow (Appendix I). The CFD model shows the same pattern of flow as that produced from the physical model, providing more detail and illustrating the swirl location and size for each corresponding flow rate as a result of choking waves. No significant shockwaves were recorded in either model for flowrate 0.5 l s<sup>-1</sup> to 1.5 l s<sup>-1</sup>, where the filling ratio ( $y_o$ ) was less than halfway up the pipe, in both models as seen in Figure 5.16 a for the physical model (photos I and II ) and CFD (top view VI). The first shockwave appeared when the flow ratio was more than halfway up the pipe ( $y_o \approx 0.6$ ), as seen in Figure 5.16 b. This shockwave expanded at the manhole outlet and manhole inlet and is obvious for the filling ratio range  $0.6 < y_o < 1$ , where the flowrate ranged between 1.5 l s<sup>-1</sup> and 4 l s<sup>-1</sup>. Figure 5.16 c and e illustrate the expansion of the shockwave with corresponding flowrate consequences. The swing phenomenon was observed for shockwaves inside the manhole when the filling ratio was  $y_o > 0.85$ . The shockwave pattern changed significantly when the flow changed from free surface flow to pressurised flow  $y_o > 0.85$  at flow rates over 4 l s<sup>-1</sup>. Figure 5.16 a, b and c (III) show that the size of the diffusion region was larger near the outlet manhole when the flow was small and the swirl effects were located at both sides of the jet zone at the centre of the manhole; the swirl zone extended to join the inlet flow at the manhole inlet. The shape of the jet flow changed when the flow rate increased, affected by the backwater flow from choking, while the centre of the swirl zone shifted from the centre of the manhole to the zone towards the inlet pipe (Figure 5.16 d and e (III)).

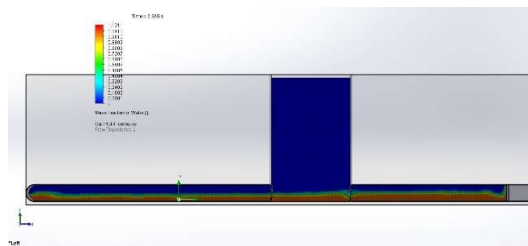




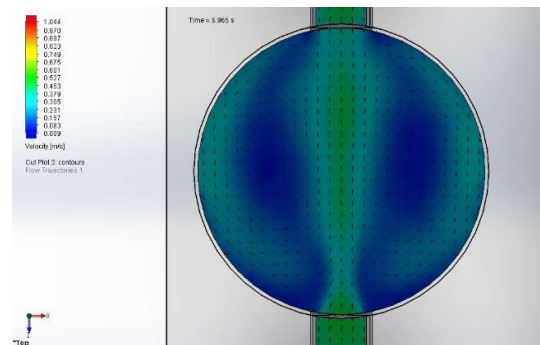
I



II



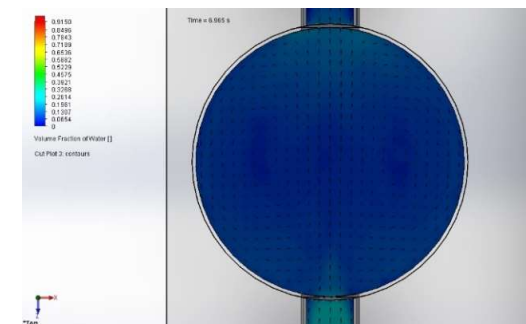
III



IV

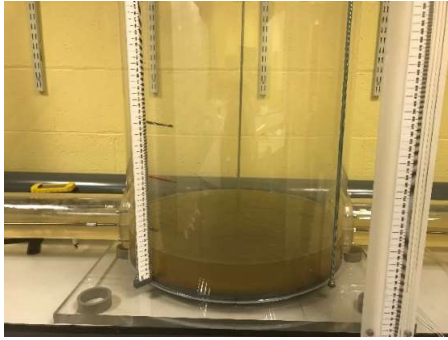


V

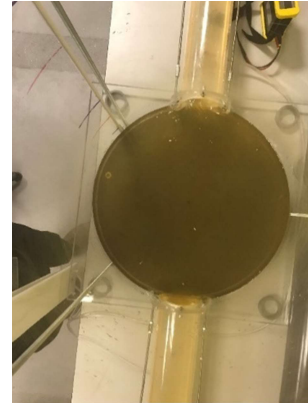


VI

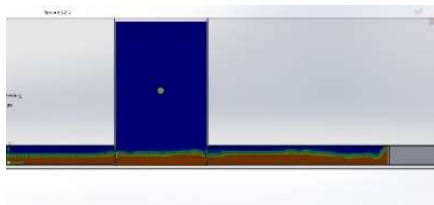
(a)  $0.5 \times 10^{-3} \text{ m}^3 \text{ s}^{-1}$



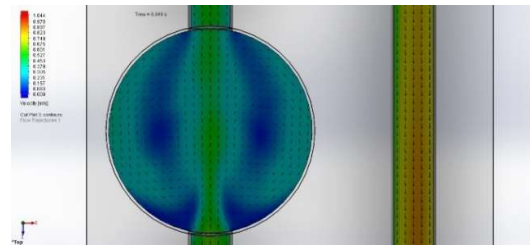
I



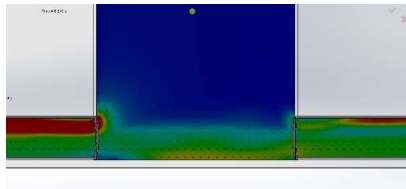
II



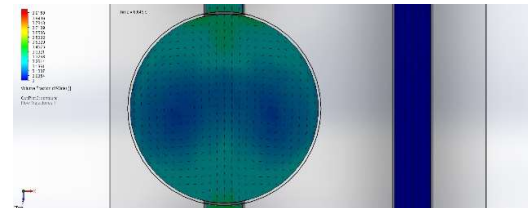
III



IV



V



VI

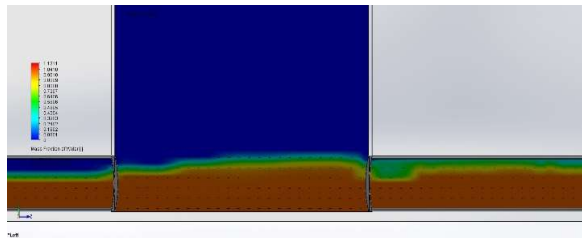
(b)  $1.5 \times 10^{-3} \text{ m}^3 \text{ s}^{-1}$



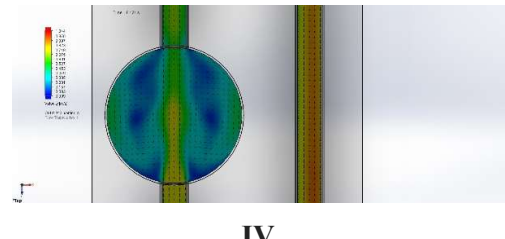
I



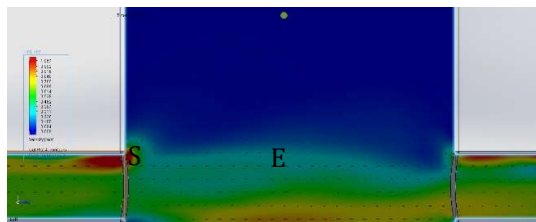
II



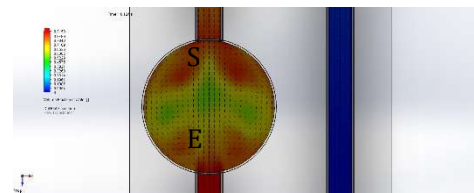
III



IV

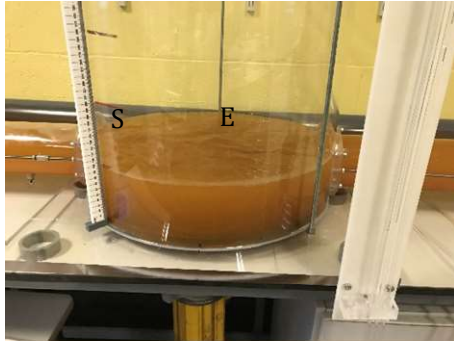


V



VI

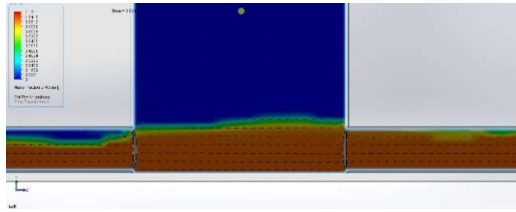
(c)  $3 \times 10^{-3} \text{ m}^3 \text{ s}^{-1}$



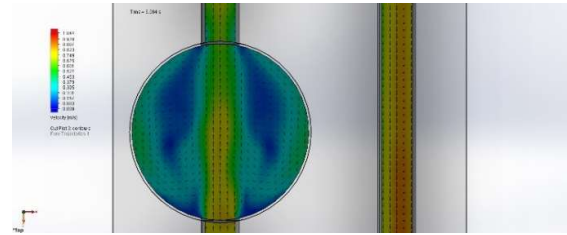
I



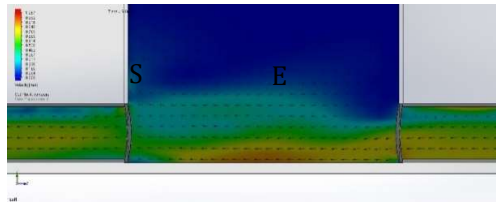
II



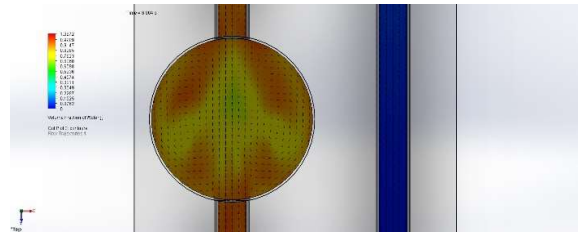
III



IV

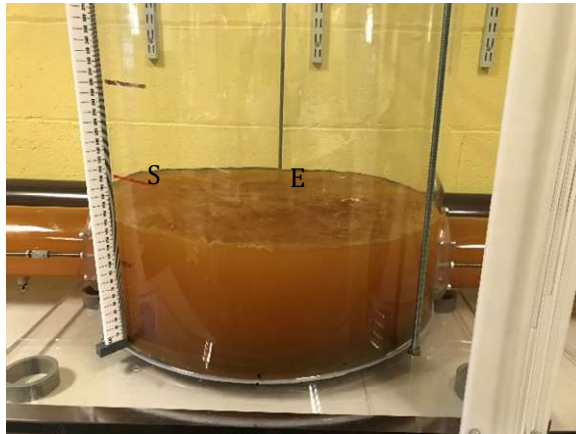


V



VI

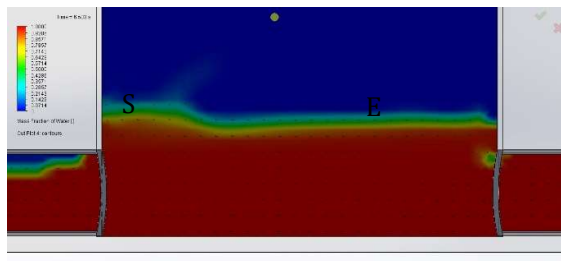
(d)  $4 \times 10^{-3} \text{ m}^3 \text{ s}^{-1}$



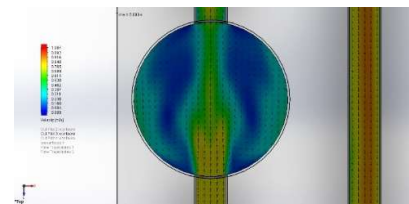
I



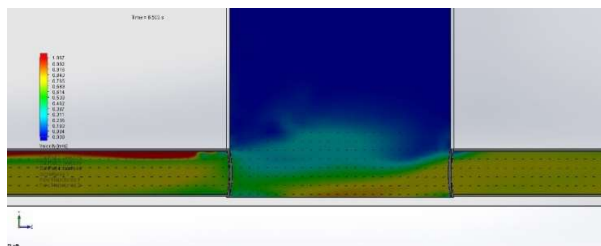
II



III



IV



V

(e)  $5.5 \times 10^{-3} \text{ m}^3 \text{ s}^{-1}$

Figure 5.16 The pattern of flow in the conventional manhole at different flow rates.

The amplitude of the shockwaves inside the conventional manhole was qualified using the shockwave velocity in the flow direction (x-axis) as an indicator, this extracted from the results of the Doppler apparatus. Figure 5.17 shows the range of amplitude for different flow rates for the transitional flow ( $y_o > 0.5$ ) through the conventional manhole. The strength of swing increased gradually with a filling ratio of  $0.5 < y_o < 0.85$ , this increasing rapidly for filling ratio  $0.85 < y_o < 1$ . The strength tended to be constant at high intensity under full flow ( $\beta_{ip} > 1$ ).

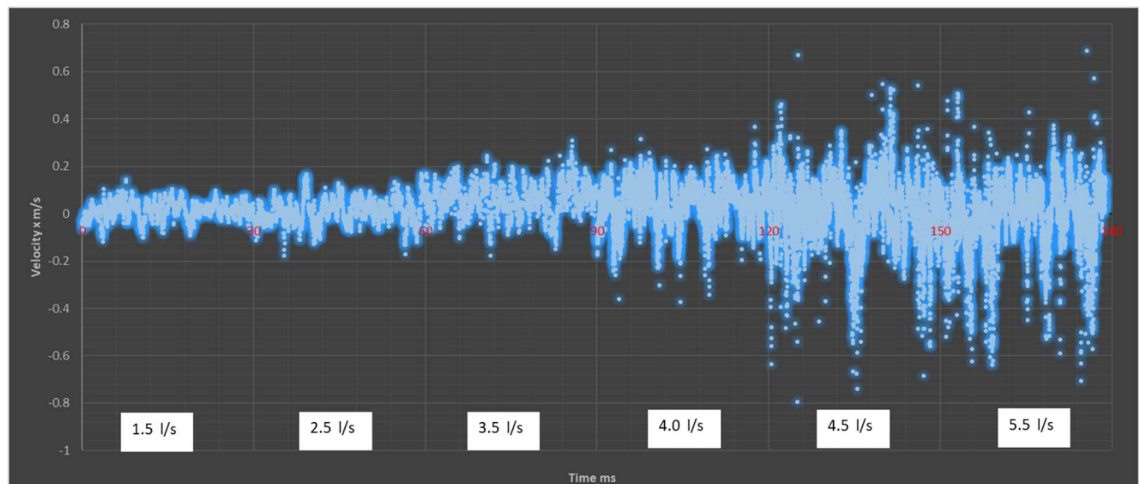


Figure 5.17 Turbulent amplitude in the conventional manhole at different flow rates using the velocity in x direction as indicator.

#### 5.2.2.2 New manhole design

The shape of the storm chamber in the new manhole generates a new flow pattern and hydraulic properties. Observations of the flow pattern in the new manhole using the physical model, show that it is different from the flow pattern in the conventional manhole at transitional and supercritical flows. The jet of flow at the manhole entrance impinges on the inner wall, generating shockwave A. The inlet jet splits into two new small jets, which flow towards the external wall and

impinge on the external wall at both sides of the manhole, generating shockwave B. Shockwave C at the outlet manhole, is generated by the choking flow, impinging on the arc-shaped sides and the top wall, this causing a so-called swell wave and choking; it is same as shockwave S in a conventional manhole (Hager and Gissoni, 2005). The reaction of shockwaves B and C, generate shockwave b when the flow impinges on the internal wall surface. The generation of these shockwaves is related to the filling ratio ( $\beta_{ip} = y_o = h_o/D_p$ ) and Fr (Gargano and Hager, 2002).

Investigations into the dispersion of energy through the new manhole, using measurements of velocity and pressure at the inlet manhole, outlet manhole and the centre of one bend of the manhole (measuring points 3, 16 and 6), were conducted in the physical model for different flow rates. These points are used to illustrate the CFD model's output under the same range of flow rates. Figure 5.18 shows the velocities measured in physical and CFD models at a corresponding flow rate. The correlation between the CFD output and experimental results was 87%, illustrating a good match between results for the filling ratio  $< 0.85$  (the flow rate below  $3 \times 10^{-3} \text{ m}^3 \text{ s}^{-1}$ ). The change from free surface flow to pressurised flow at a flow rate over  $3 \times 10^{-3} \text{ m}^3 \text{ s}^{-1}$ , produces a small variation between the two models. Figure 5.19 illustrates the differences in head pressures between the inlet manhole and outlet manhole for the new design, the correlation between CFD and experimental model reaching 72%. The results for flows  $3.5 \times 10^{-3} \text{ m}^3 \text{ s}^{-1}$  and  $4.5 \times 10^{-3} \text{ m}^3 \text{ s}^{-1}$  had the same fluctuation in pressure as seen in the conventional manhole, between manhole inlet and outlet at transitional flow. This result shows the need for more research to explore the performance of CFD to simulate the transitional flow in both manholes.



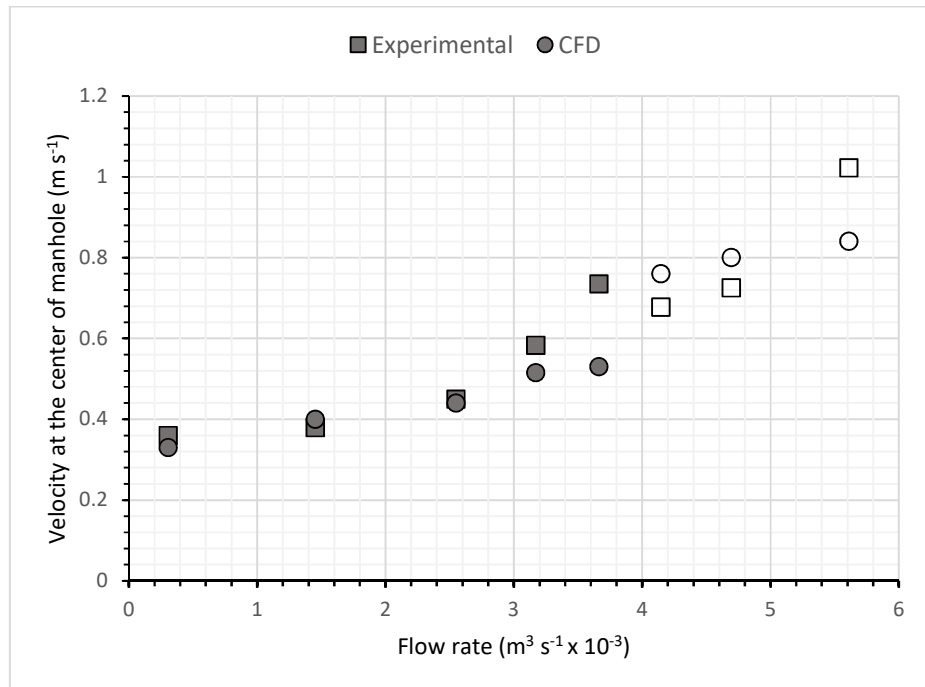


Figure 5.18 A comparison between the velocities measured at the centre of the new manhole for both the CFD and physical model.

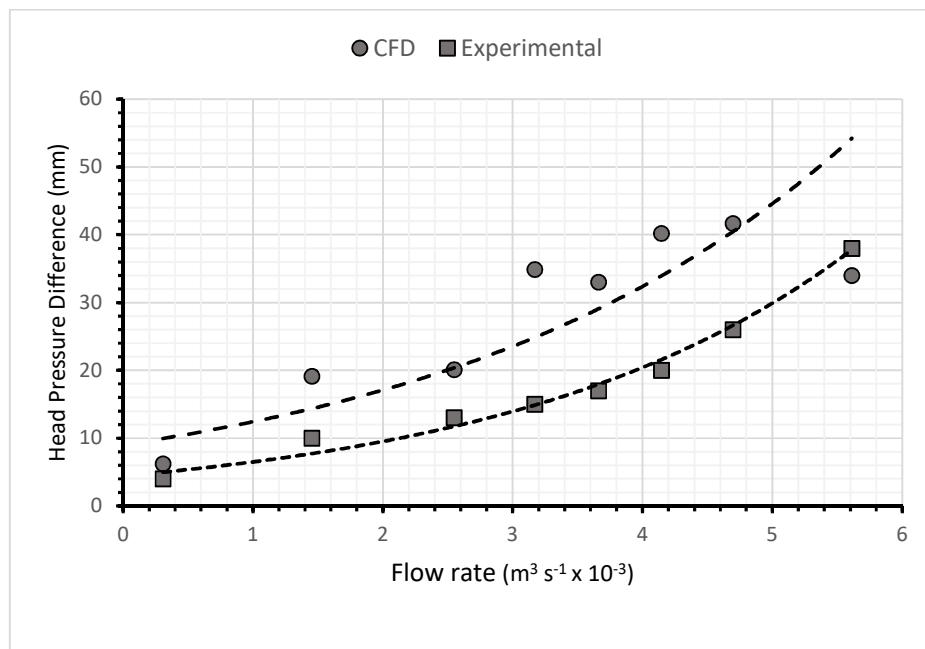
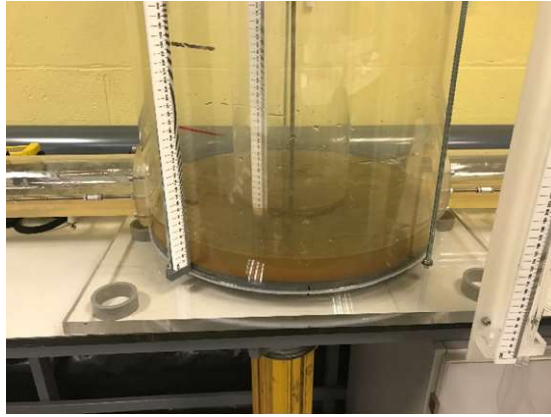


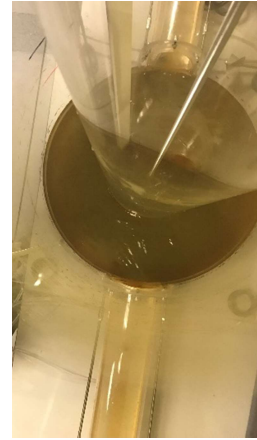
Figure 5.19 A comparison between the differences in head pressure measured at the inlet and outlet of the new manhole for both the CFD and physical model.



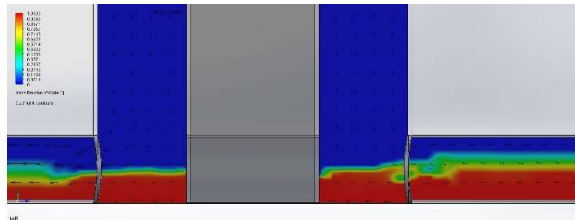
The shockwaves generated in the new manhole were observed under the same rate of flow as that used for the conventional manhole. A significant change in the design and the flow paths of stormwater inside the new manhole created a new pattern of shockwaves; Figure 5.20 a, b, c, d and e present the correspondence between the physical model production and simulation of the flow pattern produced by the CFD for each flow rate. The area of swell and swirling results from the choking wave was smaller than that seen in the conventional manhole. Six swirling zones were observed in the new manhole located at both sides of the manhole between the inner manhole wall and both the central and outlet manholes, while small effects of swirling extended to the manhole entrance. The area of swirling decreased with an increase in flow rate. The surcharge ratio represented by the depth of water in the manhole as illustrated in Figure 5.20 a, b, c, d, shows a good match between the level of water mass generated by the CFD and the level of water surface recorded in the physical model for corresponding flow rates. Figure 5.20 a shows there is no significant shockwave noted for the filling ratio  $y_o < 0.5$  in either model; CFD shows a disruption in flow at the beginning of the outlet pipe as an effect of the interaction of air and flow of water. The first shockwave (A), seen in both models, was at flow  $1.5 \times 10^{-3} \text{ m}^3 \text{ s}^{-1}$  ( $y_o \approx 0.6$ ), as seen in Figure 5.20 b. The other shockwaves (B and C), were clearly measured at a flowrate of over  $1.5 \times 10^{-3} \text{ m}^3 \text{ s}^{-1}$ ; Figure 5.20 c shows these shockwaves in both the CFD and the physical model at a  $3 \times 10^{-3} \text{ m}^3 \text{ s}^{-1}$  flow rate. At a high flow rate, over  $3 \text{ l s}^{-1}$ , these shockwaves interact and generate significant turbulence for the flow. Figure 5.20 d shows this turbulence and mixing in both models, the physical model and CFD model, which makes it difficult to determine a specific zone for each shockwave.



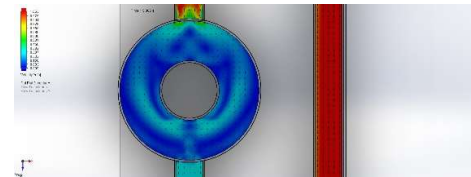
I



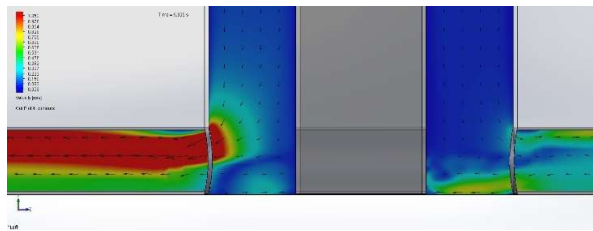
II



III

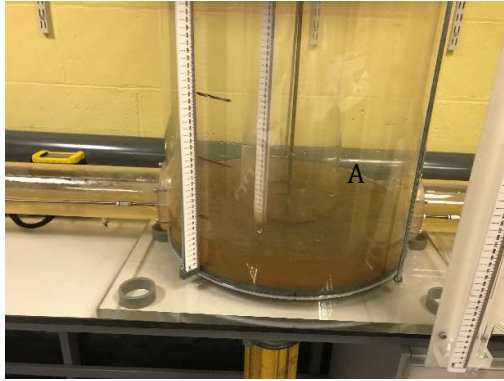


IV



V

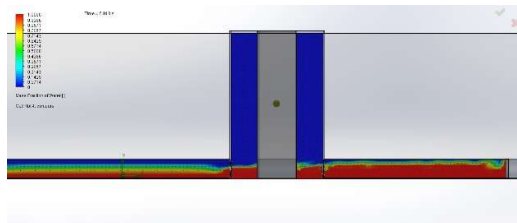
(a)  $0.5 \times 10^{-3} \text{ m}^3 \text{ s}^{-1}$



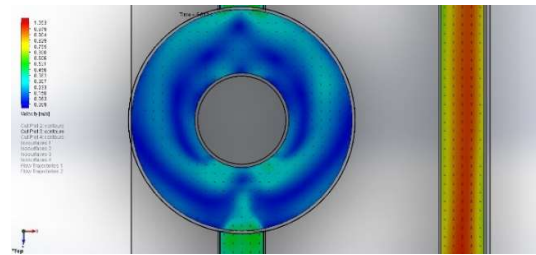
I



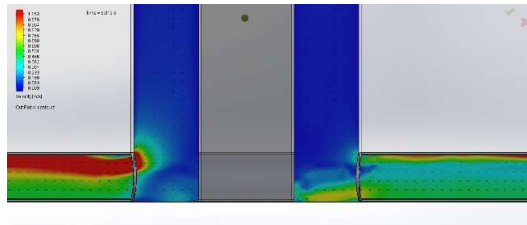
II



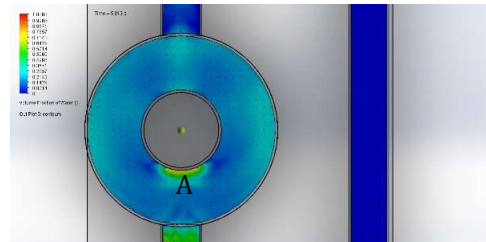
III



IV

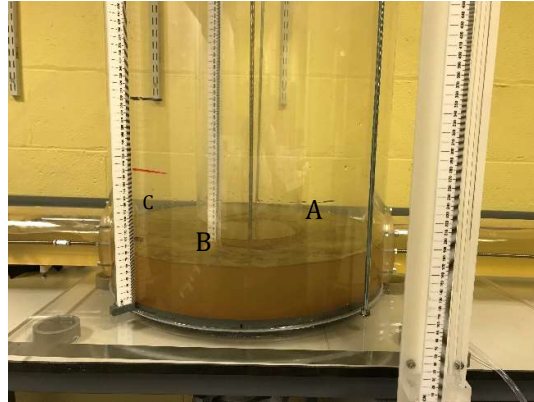


V

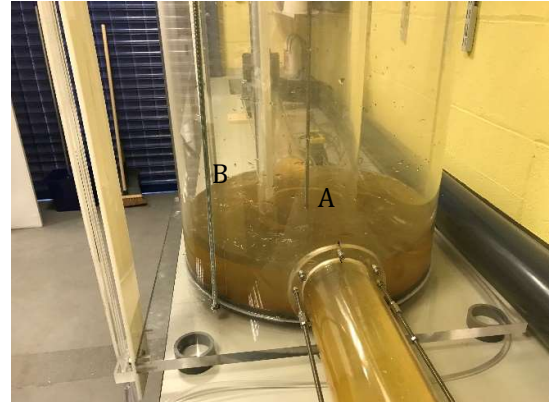


VI

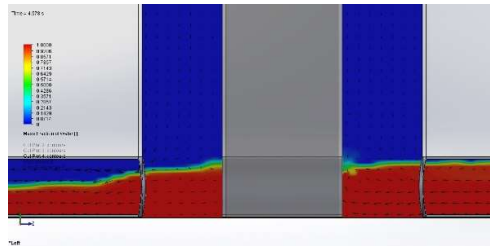
(b)  $1.5 \times 10^{-3} \text{ m}^3 \text{ s}^{-1}$



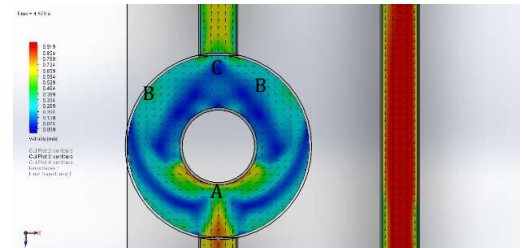
I



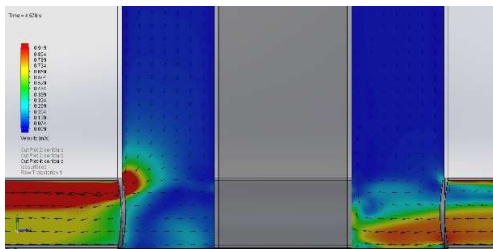
II



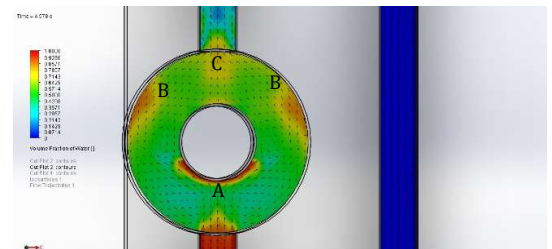
III



IV

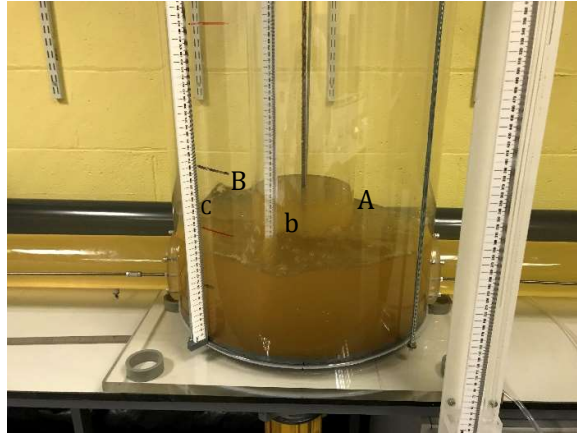


V

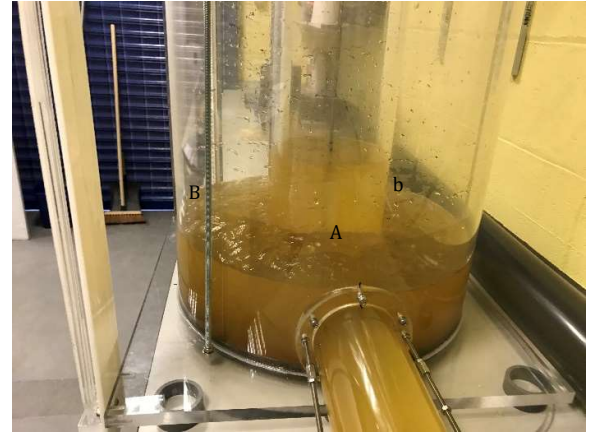


VI

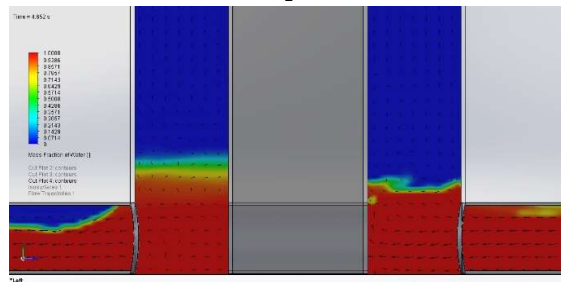
(c)  $3 \times 10^{-3} \text{ m}^3 \text{ s}^{-1}$



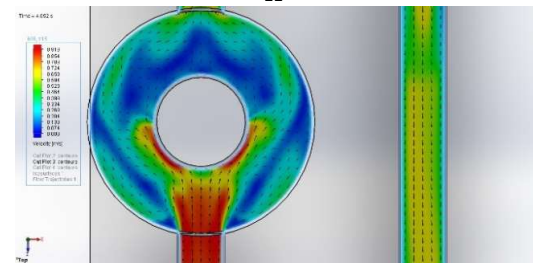
I



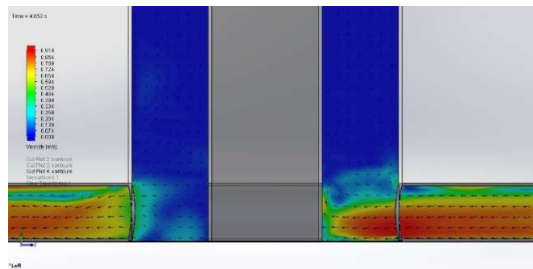
II



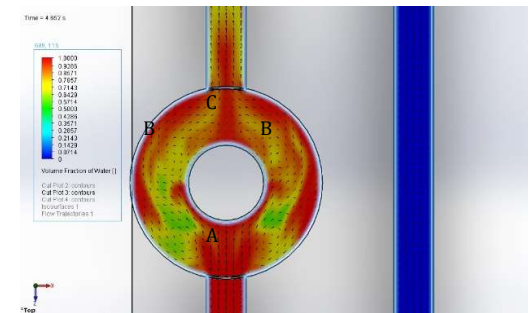
III



IV



V



VI

(d)  $5.5 \times 10^{-3} \text{ m}^3 \text{ s}^{-1}$

Figure 5.20 The pattern of flow in the new manhole at different flow rates.

The three shockwaves and choking gathered to generate a significant swing wave at a filling ratio ( $\gamma_o > 0.6$ ) in the new manhole compared to the swing generated in the conventional manhole.



Figure 5.21 shows the intensity of the swing using the velocity in the flow direction as an indicator; the strength of the swing increased rapidly when the flow rate was over  $1.5 \text{ l s}^{-1}$ . The intensity of amplitude increased gradually and slowly when the flow rate subsequently increased. The change in flow rate from free surface to pressurised flow (the flow rate between  $4 \text{ l s}^{-1}$  and  $4.5 \text{ l s}^{-1}$ ), resulted in a substantial change in the intensity of the shockwaves. There was no big increase in strength of swing for a filling ratio  $> 1$ , but it was larger than that measured in the conventional manhole.

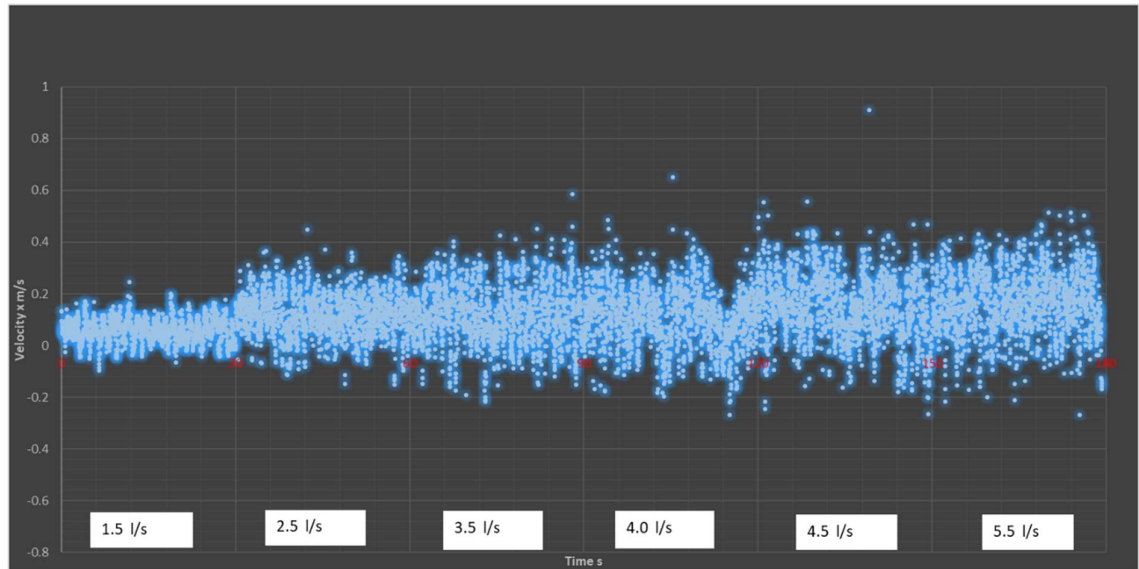


Figure 5.21 Turbulent amplitude in the new manhole design at different flow rates using the velocity in x direction as the indicator.

The swing waves generated by the four shockwaves, were used to express the characteristics of the average flow wave inside the storm chamber of the new manhole. The relatively high amplitude shockwaves  $Y_i = (h_i - h_o) / h_o$ , which varied with the non-dimensional Reynolds number ( $Re$ ), were used to quantify the shockwaves pattern. Figure 5.22 illustrates the  $Y_i - Re$  relationship for both the

conventional and the new manhole. High amplitude shockwaves were generated in the new manhole when flow transferred from a subcritical to transitional flow, increasing rapidly when the flow changed from a free surface to pressurised flow. The conventional manhole had shockwaves of lower amplitude and this was clearly observed at transitional flow ( $Re > 30000$ ). When the flow changed from free surface to pressurised ( $50000 < Re < 70000$ ), the amplitude increased rapidly and tended to settle down when the flow was pressurized ( $Re > 70000$ ). These relationships were quantified for both manholes using Equation 5-7 for the new manhole and Equation 5-8 for the conventional manhole (Appendix IV).

$$Y_{i(ND)} = 0.071 \ln(Re) - 0.66 \quad \text{Equation 5-7}$$

$$Y_{i(o)} = 0.074 \ln(Re) - 0.73 \quad \text{Equation 5-8}$$

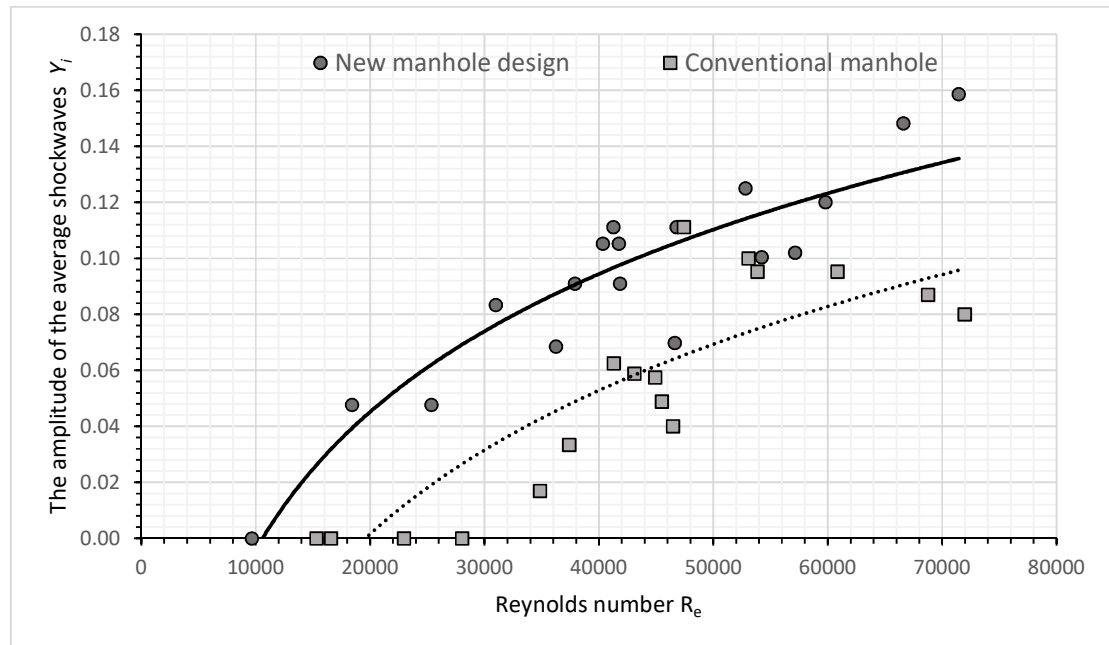


Figure 5.22 The amplitude of the average shockwaves ( $Y_i$ ) against non-dimensional Reynolds number ( $Re$ ) for both the conventional and new manhole.

### 5.3 Summary

This chapter has explored the hydraulic performance of the new manhole. The new shape of the manhole generates a new flow pattern for stormwater. It is, therefore, important to understand the hydraulic properties of sewer systems using the newly designed storm water manhole chamber. A physical model was employed in order to carry out a systematic investigation to explore the flow characteristics of the manhole under subcritical and transitional flow conditions. Experimental works were conducted to explore and quantify the hydraulic properties of the new manhole, comparing these with a conventional manhole. The head loss coefficient and pattern of shockwaves were studied for both manholes, under the same circumstances, using independent dimensionless parameters for each manhole: ratio of surcharge ( $\beta_{im}$ ), approach flow Froude numbers ( $Fr_o$ ), and filling ratios ( $\beta_{ip}$ ). The new manhole generates higher head losses, about twice the head loss as that generated in a conventional manhole, at low  $\beta_{im}$ . The head loss of both manholes tends to be stable and maintains a lower constant value when the flow transitions from free surface to pressurized flow (at high  $\beta_{im}$ ). Four shockwaves were identified in the storm chamber of the new manhole: (1) A results from impingement of the direct flow in the inlet pipe on the inner manhole wall; (2) B and b were generated from a change in flow direction caused by two bends in the storm chamber, and (4) C was generated from flow choking at the outlet manhole. The locations of these shockwaves were determined, and the average amplitude of swing generated from the combined effects of these shockwaves. These were quantified with the non-dimensional dynamic moment  $Fr_o\beta_{ip}$ , showing a significant increase in amplitude in the



shockwaves in the new manhole. Hydraulic integrity, tested by breaking up the flow downstream of the model, revealed that the amplitude and swing of the shockwaves decreased with an increase in surcharge ratio ( $\beta_{im}$ ), demonstrating that the new manhole design is safe in terms of structural damage and associated risks from geysering.

This chapter also reported on an experimental hydraulic study to validate the computational fluid dynamics (CFD) model of the geometry of the new manhole. Velocity, pressure and shockwaves were selected to conduct the validation between the CFD model and the physical model. The validation process confirmed that CFD tools are appropriate to use to simulate the hydraulic properties of complicated flows such as the flow through the manhole. Correlations between the CFD output and experimental results, ranged between 0.55 and 0.95, with appropriate matching in most cases of flow. The size and areas of swirling were determined for both manholes, measured as two for the conventional manhole, generated at the centre and shaft towards the manhole inlet when the flow rate increased, and six for the new manhole; two at the inlet, two at the centre and two at the outlet.

The results reveal that CFD is an appropriate method to simulate the flow through a manhole, matching experimental output. The validated CFD model can be used with confidence to improve manhole design and test it under different circumstances.

Approving the hydraulic integrity of the manhole lead to the testing of the new positions for buried pipes; one over each other in one trench.

## CHAPTER 6

### **BURIED PIPE MODELLING**

This chapter discusses the structural performance of flexible pipes buried in a trench. It compares the conventional method of installation of a separate sewer system when one pipe is in each trench, to the new method of installation where two pipes are set in one trench, one on top of the other. Physical models were used to test the behaviour of the buried pipes in both installations. The experimental results were then used to validate the FE model of the physical model. The validated FE model was consequently upgraded to a full-scale model to test the structural integrity of the new installation method, compared to the traditional method. The traditional empirical formula (Iowa formula), which is normally used to estimate the deflection of one buried pipe when exposed to traffic loads, was developed through this research to be used to calculate the deflection of two buried flexible pipes in one trench.

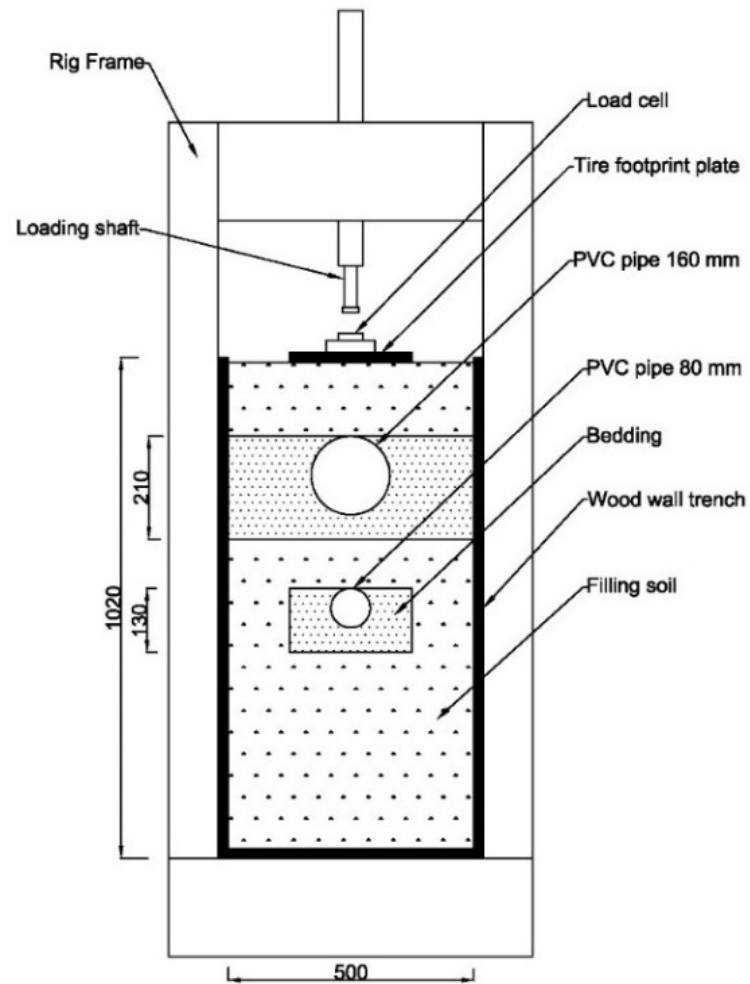
#### **6.1 The Physical Model**

Because there is a lack of field data concerning the configuration of one-over-one pipes installed in one trench, it was essential to build a physical model in the laboratory to carry out the tests required to identify the mechanical properties and boundary condition parameters for the system under applied loading. As such, a physical model was built in the laboratory to test the performance of two PVC pipes of 80 mm and 160 mm diameter.

A wooden trench configured in a hydraulic steel rig, was used to lay the two PVC pipes with the large pipe at the top and the small pipe at the bottom. The physical model had dimensions of  $2.5 \times 0.5 \times 1 \text{ m}^3$  and was embedded in the hydraulic rig which was used to provide lateral support for the trench walls and to apply live loads. The maximum capacity of the rig was 10 tons. Normal composite soil, corresponding to the soil used within the UK to embed sewer systems, was used to bury the pipe system. The properties of this soil was presented in Chapter 3. Filling soil was added in 5-10 cm thick layers to achieve the required compaction degree. The bedding layer was used to nestle the two pipes, a 160 mm diameter PVC pipe representing the storm pipe, and an 80 mm pipe used as a sanitary pipe (DEFRA, 2011). GFRA-3-70 strain gauges, which are appropriate to measure the strain of plastic material (TML, 2017), were fixed on the surfaces of the pipes to monitor the strain resulting from the filling soil and the compaction process. Steel beams were attached to the top and bottom of the pipes using screws. These beams were housed in a plastic tube to allow them to move freely when buried in the soil and reflect deformation at both the top and bottom of the pipe. Linear vertical displacement transducers (LVDTs, Micro-Measurements HS 50) were positioned at the top of the beam(s) to measure beam movement, reflecting deformation at the top and bottom of the pipe.

Two sets of LVDTs were used for each pipe, on two sides, approximately 30 cm from the centre where the live load was applied. The strain gauges and LVDTs were connected to a P3 Strain Indicator and Recorder to continuously record the strain gauge motion caused by the filling and compaction process, in addition to the pipe deflections from the LVDTs when the live load was applied. A steel plate with dimensions  $0.5 \times 0.25 \text{ m}^2$  was used to simulate a truck tyre footprint (Kang et

al, 2013b) using a compression load cell located between the hydraulic load arm and the tyre footprint to synchronize the applied load with the measured displacement. Figure 6.1 a, b and c show the configuration of the physical model.



(a)



c

Figure 6.1 The physical model setup (a) setup of the trench in the hydraulic rig to test the performance of the buried structural pipes, (b) Cross section of the configuration of the physical model in the laboratory, equipped with measurement and recording devices and (c) The physical model in the lab.

A sewer system is normally laid under 1 to 6 m of soil. Critical loads, including traffic loads, occur during the installation stage, the maximum influence of live loads corresponding to the minimum soil cover (Kang et al, 2013a; Kang et al, 2013b; Talesnick and Frydman, 2018).

The wheel load was simulated by applying a hydraulic load on the steel plate in the physical model. The same series of loads applied to the physical model in the laboratory, were also applied in the FE model. The categories of traffic loads from AASHTO as shown in Table 2.4 (ASTM-C890, 2006), were used as the series of applied loads in both the physical model and the FE models. The pyramid method was used to calculate the distribution of pressure from the load of tyre footprints on the pipe surface, taking into consideration the conditions and dimensions of the physical trench.

Two configurations for setting pipes were tested in the physical model. The first corresponded to the conventional approach with one pipe in the trench. An 80 mm sanitary pipe was laid under 40 cm of cover soil. A bedding layer was used to accommodate the pipe, according to HM-Government (2010) standards. The second test configuration involved locating the sanitary pipe in the same position and laying the storm pipe on top. Pipe strain was measured through applying each layer of soil in both cases; when the sanitary pipe was independent and when it was positioned near the storm pipe. The results presented in Figure 6.2 show a fluctuation in pipe deformation associated with compaction. There was no significant change in the strain to which the sanitary pipe was exposed. In both cases, the displacement was between 0.3 and 0.4 mm. The additional load comes from adding the storm pipe bedding layer, which has a higher density than the

filling soil which had been removed. This load was balanced by the decreased load resulting from adding the storm pipe at the top and replacing the filling soil. This case was tested when the pipe was empty; however, water flow can add a supplementary load (classified as a live load).

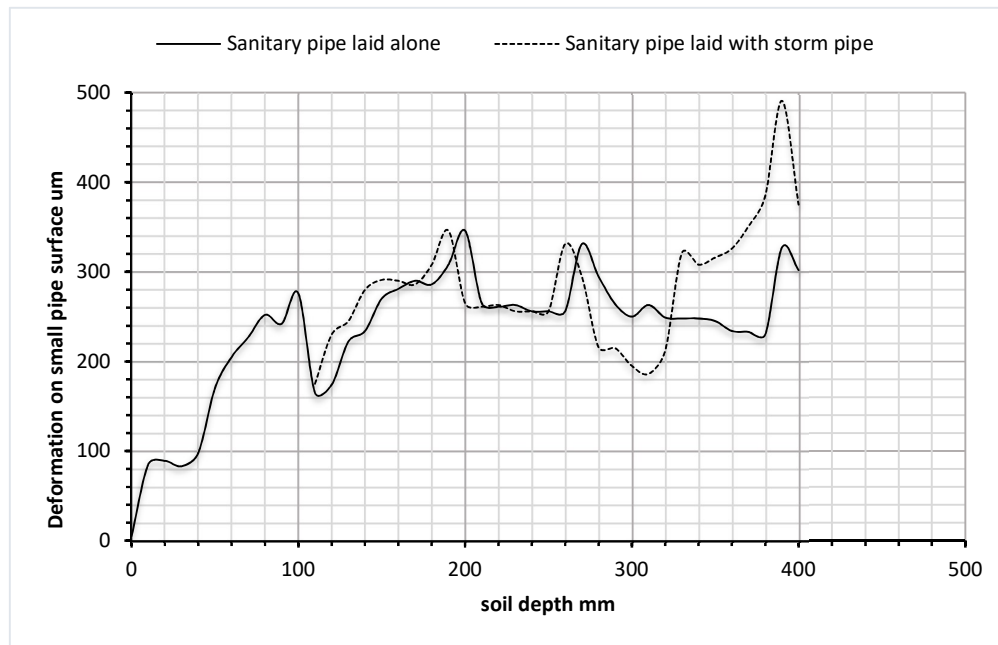
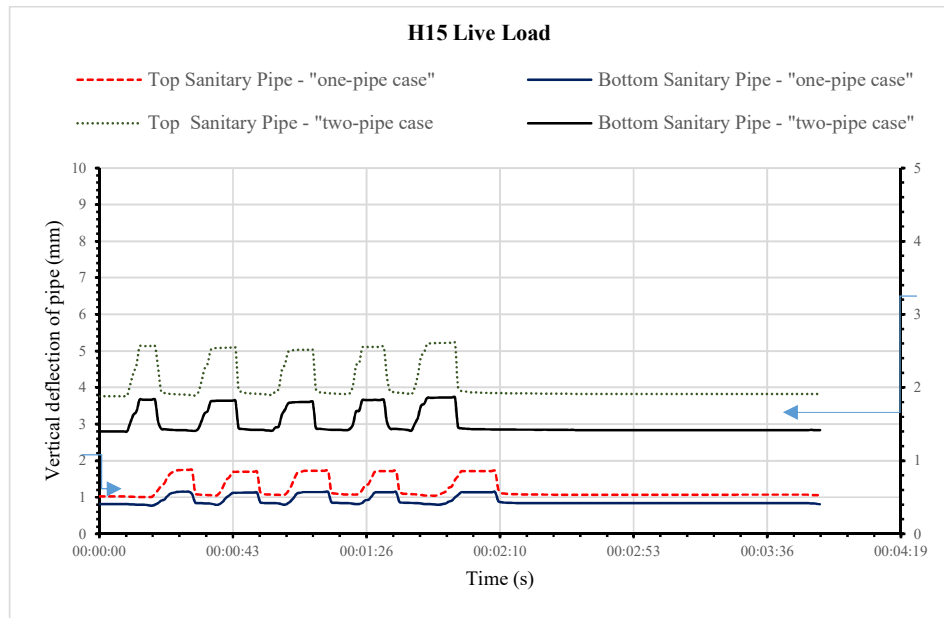
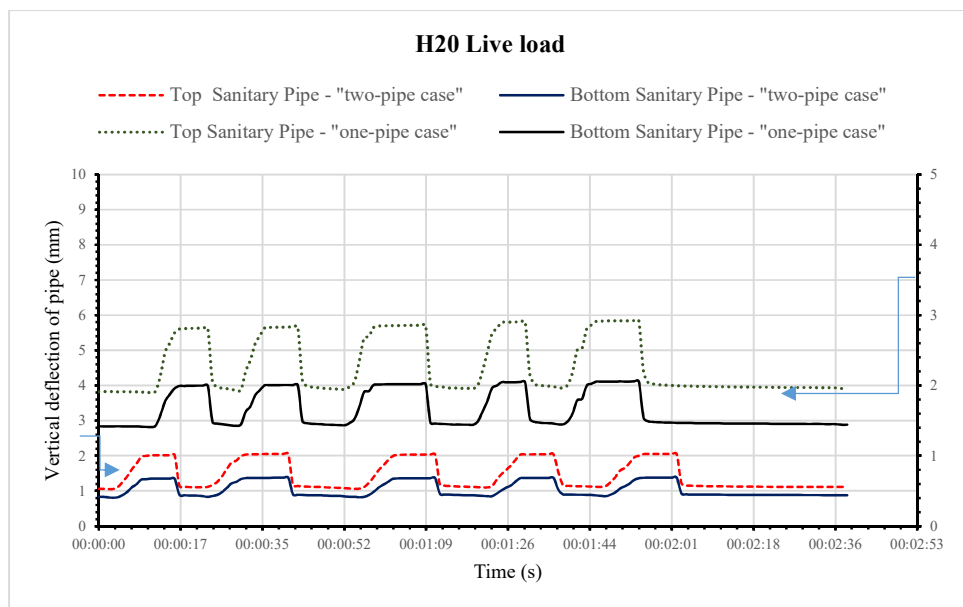


Figure 6.2 Strain on the small (sanitary) pipe during the soil-filling and compaction processes.

Transducers were used to measure the deformation of both pipes under a series of applied live loads. Sanitary pipe deformations are presented for both cases; when sanitary pipe is laid alone in the trench and when the storm pipe is laid above it. The results presented in Figure 6.3 a, b and c show the behaviour of the sanitary pipe under applied live loads of H15, H20 and H25.

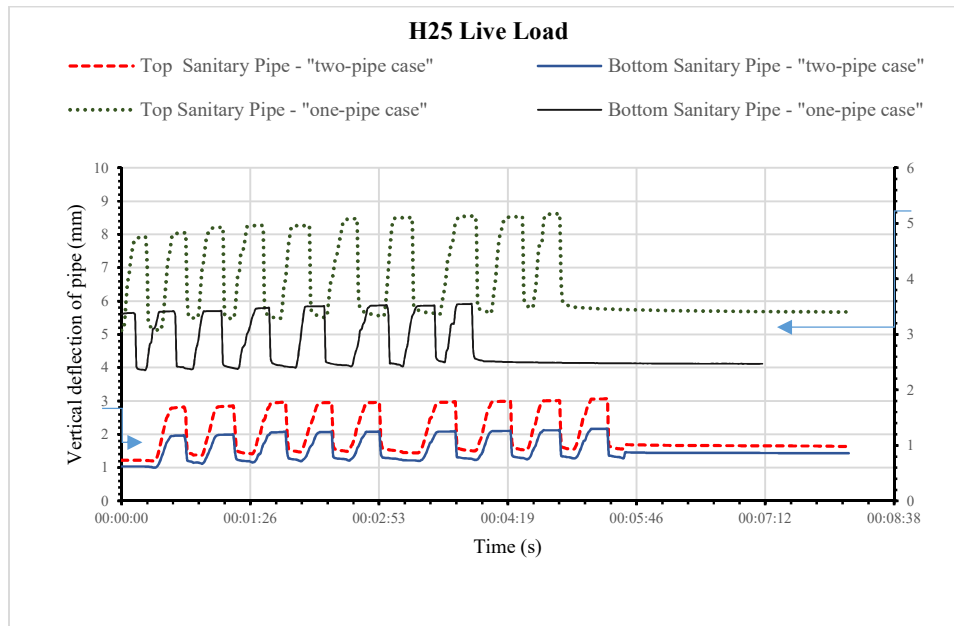


(a)



(b)





(c)

Figure 6.3 Comparison of the deflection of the small (sanitary) pipe when set alone in the trench with that when set below a storm pipe under a series of applied live loads (a) H15, (b) H20 and (c) H25.

The results from testing the buried sanitary pipe, indicate a reduction in pipe displacement when changing from a pipe lying alone in the trench to one lying below a storm pipe. The displacement of the top sanitary pipe was 2.6 mm when alone and 1.9 mm when laid below the storm pipe, under an H15 load. The displacement was 2.92 mm when laid alone and 2.1 mm when laid below the storm pipe at H20, and 5.1 mm when laid alone and 3 mm when laid below the storm pipe at H25. These physical model experimental results were used to validate the FE model using the same dimensions, objects, boundary conditions and material properties. The validation process was necessary to increase confidence when transitioning from the FE model to a real-scale model (Moser and Folkman, 2008).

## 6.2 FE Model

Two 3D, FE models were created using ABAQUS 2017 to simulate the new design. The first was built to simulate the physical laboratory model and was then used to extract and validate the model parameters and boundary conditions. The second used the full-scale dimensions of a separate sewer system with two different ranges of pipe diameters, those normally used in intermediate sewer system networks i.e., sewer systems between lateral sewers and trunk lines. The second model was used to investigate the structural performance of the proposed separate sewer system configuration (two PVC pipes set in one trench), relative to conventional full-scale systems under an H20 traffic load (which is considered intermediate) to validate the structural integrity of the proposed method.

### 6.2.1 *FE model of physical model*

FE models were created using ABAQUS software to simulate the physical laboratory model, including the plate of the tyre footprint, the load cell, pipes, bedding layers and filling soil. The models have the same dimensions and boundary conditions as the physical model. Figure 6.4 shows the FE model of a sanitary pipe lying alone in the trench, while Figure 6.5 shows the FE model consisting of a storm pipe lying above the sanitary pipe in the same trench. The mesh of the model includes 177,062 linear hexahedral elements of type C3D8R in the case of one pipe, and 210,782 elements in the case of two pipes laid in one trench. The same series of loads applied in the physical model were used in the FE model.

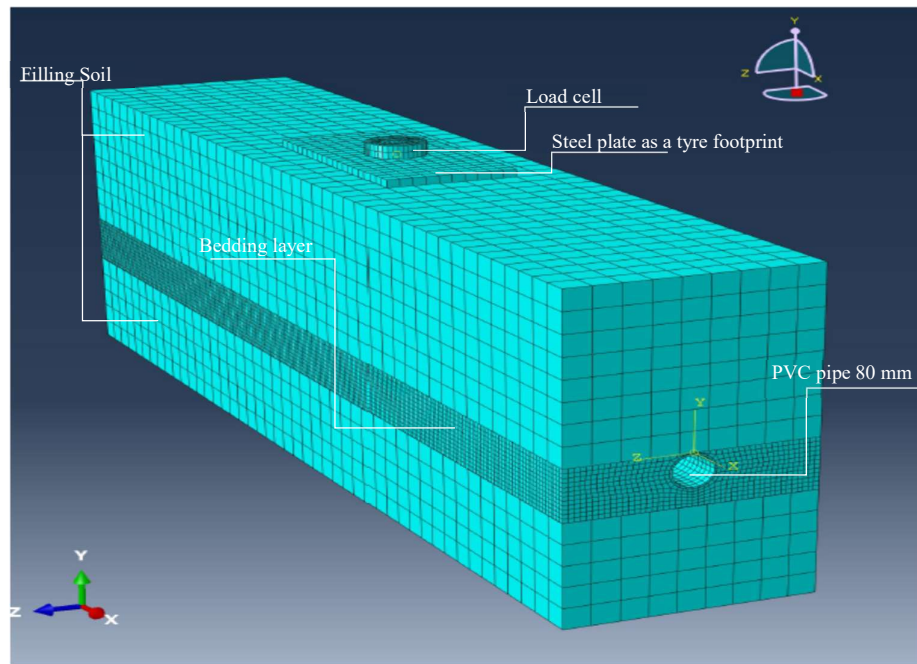


Figure 6.4 3D FE model used to simulate the physical laboratory model of one pipe set in a trench.

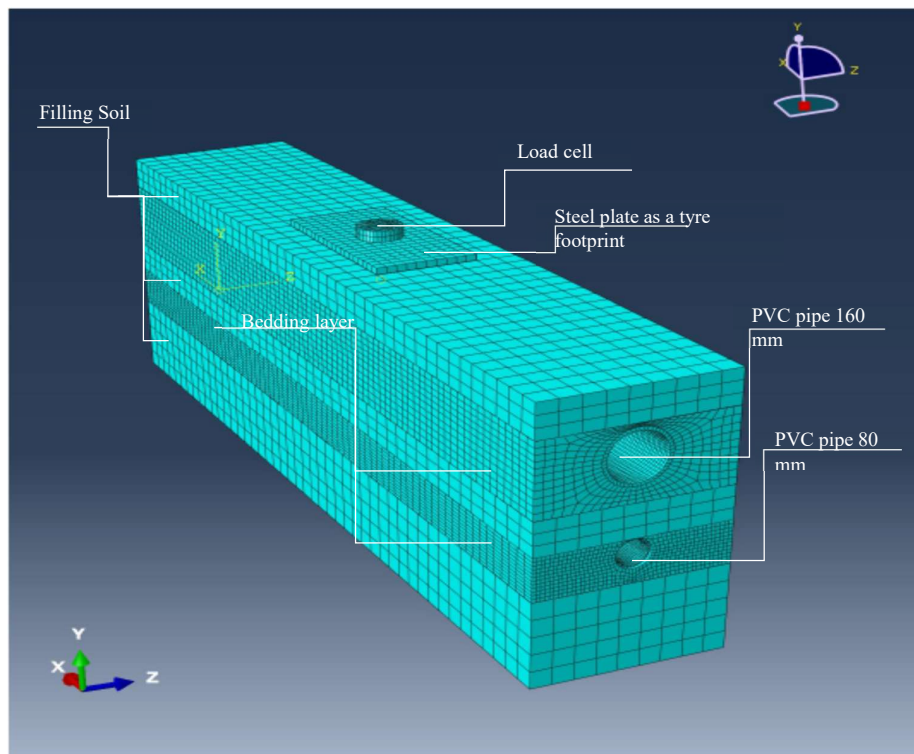


Figure 6.5 3D FE model used to simulate the physical laboratory model of two pipes set in one trench.

The boundary conditions and dimensions applied in the physical model were determined for the FE model. The material properties extracted from laboratory tests of each object were identified for the FE model using a modified Drucker-Prager cap constitutive model for both the physical FE model and the real-scale model, to simulate soil behaviour (section 3.2.1.2.3). A convergence study was conducted until an acceptable mesh was obtained (Brinkgreve, 2013). The same series of loads applied in the physical model were used in the FE model to explore the behaviours of the pipes and compare the physical and FE model results for validation. Figure 6.6 shows a sample of the visualization results produced by the FE physical model with two pipes in one trench.

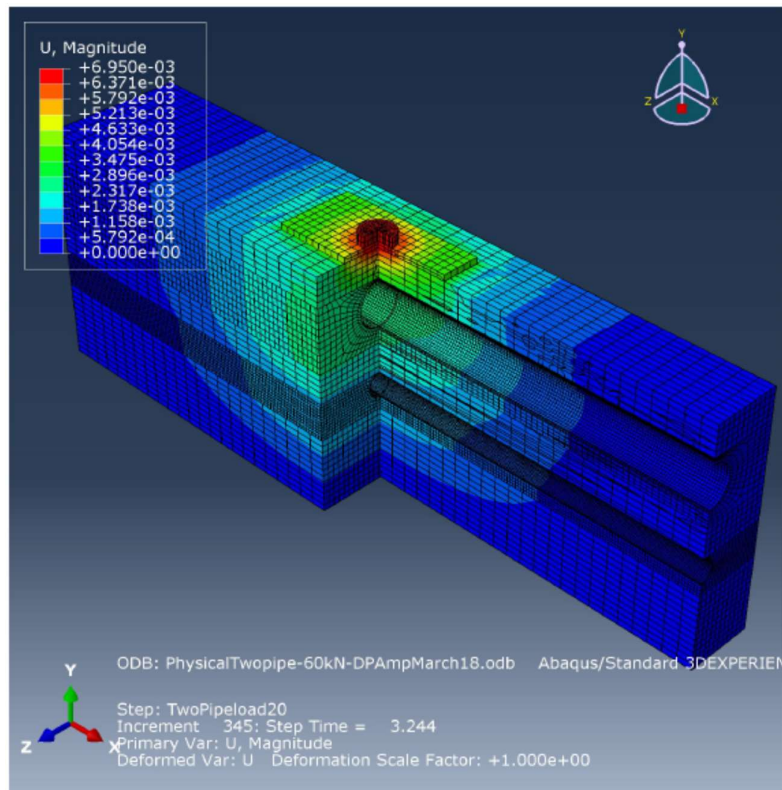
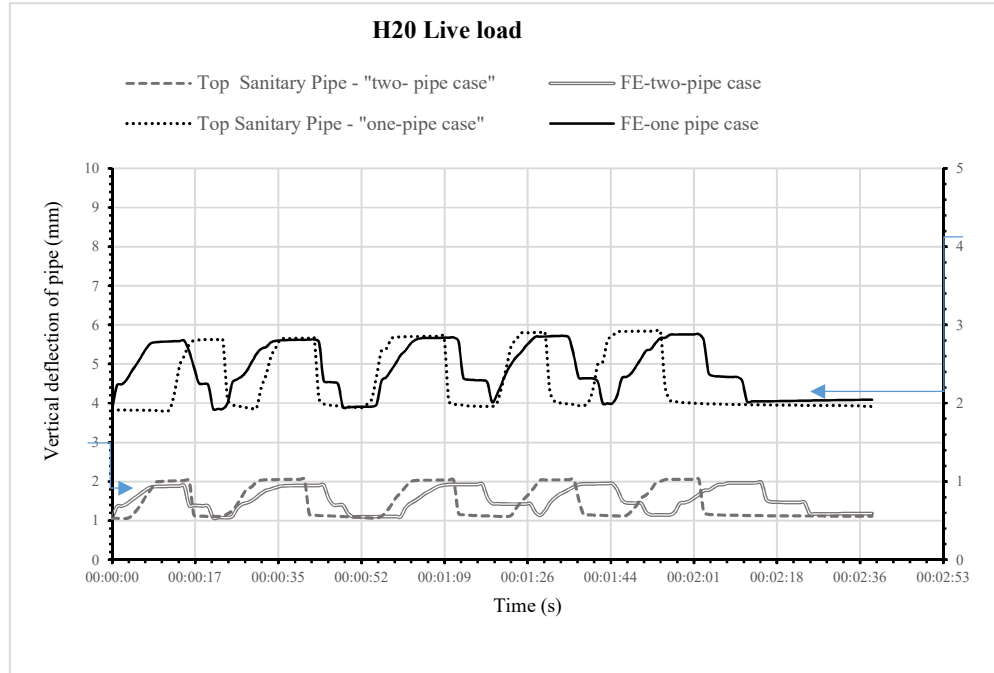
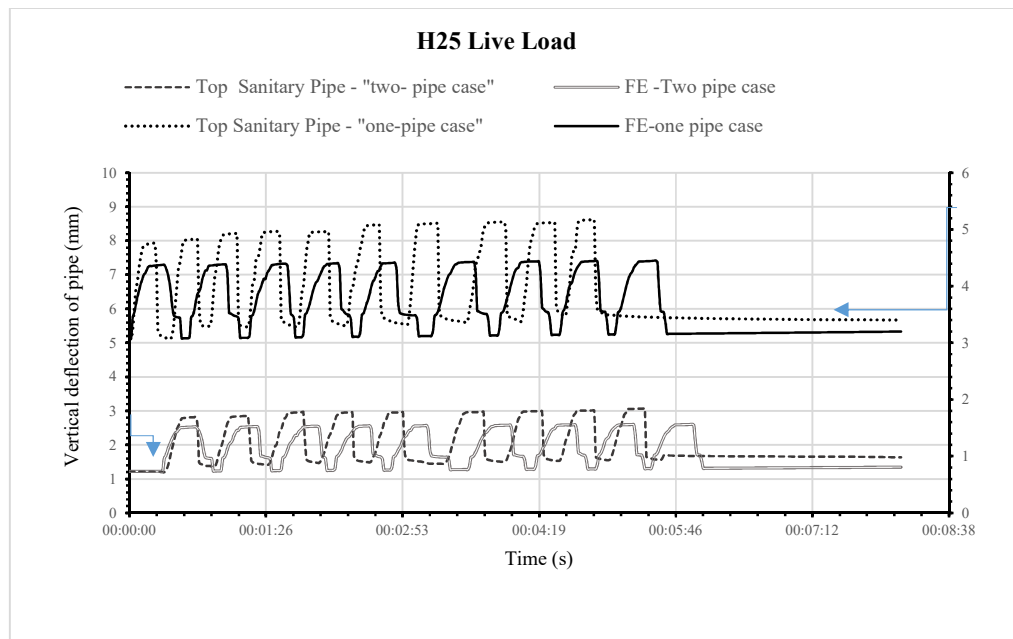


Figure 6.6 Visualization results for the FE model with two pipes set in one trench under an H20 live load.

The results of an applied series of loads in both cases of the FE model (i.e., for one and two pipes set in one trench), are presented in Figure 6.7 (a) for a system subject to an applied H20 live load, and (b) the same configurations for the pipes under an applied H25 live load. These results were compared with the experimental results from the physical model and found to show acceptable consistency. The results from both models demonstrate the mitigation of strain in the sanitary pipe when it is positioned below the storm pipe.



(a)



(b)

Figure 6.7 Comparison of the experimental and FE results for the deflection of the small (sanitary) pipe when set alone in the trench with that when it is set below a storm pipe under an applied (a) H20 live load (b) H25 live load.

A comparison of the FE and experimental results for the deflection of the sanitary pipe reveals an almost identical match for both cases under an H20 load (Appendix IV) . The displacements were 2.92 mm in the experimental and 2.87 mm in the FE analysis for the case of one pipe, and 2.1 mm and 1.96 mm, respectively, for the case of two pipes. Under an H25 load, the displacements were 5.1 mm (experimental) and 4.4 mm (FE model) for one pipe and 3 mm and 2.6 mm, respectively, for two pipes. In both cases, the results show that the deflection of the sanitary pipe was reduced when it was positioned below the storm pipe.

#### 6.2.2 *Full-scale FE model*

The 3D FE model, which was validated as discussed earlier, was developed to the actual model scale.

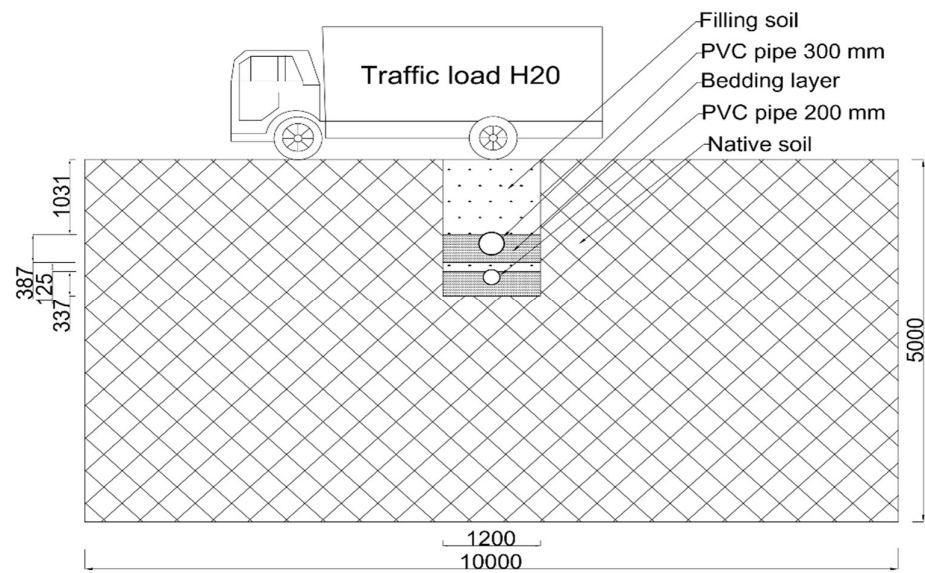
Conventional sewer systems typically use minimum diameters of 200 mm for sanitary networks and 300 mm for storm networks. The minimum cover depth used to provide protection for a sewer system network is 1 m for pipes with diameters of 200-1000 mm and 2 m for pipes with diameters of 1000 mm and above (Read, 2004; Bizier, 2007). The minimum sewer system design criteria were selected to test the structural integrity of the new installation method for a separate sewer system.

The 3D FE model was applied using the real-scale dimensions of the two sets of pipes. The first set included two PVC pipes, a 200 mm diameter sanitary pipe and a 300 mm diameter storm pipe, buried at a soil cover depth of 1 m. The second set also included two PVC pipes buried at a soil cover depth of 2 m: a 500 mm sanitary

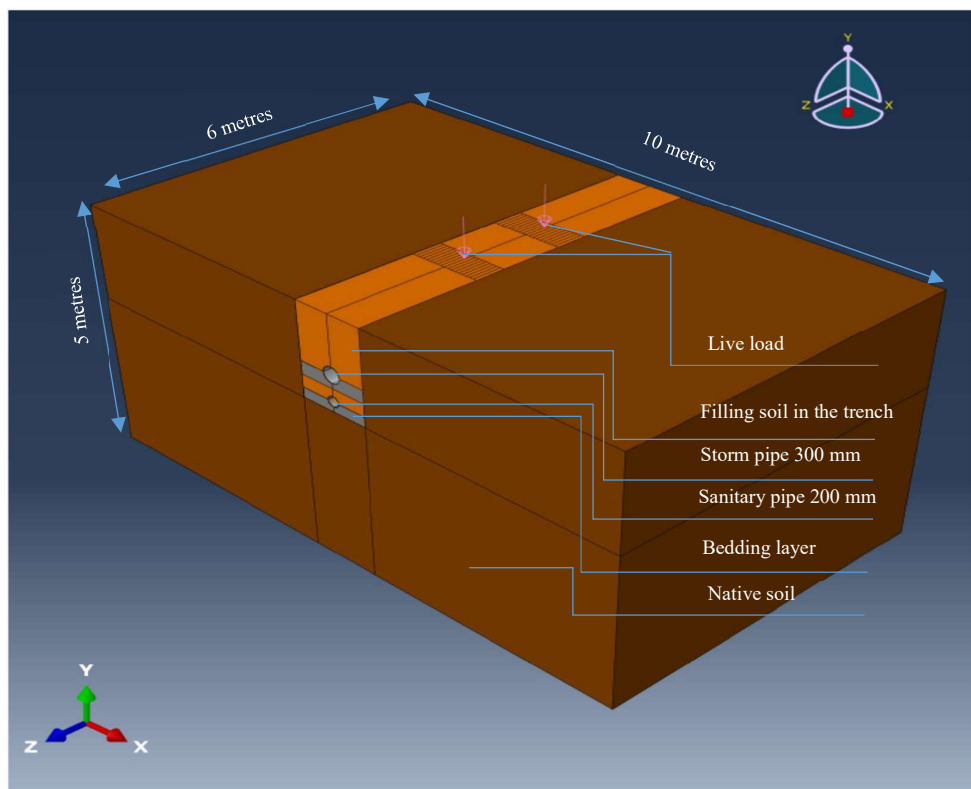
pipe and a 1000 mm storm. The same soil and bedding material properties used in the laboratory for the physical model, were also used for the 3D FE real-scale model. The width and height of the whole model were selected to measure the extent to which a live load can affect the native soil around the trench occupied by the pipes (Najafi and Sever, 2015b). The dimensions of the model were  $10 \times 6 \times 5 \text{ m}^3$  for the first set of experiments and  $10 \times 6 \times 10 \text{ m}^3$  for the second set. Two lanes representing two wheels of an H20 truck passing over the buried pipe section, were positioned on the surface to apply the live load. Figure 6.8 a and b illustrates the model of the first set of pipes (200-300 mm), two pipes in one trench. Figure 6.9 a and b shows the same case for the second set of pipes (500-1000 mm) with the storm pipe lying above the sanitary pipe in the same trench. Two types of ground surfaces were tested. The first used only soil cover which corresponded to a critical case scenario during the installation process, while the second used normal road surface layers i.e., subgrade and pavement. The properties of the pavement used for the FE model were as follows: density =  $2315 \text{ kg/m}^3$ ; modulus of elasticity =  $1400 \text{ MPa}$ .

The ABAQUS 2017 package was used to implement the 3D FE model on the LJMU cluster, as the dimensions of the model required powerful, high-performance computing. The first model (200-300 mm) included 452,564 linear hexahedral elements of type C3D8R, while the second model (500-1000 mm) included 397,764 linear hexahedral elements of the same type.



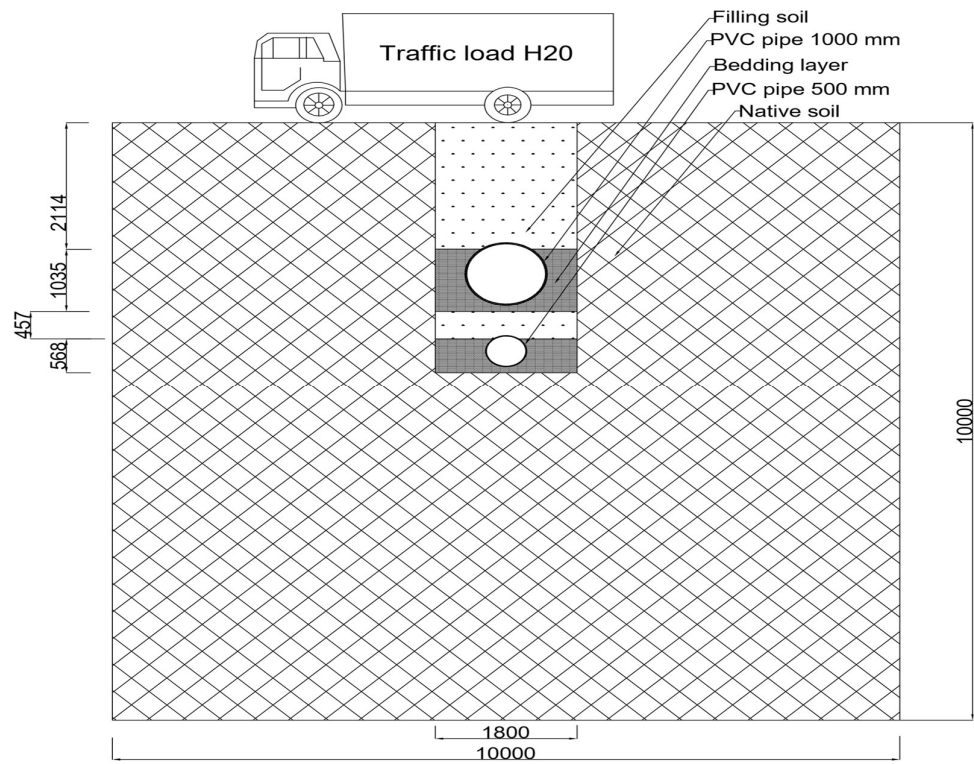


(a)

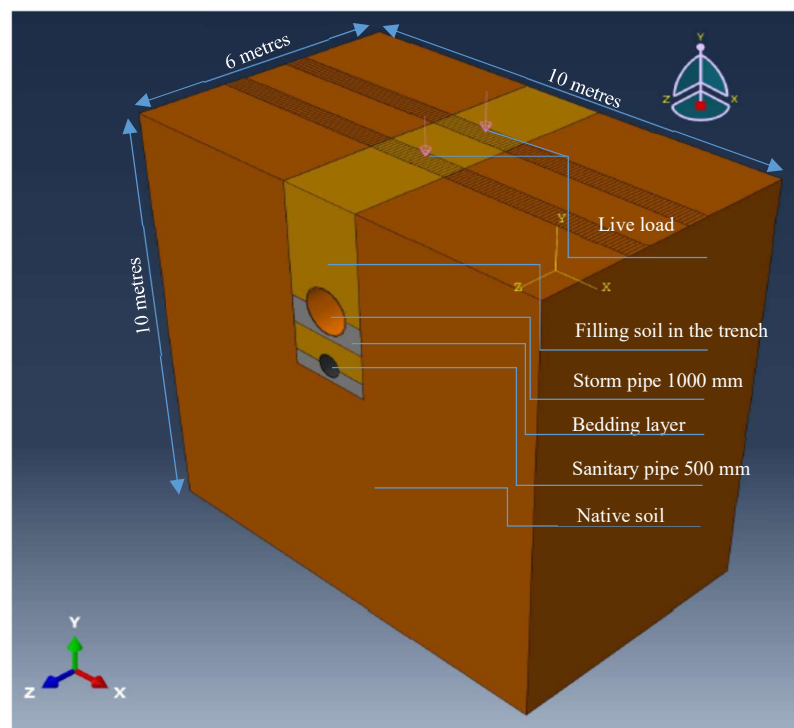


(b)

Figure 6.8 a and b. The model of a 300 mm diameter storm pipe and 200 mm diameter sanitary pipe in one trench.



(a)



(b)

Figure 6.9 a and b. The model of a 1000 mm diameter storm pipe and 500 mm diameter sanitary pipe in one trench.

The 3D FE full-scale model was used to verify the structural integrity of the proposed system; two sets of pipe diameters were used in two different cases. A traffic live load of H20 was selected for application to the real-scale model. Figure 6.10 shows a sample of the visualization of the 500-1000 mm diameter model with two pipes set in one trench.

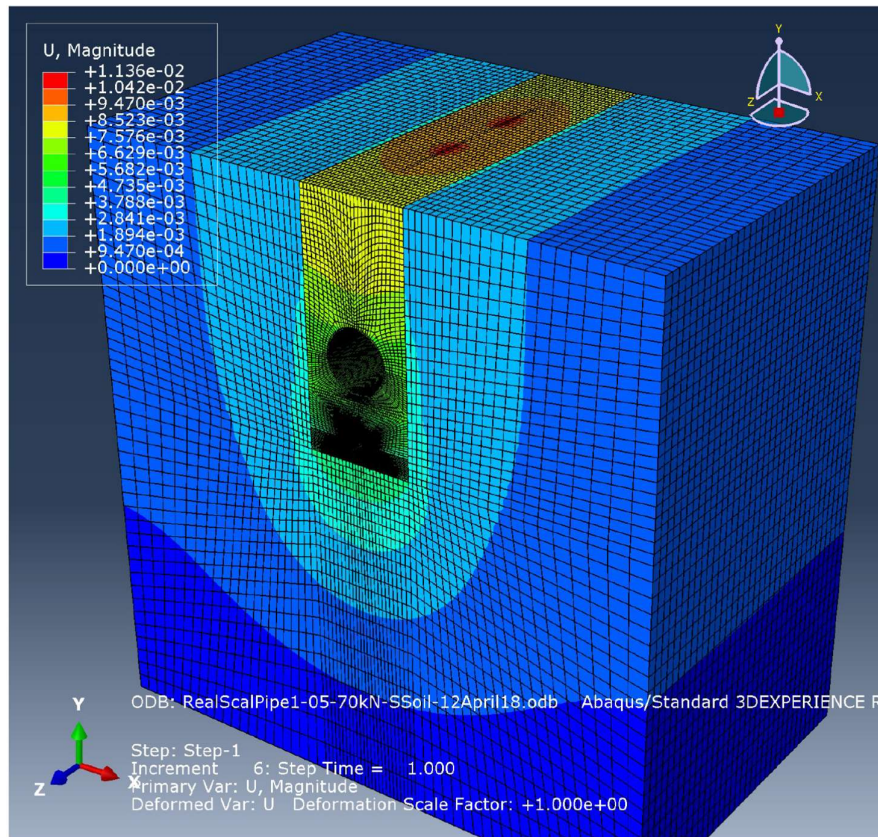


Figure 6.10 Visualization results for the FE samples of the real-scale model when two pipes lie in one trench under an applied H20 live load.

The first case involved a test of the system when a 300 mm diameter PVC pipe was used for the storm pipe and a 200 mm diameter PVC pipe used for the sanitary pipe. In one configuration, both pipes are laid in one trench; in the other

configurations, either the sanitary pipe or the storm pipe is lying alone in the trench. Figure 6.11 demonstrates the deflection of the storm pipe in the two configurations. The first step, when only the static load of the soil column weight is applied, produced a displacement of 2.05 mm to both pipes and a displacement of 2.28 mm for the single pipe in the trench. The displacements from the applied live load were 4.95 mm when the storm pipe was laid above the sanitary pipe and 5.52 mm when the storm pipe was laid alone. Figure 6.12 presents the deflections of the sanitary pipe which were 1.61 mm when both pipes were laid in the trench and 1.84 mm for the case of one pipe under a static load. The displacements were 3.49 mm when the sanitary pipe was set below the storm pipe and 4.75 mm when the sanitary pipe was set alone under a live load. The longitudinal shape deformations of both the storm pipe and the sanitary pipe, exhibited the same pattern. The results show that the new configurations for setting two pipes in one trench reduces the deflection of both pipes. This result occurs because the contact area between the side systems (i.e., the two pipes and the side soil) increases, allowing an additional load to be transferred to the side soil, according to Spangler (1941). Figure 6.13 illustrates the deformation of the surface soil for all three cases. The deformations were 17.82 mm when two pipes were set in the trench, 18.36 mm when only the storm pipe was set in the trench, and 19.51 mm when only the sanitary pipe was laid in the trench. We conclude that applying two bedding layers to accommodate a two-pipe system in one trench, partially increases the soil stiffness, thereby reducing the deflection of the soil surface. The depth of the trench with only one pipe affects the deformation of the surface, as the deformation with only the sanitary pipe (at greater depth) was slightly larger than that in the case with only the storm pipe (at shallower depth).

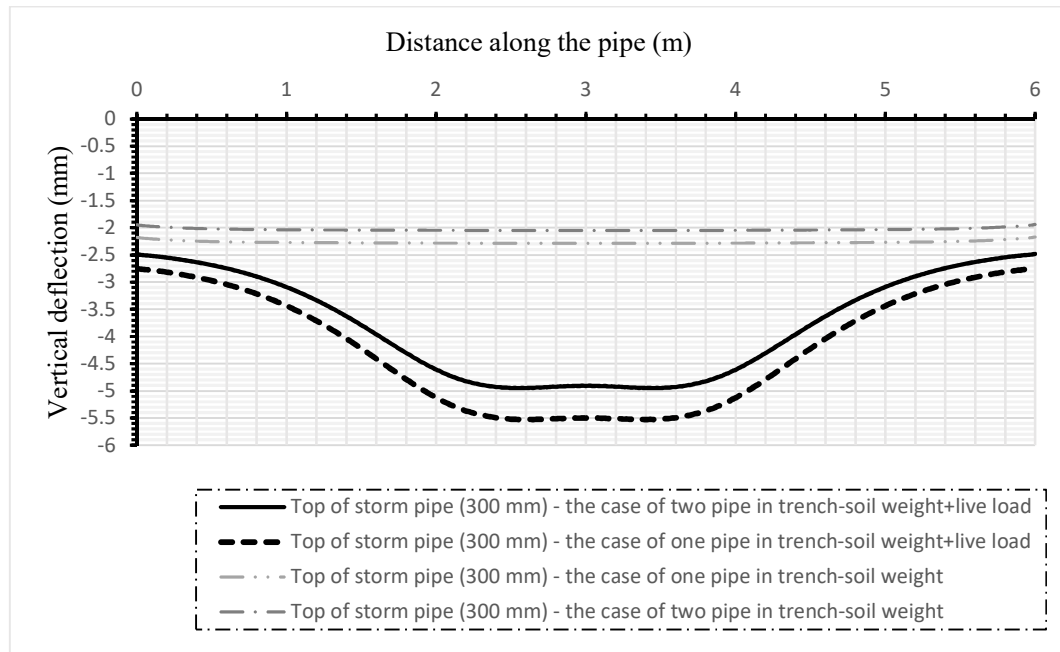


Figure 6.11 Comparison between the deflections of a storm pipe (300 mm) when set alone and when set above a sanitary pipe in one trench.

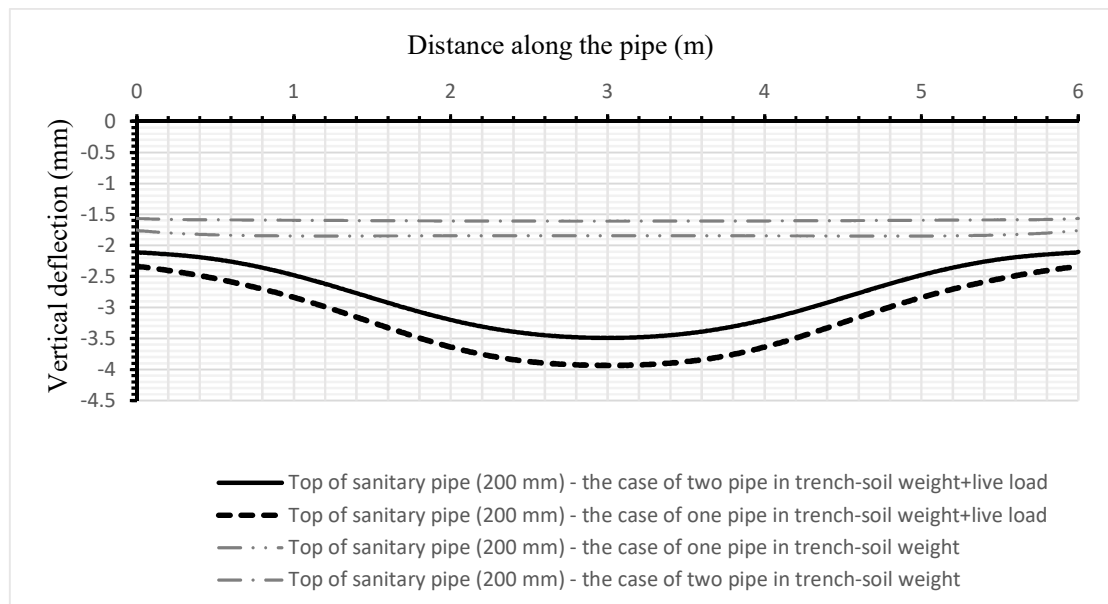


Figure 6.12 Comparison between the deflections of a sanitary pipe (200 mm) when set alone and when set below a storm pipe in one trench.

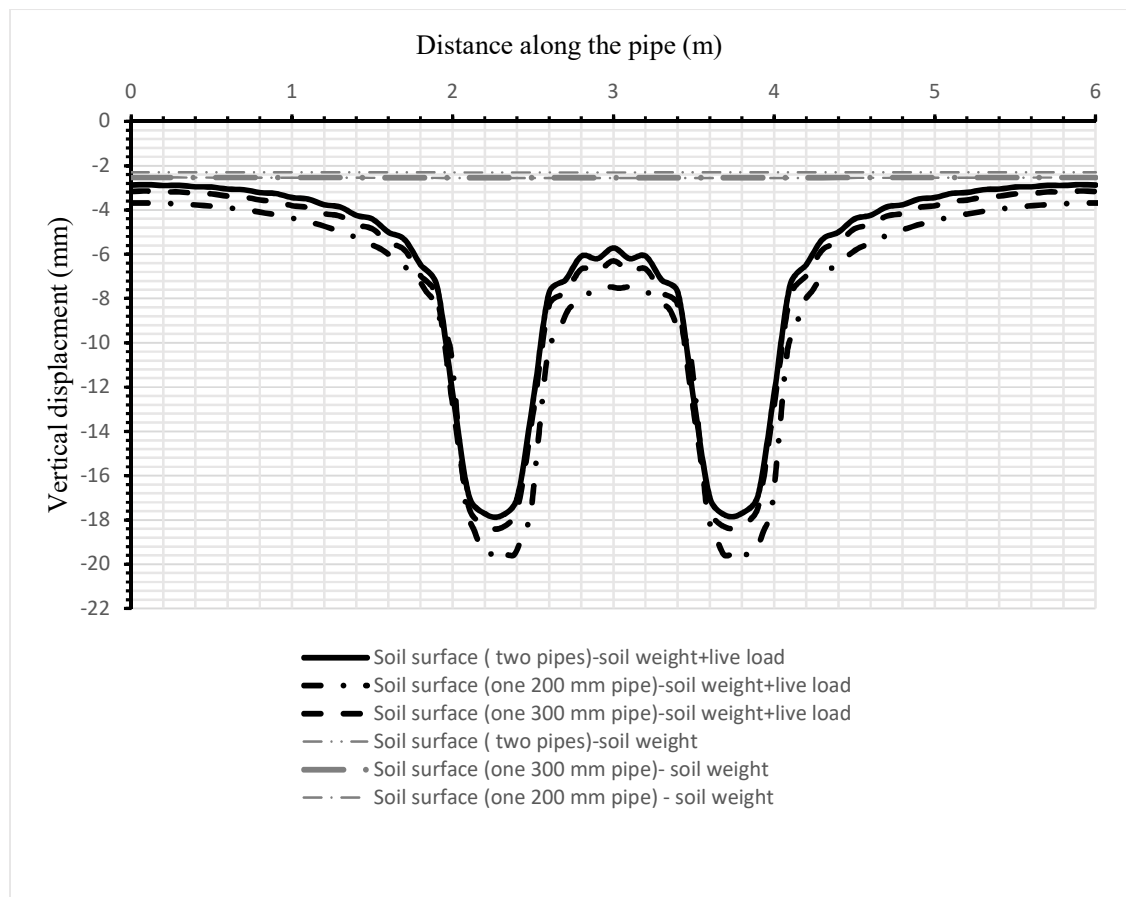


Figure 6.13 Comparison between the deflections of the soil surface in three cases for two pipes, and when either one sanitary pipe, or one storm pipe, are set in the trench.

The second case in the 3D FE real-scale model involved a 1000 mm diameter storm pipe and a 500 mm diameter sanitary pipe. These are the normal range of pipe diameters found in a conventional separate system, because the diameter of the storm pipe rapidly becomes larger than the sanitary pipe diameter downstream, within the sewer network. The same series of pipe configurations used in the first case were used for the second case, but with an increased cover depth, from 1 m to 2 m.

Figure 6.14 presents the results of the storm pipe (1000 mm) deflection when laid alone and when laid above the sanitary pipe (500 mm) in the first step, when only the static load of the soil column weight was applied. The displacements were 7.32 mm with two pipes in the trench and 8.21 mm with the storm pipe alone. The maximum displacements from the applied live load were located at the centre of the pipe, measuring 9.35 mm for two pipes and 10.38 mm for one pipe. Figure 6.15 shows the results for the same case but with a 10 cm asphalt layer and a subgrade layer (15 cm) at the surface, used to replace the same thickness of soil. The results show that there was no significant difference in pipe displacement, because the soil cover depth provided sufficient protection for the pipes against live loads at the surface. The structural behaviours were the same as the deflections observed with two pipes in the trench and less than that with one pipe in the trench.

Figure 6.16 shows the displacement of the sanitary pipe (500 mm) in two configurations; when set alone and when set below the storm pipe (1000 mm). The deformations in the first step (when only the static load of the soil column weight was applied) were 4.94 mm in the first position (with the sanitary pipe below the storm pipe) and 5.84 mm in the second position (when only one pipe was in the trench). The location of maximum deformation was not at the centre of the pipe. The deflections from the applied live load were 6 mm when two pipes were in the trench and 7.17 mm at the centre of the pipe when one pipe was in the trench.

Longitudinal deformations differed between the two configurations for the sanitary pipe i.e., when set alone and when set below the storm pipe. The displacement was less when the sanitary pipe was set below the storm pipe,

because the large storm pipe transferred some of the load to the side soil, this generated by horizontal deformation. The load on the side of the sanitary pipe balanced the load on top (Spangler, 1941; Watkins, 1957). Furthermore, the diameter of the pipe had a significant influence on the generation of lateral pressure on the side, this in addition to the effects of soil type and compaction efficiency (Elshimi Tamer and Moore Ian, 2013; Chakraborty, 2018). There are two reasons for this phenomenon; the width of the trench and the ratio of the pipe diameters, as the diameter of the storm pipe is approximately twice the diameter of the sanitary pipe. This effect was not detected for the first set of pipes (200-300 mm) because the difference between the pipe diameters was not as large.

Deformation of the surface soil was also explored for all three configurations of the second set of pipes. Figure 6.17 shows that there was more soil surface deformation when only the sanitary pipe was in the trench, than when only the storm pipe was in the trench. There was also less surface soil deformation when both pipes were set in the trench as a result of an increase in the soil stiffness because two bedding layers were used, one for each pipe. For the second set of pipes, soil settlement due to the weight of the soil column was 9 mm, which is more than the 3 mm of soil settlement for the first set. Because the diameters of the second set of pipes were larger, they required larger bedding layers thereby increasing the soil column weight and trench width. These two criteria explain why the soil settlement as a result of the weight of the soil column, was larger in the second case (Zhou et al, 2017).



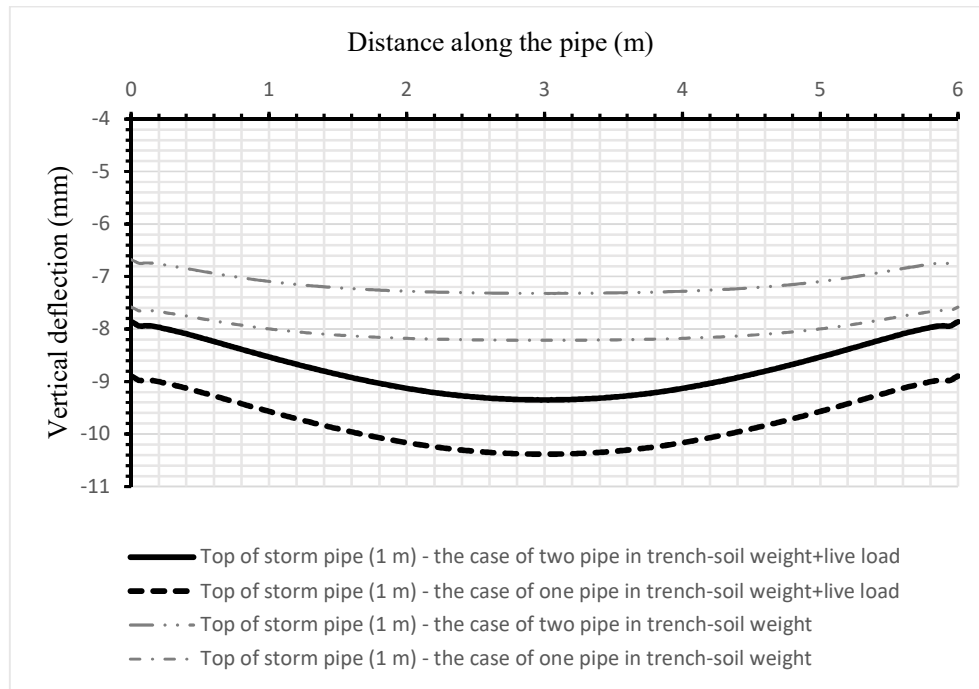


Figure 6.14 Comparison between the deflections of the storm pipe (1000 mm) when set alone and when set above a sanitary pipe in one trench.

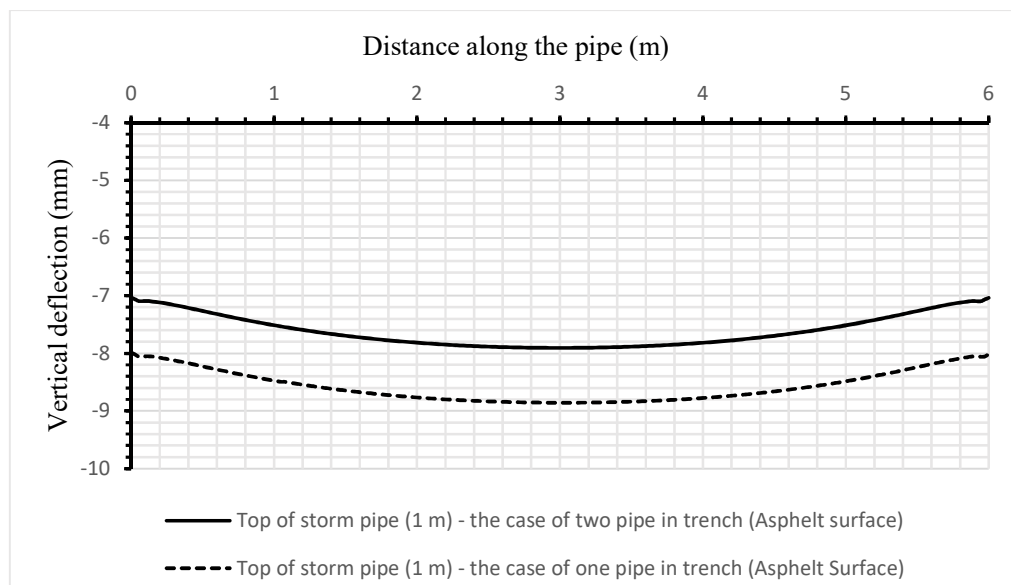


Figure 6.15 Comparison between the deflections of a storm pipe (1000 mm) when set alone and when set above a sanitary pipe in one trench using an asphalt layer on the surface.

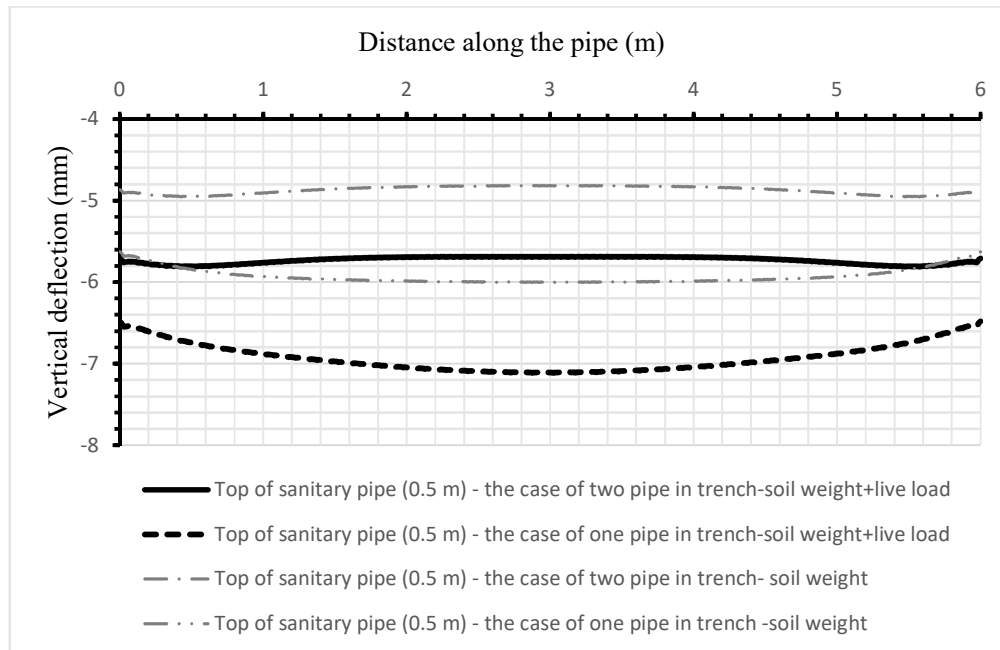


Figure 6.16 Comparison between the deflections of the sanitary pipe (500 mm) when set alone and when set below a storm pipe (1000 mm) in one trench.

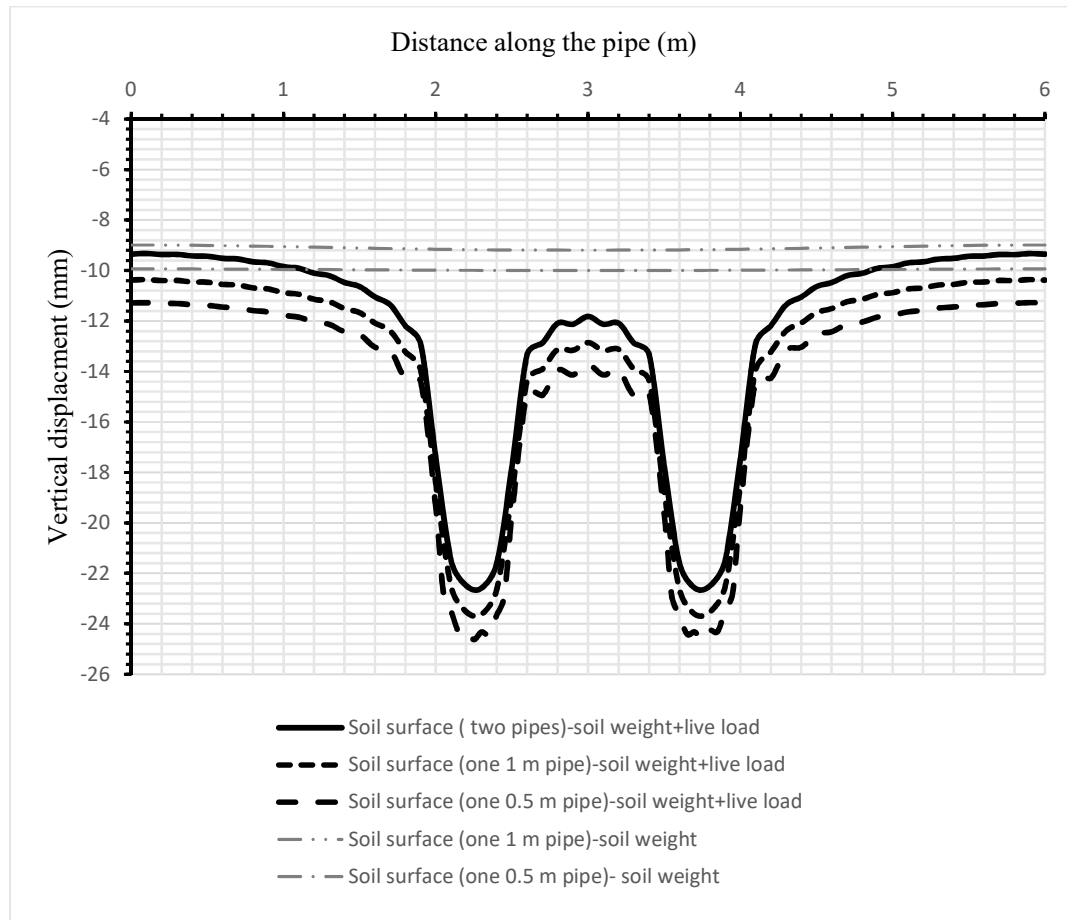


Figure 6.17 Comparison between the deflections of the soil surface under three cases for two pipes and when either one sanitary pipe or one storm pipe are in the trench for the second set.

The results for both the physical model and the 3D FE models, show that pipe deformation decreases when two pipes share a trench in a one-over-one configuration, specifically when the larger pipe is on top. The flexible pipe stiffness and the side soil support stiffness play a significant role in decreasing the strain on both pipes. This relationship is clearly shown in the work of both Spangler (1941) and his student Watkins (1957) using the Iowa formula, which is used to calculate flexible pipe deflection (ASTM-D2412, 2008).

$$\Delta x = \frac{D_L K W_c r^3}{EI + 0.061 M_s r^3} \quad \text{Equation 2-15}$$

The proposed separate sewer system configuration increases pipe elasticity in the denominator of Equation 2-15 because the two pipes are set in one trench, where static and live loads can both affect the system vertically. The contact area of the system (two flexible pipes) also increases, as represented by the mean pipe radius. This configuration allows the side soil to exhibit a greater influence on the pipe sides; more applied load is transferred to the side soil than in the conventional case with one pipe set in the trench.

The deflections of the pipes were within the design requirement criteria for flexible pipes (less than 2%) in both cases i.e., both the conventional configuration of a separate sewer system and the proposed configuration of two pipes in the same trench. The new method shows a slight reduction in deflections of both pipes in the trench and in the soil surface deformation, confirming the structural integrity of the new system for both the pipes and the road surface.

### 6.3 Development of the Iowa formula to calculate pipe deformation when set vertically in one trench

The Iowa equation and the McGrath simplified equation were designed to calculate the deflection of one flexible pipe buried in soil. Although a similar condition can generally be found when pipelines intersect at different levels (Figure 6.18), where two pipes are set vertically on the top of each other, based on the knowledge of the authors, only a limited numbers of studies have examined pipes set in vertical positions (overlapping pipes).

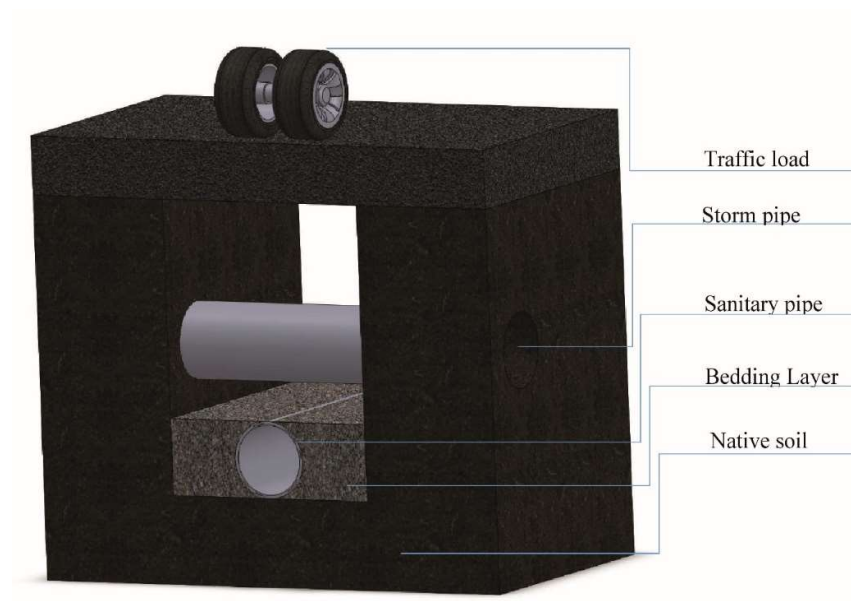


Figure 6.18 Typical intersection between a sanitary pipe and a storm pipe in a traditional separate sewer system.

### 6.3.1 *Distribution of load on buried pipes set vertically*

A flexible pipe is designed to transfer the load on the pipe to the soil at the sides of the pipe (Suleiman, 2002). The horizontal deflection of the pipe is resisted by the stiffness of the soil surrounding the pipe and its elastic modulus.

All theories used to evaluate pressure distribution models for flexible pipes were developed using similar assumptions to that used by Spangler's derivation of the Iowa formula. Figure 6.19 demonstrates three samples of these models: Spangler's expression used worldwide, Molin's expression use in Sweden and Germany and Gerbault's expression use in France (McGrath et al, 2009).

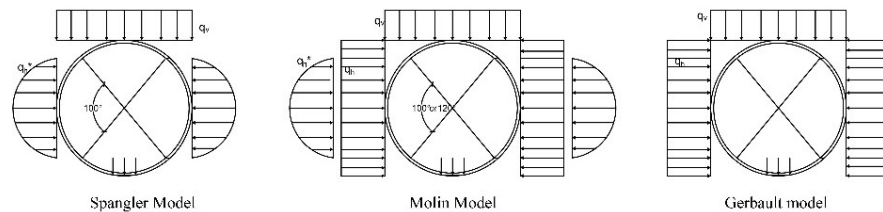


Figure 6.19 The pattern of load distributions for the flexible pipe (McGrath et al, 2009). [Reprinted with permission from Transportation Research Board]

The Iowa formula, and its successive modifications, are conventionally used to calculate deflection. However, it is limited to the elastic behaviors of the pipe and the soil. Pipe deflection occurs in both the horizontal and vertical planes, and when loads are applied, a reduction in the vertical pipe diameter ( $\Delta y$ ) can be observed, along with an increase in the pipe's horizontal diameter ( $\Delta x$ ). Pipe deflection can be calculated using the same principles as used by Spangler (1941).

$$\text{Pipe deflection} = \frac{\text{constant} \times \text{load on the pipe}}{\text{pipe stiffness factor} + \text{soil stiffness factor}}$$

The Iowa formula has been extensively tested in the case where one pipe is buried in soil. This research aims to evaluate the potential of using the Iowa formula when applied to two pipes buried in one trench, with the center of the pipes vertically aligned. The Iowa formula has been modified to be applicable to the case of overlapping pipes. The stiffness of the sanitary (small) pipe at the bottom is included as a parameter when calculating the deflection for the large pipe on the top. The load transfer from the top pipe to the lower pipe, is alleviated by the elasticity of the top pipe and side soil support. As a result, the load that reaches the sanitary pipe surface is integrated and dependent on the load on the top pipe and the weight of the soil column between the two pipes. Improvements in stress distribution, as hypothesized by Spangler (1941), are introduced to reveal the mechanism of stress distribution when two pipes are in a single trench, longitudinally aligned on top of each other.

Figure 6.20 illustrates the distribution of the loads between the two pipes. Two parameters are used to interpret this relationship and to modify the Iowa formula. The first is related to the diameters of the pipes, the second to the vertical distance (gap) between the two pipes. These two variables affect the relationship between the two pipes and how the applied load is shared.

These are then used to calculate an effective angle ( $\theta$ ), which controls the amount of load transferred from the top pipe to the bottom pipe, and the percentage of

stiffness of the bottom pipe that influences the calculation of the deformation in the top pipe. The angle ( $\theta$ ), which is calculated using Equation 6-1, is a function of the diameters of the two pipes and the gap separating them. The triangle length height, as considered from the spring line of the top pipe to the spring line of the bottom pipe, equals the sum of the radius of the top pipe, the gap between the pipes ( $L$ ), and the radius of the bottom pipe (small) pipe. The base is equal to the radius of the bottom pipe. Figure 6.21 presents the case when the pipes are equal in diameter and the top pipe is set directly over the bottom pipe ( $L = 0$ ). In this case, the calculated angle would be  $\theta = 90$ , revealing that all the load from the top pipe is transferred to the bottom pipe, and that the entire stiffness value of the bottom pipe should be included in the calculation of the deflection of the top pipe. This hypothesis is used to modify Equation 2-15 to calculate the pressure load transfer to the pipe at the bottom (Equation 6-2), and the total deflection in both pipes (Equation 6-3). Equation 6-3 uses the same principles as those used to derive the original Iowa formula. However, only the distribution of loads applied between the two shallow buried pipes and the influence of the stiffness of the bottom pipe on the deflection of top pipe have been studied in this research.

The output of Equation 6-3 was validated using the results obtained from the experimental apparatus used in this research. However, more research is required to test different flexible pipe materials, as this research was limited to the use of only PVC pipes; a real scale test is highly recommended.



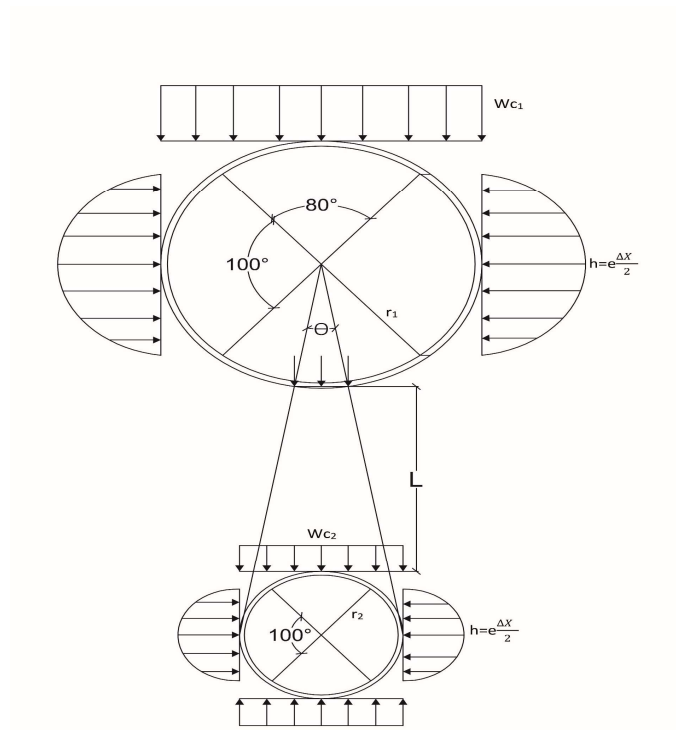


Figure 6.20 Hypothesized improvements in stress distribution between two flexible pipes: the large pipe at the top and small pipe at the bottom.

Geometrically,

$$\theta = 2 \tan^{-1} \frac{r_2}{(r_1 + L)} \quad \text{Equation 6-1}$$

with  $0 < \theta < 90$

The load on the small pipe (pipe at the bottom) would result in:

$$W_{c2} = \int_0^\theta \frac{W_{c1} \times 2r_1 \times \cos \theta \, d\theta}{2r_2} + \int_0^L \gamma \, dL \, 2r_2 + \gamma 0.11 \times 4r \quad \text{Equation 6-2}$$

where:

$W_{C1}$  = load on the big pipe (pipe at the top)

$W_{C2}$  = load on the small pipe (pipe at the bottom)

$r_1$  = radius of big pipe 1

$r_2$  = radius of small pipe 2

$L$  = the gap between two pipes

$\gamma$  = soil density.

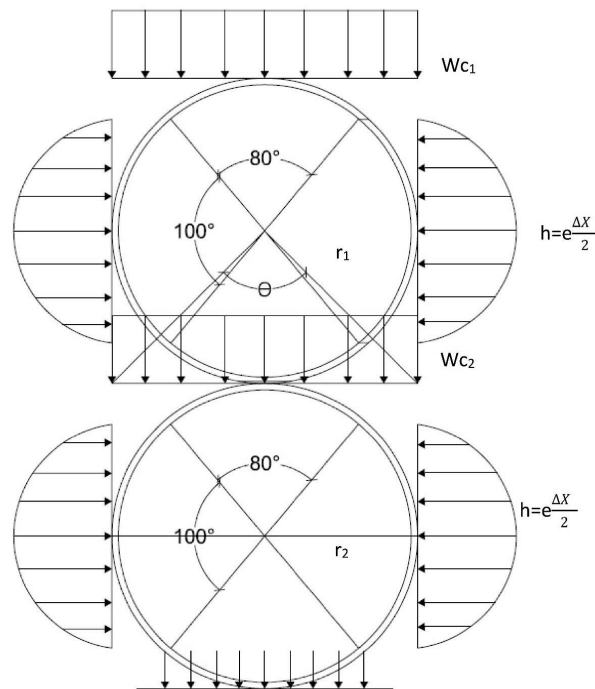


Figure 6.21 Nearly all the load from the top pipe will transfer to the bottom pipe when the bottom pipe is laid directly below the top pipe and is of the same size ( $\theta \approx 90^\circ$ ).

When the sanitary pipe is located below the storm pipe and separated by a large distance ( $\theta \approx 0^\circ$ ), the load on the small pipe is only generated by the total weight of the column of soil.

The modified Iowa formula Masada (2000) used to calculate the ratio of ( $\Delta y/\Delta x$ ) is:

$$\frac{\Delta y}{\Delta x} = 1 + \frac{0.0094E'}{PS} \quad \text{Equation 2-16}$$

The total combined vertical deformation for both pipes (storm pipe and sanitary pipe) can be calculated using:

$$\Delta y = \left( \frac{(D_L K W_c)_1}{\left(\frac{EI}{r^3}\right)_1 + \left[\left(\frac{EI}{r^3}\right)_2 \times \sin \theta\right] + 0.061E'} + \frac{D_L K \left(\frac{W_{c1} \times 2r_1 \times \sin \theta}{2r_2} + \gamma L r_2\right)}{\left(\frac{EI}{r^3}\right)_2 + 0.061E'} \right) \left( 1 + \frac{0.0094E'}{PS} \right)$$

Equation 6-3

In this work, it is assumed that the value of  $\theta$  depends on only two parameters: the diameter of the pipes and the vertical distance between the pipes. However, more research is required to determine the value of  $\theta$  when the effect of the upper pipe is negligible, i.e., when the load on the pipe at the bottom can be calculated using the traditional Marston load theory and the live load (Equation 2-12):

$$W_{c2} = C_d \gamma H 2r_2 B_d + \text{live load} \quad \text{Equation 2-12}$$

where:

$C_d$  = the Marston load coefficient

$B_d$  = the width of the trench

$H$  = the depth of soil cover above the lower pipe top edge

### 6.3.2 *Testing the improved Iowa formula*

The deformation of the sanitary pipe presented in Figure 6.3, was compared with output from both the traditional Iowa formula and Improved Iowa formula. A significant drop in sanitary pipe deformation was noted in the new system, decreasing from 1.26 mm to 0.77 mm under an H-20 load, and from 1.47 mm to 0.9 mm under an H-25 load, after eliminating the soil settlement from these results. In both cases, the deformation was within the design criteria for a sewer system at less than 2%. Figure 6.22 illustrates the comparison between the experimental results, the improved Iowa formula and the original Iowa formula output for the sanitary pipe. The Improved Iowa calculation shows a reduction in sanitary pipe deflection, but it is still overestimated, this constituting an improved degree of safety at the design stage. It is similar to the original Iowa formula which is limited when compared with finite-element techniques and the elastoplastic behavior of the soil-pipe interaction. The simplicity of this formula is still the biggest advantage for the designer. However, real scale testing and more research is required to test the integrity of the improved Iowa formula for other flexible pipe materials and pipe diameters, such as HDPE pipes, glass fiber reinforced plastic (GRP) pipes, and steel pipes. Both test methods revealed that the novel system of overlapping pipes, creates a situation where the stress of the top pipe on the sanitary type at the bottom is decreased by between 10 and 20%. The resulting percentages are dependent on the cover depth, pipe size and the gap between the two pipes.

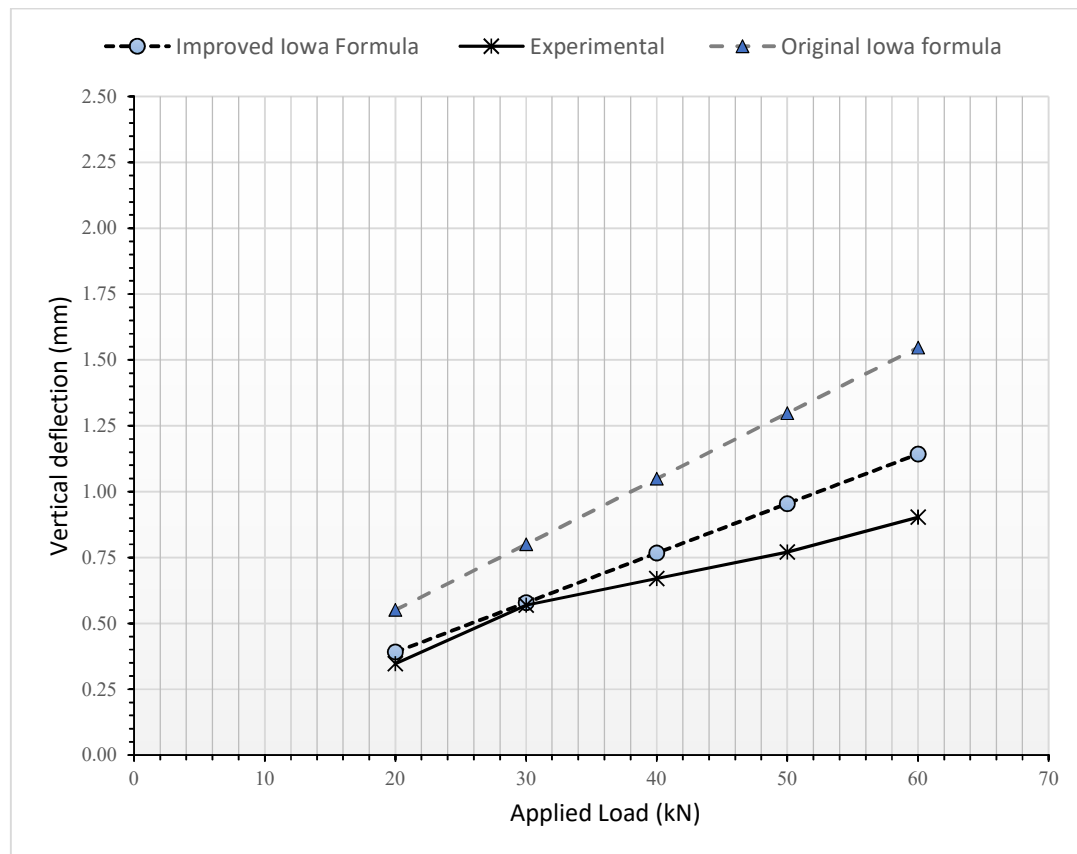


Figure 6.22 Comparison of deflection of the sanitary pipe when two pipes are set in one trench using the developed Iowa formula, the original Iowa formula and the experimental results.

The first trench was narrow in order to simulate the trench properties described by Marston, cited by Moser and Folkman (2008) (Figure 2.13). Concerns about the width of the first rig used to test the new setup of pipelines, led the researcher to test the new method using a wider rig to eliminate worries about the effect of the width of the trench on the experimental results. The dimensions of the rig were 1 m wide x 1 m long x 1.5 m high. It has a steel wall on three sides, the fourth side built from secure glass. The rig has an applied load capacity of a maximum of 10 tons. The cell is designed to accommodate two buried pipes (160 mm and 80 mm) and the sand soil. The properties of the sand were determined through a direct

shear test, the bulk density identified as medium-dense, the  $E_s$  and  $\nu$  determined by Berney and Smith (2008), as shown in Table 6-1. The rig is equipped with an adjustable loading system at the top and a data acquisition system to monitor the degree of displacement for both the soil and pipes. Strain gauges of type GF, were fixed on both pipes to measure vertical and horizontal deflections, synchronized with the applied loads.

Table 6-1 The mechanical properties of the sand.

Soil	Density	Young modulus $E$	Poisson ratio $\nu$	Angle of friction $\phi$	Cohesion $C$
	[kg/m <sup>3</sup> ]	[kPa]	[-]	[-]	[kPa]
Sand	1700	35000	0.25	37.50	0

Two pipe installations were tested. The first assessed the behaviour of the 80 mm pipe installed alone under 500 mm of sand, subject to applied loads (Figure 6.23). For the second test, the 160 mm pipe was installed at the top under 300 mm of sand, the 80 mm pipe kept at the bottom, with the same cover depth. The same series of cycle loading 100kpa were applied to compare the degree of deformation of the small pipe in both case. The experimental results, the improved Iowa formula and the traditional Iowa formula, all used to calculate the horizontal deflection of the small pipe, was reported in Table 6-2. The results provided the same conclusion as that produced from the first tests: the deflection of the smaller pipe (80 mm) is significantly decreased when the pipe is laid at the bottom of the trench, below the larger pipe (160 mm). The improved Iowa calculation is the best at simulating small pipe behaviour, for both rig tests, when compared to the traditional Iowa formula.

Table 6-2 Comparison between the experimental results, the traditional Iowa formula and Improved Iowa formula.

Pipe Dimeter	Load	Vertical deflection in PVC pipe			
		One pipe in trench		Two pipes in trench	
		Experimental	Traditional Iowa Formula	Experimental	Improved Iowa formula
[mm]	[kPa]	[mm]	[mm]	[mm]	[mm]
80	100	0.790	0.898	0.300	0.408

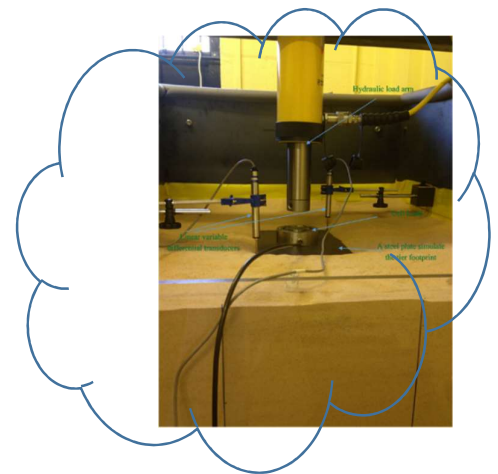
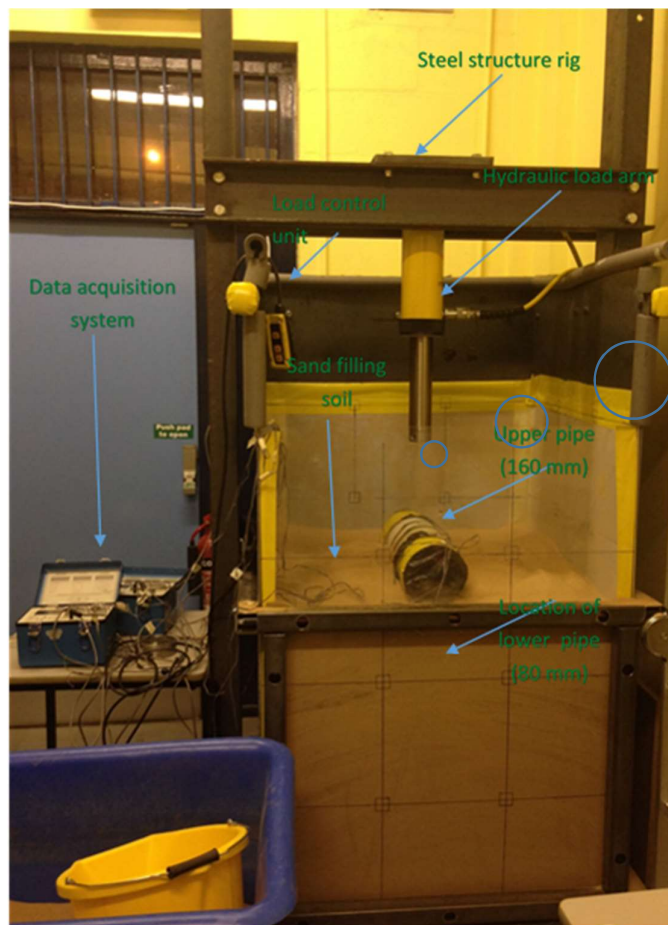


Figure 6.23 The setup of the rig with equipment, sand and buried pipes for the new test.

## 6.4 Summary

This chapter explored the structural performance of two flexible pipes set in one trench, where the pipe with the larger diameter (the storm pipe) was situated above the smaller diameter pipe (the sanitary pipe), the results compared to the traditional method when one pipe is set in a trench. A physical model was built in the laboratory to test the performance of two PVC pipes (160 mm and 80 mm) when set together, and when set alone in a trench, under an applied live load. The results of the physical model were used to validate the 3D FE model using the same objects, dimensions, material properties and boundary conditions.

The results of the FE analysis modelling flexible pipes buried in soil, showed an acceptable match with the responses from the physical model test data. The physical 3D FE model was then upgraded to a real-scale 3D FE model, which was used to test two sets of pipes of different diameter in the new configuration. The first set of pipes had diameters of 200 mm and 300 mm, the second set having diameters of 500 mm and 1000 mm, which correspond to the range of pipes typically used in conventional separate sewer systems. The results revealed that the new configuration decreases deflection in both pipes and deformation of the surface soil, relative to conventional methods by which a single pipe is placed in a trench. For the first set of pipes, a 200 mm diameter sanitary pipe and a 300 mm diameter storm pipe, the decrease in the deformation of the storm pipe under the live load was approximately 10%. The reduction in the deformation of the sanitary pipe was approximately 26% when the pipe was set below the storm pipe in comparison to when it was set alone in the trench. For the second set of pipes, a 500 mm diameter sanitary pipe and a 1000 mm diameter storm pipe, the



reductions in deformation under the applied live load were 10% in the storm pipe and 15% in the sanitary pipe.

The Iowa formula was applied to explain the observed reductions in pipe deformation in terms of an increase in the elasticity of the pipe and the contact area between the pipe sides and soil, these used as parameters in the denominator of the Iowa formula. The Iowa Formula was improved in this work to calculate the total vertical deflection when two sets of pipes are laid in one trench. The Improved Iowa formula was tested by comparison to the experimental results from the physical model, the results revealing an acceptable match between the two (97% correlation).

## CHAPTER 7

### CONCLUSIONS AND ECOMMENDATIONS

#### 7.1 Conclusions

A separate sewer system is required by recent environmental regulations in many countries, but installing a traditional separate sewer system in narrow streets, common around the world, especially in the UK, Europe and other densely populated areas, is too challenging.

This research presents a novel design for the geometry of a manhole, integrating a stormwater and sanitary system in one combined structure, while maintaining separate functions. The system is designed to ensure that no mixing of stormwater and sewage will take place. The manhole is cylindrical and has two chambers which are arranged coaxially: the external chamber is used as a storm manhole, the internal chamber used as a sanitary manhole. This design of a separate sewer system combines the important advantages of the traditional separate sewer system (less pollution on the watercourse) and that of the combined sewer system (lower cost and smaller footprint). The structural performance of the new system under traffic loadings, and the hydraulic integrity at different flowrates and surcharge ratios, have been tested and compared to the performance of the traditional design. Two methods were used to conduct the research, the first using a physical model to test the structural and hydraulic behaviour of the new manhole design, the second using a physical model to test the behaviour of the flexible pipes when set in one trench. Both sets of experimental results were used to validate and upgrade the FE and CFD models to full-scale models.

A summary of the main conclusions from this work are listed as follows:

**Manhole:**

*Structural*

The new manhole was tested and compared with the traditional manhole under a series applied traffic loads: HS20, HS25 and double HS25. Reinforced and non-reinforced concretes were used as materials for both manholes.

- The weight of the new manhole added a dead load to the applied loads, this affecting the behaviour of the manhole. The displacement was 2 mm more than that for a traditional manhole, 1 mm under a weight effect or a small live load. This effect is expected to disperse during the construction stage with good compaction processes.
- Under heavy loads (HS20 and HS25), both the new and traditional manhole exhibit the same behaviour, settlement of approximately 4 – 5 mm and both operate within standard limitations (less than 13 mm).
- The new manhole has very good stability in terms of displacement, under extremely high loads (displacement approximately 6.5 mm); the traditional manhole experienced more settlement under the same load, approximately 8 mm. However, the bending moment was close to the cracking moment at the base of the storm chamber under a double heavy load; reinforcement was recommended for the slab (cover) and the base of the manhole. The levels of soil stress in the new manhole were dramatically reduced in comparison to soil stress in the traditional manhole structure, under identical loads.

### *Hydraulic properties*

The head loss coefficient and the pattern of the shockwaves were studied for both manholes, under the same conditions, using independent dimensionless parameters for each manhole: ratio of surcharge ( $\beta_{im}$ ), approach flow Froude numbers ( $F_{ro}$ ), and the filling ratios ( $\beta_{ip}$ ).

- The new manhole design generates higher head losses, about 200% the head loss generated in conventional manholes, at a low  $\beta_{im}$ . The head loss of both manholes tends to be stable, and maintains a lower constant value, when the flow transitions from free surface flow to pressurized flow (at a high  $\beta_{im}$ ).
- Four shockwaves were identified in the storm chamber of the new manhole design: (1) 'A' results from impingement of the direct flow in the inlet pipe onto the inner manhole wall; (2 & 3) 'B' and 'b' were generated from the change in flow direction caused by the two bends of the storm chamber and (4) 'C' was generated from flow choking at the outlet manhole. The locations of these shockwaves were determined, the average amplitude of swing generated from the combined effects of the shockwaves quantified with the non-dimensional dynamic moment  $F_{ro}\beta_{ip}$ , showing a significant increase in amplitude of shockwaves in the new manhole.
- Hydraulic integrity, tested by breaking up the flow downstream of the model, illustrated that the amplitude and swing of the shockwaves decreases with an increase in the surcharge ratio ( $\beta_{im}$ ). This indicates that the manhole design is safe in terms of structural damage and geysering phenomena associated risks.

### **Pipe installation**

The new position of two flexible pipes set in one trench, where the pipe with the larger diameter is located above the smaller diameter pipe, was tested using two sets of pipes. The first set of pipes had diameters of 200 mm and 300 mm, the second set diameters of 500 mm and 1000 mm, which correspond to the range of pipes typically used in conventional separate sewer systems. An H20 live load was applied at the surface, in two places over the centre of the trench, to simulate a two-axle truck.

- For the first set of pipes, the decrease in deformation of the storm pipe under the live load was approximately 10%. The reduction in the deformation of the sanitary pipe was approximately 26% when the pipe was set below the storm pipe, relative to when it was set alone in the trench.
- For the second set of pipes, the reductions in deformation under the applied live load were 10% in the storm pipe and 15% in the sanitary pipe.
- Surface soil deformation was explored for both sets of pipes and found to decrease slightly, 3% and 10%, when using two pipes in one trench compared with using one pipe. This finding can be explained in terms of the slight increase in soil stiffness, as two bedding layers were used in the trench with one pipe.
- The Iowa formula, normally used to calculate the deflection of one buried pipe, was improved to calculate the total deflection when pipes are set in the new position, one over another in one trench. The output of this improved formula (as developed in this research) was compared with the experimental

results. The results of the application of the improved formula reveal an acceptable match with the experimental results (97% correlation).

### **Economic advantages of the new system**

#### **➤ Cost**

Providing the funds to build and operate a separate drainage infrastructure, is one of the main barriers facing decision makers, therefore, reducing the SSS initial construction costs can encourage planners to use it. The new system reduced the initial cost of laying the sewer system by using one trench to accommodate the two pipelines compared with using two separate trenches in the traditional system. The time factor influences the cost as well because sewer projects cause disturbances in populated areas, affecting community and business activities.

#### **➤ Footprint**

Sewer systems have a larger street footprint compared with that of any other infrastructure services, such as potable water pipelines, electrical cables, communication cables and gas pipelines. The sewer system has larger pipes and is set at deeper levels meaning that the installation process requires a large section of the street to be excavated when using open-cut methods. This larger footprint increases the risk of sewer system installation activities interfering with other utilities. The new system occupied a smaller area than that used by the traditional system; this can give a margin of space to other utilities, an important consideration in narrow streets.

➤ Hydraulics

The new system significantly improved the hydraulic integrity of the storm network. It increased storage capacity by 280%, compared to the traditional separate system, and increased the retention time for stormwater flow inside the storm network by 200%, compared to the storm flow retention time in the traditional system.

## 7.2 Recommendations for further work

- Testing a full-scale model of the new manhole design and new position of the separate pipes in a trench by means of a field study, is necessary to extend knowledge and understanding of the structural and hydraulically performance of the new system.
- Investigate the use of hybrid materials to build the new manhole by using plastic materials such as HDPE or GRP for one chamber and concrete for the other. This will improve the structural performance because it will decrease the weight of the new manhole and the cost.
- Develop the validated CFD model tested in this research to a full-scale CFD model to test the hydraulic properties. Installing breaker jetting, or changing the shape of the inner manhole from circular to elliptical, can help improve the hydraulic flow of stormwater. Using U-shaped profiles for the storm flow path inside the storm chamber instead of a flat base, can create different flow behaviours especially when  $\beta i_p < 0.5$ . All these changes in design can improve the flow pattern and avoid the dead zone inside storm chamber, where there is low velocity.
- Hydraulic testing was carried out on the direct flow where pipes connect with the storm chamber. The storm chamber junction needs to be investigated to identify the pattern of storm flow when lateral pipes are connected to the storm chamber.
- Studying practical suspended solid settlements and the residual time of flow inside the new stormwater chamber.



- This research used flexible pipes in their new position, pipe over pipe. Using rigid pipe in this position can generate different behaviours and distribution of stress between pipe and soil. This should be examined in subsequent research.
- Further research is recommended to test the Improved Iowa formula using different flexible pipe materials and different sizes of pipe.

## References

ABAQUS (2012) *ABAQUS 6.12, Analysis User's Manual*. Systèmes, D. USA: Dassault Systèmes. III.

Abbas, A., Ruddock, F., Alkhaddar, R., Rothwell, G. and Andoh, R. (2017) Pipeline–Soil Interaction Simulation under Live Loads Using Elastoplastic Finite Element Models with Laboratory Validation. *World Environmental and Water Resources Congress 2017* of Conference, Florida, USA.

Abbas, A., Ruddock, F., Alkhaddar, R., Rothwell, G. and Andoh, R. (2018) Improving the geometry of manholes designed for separate sewer systems. *Canadian Journal of Civil Engineering*, 46 (999), 13-25.

Abdellatif, M., Atherton, W., Alkhaddar, R.M. and Osman, Y.Z. (2015) Quantitative assessment of sewer overflow performance with climate change in northwest England. *Hydrological Sciences Journal*, 60 (4), 636-650.

Abolmaali, A. and Kararam, A. (2010) Nonlinear Finite-Element-Based Investigation of the Effect of Bedding Thickness on Buried Concrete Pipe. *Journal of Transportation Engineering* © ASCE, 136 (9), 6.

ACPA, A.C.P.A. (2008) *Design data 20: Circular precast concrete manhole*. Virginia, USA: American Concrete Pipe Association.

Ahn, N., Park, D.K., Lee, J. and Lee, M.K. (2009) Structural test of precast polymer concrete. *Journal of Applied Polymer Science*, 114 (3), 1370-1376.

Akinay, E. and Kilic, H. (2010) Use of empirical approaches and numerical analyses in design of buried flexible pipes. *Scientific Research and Essays*, 5 (24), 3972-3986.

Al-Saleem, H.I. and Langdon, W. (2016) Precast concrete manholes - a review and upgrade of current Practice. *In water New Zealand 2016 Stormwater Conference, New Zealand*.

- Alam, S., Allouche, E.N., Bartlett, C., Sherpa, A. and Keil, B. (2013) Experimental evaluation of soil-pipe friction coefficients for coated steel pipes. In: (ed.) *Pipelines 2013: Pipelines and Trenchless Construction and Renewals—A Global Perspective*. pp. 360-371.
- Albertson, M.L. (1948) Diffusion of submerged jets. *Am. Soc. Civil Engrs., Papers*, 74, 1571-1596.
- Andoh, R.Y.G., Stephenson, A.J. and Collins, P. (2005) Approaches to urban drainage systems management for the 21<sup>st</sup> century. *National Hydrology Seminar*.
- Arao, S., Kusuda, T., Moriyama, K., Hiratsuka, S., Asada, J. and Hirose, N. (2012) Energy losses at three-way circular drop manholes under surcharged conditions. *Water Science and Technology*, 66 (1), 45-52.
- Arao, S., Mihara, T. and Kusuda, T. (1999) An optimal design method of storm sewer network considered with manhole energy loss. *Doboku Gakkai Ronbunshu*, 1999 (614), 109-120.
- Arockiasamy, M., Chaallal, O. and Limpeteepakarn, T. (2006) Full-Scale Field Tests on Flexible Pipes under Live Load Application. *Journal of Performance of Constructed Facilities*, 20 (1), 21-27.
- Ashgriz, N. and Mostaghimi, J. (2002) An introduction to computational fluid dynamics. *Fluid flow handbook, 1*, pp.1-49.
- ASTM-C890 (2006) *Standard Practice for Minimum Structural Design Loading for Monolithic or Sectional Precast Concrete Water and Wastewater Structures*. United States.: American Section of the International Association for Testing Materials.
- ASTM-D2412 (2008) *Standard Test Method for Determination of External Loading Characteristics of Plastic Pipe by Parallel-Plate Loading*. ASTM D2412-02. USA: American National Standard. D2412.
- ATV-DVWK, D.V.f.W., Abwasser und Abfall (2000) *ATV-DVWK-Regelwerk: Static calculation of drains and sewers. A 127. Englische Ausg.* ATV-DVWK.

Bandler, A. (2007) *The Structural Capacity of Repaired Manholes*. M.S.c. Thesis thesis, Queen's University, Kingston, Canada.

Beieles, R.W., Environmental and Water Resources, I. (2013) *Pipelines for Water Conveyance and Drainage*. Reston, Virginia: American Society of Civil Engineers.

Bennett, P. (2012) *Evaluation of the solute transport characteristics of surcharged manholes using a RANS solution*thesis, University of Sheffield, UK.

Berney, E.S. and Smith, D.M. (2008) *Mechanical and Physical Properties of ASTM C33 Sand*.Geotechnical and Structures Laboratory. USA: US Army Corps of Engineers , Engineer Research and Development Center.

Bettez, J., Townsend, R.D. and Comeau, A. (2001) Scale model testing and calibration of City of Ottawa sewer weirs. *Canadian Journal of Civil Engineering*, 28 (4), 627-639.

Bizier, P. (2007) *Gravity Sanitary Sewer Design and Construction*. USA American Society of Civil Engineers.

Brachman, R.W., Moore, I.D. and Rowe, R.K. (2001) The performance of a laboratory facility for evaluating the structural response of small-diameter buried pipes. *Canadian Geotechnical Journal*, 38 (2), 260-275.

Brinkgreve, R.B.J. (2013) *Validating Numerical Modelling in Geotechnical Engineering*. NAFEMS.

Brown, S.F. and Brown, C.J. (2000) *The structural characteristics of manhole installations in pavements*.

BS, E. (2013) *Plastics piping systems for drainage and sewerage. Glass-reinforced thermosetting plastics (GRP) based on polyester resin (UP). Manholes and inspection chambers*.UK: BSI Standards Publication.

BS EN (2013) *Drain and sewer systems outside buildings*. UK: British Standards Institution (BSI): 180.

BSEN476 (2011) *General requirements for components used in drains and sewers*. UK: BSI British Standards: 25.

BSEN752:2008 (2013) *Drain and sewer systems outside buildings*. UK: British Standards.

Butler, D. and Davis, J.W. (2011) *Urban drainage*. 3rd ed. Crc Press, London.

Camp, T.R. (1966) The Problem of Separation in Planning Sewer Systems. *Journal (Water Pollution Control Federation)*, 38 (12), 1959-1962.

Can-Hua, Z., Zhu, D.Z. and Rajaratnam, N. (2008) Computational and Experimental Study of Surcharged Flow at a 90° Combining Sewer Junction. *Journal of Hydraulic Engineering*, 134 (6), 688-700.

Cembrano, G. (2004) Optimal control of urban drainage systems. A case study. *Control Engineering Practice*, 12 (1), 1-9.

Chaallal, O., Arockiasamy, M. and Godat, A. (2015) Field Test Performance of Buried Flexible Pipes under Live Truck Loads. *Journal of Performance of Constructed Facilities*, 29 (5).

Chakraborty, D. (2018) Lateral Resistance of Buried Pipeline in  $c-\phi$  Soil. *Journal of Pipeline Systems Engineering and Practice*, 9 (1), 06017006.

Chang, J.R., Yang, S.R. and Lin, K.H. (2014) Performance of new resin cement in rapid manhole vertical adjustment. *Materials Research Innovations*, 18 (S2), 2-2.

Christodoulou, G.C. (1991) Drop manholes in supercritical pipelines. *Journal of Irrigation and Drainage Engineering*, 117 (1), 37-47.

Chung, T.J. (2010) *Computational fluid dynamics*. Second edition, Cambridge University Press.

Corey, R.A. (2015) *Protection of Buried Flexible Pipes with a Geosynthetic: Experimental and Numerical Studies* thesis, University of Kansas, USA.

Cozzolino, L., Cimorelli, L., Covelli, C., Mucherino, C. and Pianese, D. (2015) An Innovative Approach for Drainage Network Sizing. *Water*, 7 (2), 546-567.

CPAA, C.P.A.o.A. (2016) *Loads on Circular Precast Concrete Manholes and Access Chambers. GUIDANCE NOTE (NZ)*. Australia: 8.

Crispino, G., Pfister, M. and Gissoni, C. (2018) Supercritical flow in junction manholes under invert-and obvert-aligned set-ups. *Journal of Hydraulic Research*, 1-13.

De Martino, F., Gissoni, C. and Hager, W.H. (2002) Drop in Combined Sewer Manhole for Supercritical Flow. *Journal of Irrigation & Drainage Engineering*, 128 (6), 397.

DEFRA (2011) *National Build Standards Design and Construction of new gravity foul sewers and lateral drains. Water Industry Act 1991 Section 106B, Flood and Water Management Act 2010 Section 42*. UK: Department for Environment Food and Rural Affairs. Annex B: 36.

Dennis, P. (2000) *Longitudinal dispersion due to surcharged manholes*, PhD thesis, University of Sheffield.

Dhakal, K.P. and Chevalier, L.R. (2017) Managing urban stormwater for urban sustainability: Barriers and policy solutions for green infrastructure application. *Journal of Environmental Management*, 203, 171-181.

Dhar, A.S., Moore, I.D. and McGrath, T.J. (2002) Evaluation of Simplified Design Methods for Buried Thermoplastic Pipe. *Pipeline Division Specialty*

Duque, N., Duque, D. and Saldarriaga, J. (2016) A new methodology for the optimal design of series of pipes in sewer systems. *Journal of Hydroinformatics*, 18 (5), 757-772.

Elshimi Tamer, M. and Moore Ian, D. (2013) Modeling the Effects of Backfilling and Soil Compaction beside Shallow Buried Pipes. *Journal of Pipeline Systems Engineering and Practice*, 4 (4), 04013004.

Faria, H.Q.d. (2005) *Failure analysis of GRP pipes under compressive ring loads*. Master of Science thesis, Universidade do Porto, Portugal.

Gargano, R. and Hager, W.H. (2002) Supercritical Flow across Sewer Manholes. *Journal of Hydraulic Engineering*, 128 (11), 1014-1017.

Goormans, T., Engelen, D., Bouteligier, R., Willems, P. and Berlamont, J. (2009) Design of self-cleansing sanitary sewer systems with the use of flushing devices. *Water Science and Technology*, 60 (4), 901-908.

Granata, F., De Marinis, G. and Gargano, R. (2014) Flow-improving elements in circular drop manholes. *Journal of Hydraulic Research*, 1-9.

Gross, D. and Seelig, T. (2011) *Fracture Mechanics With an Introduction to Micromechanics*. New York: Springer-Verlag Berlin Heidelberg.

Guymer, I., Dennis, P., O'Brien, R. and Saiyudthong, C. (2005a) Diameter and Surge Effects on Solute Transport across Surcharged Manholes. *Journal of Hydraulic Engineering*, 131 (4), 312-321.

Guymer, I., Dennis, P., O'Brien, R. and Saiyudthong, C. (2005b) Diameter and Surge Effects on Solute Transport across surcharged manhole *Journal of Hydraulic Engineering*, 131 (4), 10.

Guymer, I. and O'Brien, R. (2000) Longitudinal Dispersion due to Surcharged Manhole. *Journal of Hydraulic Engineering*, 126 (2), 137-149.

Hager, W.H. (2010) *Wastewater Hydraulics Theory and Practice*. Verlag Berlin Heidelberg: Springer.

Hager, W.H. and Gissoni, C. (2005) Supercritical flow in sewer manholes. *Journal of Hydraulic Research*, 43 (6), 660-667.

Hall, W.J. and Newmark, N.M. (1978) Seismic Design Criteria for Pipelines Facilities. *Journal of the Technical Councils of ASCE*, 104(1), pp.91-107.

Hamill, L. (2006) *Understanding Hydraulics* Palgrave Macmillan New York.

Hassan, K., Alam, S., Bartlett, C. and Allouche, E.N. (2014) Experimental Investigation of Soil-Pipe Friction Coefficients for Thermoplastic Pipes Installed in Selected Geological Materials. *North American Society for Trenchless Technology (NASTT)*, MM-T6-03.

Heller, V. (2011) Scale effects in physical hydraulic engineering models. *Journal of Hydraulic Research*, 49 (3), 293-306.

Helwany, S. (2007) *Applied Soil Mechanics with ABAQUS Applications*. Hoboken, NJ, USA: John Wiley & Sons, Inc.

Hides, S., Andoh, R. and Carroll, P. (2007) Approaches to Urban Wet-Weather Management for the 21<sup>ST</sup> Century. *South Pacific Stormwater Conference*,

HM-Government (2010) *Drainage and waste disposal. The Building Regulation UK*: NBS.

Hughes, J.B. (2009) *Manhole Inspection and Rehabilitation*. Reston, Va: American Society of Civil Engineers ASCE.

IKT, I.f.U.I. (2012) *Rehabilitation of Wastewater Manholes: Large Scale Tests and in-Situ Studies* Germany Institute for Underground Infrastructure: 26.



Islam, M.S. (2017) Comparative evaluation of vacuum sewer and gravity sewer systems. *International Journal of System Assurance Engineering and Management*, 8 (1), 37-53.

Ito, H. (1960) Pressure losses in smooth pipe bends. *Journal of Basic Engineering*, 82 (1), 131-140.

Jones, J.E. (2006) ASCE Combined Sewer Separation Project Progress. In: (ed.) *Great Works on Urban Water Resources (1962-2001)*. pp. 73-88.

Jung, J.K. (2011) *Soil-pipe interaction under plane strain conditions*. PhD thesis, Cornell University, USA.

Jung, J.K., Koo, D.H. and Zhang, K. (2014) Verification of the Pipe Depth Dependent Model using a finite element analysis. *Tunnelling and Underground Space Technology*, 39 (Supplement C), 34-40.

Kang, J., Jung, Y. and Ahn, Y. (2013) Cover requirements of thermoplastic pipes used under highways. *Composites Part B*, 55, 184.

Kang, J.S., Stuart, S.J. and Davidson, J.S. (2013) Analytical evaluation of maximum cover limits for thermoplastic pipes used in highway construction. *Structure and Infrastructure Engineering*, 9 (7), 667-674.

Kavvas, M. (2002) An appraisal of sewer system problems in developing countries. *Water Policy*, 4 (2002), 16.

Khondker, S. and Farag, M. (2008) An Innovative Storm Sewer Design in an Urban Environment. *World Environmental and Water Resources Congress*, USA of Conference.

Kleidorfer, M., Mikovits, C., Jasper-Tönnies, A., Huttenlau, M., Einfalt, T. and Rauch, W. (2014) Impact of a Changing Environment on Drainage System Performance. *Procedia Engineering*, 70, 943-950.

- Kouretzis, G.P., Sheng, D. and Sloan, S.W. (2013) Sand–pipeline–trench lateral interaction effects for shallow buried pipelines. *Computers and Geotechnics*, 54 (Supplement C), 53-59.
- Lau, S.-T.D. (2007) *Scaling dispersion processes in surcharged manholes*. PhD thesis, University of Sheffield, UK.
- Lees, A. (2012) *Obtaining Parameters for Geotechnical Analysis*. NAFEMS.
- Li, G. and Matthew, R.G.S. (1990) New Approach for Optomization of Urban Drainage Systems. *Journal of Environmental Engineering*, 116 (5), 18.
- Li, J., Joksimovic, D. and Tran, J. (2015) A Right-of-Way Stormwater Low Impact Development Practice. *Journal of Water Management Modeling*, C390.
- Marsalek, J. and Schreier, H. (2009) Overveiw of the Theme Issue: Innovation in Stormwater Management in Canada: The Way Forward *Water Quality Research Journal of Canada*, 44 (1), 6.
- Marvin, S. and Slater, S. (1997) Urban Infrastructure: The Contemporary Conflict Between Roads and Utilities. *Progress in Planning*, 48, 71.
- Masada, T. (2000) Modified Iowa Formula for vertical deflection of buried flexible pipe *Journal of Transportation Engineering*, 126 (5), 440.
- Maurer, M., Wolfram, M. and Anja, H. (2010) Factors affecting economies of scale in combined sewer systems. *Water Sci Technol*, 62 (1), 36-41.
- McGrath, T. (1998) *Design method for flexible pipe*. Arlington, MA: AASHTO Flexible Culvert Liaison Committe.
- McGrath, T.J., Moore, I.D., Hsuan, Y.G., Board, N.R.C.T.R., Program, N.C.H.R., Highway, A.A.o.S., Officials, T. and Administration, U.S.F.H. (2009) *Updated Test and Design Methods for Thermoplastic Drainage Pipe*. Transportation Research Board.

Moser, A.P. and Folkman, S. (2008) *Buried Pipe Design* 3rd ed. McGraw-Hill.

Najafi, M. and Sever, V.F. (2015a) *Structural Capabilities of No-Dig Manhole Reha.* USA Water Environment Research Foundation: 224.

Najafi, M. and Sever, V.F. (2015b) *Structural Capabilities of No-Dig Manhole Rehabilitation.* Water Environment Research Foundation. USA: 223.

Nguyen Long, D., Nguyen Thang, K.N., Tran Dai, Q. and Villiers, C. (2014) Productivity in Daytime and Nighttime Construction of Urban Sewer Systems. *Journal of Construction Engineering and Management*, 140 (7), 04014021.

Pedersen, F.B. and Mark, O. (1990) Head losses in storm sewer manholes: submerged jet theory. *Journal of Hydraulic Engineering*, 116 (11), 1317-1328.

Petroff, L.J. (1994) Design methodology for high density polyethylene manholes. In: Eckstein, D. (ed.) *Buried Plastic Pipe Technology*. ASTM STP 1222. pp. 52–65.

Pfister, M. and Gissoni, C. (2014) Head losses in junction manholes for free surface flows in circular conduits. *Journal of Hydraulic Engineering*, 140 (9), 06014015.

Pichler, T., Pucker, T., Hamann, T., Henke, S. and Qiu, G. (2012) High-Performance ABAQUS Simulations in Soil Mechanics Reloaded – Chances and Frontiers. *SIMULIA Community Conference*, USA, May 15-17 of Conference.

Polaskova, K., Hlavinek, P. and Haloun, R. (2006) Integrated approach for protection of an urban catchment area. *Desalination*, 188 (1-3), 51-59.

Rani, S., Prasad, N. and Krishna, S. (2014) Applicablity of Mohr Coulomb and Drucker Prager Models for Assessment of Undrained Shear Behaviour of Clayey Soils. *International Journal of Civil Engineering and Technology (IJCIET)*, 5 (10), 19.

Read, G.F. (2004) *Sewers : replacement and new construction*. Oxford : Elsevier Butterworth-Heinemann.

Read, G.F. and Vickridge, I. (2004) 17 - Social or indirect costs of public utility works. In: (ed.) *Sewers*. Oxford: Butterworth-Heinemann. pp. 339-366.

Riley, C.L. and Wilson, M. (2006) *Pipeline Separation Design and Installation Reference Guide*. USA: Washington State Department of Ecology and Washington State Department of Health. Version 9.

Rossman, L. and Huber, W. (2016) Storm Water Management Model Reference Manual Volume I–Hydrology (Revised). *US Environmental Protection Agency: Cincinnati, OH, USA*.

Rubinato, M. (2015) *Physical scale modelling of urban flood systems*, PhD thesis, University of Sheffield, UK.

Saadeldin, R.M. (2016) *A Novel Approach for Simulating Soil and Pipe Response to Seasonal, Environmental and Field Conditions*thesis, Faculty of Graduate Studies and Research, University of Regina.

Sabouni, R. and El Naggar, M.H. (2011a) Circular precast concrete manholes: experimental investigation. *Canadian Journal of Civil Engineering*, 38 (3), 319-330.

Sabouni, R. and El Naggar, M.H. (2011b) Circular precast concrete manholes: numerical modeling. *Canadian Journal of Civil Engineering*, 38 (8), 909-920.

Saldarriaga, J., Rincon, G., Moscote, G. and Trujillo, M. (2017) Symmetric junction manholes under supercritical flow conditions. *Journal of Hydraulic Research*, 55 (1), 135-142.

Sangster, W., Wood, H., Smerdon, E. and Bossy, H. (1958) Pressure changes at storm drain junctions.

Sargand, S. and Masada, T. (2003) Soil arching over deeply buried thermoplastic pipe. *Transportation Research Record: Journal of the Transportation Research Board*, (1849), 109-123

Sargand, S.M., Masada, T., Tarawneh, B. and Gruver, D. (2005) Field performance and analysis of large-diameter high-density polyethylene pipe under deep soil fill. *Geotechnical and Geoenvironmental Engineering*, 131 (1), 13.

Saricimen, H., Shameem, M., Barry, M.S., Ibrahim, M. and Abbasi, T.A. (2003) Durability of proprietary cementitious materials for use in wastewater transport systems. *Cement and Concrete Composites*, 25, 421-427.

Sawko, R. (2012) *Mathematical and computational methods of non-Newtonian, multiphase flows*. PhD thesis, Cranfield University, UK.

Shamsi, U.M., Benner, S.P. and Fletcher, B.A. (1996) A Computer Mapping Program for Sewer Systems. In: James, W. (ed.) *Advances in Modeling the Management of Stormwater Impacts*. 121 South Main Street, Chelsea, Michigan 48118: Ann Arbor Press, Inc. pp. 97-114.

Simpson, G.H. (2009) *Investigation of Suitable Soil Constitutive Models for 3-D Finite Element Studies of Live Load Distribution Through Fills Onto Culverts*. Project 15-29: CNA Consulting Engineers. Appendix A: 145.

Sonnenwald, F.C. (2014) *Identifying the residence time distributions of urban drainage structures from solute transport data using maximum entropy deconvolution*, PhD thesis, University of Sheffield, UK.

Sousa, V., Almeida, N.M., Dias, L.A. and Branco, F.A. (2014) Risk-Informed Time-Cost Relationship Models for Sanitation Projects. *Journal of Construction Engineering and Management*, 140 (5).

Spangler, M.G. (1941) The Structural Design of Flexible Pipe Culverts. *Iowa Engineering Experiment Station*, Bulletin 153.

Starkl, M., Brunner, N., Flogl, W. and Wimmer, J. (2009) Design of an institutional decision-making process: The case of urban water management. *Journal of Environmental Management*, 90 (2), 1030.

Stovin, V., Guymer, I. and Lau, S. (2008) Approaches to validating a 3D CFD manhole model. *11th international conference on urban drainage of Conference*.

Suleiman, M.T. (2002) *The structural performance of flexible pipes*. PhD thesis, Digital Repository @ Iowa State University, USA.

Swamee, P.K. and Sharma, A.K. (2013) Optimal design of a sewer line using Linear Programming. *Applied Mathematical Modelling*, 37 (6), 4430-4439.

Tait, S.J., Ashley, R.M., Cashman, A., Blanksby, J. and Saul, A.J. (2008) Sewer system operation into the 21st century, study of selected responses from a UK perspective. *Urban Water Journal*, 5 (1), 79-88.

Talesnick, M.L. and Frydman, S. (2018) Soil pressure and pipe deformation measurements for characterizing flexible pipe-soil systems under shallow cover. *Journal of Pipeline Systems Engineering and Practice*, 9 (1), 11.

Thompson, B. (2012) *Combined Sewer Overflow (CSOs) & CSO Screens Stockton-on-Tees TS18 3BB, TRPM-TN002*: Thompson Research - Project Management Ltd: 7.

Ti, K.S., Bujang B.K. Huat, J.N., Moh'd Saleh Jaafar and Sew, G.S. (2009) A Review of Basic Soil Constitutive Models for Geotechnical Application. *Electronic Journal of Geotechnical Engineering*, 14, 18.

Tian, Y., Liu, H., Jiang, X. and Yu, R. (2015) Analysis of stress and deformation of a positive buried pipe using the improved Spangler model. *Soils and Foundations*, 55 (3), 485-492.

TML (2017) *Precise & Flexible Strain Gauges* Tokyo Sokki Kenkyujo Co., L. Tokyo, Japan.

Tsai, C.-C., Meymand, P., Dawson, E. and Wong, S.A. (2015) Behaviour of segmental pipeline protective vaults subjected to fault offset. *Structure and Infrastructure Engineering*, 11 (10), 1369-1382.

Uzomah, V. (2016) *Rapid decision support tool based on novel ecosystem service variables for retrofitting sustainable drainage systems in the presence of trees* thesis, University of Salford, UK.

Wang, F., Du, Y.-J., Zhou, M. and Zhang, Y.-J. (2016) Experimental Study of the Effects Produced by a Backfilling Process on Full-Scale Buried Corrugated HDPE Pipes in Fine-Grained Soils. *Journal of Pipeline Systems Engineering and Practice*, 7 (1).

Watkins, R.K. (1957) *Characteristics of the modulus of passive resistance of soil*. Doctor of Philosophy thesis, Iowa State University.

WEF, W.E.F. (2008) *Alternative sewer systems*. Water Environment Federation manual of practice, USA.

Willi, G. (1998) *Schacht für Kontroll-, Wartungs- oder Reparaturarbeiten* Office, E. P. Germany: 2.

Würmseher, H. (2014) *Abwasserschacht (Manhole)* Markenamt, D. P.-u. Germany DE202014000333U1: 7.

Zhao, C.-H., Zhu, D.Z. and Rajaratnam, N. (2006) Experimental Study of Surcharged Flow at Combining Sewer Junctions. *Journal of Hydraulic Engineering*, 132 (12), 1259-1271.

Zhou, M., Du, Y.-J., Wang, F., Arulrajah, A. and Horpibulsuk, S. (2017) Earth pressures on the trenched HDPE pipes in fine-grained soils during construction phase: Full-scale field trial and finite element modeling. *Transportation Geotechnics*, 12 (Supplement C), 56-69.

## **Appendices**

### Appendix I

**(CD ) videos of the hydraulic experiments applied to the manholes**



## Appendix II

### Similitude of Applied Loads

#### II.1 The Physical Model

Engineering is basically design and analysis with attention paid to cost, risk and safety. In this section, the design considered is a buried manhole and pipe. Analysis is achieved through a model that predicts performance. Mathematical models are convenient while physical, small-scale models are better for complex pipe-soil interaction. The most dependable models are full-scale prototypes (Moser and Folkman, 2008). Mathematical models are often written to describe prototype performance because it is impractical to perform a full-scale prototype study for every buried pipe to be installed. The set of principles upon which a model can be related to the prototype for predicting prototype performance is called similitude. Similitude applies to all models— mathematical, small-scale and prototype.

There are three basic steps to achieve similitude.

1. Fundamental variables (FVs) are all the variables that affect the phenomenon. All the FVs must be interdependent.
2. Basic dimensions (BDs) are the dimensions by which the FVs can be written. The basic dimensions for buried pipes are usually force (F) and length (L).
3. Pi terms are combinations of FVs that meet the following three requirements:  
(a) The number of pi terms must be at least the number of FVs minus the number of BDs. (b) The pi terms must all be dimensionless.

The pi term for the physical model in this research can be written by using:

<b><u>FVs</u></b>	<b><u>BDs</u></b>
W = wheel load	F
D = Diameter of manhole or pipe	L
EI = wall stiffness	FL
E' = soil modulus	FL <sup>2</sup>
H = height of soil cover	L
P = all pressures	FL <sup>2</sup>

To calculate the applied load on the physical manhole model, the pi terms (P/E') are used. The models have been designed to have equal pi terms for both the physical model and real scale model.

$$(P/E') \text{ physical model} = (P/E') \text{ Real scale model}$$

The assumption is that the same soil could be placed and compacted in the same way for both models. Therefore, all pressures P must be the same in the physical model and at corresponding points in the real scale model. For example, tyre pressures must be the same in the model and prototype. The soil pressure must be the same at corresponding depths in the model and prototype (Moser and Folkman, 2008).

### II.1.1 *Applied Load on Manhole*

Tyre footprint pressure, generated from AASHTO categories of traffic loads (HS15, HS20 and HS25), and a double heavy load, were applied on the cover of the prototype (Table 0-1). This level of loading (double heavy load) was heavier than that which should have been applied to the prototype because the researcher wanted to test an extreme case and generate data about the displacement of the new manhole compared to the traditional one. These data were compared with the FE model results under the same series of applied loads and boundary conditions.

The wheel load H25 on a real scale model, approximately 89 200 N, applied on the tyre foot print (0.508 m x 0.254 m) results in a pressure reading of 691kPa, this equivalent to the pressure applied on the physical model (0.03976 m<sup>2</sup>). This requires a load of between 25 and 35 kN.

Table 0-1 The applied load on the Physical model.

Categories of traffic load	Pressure kPa	Applied load kN	Applied Pressure kPa
	Real scale model		physical model
HS15	414	15-20	377.25-503
HS20	552	20-25	503-628.76
HS25	691	25-35	628.76-880.25
Double heavy loads	1383	40-50	1006-1257.5

### II.1.2 *Applied load on the pipe*

The transferred load is distributed on an area that increases vertically with depth (pyramid slope), dependent on the soil friction angle (30°). The pressure on the pipe is the pressure at the base of the pyramid in a direction along the length and

is limited by the trench wall in a direction along the width (Figure II.1). This method is used to estimate the load applied on the crown of a pipe as shown in Table II-2 , taking into consideration the width of the trench while decreasing the friction between the trench walls and filling soil. The small dimensions of the trench and the supposedly rigid sidewall, enables calculation of the load transferred from the tyre footprint to the soil projection on the pipe level, as shown in Figure II.1 below.

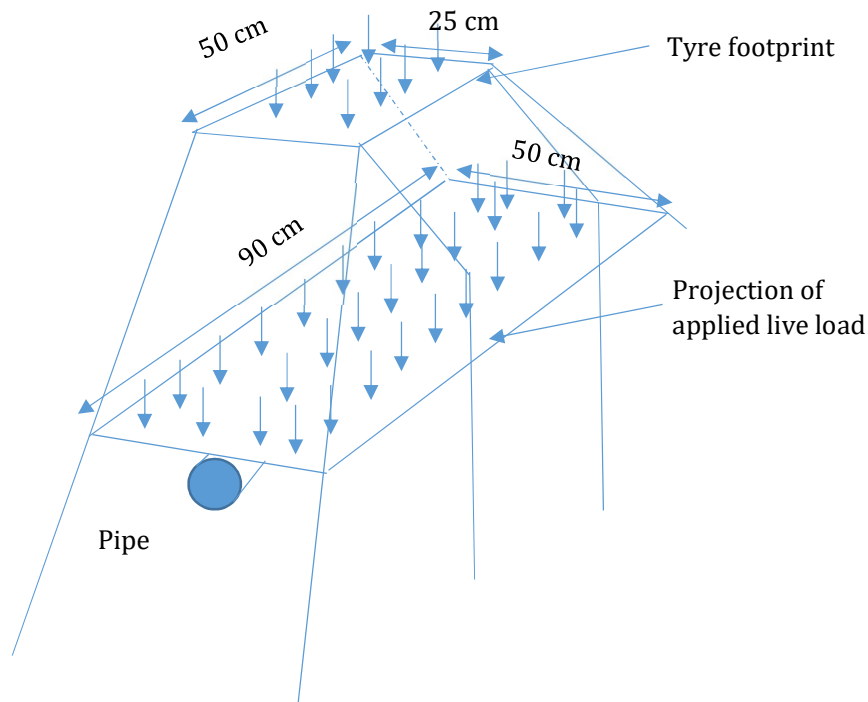


Figure II.1 Sketch of the distribution of the applied load on the soil through the trench at the crown pipe level.

Table II-2 Live load data for AASHTO H-20 and H-25.

Cover depth [m]	AASHTO H-20 Live load transferred to pipe [N/mm <sup>2</sup> ]	AASHTO H-25 Live load transferred to pipe [N/mm <sup>2</sup> ]
0.3	0.0862	0.108
0.6	0.0383	0.048
0.9	0.0288	0.036

## II.2 Hydraulic physical model

Physical hydraulic model tests always involve scale effects if the scale ratio  $\neq 1$  because it is impossible to correctly model all force ratios. The comparison study and dimensionless parameters include geometrical ratios as well as force ratios ( $Fr$ ) which are used to mitigate the scale effects and to decrease the expected error. These dimensionless parameters are widely applied in hydraulic modelling, allowing for a general presentation of the results. Because they are related as a function of dimensionless parameters, no scale ratios are required to up-scale them (Heller, 2011).

In addition, the authors used a relatively a small scale ratio (1:3 for conventional manhole and 1:5 for new design of manhole) to reduce scale effects, this ratio used by many researchers who have studied the hydraulic properties of manholes (Gargano and Hager, 2002; Zhao et al, 2006; Stovin et al, 2008; Granata et al, 2011; Arao et al, 2012). Pfister and Gisonni (2014); Crispino et al (2018) stated that the scale effects due to surface tension can be negligible for the manhole when  $h \geq 0.04$  m. The scale effects due to viscosity can be ignored for open boundary hydraulic models when the scale ratio is bigger than (1/10) or  $Re > 4000$  (Hamill, 2006).

As mentioned above the parameters used in this research have been used by many researchers investigating the hydraulic performance of manholes. Christodoulou (1991) stated that local head loss in a manhole is essentially dependent on the geometrical characteristics and a dynamic parameter in the form of a Froude number, expressed in terms of the flow velocity and the depth of flow. Pedersen and Mark (1990) proposed that the head loss of the manhole is a function of the

diameter ratio (manhole diameter and pipe diameter) and the shape of the manhole.

The head loss ( $\Delta H$ ) under free-surface conditions and surcharge flow in this experiment, for both manholes, is mainly depend on the following dimensional variables:

$$\Delta H = f(v, D_m, D_p, h_o, g)$$

It is assumed that the slope of the pipe is gradual, and that the pipe and manhole are circular. The energy loss coefficient ( $K$ ) is then expressed as a function of non-dimensional, independent variables representing the geometrical ratios as well as force ratios, as shown in the equation below.

$$\frac{\Delta H}{\frac{v^2}{2g}} = f\left(\frac{h_o}{D_m}, \frac{h_o}{D_p}, \frac{v^2}{gh_o}\right) \text{ that means } K = f(\beta_{im}, \beta_{ip}, Fr) \quad (\text{Christodoulou, 1991; Arao et al, 2012})$$

## Appendix III

### Type of Elements in ABAQUS

#### III.1 Type of Elements

The type of elements in the FE using by ABAQUS, can be characterized by the following:

- Family
- Degrees of freedom (directly related to the element family)
- Number of nodes
- Formulation
- Integration

Each element in ABAQUS has a unique name, such as T2D2, S4R or C3D8I. The element name identifies each of the five aspects of an element.

##### *III.1.1 Family*

Figure III. shows the element families most commonly used in a stress analysis. One of the major distinctions between different element families is the geometry type that each family assumes.

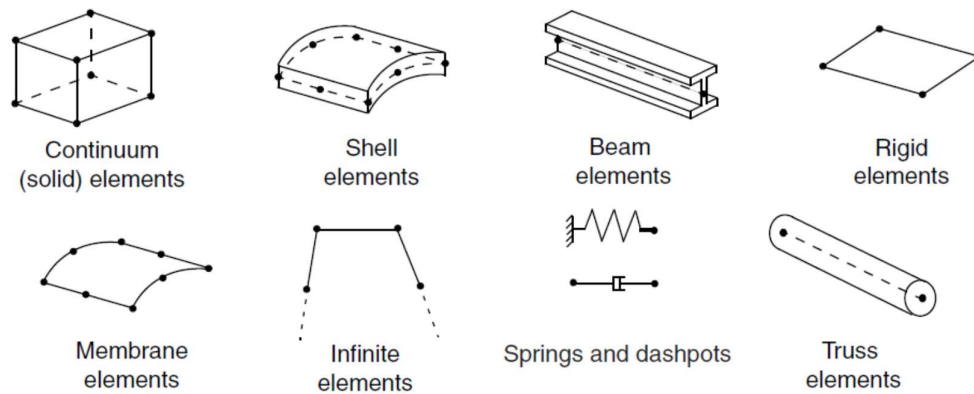


Figure III.1 Commonly used element families (ABAQUS, 2012). [Reprinted with permission from Dassault Systemes Simulia Corp]

The first letter or letters of an element's name indicates which family the element belongs to. For example, the S in S4R indicates this is a shell element, while the C in C3D8I, indicates this is a continuum element.

### ***III.1.2 Number of nodes***

Displacements, rotations and the other degrees of freedom are calculated only at the nodes of the element. At any other point in the element, displacements are obtained by interpolation from the nodal displacements. Normally the interpolation order is determined by the number of nodes used in the element. Elements that have nodes only at their corners, such as the 8-node brick shown in Figure III.(a), use linear interpolation in each direction and are often called linear elements or first-order elements. Elements with mid-side nodes, such as the 20-node brick shown in Figure III. (b), use quadratic interpolation and are often called quadratic elements or second-order elements. Modified triangular or tetrahedral



elements with midside nodes, such as the 10-node tetrahedron, are shown in Figure III. (c).

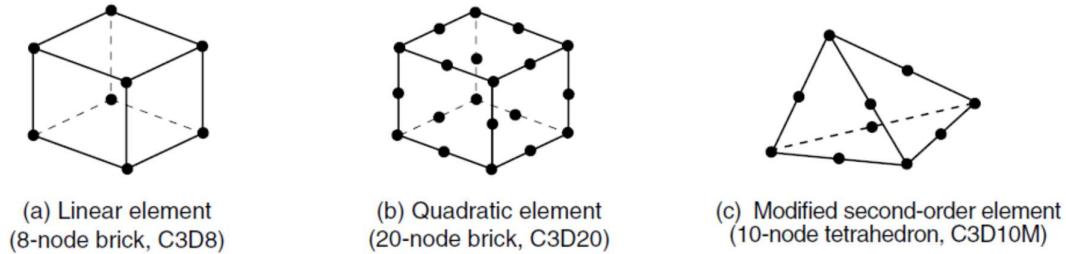


Figure III.2 Linear brick, quadratic brick and modified tetrahedral elements (ABAQUS, 2012). [Reprinted with permission from Dassault Systemes Simulia Corp]

### ***III.1.3 Formulation***

An element's formulation refers to the mathematical theory used to define the element's behaviour. In the absence of adaptive meshing, all the stress/displacement elements in ABAQUS are based on the Lagrangian, or material description of behaviour: the material associated with an element remains associated with the element throughout the analysis: material cannot flow across element boundaries. In the alternative Eulerian or spatial description, elements are fixed in space as the material flows through them. Eulerian methods are commonly used in fluid mechanics simulations.

### ***III.1.4 Integration***

ABAQUS uses numerical techniques to integrate various quantities over the volume of each element. Using Gaussian quadrature for most elements, ABAQUS evaluates the material response at each integration point in each element.

ABAQUS uses the letter "R" at the end of the element name to distinguish reduced-integration elements.

In this research, and as a reason for using increased thickness for the features used in the FE models such as manhole, pipes and soil, two main type elements were selected.

### **III.2 Continuum elements**

The continuum (solid) family of stress/displacement elements is the most comprehensive of the element libraries in ABAQUS. Among the different element families, continuum or solid elements can be used to model the widest variety of components. Conceptually, continuum elements simply model small blocks of material in a component. Since they may be connected to other elements on any of their faces, continuum elements, like bricks in a building or tiles in a mosaic, can be used to build models of almost any shape, subject to a wide range of loadings. Continuum stress/displacement elements in ABAQUS have names that begin with the letter "C." The next two letters indicate the dimensionality and usually, but not always, the active degrees of freedom in the element. The letters "3D" indicate a three-dimensional element.

### **III.3 Beam elements**

Beam elements are used to model components in which one dimension (the length) is significantly greater than the other two dimensions and only the stress

in the direction along the axis of the beam is significant, such as a steel bar reinforcement used in a manhole.

Beam element names in ABAQUS begin with the letter "B." The next character indicates the dimensionality of the element, "3" used for three-dimensional beams.

The third character indicates the interpolation used; "1" for linear interpolation, "2" for quadratic interpolation and "3" for cubic interpolation.

#### **III.4 The methodology followed for selecting elements**

We tried to minimize the mesh distortion as much as possible by using a fine mesh of linear, reduced-integration elements (C3D8R) as recommended by the ABAQUS guidelines. The 3D model used in this research meant using hexahedral (brick-shaped) elements wherever possible. They give the best results for the minimum cost (less running time). Complex geometries can be difficult to mesh completely with hexahedrons therefore, beam and tetrahedral elements may be used in some analyses.

The figures below illustrate the method used to identify the type of elements, the contact between the features and the process used to identify the steps for running the job in ABAQUS.

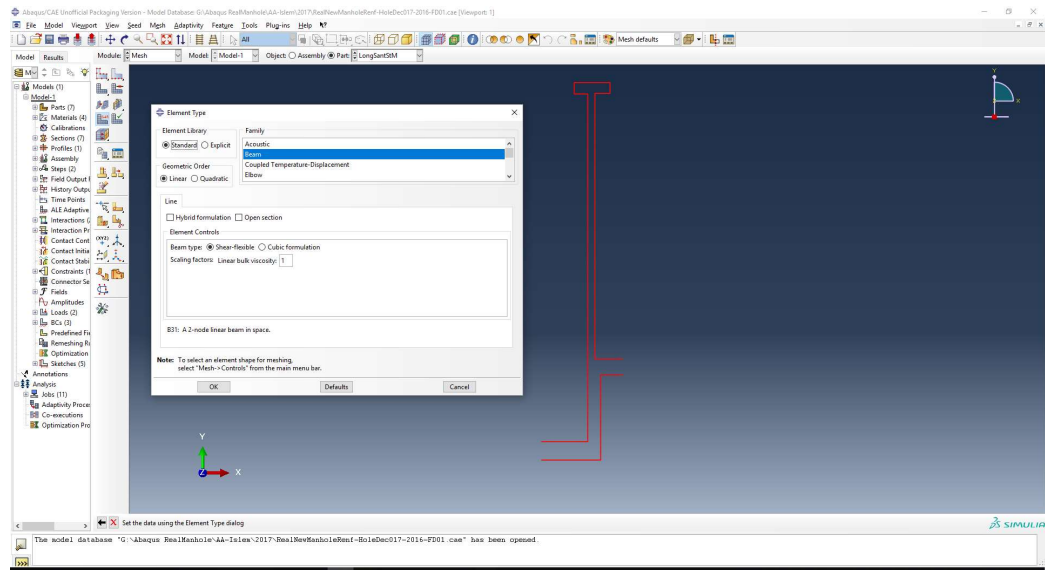


Figure III.3 Selecting the beam element type for the reinforcement bar in the ABAQUS FE manhole model.

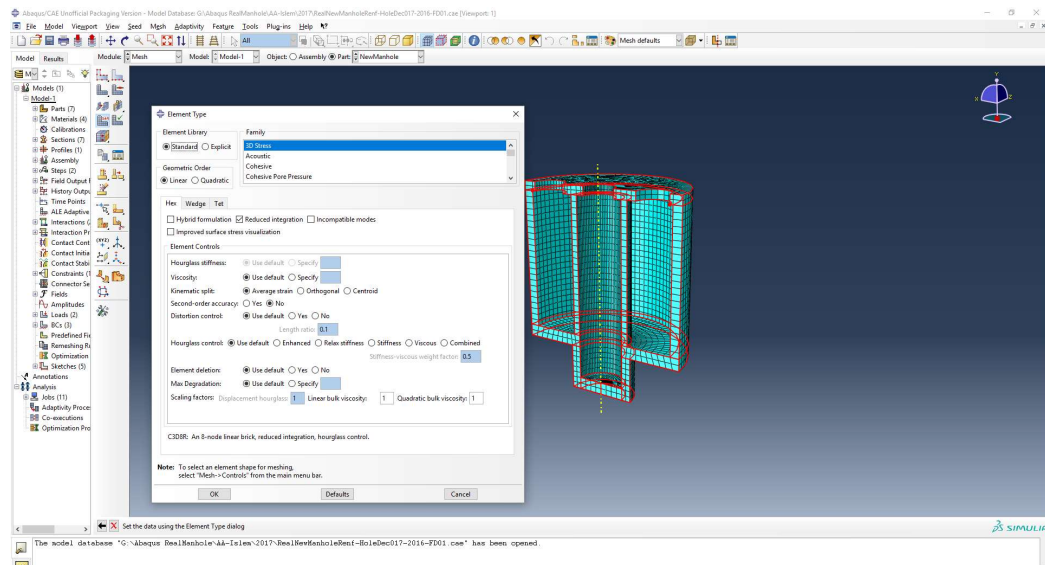


Figure III.4 Selecting the continuum elements type for the manhole structure in the ABAQUS FE manhole model.

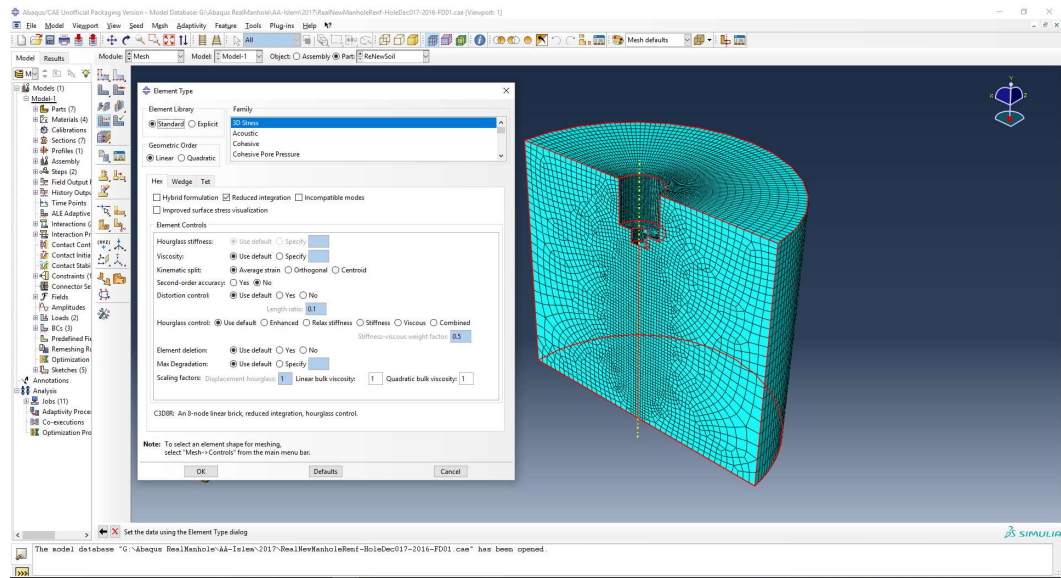


Figure III.5 Selecting the continuum elements type for the soil in the ABAQUS FE manhole model.

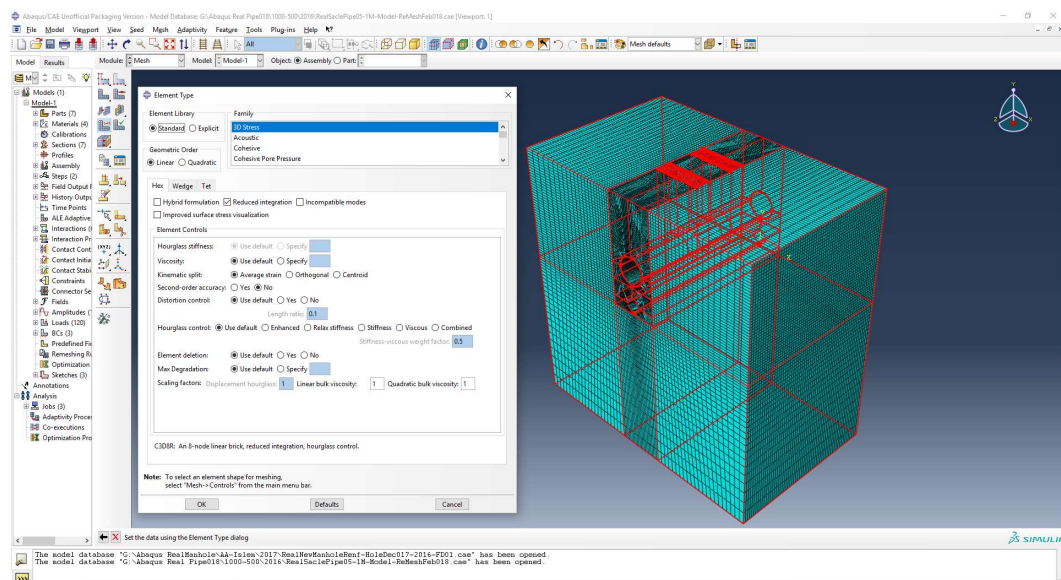


Figure III.6 Selecting the continuum elements type for the system in the ABAQUS FE buried pipe model.

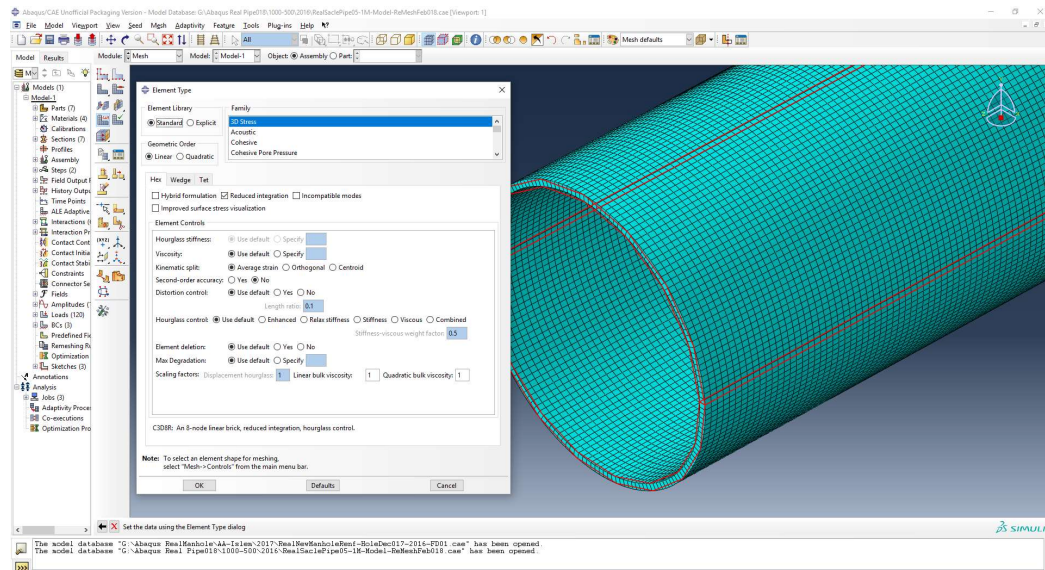


Figure III.7 Selecting the continuum elements type for the pipe in the ABAQUS FE buried pipe model.

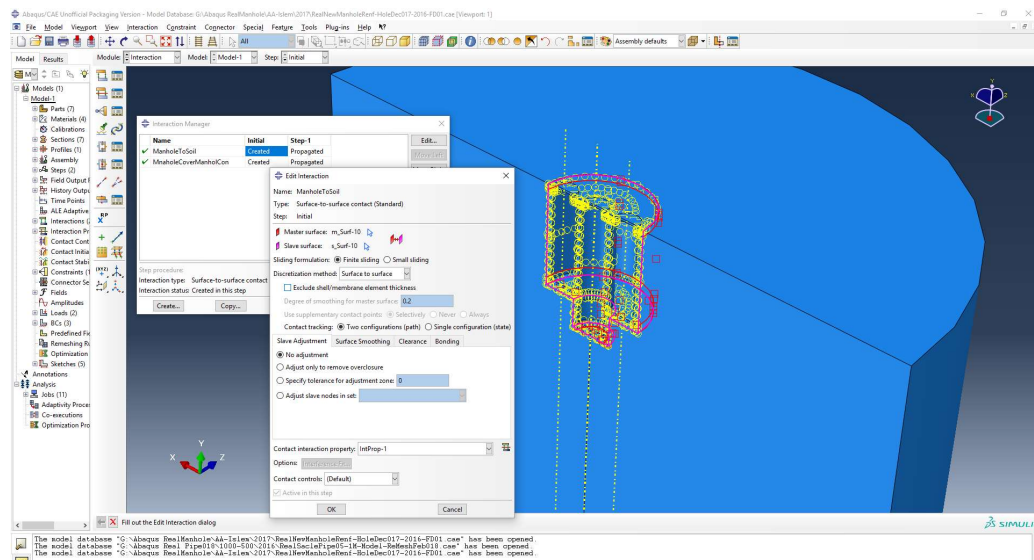


Figure III.8 Identifying the surface- surface contact regime between the manhole and the surrounding soil in the ABAQUS FE manhole model.



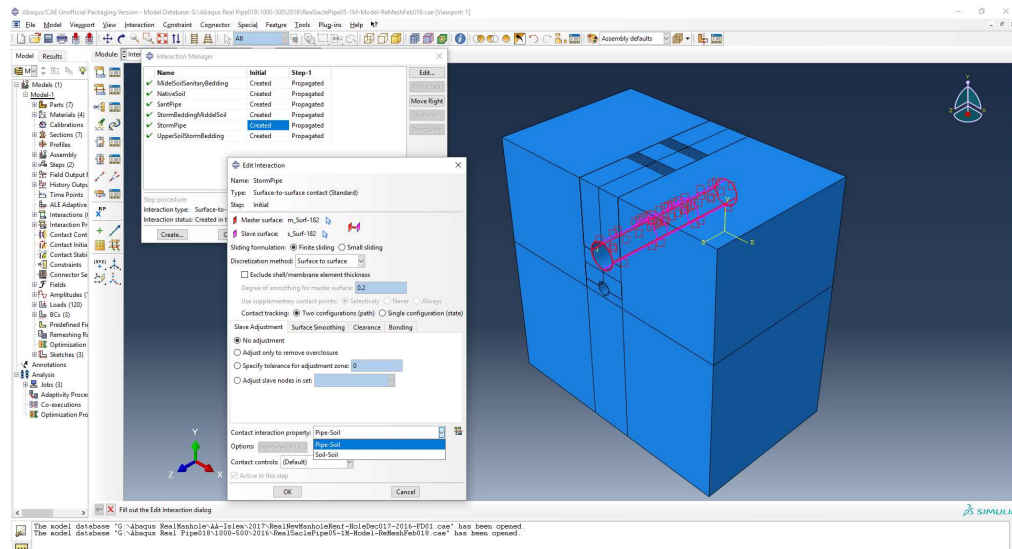


Figure III.9 Identifying the surface- surface contact regime between the pipe and the surrounding soil in the ABAQUS FE buried pipe model.

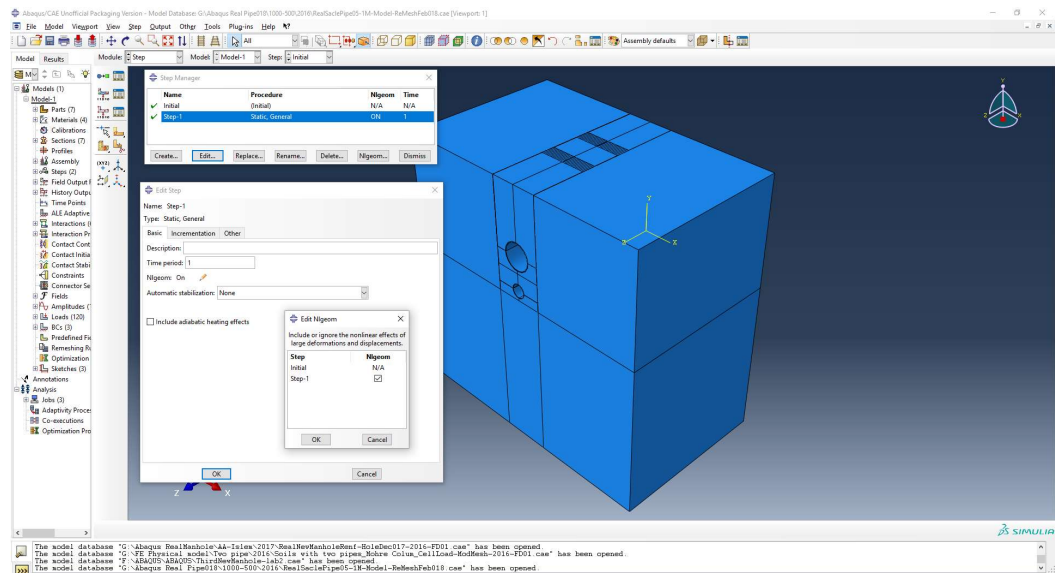


Figure III.2 Identifying the nonlinear solution for the step in the ABAQUS FE buried pipe model.

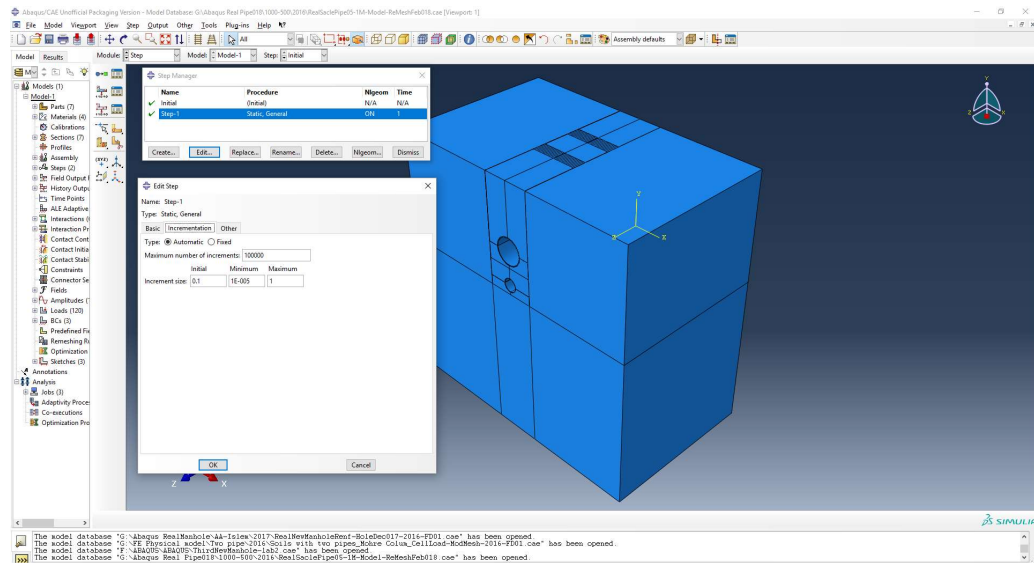


Figure III.3 Identifying the number of increments for the step in the ABAQUS FE buried pipe model.

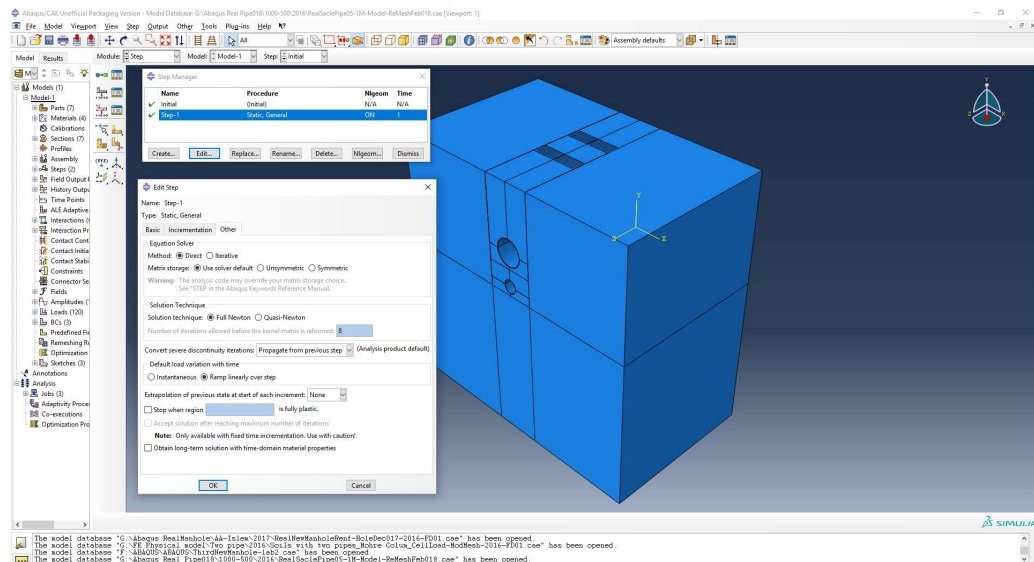


Figure III.4 Identifying a full newton solution for the step in the ABAQUS FE buried pipe model.





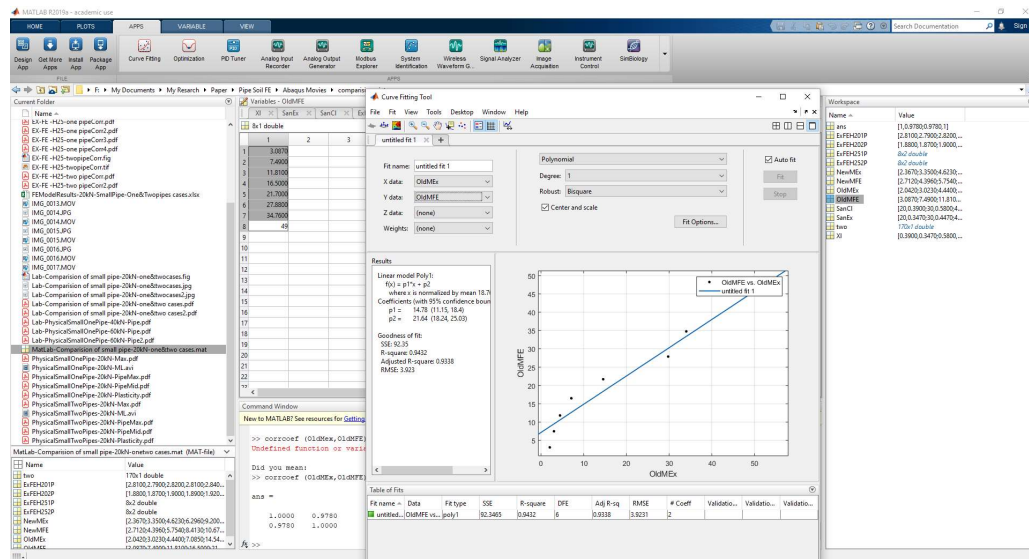


Figure IV.2 The method used to calculate  $R^2$  for the results presented in Figure 4.18, comparison of the displacement results from both experimental works and the FE model for the conventional manhole prototype in soil under live loads.

The validation process for the new placement of pipes was conducted in this research, as there is a scarcity of field or research data available for this new pipe position. The validation was conducted on the physical lab model under a series of applied loads (H20 and H25). An FE model for this physical model was established using the same dimensions, materials and boundary conditions, and exposed to the same series of loads. The validation process is discussed in detail in the FE model of the physical model, which compares the experimental and FE model results for the physical lab model.

The results show acceptable consistency,  $R = 0.84$  to  $0.93$  for the H20 applied load and  $R = 0.93$  to  $0.95$  for the H25 applied load, as demonstrated in Figure IV., Figure IV., Figure IV.5 and Figure IV.. This is an acceptable validation process allowing the researchers to upgrade the FE model to a full-scale model.

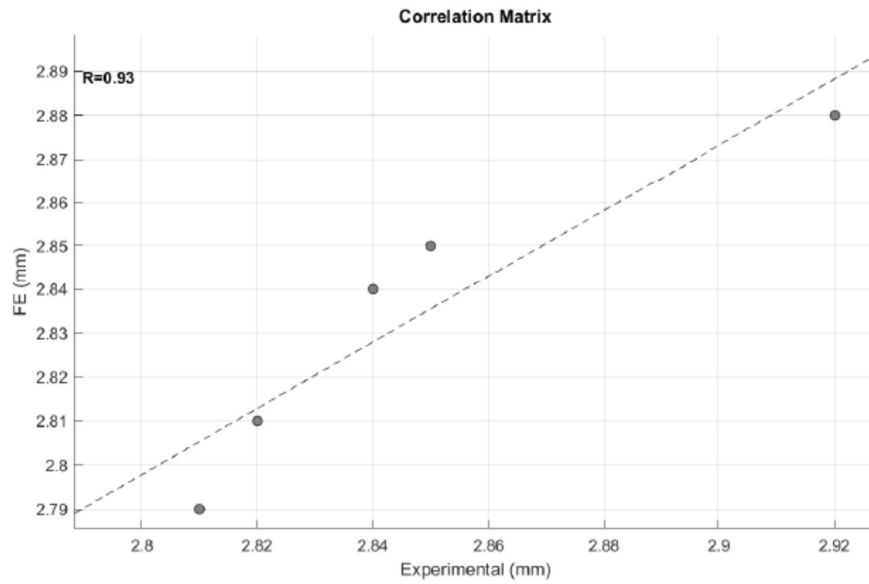


Figure IV.3 The correlation between FE output and experimental results for sanitary pipe deflection, lying in the trench under H2O applied load, as shown in Figure 6.7 (a).

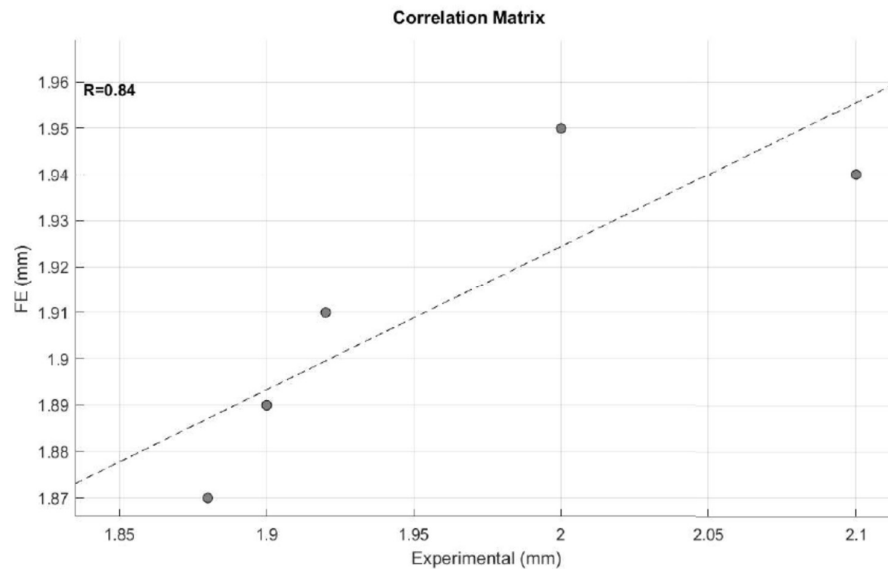


Figure IV.4 The correlation between FE output and experimental results for sanitary pipe deflection, lying in the trench below the storm pipe under H2O applied load, as shown in Figure 6.7 (a).

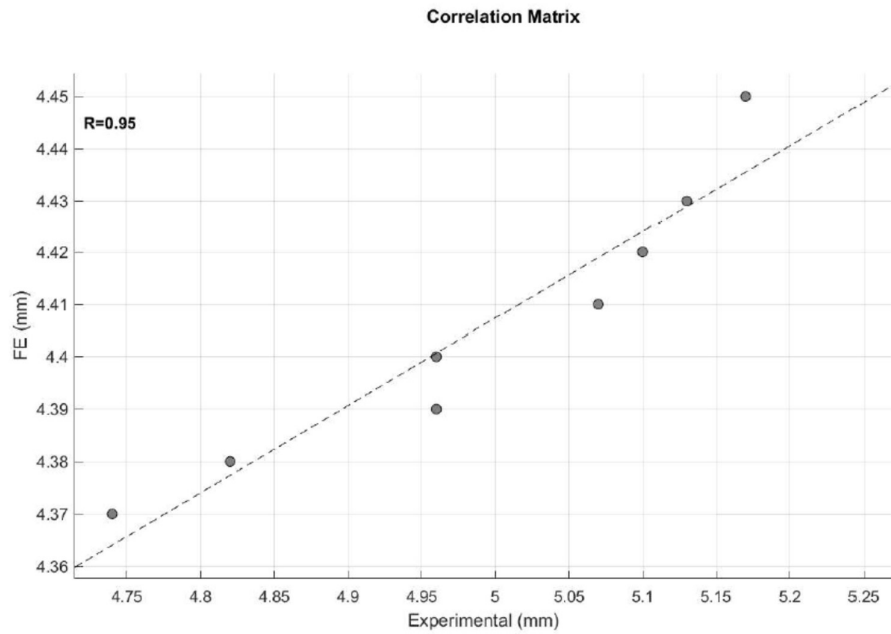


Figure IV.5 The correlation between FE output and experimental results for sanitary pipe deflection, lying in the trench under H25 applied load, as shown in Figure 6.7 (b).

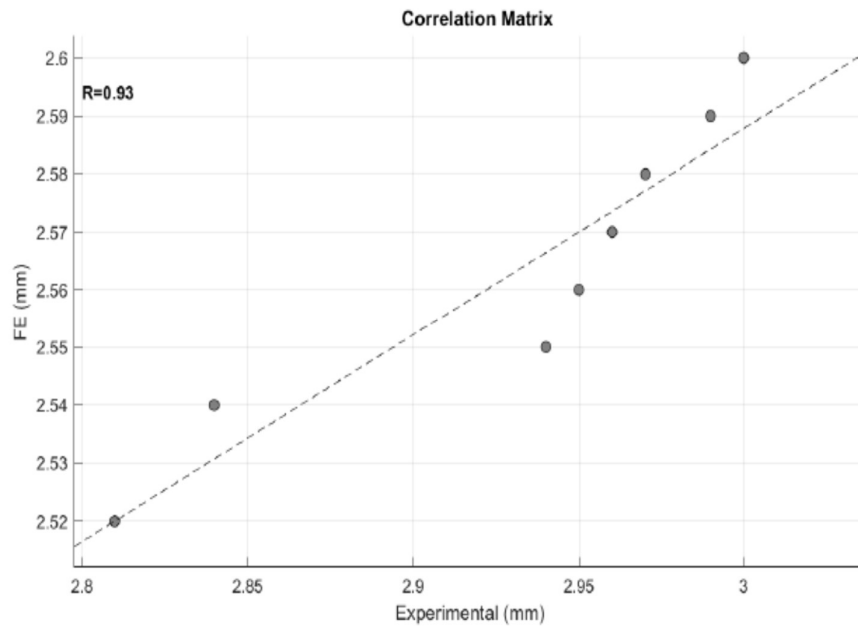


Figure IV.6 The correlation between FE output and experimental results for sanitary pipe deflection, lying in the trench below the storm pipe under H25 applied load, as shown in Figure 6.7 (b).

Correlations between the CFD outputs and the hydraulic experimental results are presented in Figure IV., Figure IV.6, Figure IV. and Figure IV.7.

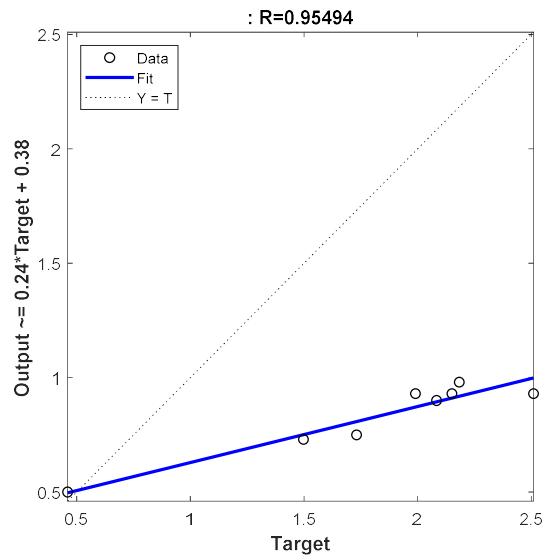


Figure IV.7 The correlation between the CFD output and experimental results for Figure 5.14, a comparison between the velocities measured at the centre of both the CFD and the physical model manholes.

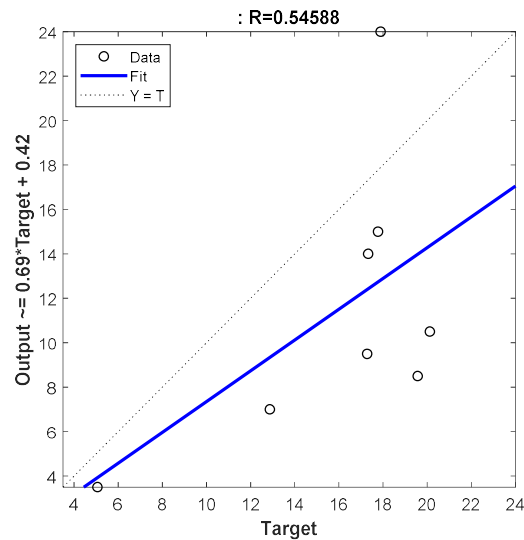


Figure IV.6 The correlation between the CFD output and experimental results for Figure 5.15, a comparison between the differences in head pressures measured at the inlet and outlet of the manhole for both the CFD and the physical model.

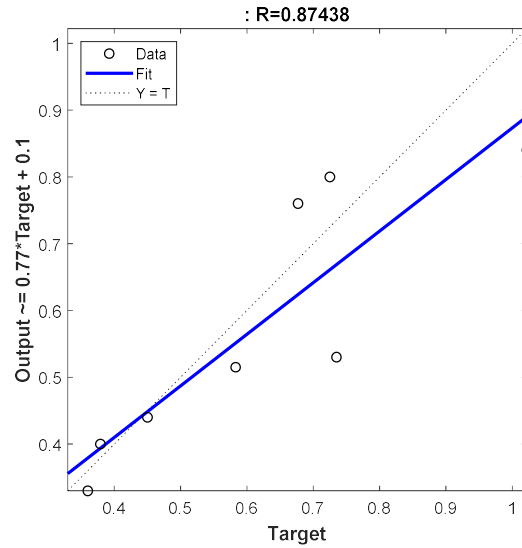


Figure IV.9 The correlation between the CFD output and experimental results for Figure 5.18, a comparison between the velocities measured at the centre of the new manhole for both the CFD and physical model.

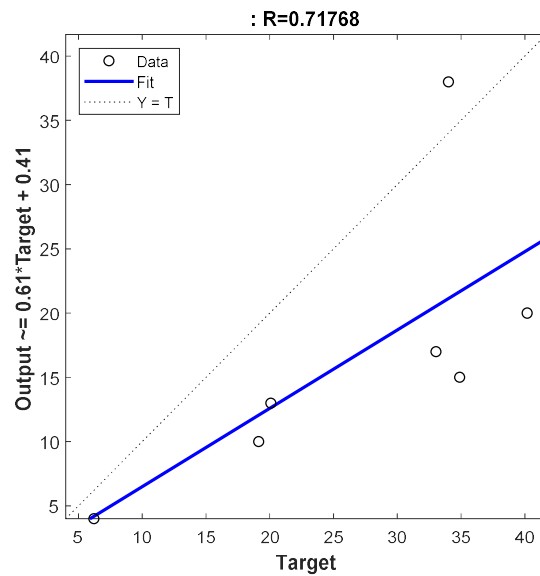


Figure IV.7 The correlation between the CFD output and experimental results for Figure 5.19, a comparison between the differences in head pressures measured at the inlet and outlet of the new manhole for both the CFD and physical model.

The correlation between the experimental results and the output of the improved Iowa formula was approximately 0.99%, which is a good match, as shown in Figure IV..

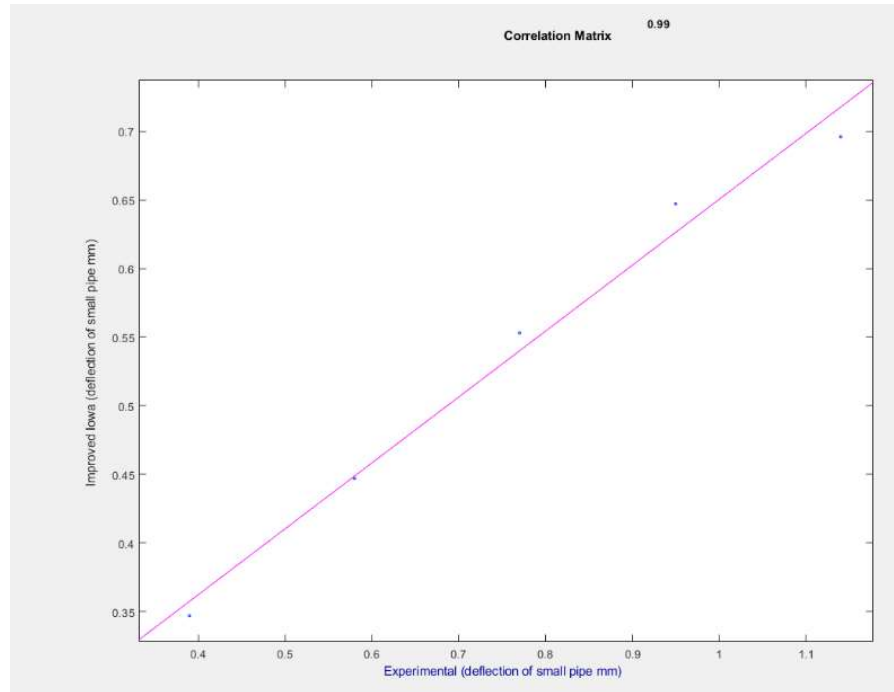


Figure IV.11 The correlation between the experimental results and improved Iowa formula output Figure 6.22, comparison of deflection of the sanitary pipe when two pipes are set in one trench using the developed Iowa formula, the original Iowa formula and the experiment.

## IV.2 Equations derived from the results data

Excel (2016) was used to simulate the data in equations using Trendline tools to intercept the best-fit line for said data. After charting the data, several different line fits available to define the trend line beyond the data set, such as power, were used to derive Equations 5-3 and 5-4 (Figure IV.12). The Logarithmic trendline option was used to simulate the data in equations 5-5 to 5-8, shown in Figure IV. and Figure IV..

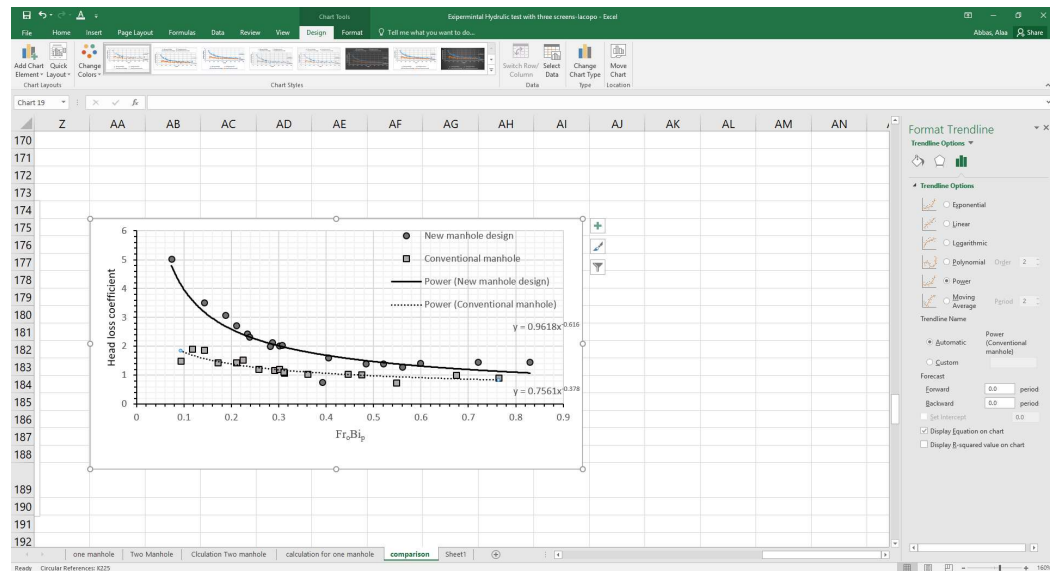


Figure IV.12 Use of the Excel curve fit method to derive the equations for the data presented in Figure 5.8, relationship between the head loss coefficient and the non-dimensional dynamic momentum component ( $Fr_0 B_i \rho$ ) for the new and conventional manholes.



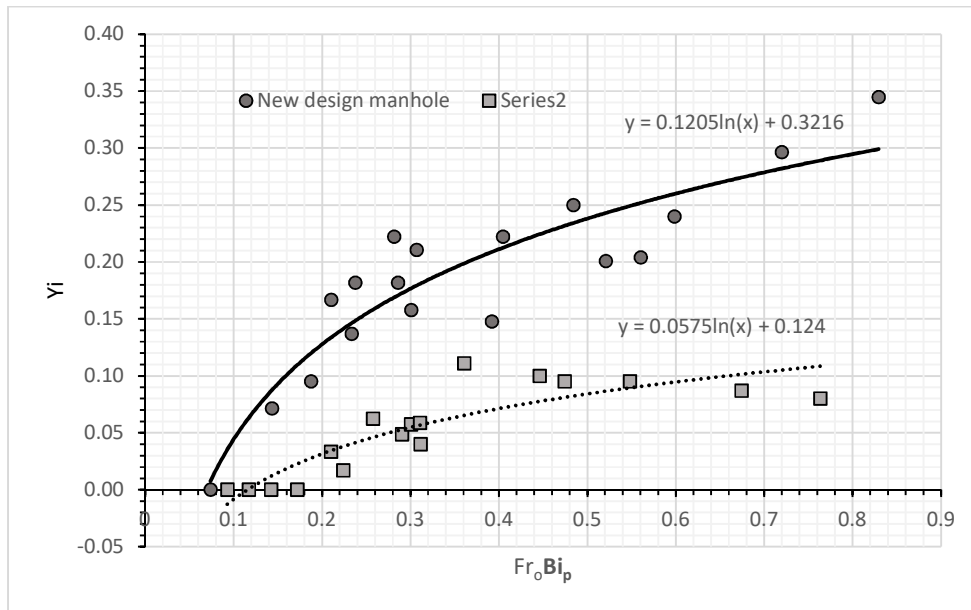


Figure IV.13 Use of the Excel curve fit method to derive the equations for the data presented in Figure 5.11, the amplitude of average shockwaves ( $Y_i$ ) against the non-dimensional dynamic momentum component ( $Fr_0 Bi_p$ ) for both the conventional and the new manhole.

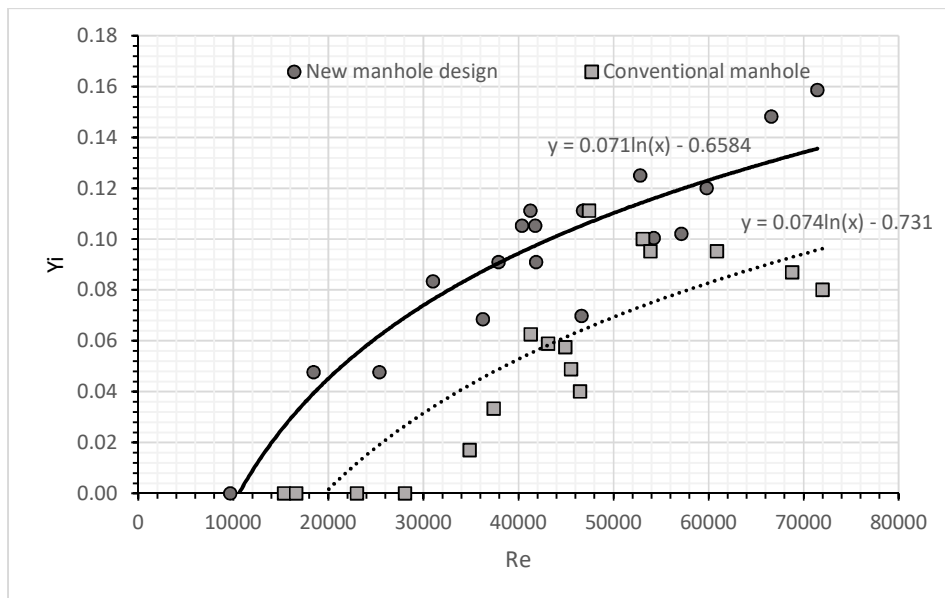


Figure IV.14 Use of the Excel curve fit method to derive the equations for the data presented in Figure 5.22, the amplitude of average shockwaves ( $Y_i$ ) against non-dimensional Reynolds number ( $Re$ ) for both the conventional and new manhole.

## **Appendix V**

### **List of Publications**

#### **Published journal papers:**

- 1- Abbas, A., Ruddock, F., Alkhaddar, R., Rothwell, G. and Andoh, R. (2018a) Improving the geometry of manholes designed for separate sewer systems. *Canadian Journal of Civil Engineering*, 46 (999), 13-25.
- 2- Abbas, A., Ruddock, F., Alkhaddar, R., Rothwell, G., Carnacina, I. and Andoh, R. (2018b) 3D Finite Element Model Simulating the Behaviour of Filling Soils Used to Set Up a New Placement Method for Separate Sewer Systems. *Journal of Civil Engineering and Construction*.
- 3- Abbas, A., Salloom, G., Ruddock, F., Alkhaddar, R., Hammoudi, S., Andoh, R. and Carnacina, I., 2019. Modelling Data of an Urban Drainage Design Using a Geographic Information System (GIS) Database. *Journal of Hydrology*.

#### **Journal papers under reviewing:**

- 1- Abbas, A., Ruddock, F., Alkhaddar, R., Rothwell, G., Carnacina, I. and Andoh, R. (2019) Hydraulic performance of a new manhole designed to separate sewer systems. *Journal of Hydraulic Research*.
- 2- Abbas, A., Ruddock, F., Alkhaddar, R., Rothwell, G., Carnacina, I. and Andoh, R. (2019) Nonlinear Finite Element-Based Investigation of the Structural Performance of Two Flexible Pipes Set in One Trench with a New Placement Method for Separate Sewer Systems. *Journal of Tunnelling and Underground Space Technology*.

#### **Published conference papers:**

1. Abbas, A., Dissanayake, K., Ruddock, F., Alkhaddar, R. and Andoh, R. (2016) An Innovative Design for Lateral Pipes in Sewer Systems. *11th Pipeline Technology Conference 2016*.
2. Abbas, A., Dulaimi, A., Shanbara, H. and Ruddock, F. (2017a) Impact of New Method for Laying Separate Sewer System on Pavement Layers. *The 3<sup>rd</sup> BUiD Doctoral Research Conference*, Dubai, UAE.
3. Abbas, A., Ruddock, F., Alkhaddar, R., Rothwell, G. and Andoh, R. (2017b) Pipeline–Soil Interaction Simulation under Live Loads Using Elastoplastic Finite

Element Models with Laboratory Validation. In *World Environmental and Water Resources Congress 2017* (pp. 453-464).

4. Abbas, A., Ruddock, F., Alkhaddar, R., Rothwell, G. and Andoh, R. (2017c) Impact of new method for laying separate sewer system on street surface using Cold Mix pavement layer. Cutting Edge 2017, UK.
5. Abbas, A., Ruddock, F., Alkhaddar, R., Rothwell, G. and Andoh, R. (2017d) An innovative method for the construction of a separate sewer system in narrow streets in UK and EU cities. Faculty Research Week, UK.
6. Abbas, A., Ruddock, F., Alkhaddar, R., Rothwell, G. and Andoh, R. (2017e) A novel method for design drainage system in sustainable city. 9th Manchester Metropolitan University Postgraduate Research Conference, Manchester, UK.
7. Abbas, A., Ruddock, F., Alkhaddar, R., Rothwell, G. and Andoh, R., (2017f) A Novel Method for Laying Sustainable Separate Sewer Systems. International Conference on Sustainable Infrastructure 2017 (pp. 13-25).
8. Abbas, A., Ruddock, F., Alkhaddar, R., Rothwell, G. and Andoh, R. (2017h). Standardised System Methodology for National and International Identification of Sewer Systems. International Conference on Sustainable Infrastructure 2017(pp. 367-374).
9. Abbas, A. (2018a) Advantages of using flexible pipes in innovative method for designing a separated sewer system. Plastic Pipes in Infrastructure, UK.
10. Abbas, A., Carnacina, I., Ruddock, F., Alkhaddar, R., Rothwell, G. and Andoh, R., (2018b) September. Improving the Hydraulic Integrity to Separate the Sewer System in Hilly Regions Using a New Manhole Design. International Conference on Urban Drainage Modelling (pp. 825-829). Springer, Cham.
11. Abbas, A., Ruddock, F., Alkhaddar, R. and Rothwell, G. (2018c) FE Model to Test the Structural Performance of a New Design For Manhole Buried in the Soil. Taking Engineering Analysis And Simulation To The Next Level, UK.
12. Abbas, A., Ruddock, F., Alkhaddar, R., Rothwell, G. and Andoh, R. (2018d) Impact of the External Surface Area of a Manhole on the Behaviour of a Manhole Structure Buried in the Sand. World Environmental and Water Resources, USA.
13. Abbas, A., Ruddock, F., Alkhaddar, R., Rothwell, G. and Andoh, R. (2018e) Testing the Modified Iowa Formula to Calculate the Deflection of Two Flexible Pipes Buried in Sand into One Trench under Live Loads. Pipelines 2018, Canada.

#### **Patents:**

- 1- Abbas, A. (2017) *Improvements relating to lateral pipes*. Intellectual Property Office UK.
- 2- Abbas, A., Alkhaddar, R. and Ruddock, F. (2018) *Manhole and Sewer Networks* World Intellectual Property, UK.